

**NONINVASIVE FLUORESCENCE MONITORING FOR FUNCTIONAL
ASSESSMENT OF MURINE GLIOMA TREATMENT**

A Thesis
Submitted to the Faculty
in partial fulfillment of the requirements for the
degree of

Doctor of Philosophy

by

SUMMER LYNNE GIBBS-STRAUSS

Thayer School of Engineering
Dartmouth College
Hanover, New Hampshire

May 2008

Examining Committee:

Chairman _____
Brian W. Pogue

Member _____
P. Jack Hoopes

Member _____
Julia A. O'Hara

Member _____
Keith D. Paulsen

Member _____
Tayyaba Hasan

Charles K. Barlowe
Dean of Graduate Studies

© 2008 Trustees of Dartmouth College

(Signature of Author)

**Thayer School of Engineering
Dartmouth College**

**“Noninvasive Fluorescence Monitoring for Functional Assessment of Murine
Glioma Treatment”**

Summer L. Gibbs-Strauss

Doctor of Philosophy

Committee:

Brian W. Pogue

Julia A. O’Hara

P. Jack Hoopes

Keith D. Paulsen

Tayyaba Hasan

ABSTRACT

Molecular optical imaging *in vivo* has potential for functional assessment of tumor tissue at the cellular and subcellular level. Advances in biological understanding of genomics and proteomics have increased the knowledge of possible cellular targets, allowing for functional detection, diagnosis, characterization and treatment monitoring of disease *in situ*. Yet current cancer treatment monitoring largely relies on structural imaging to quantify tumor size change, which can occur well after many identified molecular events have transpired. In this work, three model glioma cell lines were implanted orthotopically, including a green fluorescent protein (GFP) expressing rat gliosarcoma (9L-GFP), a human glioma (U251) and the GFP variant of this (U251-GFP). Tumor morphology was assessed through magnetic resonance imaging (MRI) and *ex vivo* pathology, which confirmed distinct phenotypic growth patterns of the three tumor models. The tumors were non-invasively monitored using an optical transmission spectroscopy system targeted at imaging tumor cell metabolism and EGFR activity with

near-infrared light. Monitoring of tumor cell metabolism was accomplished through detection of Protoporphyrin IX (PpIX) which is formed via the Heme synthesis pathway from the administered prodrug, Aminolevulinic Acid (ALA), and assesses mitochondrial activity. The molecular expression of epidermal growth factor receptor (EGFR) was quantified using an infrared dye (IRDye 800CW) conjugated to epidermal growth factor (EGF). Monitoring tumor cell metabolism and molecular expression of EGFR via transmission spectroscopy provided early functional information of *in vivo* tumor tissues which could be correlated to later occurring structural changes seen by MRI. Animals were treated with Erbitux (Cetuximab), a monoclonal antibody therapy which inhibits EGFR, and monitored noninvasively for response to therapy via fluorescence signature changes, which corresponded to changes in uptake of EGF conjugated to IRDye 800CW. Fluorescence signatures attained for populations of mice for both PpIX and EGF conjugated IRDye 800CW were variable highlighting the heterogeneity of cancer as a disease. Functional monitoring of glioma tissue was achieved with noninvasive near-infrared transmission spectroscopy and will increase the ability of molecular imaging strategies to interpret cancer as an individual disease. Throughout this work, there were several technological strategies for optimal measurement of the signal developed which included transmission based spectroscopic imaging, normalization of the transmitted fluorescence signal to the transmitted excitation signal and spectral fitting of the fluorescence signal to deconvolve the fluorescent signal from any non-specific background signal. In this work these strategies were optimized to attain the most possible signal and incorporated into a prototype monitor that would allow widespread use in cancer screening and monitoring.

ACKNOWLEDGEMENTS

My experience at the Thayer School of Engineering as a graduate student has been a very positive one which I will always look back on fondly. I owe much of my happiness over the last five years to my advisor Professor Brian Pogue, without whom this thesis could not have been completed. Brian is an outstanding advisor who is truly committed to student learning and his students' professional development. I greatly appreciate his availability to discuss everything from experiments and data to career options. Brian's enthusiasm for research is contagious and has carried me through the difficult times when none of my research efforts seemed to yield positive results. Brian leads by example and I have greatly appreciated the opportunity to observe first hand the qualities a well respected researcher, exceptional graduate student advisor and outstanding professor exemplifies.

The assistance I received in the lab from Professor Julia O'Hara was invaluable. Her daily presence in the lab and willingness to discuss the smallest details of each experiment with me were greatly appreciated. The number of *in vitro* and *in vivo* experiments completed for this thesis work could not have been accomplished without the countless hours Julia spent helping me. I am grateful to Professor Jack Hoopes for the time he spent with me discussing pathology and examining countless slides. The sections in this thesis work on brain tumor pathology stemmed directly from stimulating discussions I had with Jack. I would also like to thank Professor Keith Paulsen and Professor Tayyaba Hasan for their useful discussions and advice as well as for serving on my thesis committee.

I would like to thank everyone in the bioimaging research group at Dartmouth both past and present. This diverse group of researchers has a wealth of knowledge and as a graduate student, the assistance was invaluable. Thanks to Dr. Shudong Jiang for helping me with any and all optical equipment, to Dr. Subha Srinivasan for all of her help with the modeling studies and Dr. Venkat Krishnaswamy for his help with the spectrometers. A special thanks to Dr. Kimberley Samkoe for her assistance with many of the *in vitro* and *in vivo* experiments that were completed as well as data discussion.

I also greatly appreciate the other graduate students in the bioimaging group. A special thanks to my friend Scott Davis with whom I have completed countless homework assignments, laboratory experiments, and had many discussions about research, career and life. Thanks also to my other group members and friends Colin Carpenter, Dax Kepshire, Imran Rizvi, Jia Wang, Zhiqiu Li and Ashley Laughney. Thanks to all my friends currently at Thayer and Dartmouth and to those who have moved on, I have greatly appreciated your friendship and hope that we will stay in touch.

I have had the opportunity to collaborate with Dr. Mark Israel and Dr. Nathan Watson and this work have benefited from useful discussions with them and their research group on brain cancer and its complexities. I would also like to thank Rendy Strawbridge for helping me find everything in the labs at DHMC.

Last but certainly not least, I would like to thank my family for their everlasting love and support. To my parents Barbara and Marvin Gibbs for listening to me prattle on endlessly about my research and for always supporting, loving and encouraging me and to my sister Ashley Gibbs for being a most wonderful friend and confidant. A special

thanks to my husband Matthew Strauss for his patience, love and endless support as I worked to finish my degree for which I will be forever grateful.

TABLE OF CONTENTS

ABSTRACT.....	ii
ACKNOWLEDGEMENTS	iv
LIST OF TABLES.....	xii
LIST OF FIGURES	xiv
Chapter 1 - Introduction & Overview	1
1.1. Project Rational.....	1
1.2. Background.....	3
1.2.1. Brain Cancer & Treatment Options.....	3
1.2.2. Epidermal Growth Factor Receptor Biology & Erbitux Therapy	5
1.2.3. Experience with ALA-PpIX & Brain Cancer.....	8
1.2.4. Brain Cancer Therapy Monitoring: Current State & Promising Research.....	10
1.2.5. Optical Molecular Imaging.....	14
1.3. Thesis Overview	15
Chapter 2 - <i>In Vitro</i> PpIX Studies & <i>In Vivo</i> Brain Tumor Models	17
2.1. Introduction.....	17
2.2. <i>In Vitro</i> PpIX Production Variability.....	21
2.2.1. <i>In Vitro</i> PpIX Production Variability Materials & Methods.....	21
2.2.2. <i>In Vitro</i> PpIX Production Variability Results	25
2.3. <i>In Vitro</i> Variability of PpIX Production in Brain Tumor Cell Lines.....	30
2.4. Green Fluorescent Protein Transfection of U251 Human Glioma Line.....	32
2.5. Intracranial Brain Tumor Implantation Procedure.....	35

2.6. Discussion.....	39
Chapter 3 - Fluorescence Imaging Systems.....	43
3.1. Introduction.....	43
3.2. Reflectance Fluorescence Imaging	45
3.2.1. Broad Beam Imaging vs. Raster Scanning	47
3.2.2. Reflectance Imaging System Quantification	49
3.3. ALA-Induced PpIX Mouse Skin Fluorescence	55
3.4. Transmission Fluorescence Imaging	62
3.4.1. Single Channel Transmission Spectroscopy System.....	63
3.4.2. Multichannel Transmission Spectroscopy System.....	64
3.4.3. Spectral Data Post-Processing Procedure.....	67
3.5. Discussion.....	69
Chapter 4 - Phantom & Model Based Studies.....	72
4.1. Introduction.....	72
4.2. Phantom Studies of Reflectance Imaging Systems.....	73
4.3. Phantom Studies of Transmission Imaging Systems	76
4.4. Modeling Studies of Transmission Imaging Systems.....	84
4.4.1. Modeling Materials & Methods	84
4.4.2. Model of Single Channel System vs. Multichannel System	87
4.4.3. Optimal Light Paths for Tumor Detection with the Multichannel System	91
4.5. Discussion.....	100

Chapter 5 - Magnetic Resonance Imaging for the Visualization of Murine

Glioma.....	105
5.1. Introduction.....	105
5.2. Magnetic Resonance Imaging Methods.....	107
5.3. Magnetic Resonance Imaging Contrast & Tumor Detection.....	108
5.4. Case Studies: Sample MRI & <i>Ex Vivo</i> Verification	115
5.4.1. 9L-GFP Tumor-Bearing Mice	116
5.4.1.1. Case 1: T1 TSE CE MRI for 9L-GFP Tumor Detection.....	116
5.4.1.2. Case 2: T2 TSE MRI Correlation to 9L-GFP Tumor Edema.....	118
5.4.1.3. Case 3: 9L-GFP Visibility by T1 IR, T2 FLAIR & T1 Difference MRI.....	120
5.4.1.4. Case 4: 3T vs. 7T MRI for 9L-GFP Tumor Detection.....	122
5.4.2. U251 Parent Line Tumor-Bearing Mice.....	125
5.4.2.1. Case 1: T1 TSE CE & T2 TSE MRI Necessary to Characterize U251 Tumors.....	125
5.4.2.2. Case 2: U251 Tumor Border Delineation Difficult by MRI.....	129
5.4.3. U251-GFP Tumor-Bearing Mice	131
5.4.3.1. Case 1: U251-GFP Diffuse Tumor Invisible by MRI.....	132
5.4.3.2. Case 2: U251-GFP Diffuse Tumor Subtle Gadolinium Uptake Not Detectable	135
5.4.3.3. Case 1: U251-GFP Ventricle Growth Visible by Asymmetric Ventricle Swelling	137
5.4.3.4. Case 2: U251-GFP Symmetric Ventricle Growth Invisible by 3T or 7T MRI.....	140
5.4.4. U251-GFP Bulk Tumor Growth.....	143
5.4.4.1. Case 1: U251-GFP Bulk Tumor Growth Detectable by All MRI Sequences	143
5.5. Discussion.....	145

Chapter 6 - *In Vivo* PpIX Studies

6.1. Introduction.....	148
------------------------	-----

6.2. Pilot Studies for Tumor Detection & Skin Photobleaching.....	150
6.3. Skin PpIX Photobleaching Studies	155
6.3.1. Time Course Red (635 nm) Photobleaching	156
6.3.2. Blue Light (400 +/- 5 nm) Photobleaching.....	161
6.4. PpIX Tumor Detection by Transmission Spectroscopy Summary	166
6.5. PpIX Production Pattern Heterogeneity: <i>Ex Vivo</i> Analysis.....	171
6.6. Discussion.....	179
Chapter 7 - Epidermal Growth Factor Uptake & Erbitux Therapy Monitoring....	184
7.1. Introduction.....	184
7.2. Epidermal Growth Factor Uptake & Erbitux Therapy Monitoring <i>In Vitro</i>	186
7.3. Erbitux Therapy Monitoring <i>In Vivo</i>	192
7.3.1. Erbitux Therapy Monitoring In Vivo Materials & Methods	192
7.3.2. Erbitux Therapy Monitoring In Vivo Results	195
7.3.2.1. Transmission Spectroscopy Measurements Week 1	195
7.3.2.2. Transmission Spectroscopy Measurements Week 2	200
7.3.2.3. Optimal Light Paths for Multichannel System <i>In Vivo</i>	204
7.4. EGF-IRDye Fluorescence: <i>Ex vivo</i> Analysis.....	207
7.4.1. 9L-GFP Tumor-Bearing Mice	209
7.4.2. U251-GFP Tumor-Bearing Mice	213
7.5. Discussion.....	217
Chapter 8 - Imaging Case Studies	221
8.1. Introduction.....	221

8.2. Erbitux Treatment Monitoring Case Studies	223
8.3. Erbitux Treated Group Case Studies	225
8.3.1. U251-GFP Treated Mouse with Constant Fluorescence Intensity	225
8.3.2. U251-GFP Treated Mouse with Decreased Fluorescence Intensity.....	228
8.3.3. 9L-GFP Tumor Mouse with Increased Fluorescence Intensity.....	231
8.3.4. 9L-GFP Treated Mouse with Constant Fluorescence Intensity.....	233
8.4. EGF Uptake Case Studies.....	235
8.4.1. U251-GFP Untreated Mouse with Increased Fluorescence Intensity	235
8.4.2. U251-GFP Untreated Mouse with Constant Fluorescence Intensity	238
8.4.3. 9L-GFP Untreated Mouse with Increased Fluorescence Intensity	240
8.4.4. 9L-GFP Untreated Mouse with Varied Fluorescence Intensity	242
8.5. PpIX Fluorescence Case Studies	244
8.5.1. 9L-GFP Tumor with Heterogeneous PpIX Production	244
8.5.2. U251-GFP Ventricle Tumor PpIX Production Pattern	248
8.5.3. U251-GFP Diffuse Tumor PpIX Production Pattern	251
8.6. Discussion.....	253
Chapter 9 - Conclusions & Future Directions.....	257
9.1. Concluding Remarks.....	257
9.2. Future Directions	259
REFERENCES.....	262

LIST OF TABLES

Table 2.1 – Environmental factors that affect PpIX production from exogenously administered ALA <i>in vitro</i> . PpIX production is shown to increase or decrease with arrow symbols for each environmental factor listed.....	20
Table 6.1 – The red light (635 nm) photobleaching dose is tabulated in J/cm ² . A 250 mW, 635 nm laser was used for photobleaching dose administration. All photobleaching doses are rounded to the nearest whole number.....	158
Table 6.2 – p-value calculation using Student’s t-test for PpIX fluorescence difference between the tumor-bearing group and the non-tumor-bearing control group at the time points shown.	168
Table 6.3 – The area under the curve normalized to 1 as calculated from ROC curves shown in Figure 6.11. An area of 1 indicates detection with 100% specificity and sensitivity. An area of 0.5 indicates detection with 50% specificity and sensitivity.	170
Table 7.1 – The 56 measurements collected from the multichannel system were considered to determine if an optimal measurement group could be averaged to increase the statistical significance between treatment groups over averaging all measurements. The p-values calculated between the control group, U251-GFP treated and U251-GFP untreated groups during the second cycle of spectroscopy measurements 24 hours after EGF-IRDye administration for different	

measurement groups measurements are shown. (Tx = treated group, No Tx = untreated group) 207

Table 8.1 – The relative average difference was calculated for each mouse at each time point. The fluorescence to transmittance ratio for the average control mouse was subtracted and normalized point by point to each individual mouse. The 56 measurements in each data set were averaged to obtain the relative average difference, displayed in the table. Since this is the difference from the average control mouse, some values are negative. 225

LIST OF FIGURES

- Figure 2.1 – The biochemical steps in the heme synthesis pathway which occurs in and around the mitochondria of all mammalian cells [22]. 19
- Figure 2.2 – Heterogeneity in PpIX production following 1 mM ALA administration to all cell lines. PpIX content was measured prior to ALA administration (control), then at 1, 2 and 4 hours after ALA administration. The mean PpIX fluorescence intensity for 2000 cells is shown, with the error bars representing the standard error of the mean..... 25
- Figure 2.3 – (a) Mitochondrial content as measured by Mitotracker Green showed a positive correlation to the endogenous PpIX fluorescence prior to the administration of ALA. (b) The relative side scatter was well correlated with PpIX production of the eight cell lines prior to ALA administration. (c) Following ALA administration to the eight cell lines no correlation was seen between Mitotracker fluorescence and PpIX production (d) Similarly, when the side scatter measurements from flow cytometry were considered no correlation was seen between relative side scatter and PpIX production following ALA administration. 27
- Figure 2.4 – (a) Cell area as measured by fluorescence microscopy on cells in suspension was positively correlated with PpIX production following ALA administration. (b) This relationship was supported by the forward scatter data from flow cytometry which was positively correlated with PpIX production

following the administration of ALA. (c) The correlation between forward scatter and PpIX production as it relates to incubation time with ALA can be seen in the DAOY cell line. The black line represents a linear fit to the data at the 4 hour time point to allow visualization of the positive correlation between PpIX production and forward scatter. (d) The correlation between forward scatter and PpIX production as it relates to incubation time with ALA can be seen in the U-87 cell line. A positive correlation between forward scatter and PpIX production at 4 hours was observed, and is represented by the black line that signifies a linear fit to the data. 29

Figure 2.5 – (a) The mean PpIX fluorescence intensity prior to ALA administration (control), 4 hours after ALA administration and 4 hours after ALA + L1 administration is shown, with the error bars representing the standard error of the mean. (b) The cells with the lowest PpIX production following ALA administration alone show the largest percentage increase in PpIX production following ALA + L1 administration. The error bars represent standard deviation of the mean..... 30

Figure 2.6 – PpIX fluorescence time course for U251, U251-GFP, 9L and 9L-GFP cell lines. Cells were examined for endogenous, background PpIX fluorescence prior to ALA administration (Bkgrd). Exogenous PpIX production was examined following administration of 1 mM ALA to the cells at 1, 2 and 4 hours after administration. Each bar represents the average of three samples. The

error bars represent the standard deviation between the averages of the three samples..... 32

Figure 2.7 – Relative GFP fluorescence intensity of the stably transfected U251-GFP cell line compared to the stably transfected 9L-GFP cell line. Each bar represents the average of three samples. The error bars represent the coefficient of variation (standard deviation/mean expressed as a percentage). Four sets of three samples of each tumor line were measured for mean GFP fluorescence and variation in fluorescence. 34

Figure 2.8 – (a) A small incision was made in the scalp using a #10 scalpel, exposing the skull so that landmarks were visible. (b) A dremel drill with a 1 mm drill bit was used to make a hole in the skull. (c) A hole drilled part way through the skull can be seen. (d) A mouse with hole in skull prior to implantation of cells..... 37

Figure 2.9 – (a) A nude mouse being positioned in the stereotactic frame for tumor implantation. (b) A close-up photograph of the needle being inserted into brain tissue for tumor implantation. (c) The mouse positioned in the stereotactic frame ready for tumor implantation. 38

Figure 2.10 – (a) Bone wax was used to close the hole drilled in the skull for tumor implantation. (b) The incision in the scalp was closed using VetBond. (c) A top view of the mouse following completion of surgery. (d) A front view of the mouse following completion of surgery. 39

Figure 3.1 – (a) The light path for a broad beam geometry reflectance fluorescence imaging system. The laser source is expanded across the entire imaging field and the whole sample is illuminated simultaneously. (b) The light path for a raster scanning reflectance fluorescence imaging system. The laser source is scanned across the sample so that a small portion of sample is illuminated at a single time point..... 47

Figure 3.2 – Two-dimensional tissue simulating phantom with 1% Intralipid, 3% blood and varied concentration of AlPcS₂ (1.95 – 0.0038 µg/ml by serial dilution) were constructed. The data represents the mean intensity in appropriate wells of 96-well plate..... 50

Figure 3.3 – (a) Two-dimensional tissue phantom with 3% blood, 1 µg/ml AlPcS₂ and varied concentrations of Intralipid imaged in both systems and quantified for fluorescence intensity. (b) Two-dimensional tissue phantom with 1% Intralipid, 1 µg/ml AlPcS₂ and varied concentrations of blood imaged in both systems and quantified for fluorescence intensity..... 51

Figure 3.4 – Fluorescence intensity quantification of 3D tissue phantoms constructed from opaque balloons filled with 1% Intralipid, 3% blood and 1 µg/ml AlPcS₂ imaged on both the raster scanning and broad beam imaging system. 51

Figure 3.5 – Representative images of five mice 72 hours after intravenous (IV) administration of AlPcS₂ (a) in the broad beam imaging system and (b) the raster scanning system. The approximate field of view was 20 cm x 11 cm. (c)The

fluorescence images generated at each time point in the two imaging systems were used for quantitative estimation of fluorescence in the tumor versus normal tissue. The mean and standard deviation of the tumor to normal tissue ratio is shown for five tumor-bearing mice..... 54

Figure 3.6 – Reflectance, raster scanned images of subcutaneous tumors (a) transfected with green fluorescent protein, (b) with ALPcS₂ as the fluorophore of interest and (c) with PpIX as the fluorophore of interest. The same mice are shown in (a) and (c), with the tumors easily visible by GFP fluorescence in (a), but masked by the PpIX skin fluorescence in (c). 57

Figure 3.7 – (a) Skin PpIX autofluorescence prior to diet change (Days 1 - 4), following diet change (Days 5 - 14), after ALA administration (Day 15) , and during ALA induced PpIX production and clearance (Day 16 - 17). Mice in Cage 1 were fed purified diet and standard water, mice in cage 2 were fed standard diet and antibiotic water, mice in cage 3 were fed both purified diet and antibiotic water, and mice in cage four were fed standard diet and water. Following ALA administration images were obtained 1, 2, 4, 6, 8 and 24 hours after administration to determine PpIX skin fluorescence. (b) Since little to no effect was seen from the antibiotic water, the data from the mice fed standard diet (Cage 2 & 4) and the mice fed purified diet (Cage 1 & 3) were averaged so that each group contained four mice. The percentage difference in PpIX skin fluorescence was calculated between these two groups..... 59

Figure 3.8 – Raster scanned image of eight mice in the skin PpIX fluorescence study (a) during days 1 - 4 when all mice were fed standard diet and water and (b) 7 days after diet change. The mice in cages 1 and 3 received the purified diet, while the mice in cages 2 and 4 received the standard diet. 61

Figure 3.9 – (a) Mouse 1 and 2 were fed purified diet, mouse 3 and 4 were fed standard diet. Following sacrifice the autofluorescence of the skin, muscle, brain, liver, intestine, stomach and kidney were imaged with the raster scanning system. (b) The organs from mouse 1, which was fed purified diet, had lower PpIX autofluorescence than (c) the organs from mouse 3, which was fed standard diet. 62

Figure 3.10 – (a) A schematic of the single channel transmission spectroscopy system containing 635 nm laser source, Acton research spectrometer, 650 nm LP filter and computer for detection. (b) A photograph of spectroscopy system containing spectrometer and mouse holder. (c) A photograph of a mouse in the holder, with the collimator on the mouse chin, attached to the laser, and the collimator on top of the mouse head attached to the spectrometer for detection. (c) A photograph of the light-tight box closed-up and ready to obtain measurements. 64

Figure 3.11 – (a) Photograph of multichannel transmission spectroscopy system showing the 2 carts, each containing 8 spectrometers. (b) A photograph of the epoxy/resin mouse holder, with holes drilled for repeatable fiber optics

placement. (c) A photography of the mouse holder with 3 of the possible 8 fiber optics inserted for measurements..... 66

Figure 3.12 – Spectra are shown from (a) *in vivo*, endogenous PpIX fluorescence prior to the administration of ALA; (b) spectrally fitted PpIX phantom data to *in vivo*, endogenous PpIX fluorescence; (c) deconvolved PpIX fluorescence and background bleed-through signal; (d) *in vivo*, EGF-IRDye fluorescence 72 hours after IV administration; (e) spectrally fitted EGF-IRDye phantom data to *in vivo*, EGF-IRDye fluorescence; and (f) deconvolved EGF-IRDye fluorescence and background bleed through signal. 68

Figure 4.1 – The raster scanning system was compared to the broad beam system to quantify the (a) depth vs. size and (b) contrast vs. size trade-off for detection of three-dimensional phantoms containing 1 µg/ml PpIX. In both plots, any object to the right of the lines would not be detectable by each system; where as an object to the left of the lines would be detectable by each system. 75

Figure 4.2 – The results of a phantom study with the single channel spectroscopy system to examine size vs. contrast trade-off. The recovered contrast of the anomaly normalized to the background is shown, where recovered contrasts below one are not detectable..... 77

Figure 4.3 – (a) The positional dependence of fluorescence detection in the single channel spectroscopy system was determined using the mouse-shaped phantom and the AF680 fluorescent probe. The first 6 measurements were collected with

the probe below the axially positioned fiber plane. The measurement at position 7 was collected when the probe was in line with the fiber plane, and measurements following this were above the fiber plane. (b) The percentage of the fluorescent signal that was detected when the fluorophore was not at the center of the collimators is shown, with 100% signal representing when the fluorophore was directly in the fiber plane. (c) A photograph of the mouse-shaped phantom made to simulate the optical properties of tissue, which could accommodate rods with fluorophore tips, inserted in the holes at the posterior of the phantom. (d) A photograph of the mouse-shaped phantom with rod inserted and arrow showing approximate location of fluorophore within the phantom. (e) The fluorophore rod was moved caudally out of the axial plane of fibers in 1 mm increments. 79

Figure 4.4 – Results of EGF-IRDye homogeneous phantom experiment are shown, to determine detection limits of EGF-IRDye and detection linearity at *in vivo* concentrations. Liquid phantom containing concentration of EGF-IRDye ranging from 0.5 μM – 0.05 nM were imaged using 8 of the 16 available fiber optics from the multichannel transmission spectroscopy system. The results from the 0.5 μM EGF-IRDye were not included in the graphs due to saturation. Results were plot on (a) a linear scale and (b) a log-log scale..... 81

Figure 4.5 – The positional dependence of fluorescence to transmittance ratio as measured by the multichannel transmission spectroscopy system. (a) The integrated, spectrally fitted fluorescence to transmittance ratio of the mouse

shaped phantom with the Quantum Dot 800 (QD800) fluorophore rod and with the blank rod which did not contain fluorophore are illustrated. Each rod was imaged in the fiber plane and at 1 mm increments out of the fiber plane up to 1.5 cm away from the fiber plane. (b) The percentage of signal detected as the fluorophore was moved out of the plane of the fibers is graphed on a semi-log scale. When the fluorophore was in the fiber plane (position = 0 mm) the signal was considered to be 100%. The eight fiber optics positioned axially around the center of the mouse can be seen in (c) and (d)..... 83

Figure 4.6 – (a) The segmented mouse head boundary with skin, brain and bone regions defined using Mimics was used to construct (b) a three-dimensional mouse head mesh with regions segmented from the volume representing the skin (red), brain (yellow), bone (green) and adipose (blue) tissues. (c) The positions of the two fibers used to model the single channel spectroscopy system. (d) The positions of the eight fibers used to model the measurements collected with the multichannel spectroscopy system..... 86

Figure 4.7 – The effect of the tumor volume and contrast on the recovered contrast of the model using two fibers is plotted as the color scale in each figure, with different tumor positions shown as separate figures. The tumor modeled (a) at the center of the brain, (b) at the top, left edge of the brain, (c) 2 mm towards the center from the top, left edge of the brain on the x axis, (d) 2 mm towards the center from the top, left edge of the brain on the z axis and (e) 1 mm towards the center from the top, left edge of the brain on the x, y and z axes. 88

Figure 4.8 – The effect of the tumor volume and contrast on the recovered contrast of the model using eight fibers is plotted as the color scale in each figure, with different tumor positions shown as separate figures. The tumor modeled (a) at the center of the brain, (b) at the top, left edge of the brain, (c) 2 mm towards the center from the top, left edge of the brain on the x axis, (d) 2 mm towards the center from the top, left edge of the brain on the z axis and (e) 1 mm towards the center from the top, left edge of the brain on the x, y and z axes. 90

Figure 4.9 – The light paths from source-detector pairs in the model of the multichannel spectroscopy system. The fiber optics were numbered 1 - 8 and are illustrated around a circle which represents a coronal section of the mouse head. Each red line represents the light path between the two fiber optics, and thus two measurements, since each fiber can be both a source and a detector. The light paths which represent (a) transmission measurements, (b) semi-transmission measurements, (c) semi-reflectance measurements and (d) reflectance measurements from around the mouse head are illustrated. 92

Figure 4.10 – The transmission measurements illustrated in Figure 4.9(a) were averaged for the tumor (a) at the center of the brain and (b) at the 1 mm position. These results were compared to those seen when all 56 measurements were averaged by normalizing the average transmission data at each contrast and tumor volume to the same data when all 56 measurements were averaged. The normalization of the transmission data to the average of all 56 measurements for

the tumor (c) at the center of the brain and (d) at the 1 mm position are illustrated..... 94

Figure 4.11 – The recovered contrast when the transmission measurements and semi-transmission measurements (Figure 4.9(a) and (b)) were averaged for the tumor (a) at the center and (b) 1 mm position in the brain. These results were compared to those seen when all 56 measurements were averaged by normalizing the average transmission and semi-transmission data at each contrast and tumor volume to the same data when all 56 measurements were averaged. The normalization of the transmission and semi-transmission data to the average of all measurements for the tumor (c) at the center and (d) 1 mm position in the brain are illustrated..... 96

Figure 4.12 – The recovered contrast for the average of all measurements except reflectance measurements (Figure 4.9(d)) for the tumor (a) at the center and (b) 1 mm position in the brain. These results were compared to those seen when all 56 measurements were averaged by normalizing the data at each contrast and tumor volume. The normalization of the average of all measurements except the reflectance measurements to the average of all 56 measurements for the tumor (c) at the center and (d) at 1 mm position in the brain are illustrated. 97

Figure 4.13 – (a) The average of the groups of measurements at each fluorophore position are illustrated for the mouse-shaped phantom imaged in the multichannel system. (b) The percentage difference from the average of all

measurements when the fluorophore was in the fiber plane is shown for each group of measurements. 99

Figure 5.1 – (a) A photograph of the Philips 3T magnetic resonance imaging system with research rodent coil insert in magnet bore. (b) A close-up photograph of research rodent coil in magnet bore. 108

Figure 5.2 – Tumor to contralateral normal tissue contrast values are shown for (a) T1 TSE CE MRI and (b) T2 TSE MRI of the 9L-GFP, U251 and U251-GFP tumors, which grew either diffusely in the brain or as a bulk tumor. Control mice left brain hemisphere to right brain hemisphere ratio values are shown for comparison. Receiver operator characteristic (ROC) curves are shown for (c) T1 TSE gadolinium enhanced MRI and (d) T2 TSE MRI of 9L-GFP, U251 and both the diffuse and bulk tumor growth pattern of the U251-GFP tumor model. TPF is defined as the true positive fraction and FPF is defined as the false positive fraction. 111

Figure 5.3 – Additional MRI sequences were used to detect the U251-GFP diffuse growing tumors which were not readily visible by conventional MRI, including (a) T1 difference imaging, (b) T2 FLAIR (fluid attenuated inversion recovery), (c) T1 IR (inversion recovery), and (d) PDW (proton density weighted) TSE. For each type of imaging sequence the U251-GFP tumors growing diffusely in one hemisphere or in the ventricle space (labeled U251-GFP Diffuse) and the U251-GFP tumors growing as a bulk mass towards the bottom of the brain

(labeled U251-GFP Bulk) were compared with one another as well as with sham surgery implanted control mice..... 113

Figure 5.4 – (a) Tumor to normal tissue contrast for the U251-GFP tumor growing in the ventricle space or diffusely in one hemisphere of the brain for T1 TSE CE, T2 TSE, T1 difference imaging, T2 FLAIR, T1 IR, PDW TSE and T1 fast field echo (FFE) MRI. (b) ROC analysis for the U251-GFP tumor morphologies with low MRI visibility as compared to control mice is shown for all imaging sequences illustrated in (a)..... 115

Figure 5.5 – *In vivo* and *ex vivo* images of a representative 9L-GFP tumor-bearing mouse with healthy tumor tissue and surrounding brain tissue are shown. (a) T1 TSE CE MRI of the three slices most representative of the brain slice shown in the *ex vivo* (b) GFP image and (c) H+E 1x magnification image. Images at (d) 4x, (f) 20x and (h) 40x magnification of the center of the tumor illustrated healthy cells. Images at (e) 4x, (g) 20x and (i) 40x of the periphery of the tumor illustrated both healthy tumor tissue and adjacent normal brain tissue. 117

Figure 5.6 – *In vivo* and *ex vivo* images of a representative 9L-GFP tumor-bearing mouse with both proliferative and slow growing tumor tissue shown. Three representative slices of (a) T1 TSE CE and (b) T2 TSE MRI, which most closely matched the *ex vivo* (c) GFP and (d) H+E 1x magnification brain slice are shown. Images at (e) 4x, (g) 20x and (i) 40x magnification of the quickly

proliferating edge of the tumor are shown. Images at (f) 4x, (h) 20x and (j) 40x magnification of the slower growing center of the tumor are shown. 119

Figure 5.7 – *In vivo* and *ex vivo* images of a representative 9L-GFP tumor-bearing mouse are shown. Three representative slices of (a) T2 FLAIR and (b) T1 IR MRI, which most closely correlate to the *ex vivo* (c) GFP and (d) H+E 1x magnification brain slice. Images of the periphery of the tumor are shown at (e) 4x, (g) 20x and (i) 40x magnification. Images of the center of the tumor are shown at (f) 4x, (h) 20x and (j) 40x magnification..... 121

Figure 5.8 – *In vivo* and *ex vivo* images of a representative 9L-GFP tumor-bearing mouse with slow growing tumor tissue within the normal brain and proliferative tumor tissue growing beneath the brain. 3T MRI (a) T1 TSE CE, (b) T2 TSE and (c) T2 FLAIR are illustrated. For comparison 7T MRI (d) T1 TSE CE, (d) T2 TSE, (e) T2 map and (f) diffusion images in black and white as well as false color. Due to the noise in the T2 maps and diffusion images all but the brain was windowed from image. For all MR images, the image slice that most closely correlated to the *ex vivo* (h) GFP and (i) H+E 1x magnification brain section was shown. H+E images of the tumor growing beneath the brain are shown at (j) 4x, (l) 20x and (n) 40x magnification. H+E images of the tumor tissue growing within the normal brain are shown at (k) 4x, (m) 20x and (o) 40x magnification. 124

Figure 5.9 – *In vivo* and *ex vivo* images of a representative U251 tumor-bearing mouse with tumor tissue growing within the normal brain and beneath the brain, invading the cranium. Three representative slices of a (a) T1 TSE CE and (b) T2 TSE MRI are shown which most closely correlate to the *ex vivo* H+E 1x magnification brain slices shown for (c) the tumor tissue invading the normal brain and (d) the bulk tumor which was separated from the brain upon removal from the cranium. H+E images of the bulk tumor are shown at (e) 4x, (g) 20x and (i) 40x magnification. H+E images of the tumor invading the normal brain are shown at (f) 4x, (h) 20x and (j) 40x magnification. 128

Figure 5.10 – *In vivo* and *ex vivo* images of a representative U251 tumor-bearing mouse with tumor tissue growing within the normal brain. Three representative slices of a (a) T1 TSE CE and (b) T2 TSE MRI are shown which most closely correlate to the (c) *ex vivo* H+E 1x magnification brain slice. (d) An image at 4x magnification of the area of the tumor containing vasculature and hemorrhage is shown. Images at 20x magnification of the (e) center and (f) periphery of the tumor and the (g) hemorrhage next to the tumor are illustrated. Images at 40x magnification of the (h) center of the tumor, (i) tumor periphery with a blood vessel containing lymphocytes and (j) hemorrhage next to the tumor are illustrated. 130

Figure 5.11 – *In vivo* and *ex vivo* images of a representative U251-GFP tumor-bearing mouse with tumor tissue growing diffusely in the right hemisphere of the brain. A representative slice of a (a) T1 TSE CE, (b) T2 FLAIR and (c) T1 FFE MRI

are shown. Due to the difficulty with MRI visibility, it was difficult to discern which MRI slice most closely corresponded to the *ex vivo* data, so brain size and shape were used to guide selection. *Ex vivo* GFP fluorescence images of the (d) front and (e) middle of the brain are illustrated with their corresponding H+E image, where the (f) front of the brain and the (g) middle of the brain are shown at 1x magnification. Images at (h) & (i) 4x, (j) 20x and (k) 40x magnification of the front brain section are illustrated. Images at (l) 4x and (m) 20x magnification of the middle brain section are illustrated..... 134

Figure 5.12 – *In vivo* and *ex vivo* images of a representative U251-GFP tumor-bearing mouse with tumor tissue growing diffusely in the right hemisphere of the brain.

An MR image showing (a) T1 TSE CE, (b) T1 FFE and (c) T1 difference sequences with the slice shown that most closely correlated to the *ex vivo* data. Tumor presence was confirmed through *ex vivo* GFP fluorescence images of the (d) front and (e) middle of the brain and their corresponding 1x magnification H+E image, where the (f) front and (g) middle of the brain are also shown. Images of the front brain section at (h) 4x, (j) 20x and (l) 40x magnification are shown. Images of the middle brain section at (i) 4x, (k) 20x and (m) 40x magnification are shown..... 136

Figure 5.13 – *In vivo* and *ex vivo* images of a representative U251-GFP tumor-bearing mouse with tumor tissue growing in the left ventricle space are shown. An MR image showing (a) T1 TSE CE, (b) T1 FFE and (c) T1 IR sequences with the slice that most closely correlated to the *ex vivo* data are shown. Tumor presence

was confirmed through *ex vivo* (d) GFP fluorescence image and the corresponding (e) 1x magnification H+E image of the front of the brain. Images of both ends of the ventricle tumor at 4x magnification are illustrated in (f) and (i). Images of the center of the tumor at (g) 20x and (h) 40x magnification are shown. Images of the periphery of the tumor at (k) 20x and (m) 40x magnification are illustrated. The immune response of the normal brain was detectable through the presence of lymphocytes illustrated at (l) 20x and (m) 40x magnification. 139

Figure 5.14 – *In vivo* and *ex vivo* images of a representative U251-GFP tumor-bearing mouse with tumor tissue growing in both ventricles is shown. 3T MRI (a) T2 TSE, (b) PDW TSE and (c) T1 IR are illustrated. For comparison 7T MRI (d) T2, (e) T1 CE, (f) T2 map and (g) diffusion image in black and white and false color. Due to the noise in the T2 maps and diffusion images all but the brain was windowed from image. For all MR images, the image slice that most closely correlated to the *ex vivo* (h) GFP and (i) H+E 1x magnification brain section was shown. H+E images of the tumor tissue in the right ventricle are shown at (j) 4x, (k) 20x and (l) 40x magnification. H+E images of the tumor tissue in the left ventricle are shown at (m) 4x, (n) 20x and (o) 40x magnification. 142

Figure 5.15 – *In vivo* and *ex vivo* images of a representative U251-GFP tumor-bearing mouse with tumor tissue growing at the base of the brain invading the normal brain and the cranium. An MR image showing (a) T1 TSE CE, (b) T2 TSE, (c)

PDW TSE, (d) T2 FLAIR, (e) T1 IR and (f) T1 difference sequences with the slice that most closely correlated to the *ex vivo* data are shown. *Ex vivo* (g) 1x magnification H+E and (h) GFP images of the tumor invading the normal brain are illustrated. *Ex vivo* (i) 1x magnification H+E and (j) GFP images of the bulk tumor which was invading the cranium are shown. Images at (k) 4x, (l) 20x and (m) 40x magnification of the tumor tissue invading the normal brain are shown. Images at (n) 4x, (o) 20x and (p) 40x magnification of the bulk tumor tissue growing at the base of the brain are shown..... 144

Figure 6.1 – Box and whisker plots of the first pilot PpIX brain tumor detection study results. (a) The fluorescence to transmittance ratio of background PpIX fluorescence in 9L-GFP tumor-bearing mice and non-tumor-bearing mice which had not received sham surgery. (b) *In vivo* PpIX fluorescence 2 hours after the administration of 100 mg/kg ALA IP. (c) *Ex vivo* PpIX fluorescence of extracted brain tissue, 2 hours after the administration of ALA..... 151

Figure 6.2 – The results of the second pilot study of PpIX brain tumor detection is shown as box and whisker plots, using control mice with sham surgery, to have the same level of scaring and damage from implantation. (a) The fluorescence to transmittance ratio of background PpIX fluorescence in 9L-GFP tumor-bearing mice and non-tumor-bearing control mice which had received sham surgery. (b) *In vivo* PpIX fluorescence 2 hours after the administration of 100 mg/kg ALA IP. (c) *Ex vivo* PpIX fluorescence of extracted brain tissue 2 hours after ALA administration. 153

Figure 6.3 – The pilot PpIX skin fluorescence photobleaching study results are shown in box and whisker plots. The PpIX fluorescence to transmittance ratio (a) prior to ALA administration, (b) 2 hours after 100 mg/kg ALA administration, (c) after 8 J/cm² photobleaching dose was administered to one side of the head, and (d) after 8 J/cm² photobleaching dose was administered to both sides of the head. 155

Figure 6.4 – Spectroscopy measurements are summarized (a) prior to the administration of ALA, (b) *in vivo* 2 hours after the administration of ALA and (c) *ex vivo* 2 hours after the administration of ALA. The PpIX fluorescence at each time point was compared between sham surgery implanted control mice, 9L-GFP and U251 tumor-bearing mice. 157

Figure 6.5 – PpIX fluorescence to transmittance ratio of each group of mice during red light photobleaching administration. The cumulative red light dose is shown on the x-axis and corresponds to measurements obtained at the time points listed in Table 6.1, where 0 J/cm² corresponds to the measurements 2 hours after the administration of ALA, prior to any photobleaching. Each line represents the average of all mice in each group. (Control n = 4, 9L-GFP n = 9, U251 n = 7). 159

Figure 6.6 – Box and whisker plots illustrating the individual mice following (a) 1 minute of photobleaching (37 J/cm²); (b) 2 minutes of photobleaching (74 J/cm²); (c) 4 minutes of photobleaching (148 J/cm²); and (d) 8 minutes of photobleaching (296 J/cm²). 160

Figure 6.7 – (a) The mouse photobleaching box is shown with blue LEDs contained within large aluminum heat sinks. Holes were drilled to allow the light from each LED to hit the mouse skin, while the mouse was positioned on the plate in the center of the device. (b) A close-up photograph of the LED in the aluminum heat sink, as shown in (a). (c) The results from photobleaching of healthy nude mice are shown, where photobleaching doses of 4, 8 and 12 J/cm² were compared. The point at time = -2 represents the background PpIX measurement prior to the administration of ALA. The point at time = 0 represents the PpIX measurement 2 hours after the administration of ALA. Mouse numbers per group where: n=7 at 4 J/cm²; n=7 at 8 J/cm²; and n=8 at 12 J/cm². The points represent the mean of the mice in each group while the error bars show the standard deviation in each group. 163

Figure 6.8 – The summary of the single channel spectroscopy measurements from the blue light photobleaching study, (a) prior to the administration of ALA, (b) 2 hours after the administration of ALA, (c) following administration of 4 J/cm² blue light and (d) *ex vivo*..... 164

Figure 6.9 – A summary of the blue light photobleaching experiment, with the PpIX fluorescence to transmittance ratio (FT Ratio) normalized to the tumor size. The normalized FT ratio is shown (a) prior to the administration of ALA, (b) 2 hours after ALA administration, (c) following the 4 J/cm² photobleaching dose and (d) *ex vivo*. 166

Figure 6.10 – Summary PpIX fluorescence data normalized to the average controls mouse from each study are shown. The normalized PpIX fluorescence to transmittance ratio is shown (a) prior to the administration of ALA, (b) 2 hours after the administration of ALA and (c) *ex vivo*. 167

Figure 6.11 – ROC curves constructed from the PpIX summary data shown in Figure 6.10 to quantify the ability of the single channel spectroscopy system to detect 9L-GFP, U251 and U251-GFP tumor bearing mice over non-tumor-bearing control mice (a) prior to ALA administration, (b) *in vivo* 2 hours after ALA administration and (c) *ex vivo* 2 hours after ALA administration..... 170

Figure 6.12 – Images from three example mice from the 9L-GFP tumor-bearing group are shown, one in each column, where *ex vivo* GFP fluorescence, PpIX fluorescence and the corresponding H+E staining are shown in the first three rows. The T1 TSE CE MR image which was qualitatively most similar to the *ex vivo* measurements was included for comparison..... 173

Figure 6.13 – Three representative examples of U251 tumor-bearing group are shown in the three columns, where the *ex vivo* PpIX fluorescence and corresponding H+E image are shown in the top rows. The U251 tumor line was not GFP transfected and thus, GFP images are not shown. The MRI slices which qualitatively corresponds to the *ex vivo* image are shown for both T1 TSE CE images (3rd row) as well as T2 TSE images (bottom row). 175

Figure 6.14 – Three examples of the U251-GFP tumor-bearing group are shown one per column, where the *ex vivo* GFP fluorescence, PpIX fluorescence and corresponding H+E slices are shown in successive rows. T1 TSE CE MRI images 29 days and 35 days following tumor implantation are also shown. The MRI slices shown qualitatively corresponded to the *ex vivo* images..... 177

Figure 6.15 – Tumor tissue to contralateral normal tissue PpIX fluorescence measured in the control group and each of the tumor-bearing groups via the reflectance raster scanner is plotted for (a) PpIX fluorescence and (b) GFP fluorescence. The U251 parent line was not included in the GFP contrast graph since it was not a GFP transfected tumor line. 179

Figure 7.1 – The EGF uptake of a panel of brain cancer cell lines as measured via flow cytometry quantification of fluorescently labeled EGF. The blue bars represent the endogenous fluorescence of each cell line at the excitation and emission wavelengths of Alexa Fluor 647. The purple bars represent mean fluorescence from three samples for each cell line incubated with EGF-AF647, with error bars showing the standard deviation of the mean. 188

Figure 7.2 – The EGF uptake of U251-GFP cells (a) and 9L-GFP cells (b) as measured by EGF-AF647 fluorescence, following varied incubation times with different Erbitux concentrations. The bars labeled Ctrl –AF represents the background, endogenous fluorescence of the cell line at the excitation and emission wavelengths of Alexa Fluor 647. The point labeled Ctrl +AF

represents the fluorescence from EGF uptake of untreated cells. Each bar represents the average of three samples, and the error bar shows the standard deviation..... 191

Figure 7.3 – The timeline for the Erbitux therapy monitoring experiment is shown. The experiment started on day 0, with tumor implantation. Each mouse in the study received MRI, EGF-IRDye and fluorescence monitoring via spectroscopy on the days as shown. Only the mice in the treatment groups received the Erbitux therapy on the appropriate days. 194

Figure 7.4 – Integrated, spectrally fitted fluorescence to transmittance ratio normalized to the average control mouse of EGF-IRDye fluorescence at each source-detector point for the first week of spectroscopy measurements, obtained on days 14 – 16 of the experiment. The treated and untreated groups for the 9L-GFP and U251-GFP tumor-bearing mice, and a mixed treated and untreated control group are illustrated in the graphs. *In vivo* EGF-IRDye fluorescence (a) 24 hours, (b) 48 hours and (c) 72 hours after administration..... 197

Figure 7.5 – (a) A coronal slice of a T1 TSE CE MRI showing a brain tumor was used to illustrate the positioning of the fiber optics around the mouse head. Each fiber could act as both a source and a detector, but not simultaneously. The source was rotated sequentially through the 8 fiber optics, while the remaining 7 fiber optics took measurements and thus, 56 total measurements were obtained. The integrated, spectrally fitted fluorescence to transmittance ratio of each

source-detector pair for the average values at 24 hours after EGF-IRDye administration are shown for the (b) U251-GFP and (c) 9L-GFP tumor-bearing mice compared to the average of the control mice. 200

Figure 7.6 – The integrated, spectrally fitted fluorescence to transmittance ratio normalized to the average control mouse for EGF-IRDye fluorescence values at each source-detector point (obtained on days 21 – 24 of the experiment). The treated and untreated groups for the 9L-GFP and U251-GFP tumor-bearing mice, and a mixed treated and untreated control group are illustrated in the graphs. *In vivo* EGF-IRDye fluorescence (a) 24 hours, (b) 48 hours and (c) 72 hours after administration. 203

Figure 7.7 – The integrated, spectrally fitted fluorescence to transmittance ratio of each source-detector pair for the U251-GFP treated and untreated mice (a) 24 hours, (b) 48 hours and (c) 72 hours after EGF-IRDye administration. The difference between the untreated and treated groups at each source detector point is also graphed at each time point in green. 204

Figure 7.8 – The relative average difference 24 hours after EGF-IRDye administration during the second week of spectroscopy measurements. Groups of fiber measurements were considered to determine if an optimal measurements set could be determined. The average of the (a) transmission only (b) transmission and semi-transmission (c) maximum point and (d) transmission,

semi-transmission and semi-reflectance data is shown for each group of mice.

The light paths corresponding to each of these groups are shown in Figure 4.9... 205

Figure 7.9 – (a) *Ex vivo* EGF-IRDye tumor tissue fluorescence intensity normalized to healthy brain tissue fluorescence intensity. (b) *Ex vivo* fluorescence intensity normalized to healthy brain tissue fluorescence intensity divided by tumor area. . 208

Figure 7.10 – The *ex vivo* images showing the EGF-IRDye fluorescence (1st row), which can be compared to the GFP fluorescence (2nd row) as well as the corresponding H+E section (3rd row) for three example mice in the 9L-GFP treated group. The *in vivo* MR image that qualitatively matched the *ex vivo* brain slice is shown for comparison. T1 TSE CE and T2 TSE MR images are illustrated in the bottom two rows of the figure. A different mouse is shown in each column with (a) – (c) illustrating three representative mice in the 9L-GFP Erbitux treated group. 210

Figure 7.11 – The *ex vivo* images illustrating the EGF-IRDye fluorescence (1st row), which can be compared to the GFP fluorescence (2nd row) as well as the corresponding H+E section (3rd row) for three example mice in the 9L-GFP untreated group. The *in vivo* MR image that qualitatively matched the *ex vivo* brain slice is shown for comparison. T1 TSE CE and T2 TSE MR images are illustrated in the bottom two rows of the figure. A different mouse is shown in each column with (a) – (c) illustrating three representative mice in the 9L-GFP

untreated group. For mouse (c), all images are the same except a T2 FLAIR MR image is shown in the bottom row, instead of a T2 TSE image. 212

Figure 7.12 – The *ex vivo* images illustrating the EGF-IRDye fluorescence (1st row), which can be compared to the GFP fluorescence (2nd row) as well as the corresponding H+E section (3rd row) for three example mice in the U251-GFP treated group. The *in vivo* MR image that qualitatively matched the *ex vivo* brain slice is shown for comparison. T1 TSE gadolinium contrast enhanced images and T2 FLAIR images are illustrated in the bottom two rows of the figure. A different mouse is shown in each column with (a) – (c) illustrate three representative mice in the U251-GFP treated group..... 214

Figure 7.13 – The *ex vivo* images illustrating the EGF-IRDye fluorescence (1st row), which can be compared to the GFP fluorescence (2nd row) as well as the corresponding H+E section (3rd row) for three example mice in the U251-GFP untreated group. The *in vivo* MR image that qualitatively matched the *ex vivo* brain slice is shown for comparison. T1 TSE gadolinium contrast enhanced images and T2 FLAIR images are illustrated in the bottom two rows of the figure. A different mouse is shown in each column with (a) – (c) illustrate three representative mice in the U251-GFP untreated group..... 216

Figure 8.1 – EGF-IRDye fluorescence relative average difference from average control mouse at each measurement time point. Times points labeled 1 – 3 represent measurements obtained during the first week of spectroscopy 24, 48

and 72 hours after EGF-IRDye administration, respectively. Time points labeled 4 – 6 represent measurements obtained during the second week of spectroscopy 24, 48 and 72 hours after EGF-IRDye administration, respectively. The individual mice in the (a) 9L-GFP treated, (b) 9L-GFP untreated, (c) U251-GFP treated, (d) U251-GFP untreated and (e) control groups are shown at each of the time points..... 224

Figure 8.2 – Example mouse AR1 from the U251-GFP Erbitux treatment group. A coronal *ex vivo* section was imaged for (a) EGF-IRDye fluorescence, (b) GFP fluorescence and was stained with (c) H+E. The tumor tissue, which grew in the left and right ventricle space, is illustrated at 4x magnification in (d) and (e). The *in vivo* MR images that were obtained during the experiment are illustrated (f) 12 days, (g) 20 days and (h) 23 days following tumor implantation. T1 TSE CE, T2 FLAIR and T1 IR MR images of the corresponding section are illustrated..... 227

Figure 8.3 – Example mouse AQ3 from the U251-GFP Erbitux treatment group. A coronal *ex vivo* section was imaged for (a) EGF-IRDye fluorescence, (b) GFP fluorescence and was stained with (c) H+E. The tumor tissue, which grew diffusely in one hemisphere of the brain, is illustrated at (d) 4x and (e) 10x magnification. The *in vivo* MR images that were obtained during the experiment are illustrated (f) 12 days, (g) 20 days and (h) 23 days following tumor implantation. T1 TSE CE, T2 FLAIR and T1 IR MR images of the corresponding section are illustrated. 230

Figure 8.4 – Example mouse AK1 from the 9L-GFP Erbitux treatment group. A coronal *ex vivo* section was imaged for (a) EGF-IRDye fluorescence, (b) GFP fluorescence and was stained with (c) H+E. Healthy tumor tissue, which grew below the brain, is illustrated at (d) 10x magnification. (e) Some of the tumor tissue had significant hemorrhage as can be seen at 10x magnification. The *in vivo* MR images that were obtained during the experiment are illustrated (f) 12 days, (g) 20 days and (h) 23 days following tumor implantation. T1 TSE CE and T2 TSE MR images of the corresponding section are shown..... 232

Figure 8.5 – Example mouse AJ2 from the 9L-GFP Erbitux treatment group. A coronal *ex vivo* section was imaged for (a) EGF-IRDye fluorescence, (b) GFP fluorescence and was stained with (c) H+E. The tumor tissue, which grew both as a bulk mass and in the ventricle space, is illustrated at 4x magnification in (d) and (e). The *in vivo* MR images that were obtained during the experiment are illustrated (f) 12 days, (g) 20 days and (h) 23 days following tumor implantation. T1 TSE CE and T2 TSE MR images of the corresponding section are illustrated. 234

Figure 8.6 – Example mouse AS4 from the U251-GFP untreated group. A coronal *ex vivo* section was imaged for (a) EGF-IRDye fluorescence, (b) GFP fluorescence and was stained with (c) H+E. The tumor tissue, which grew in the ventricle space, is illustrated at (d) 4x and (e) 10x magnification. The *in vivo* MR images that were obtained during the experiment are illustrated (f) 12 days, (g) 20 days and (h) 23 days following tumor implantation. T1 TSE CE, T2 FLAIR and T1 IR MR images of the corresponding section are shown. 237

Figure 8.7 – Example mouse AT3 from the U251-GFP untreated group. A coronal *ex vivo* section was imaged for (a) EGF-IRDye fluorescence, (b) GFP fluorescence and was stained with (c) H+E. The tumor tissue, which grew in one ventricle, is illustrated at 4x magnification in (d) and (e). The *in vivo* MR images that were obtained during the experiment are illustrated (f) 12 days, (g) 20 days and (h) 23 days following tumor implantation. T1 TSE CE, T2 FLAIR and T1 IR MR images of the corresponding section are illustrated. 239

Figure 8.8 – Example mouse AM3 from the 9L-GFP untreated group. A coronal *ex vivo* section was imaged for (a) EGF-IRDye fluorescence, (b) GFP fluorescence and was stained with (c) H+E. The tumor tissue, which grew within the normal brain tissue and below the brain, is illustrated at 10x magnification in (d) and (e). The *in vivo* MR images that were obtained during the experiment are illustrated (f) 12 days, (g) 20 days and (h) 23 days following tumor implantation. T1 TSE CE and T2 TSE MR images of the corresponding section are illustrated. 241

Figure 8.9 – Example mouse AJ3 from the 9L-GFP untreated group. A coronal *ex vivo* section was imaged for (a) EGF-IRDye fluorescence, (b) GFP fluorescence and was stained with (c) H+E. The tumor tissue, which grew as a mass in one hemisphere of the brain, is illustrated at 10x magnification in (d) and (e). The *in vivo* MR images that were obtained during the experiment are illustrated (f) 12 days, (g) 20 days and (h) 23 days following tumor implantation. T1 TSE CE and T2 TSE MR images of the corresponding section are illustrated. 243

Figure 8.10 – (a) An example 9L-GFP tumor-bearing mouse with a large tumor visible by GFP fluorescence. (b) The PpIX production was high in some parts of the tumor and low in other portions. An H+E stained section at (c) 1x magnification is shown for comparison. Magnified H+E images matching portions of the brain with different PpIX production levels are shown in (d) – (g) with arrows pointing to the appropriate region in the PpIX section. (h) – (j) MR images of the three slices which most closely represent the *ex vivo* data are shown from the 3T and 7T MRI. The 3T MRI sequences are shown at the left of the figure and included T1 TSE CE, T2 TSE and T2 FLAIR while 7T sequences shown at the right of the figure included T1 CE and T2 images. (k) T2 maps and (l) diffusion images were calculated from images obtained with the 7T MRI. The same three sections are shown by T2 maps and diffusion images as seen in (h) – (j). 247

Figure 8.11 – An example U251-GFP tumor growing in the ventricle space is shown. The two *ex vivo* sections with corresponding cut faces are illustrated in (a) – (h), where PpIX and GFP fluorescence as well as H+E at 1x and 4x magnification are shown. Arrows from the 4x magnification H+E images show the approximate region of the magnified image on the 1x image. MR images were collected on the 3T (left hand side of figure) and the 7T (right hand side of figure) MRI, with T1 CE and T2 sequences of the three slices that most closely represent the *ex vivo* data shown in (i) – (k). The two most representative slices are shown for (l) T2 maps and (m) diffusion images collected via the 7T MRI. ... 250

Figure 8.12 – (a) An example U251-GFP tumor with diffuse tissue and small mass towards the bottom of the brain as shown by 1x magnification H+E. The *ex vivo* (b) PpIX and (c) GFP fluorescence of the same section are shown. 4x magnification images of the two visible tumor regions are shown in (d) & (e) with arrows pointing to the approximate location of image acquisition. *In vivo* MRI was obtained with both a 3T and 7T magnet. Three representative slices of a (f) T2 Map and (g) diffusion images collected via the 7T which match the *ex vivo* data are shown. (h) – (j) The same three slices are illustrated from the 3T and the 7T, showing T2 TSE, PDW and T1 IR from the 3T (right hand side of figure) and T1 CE as well as T2 from the 7T (left hand side of figure). 252

Chapter 1 - Introduction & Overview

1.1. Project Rational

Advances in medical imaging technology have assisted in the detection of cancer at earlier stages significantly improving patient outcome. Currently, most medical imaging methods focus on tissue structure imaging, where tumor tissue is detected because it is a structural abnormality. Structural detection of cancer by x-ray imaging applications, conventional magnetic resonance imaging (MRI), and ultrasound has allowed for significant improvement in the public health due to availability and accessibility of these systems for general medicine. However, cancer is a dynamic, heterogeneous disease that is different for each individual making evaluation of more than its size and structure important for patient health in diagnosis, treatment planning, and tracking treatment efficacy.

Cancer therapy has also made significant advances from conventional treatments including surgery, radiotherapy and chemotherapeutics to a vast array of new treatments including molecular therapeutics, gene therapy and other novel techniques such as photodynamic therapy. Due to the dynamic nature of cancer, the current treatment trend is towards more individualized therapy over prescription of conventional therapies for all patients. The difficulty with individualized therapy is that many of these treatment strategies are targeted towards a specific gene or molecular event that not all types of cancer or individual cases may exhibit. Thus, monitoring therapy efficacy is becoming more important with the advances in treatment strategies. Most current imaging modalities detect treatment efficacy at a rather 'late stage' as changes in tumor volume occur long after many identified molecular events have transpired. Tumor tissue cellular

and subcellular changes including metabolism, vascularity, and receptor and gene expression can be exploited via functional imaging to explore treatment efficacy at early disease stages. Together structural and functional tissue information will increase physicians' ability to make appropriate choices for patients so that valuable time is not wasted waiting for an ineffective therapy to cure cancer.

Currently, nuclear imaging systems offer the best clinical evaluation of tumor functional status. Many new positron emission tomography (PET) and single photon emission computed tomography (SPECT) tracers are being developed and used to track the status of tumor tissue metabolism, amino acid uptake and DNA production [1]. The drawbacks to nuclear imaging modalities remain the expense of their use as well as the difficulty with radioisotope production and handling. Optical imaging is a promising technology that is poised to become a common place clinical tool to provide functional cancer imaging. Hemoglobin and water are two of the most absorbing chromophores in biological tissue, however in the near-infrared (NIR) region (650 nm – 900 nm) their absorption is at a minimum, making the NIR region ideal for imaging in deep tissue [2]. Optical imaging can provide information about the absorption and scattering properties of tissue and also allow for fluorescence investigation of tissues. Technological advances in development of fluorescent probes in the NIR spectrum and optical detection technology has sparked much interest in functional optical imaging for cancer detection, diagnosis and therapy monitoring [3]. This thesis work is focused on assessing case situations where optical imaging and spectroscopic assessment would provide added benefit to assessing glioma tumor growth and treatment monitoring.

1.2. Background

1.2.1. Brain Cancer & Treatment Options

Approximately 2% of cancer deaths in the United States can be attributed to brain tumors as an estimated 18,000 new cases of primary brain tumors are diagnosed yearly [4, 5]. Half of patients are diagnosed with glioblastoma multiforme, which is both the most common and the most malignant type of brain tumor [6]. The biology of brain tumors is complex and the ability of tumor cells to diffusely invade adjacent normal brain tissue makes complete surgical resection difficult and thus adjuvant therapies are standard practice in conjunction with surgery. Moreover, the prognosis for patients with high-grade glioma is poor due to local recurrence of the tumor following treatment strategies [4]. Median survival for patients with malignant glioma is usually less than one year and almost never longer than two years even for patients with a favorable prognosis [7]. Although brain tumors account for a small percentage of overall cancer incidence, a disproportionately large fraction of cancer morbidity and mortality can be attributed to these tumors [8].

Since the late 1970's conventional therapy for malignant gliomas has consisted of surgical resection of the bulk tumor plus adjuvant fractionated radiotherapy to treat the diffusely infiltrating portion of the tumor cells [6, 7]. Advances have been made in surgical techniques, radiotherapy and chemotherapeutic agents. However, despite therapeutic advances and more than 30 years experience with this treatment regiment, virtually all malignant gliomas recur, normally within 2 cm of the prior resection margin [9]. Only recently has chemotherapy been shown to increase survival in the treatment of malignant glioma. In a randomized phase III clinical trial completed in 2005,

conventional fractionated radiotherapy was compared to combination therapy of temozolomide chemotherapy with fractionated radiotherapy [10]. Median survival was 12.1 months for the radiotherapy group and 14.6 months in the combination therapy group. Two year survival was improved to 26.5% for the combination therapy group as compared to 10.4% for the radiation therapy group [10, 11]. The Food and Drug Administration (FDA) approved temozolomide chemotherapy for the treatment of newly diagnosed glioblastoma multiforme in 2005 [12]. Thus, the standard of care for malignant glioma patients has been updated to include surgical resection of the bulk tumor followed by adjuvant fractionated radiotherapy and concomitant temozolomide chemotherapy [13]. However, even with improved chemotherapy agents that have changed the standard of care, the prognosis of patients with high-grade malignant glioma remains dismal and thus better therapy options are currently under investigation.

Novel malignant glioma treatments currently under investigation include photodynamic therapy (PDT), and a vast array of molecularly targeted therapies to inhibit vascular endothelial growth factor receptor, epidermal growth factor receptor as well as a number of gene therapies targeted at the most common mutations [14]. Since the first attempt at use of PDT for the treatment of human glioma in 1980, over 500 glioma patients have been treated with PDT, primarily using the photosensitizer hematoporphyrin derivative [4, 15]. PDT efficacy is dependent on the amount of photosensitizer localized in the tumor tissue, the amount of light of the appropriate wavelength to excite the photosensitizer reaching the tissue and the oxygen content of the tissues to react with the excited photosensitizer to selectively kill tumor cells. Glioma patients that have been treated with PDT over the past 25 years have had different light

sources, light doses, variation in photosensitizer composition and a variety of other differences making a direction comparison of the obtained results difficult to interpret [4]. However, from these studies it is apparent that the use of PDT for glioma therapy will only be successful as an adjuvant therapy to the existing standard of care and not as a stand alone therapy [4].

1.2.2. Epidermal Growth Factor Receptor Biology & Erbitux Therapy

The epidermal growth factor receptor (EGFR) is overexpressed in numerous varieties of epithelial malignancies including gliomas. EGFR is a transmembrane protein with three domains including the extracellular ligand binding domain, a hydrophobic transmembrane region and an intracellular tyrosine kinase domain [16]. The endogenous ligands that bind to EGFR enabling signals to be passed across the cellular membrane are epidermal growth factor (EGF) and transforming growth factor α (TGF α). Ligand binding to EGFR leads to homodimerization or heterodimerization, phosphorylation and a complex signaling cascade within the cell [17]. Three key signaling pathways activated by EGFR ligand binding include the mitogen-activated protein kinase (MAPK), phosphatidylinositol-3 kinase (PI3K) and the signal transducer and activator of transcription (STAT) family of proteins. These pathways mediate cellular proliferation, cell cycle progression and survival, cell division, motility, invasion and adhesion [16, 17].

EGFR is overexpressed in 40 – 60% of gliomas and its activation appears to promote the development and progression of malignancy [16, 18]. There are also various mutated forms of EGFR, one of the most well characterized EGFRvIII is detected in

about half of glioma tumors with amplified EGFR [17]. Dysregulation of EGFR is associated with proliferation, angiogenesis, metastasis, and apoptosis inhibition as well as resistance to chemotherapy, radiation therapy or both [16]. Although a number of other genetic alterations occur in glioma tumors EGFR is the most frequently amplified gene and thus a rationale target for potential therapeutics [17]. Two main classes of EGFR targeted agents have emerged as promising therapies; monoclonal antibodies (MAbs) that target the extracellular ligand-binding domain and tyrosine kinase inhibitors (TKIs) which interfere with the intracellular domain signaling [16].

TKIs are designed to selectively inhibit EGFR but generally have low specificity as compared to MAbs and may partially inhibit other receptor tyrosine kinases. TKIs also require more frequent administration to maintain constant plasma concentration as compared to MAbs, but unlike MAbs are orally available [16]. Two TKIs have been approved by the FDA including erlotinib, which was approved in 2004 for patients with advanced non-small cell lung carcinoma (NSCLC), and gefitinib, which was initially approved in 2003 for the treatment of NSCLC. However, following negative results of a phase III clinical trial approval was downgraded to administration only to patients currently benefiting from gefitinib therapy and for clinical trials [19]. Both erlotinib and gefitinib are being investigated for glioblastoma multiforme in clinical trials. Phase I/II trials with erlotinib show glioma response to the drug alone or in combination with temozolomide. Phase I/II trials with gefitinib show conflicting results where some trials have positive tumor response and others do not. Thus, clinical trial results for erlotinib appear more promising than those for gefitinib as an EGFR inhibition therapy for glioma patients [17].

MAbs specific to EGFR competitively bind to the extracellular domain preventing receptor tyrosine kinase activation and the subsequent signalling pathways. A number of MAbs specific for EGFR have been developed; one of the most successful is cetuximab which was commercialized as Erbitux by ImClone. Cetuximab was approved by the FDA in 2004 for the treatment of advanced colorectal cancer which was refractory to irinotecan. It was approved in 2006 for the treatment of head and neck cancer as a monotherapy or in combination with radiation [19]. Cetuximab has a two-log higher binding affinity for EGFR than either endogenous ligand and once bound, the receptor-antibody complex is internalized and inactivated without any activation of the tyrosine kinase domain. Thus, the tyrosine kinase signal transduction is blocked by both the downregulation of EGFR and by the competitive binding of cetuximab for remaining cell surface receptors [20]. Cetuximab also binds to the mutant EGFRvIII although not with the same affinity as to EGFR. Cetuximab has a half-life of about 7 days in humans so administration can be about a week apart to keep plasma concentrations constant. While TKIs are orally available, Cetuximab must be administered intravenously [16]. Preclinical data on systemic administration of cetuximab for animals with subcutaneous and intracranially implanted gliomas with high EGFR expression have illustrated efficacy [17, 21]. These findings are encouraging since MAbs are much larger than TKIs which might impair their ability to cross a partially intact or fully intact blood brain barrier. Phase I/II clinical trials with combination radiotherapy, temozolomide and cetuximab for newly diagnosed glioblastoma multiforme are currently ongoing [14].

1.2.3. Experience with ALA-PpIX & Brain Cancer

The Aminolevulinic Acid (ALA) – Protoporphyrin IX (PpIX) system has been studied extensively for applications in photodynamic therapy (PDT) and photodiagnosis (PDD) as well as other fluorescence imaging applications [22, 23]. Administration of ALA overloads the heme synthesis pathway, which exists in all mammalian cells, and fluorescently detectable levels of PpIX are produced [22, 24, 25]. Variable levels of PpIX are produced when ALA is administered to different cells and tissues, but it is generally the case that the tumor tissue produces higher levels of PpIX than the surrounding normal tissue. A significant difference in PpIX production has been found in brain tumor tissues over normal brain [26-29]. However, different preclinical brain tumor models have been studied and found to have varied PpIX accumulation patterns, making some models more useful for study than others [30]. Preferential accumulation of PpIX in tumor tissues over normal tissues makes it useful as both a photosensitizer for PDT and a fluorophore for PDD and other fluorescent imaging applications. Both PDT and PDD with the ALA-PpIX system have been extensively researched for cancer applications, including brain cancer applications.

ALA-based PDT is currently under research as an adjuvant therapy for gliomas and has been extensively studied in preclinical models as both a primary and adjuvant therapy [23, 25, 31, 32]. ALA-based PDT has not been shown to eradicate gliomas when used as a primary, single dose therapy in preclinical models whether the treatment is administered when the tumors are very small or after significant progression has taken place [33, 34]. Considerable improvement on ALA-PDT efficacy has been realized when it is administered as a primary, metronomic therapy in preclinical rat and rabbit models,

although significant technical challenges make this treatment less desirable as standard therapy [31, 35]. ALA-PDT has also been experimented with as a secondary therapy to treat tumor beds following surgery or in combination with other therapies. A very small clinical study was performed on five glioma patients undergoing tumor resection. ALA was administered prior to surgery and a therapeutic light dose of 635 nm light was delivered to the tumor bed following surgical resection. These patients had no side-effects and showed an effective zone of 2 cm diameter without sign of brain edema upon examination with MRI [22]. A protocol for interstitial stereotactic placement of cylindrical diffusing fibers for PDT has also been developed for patients with recurrent inoperable glioma [36]. Most current knowledge about PDT as an adjuvant treatment for glioma has been collected from studies using hematoporphyrin derivative, and as mentioned previously have been completed over the past 25 years with significant standardization issues making interpretation of results difficult [4]. Thus, much research on the efficacy of ALA-PDT on gliomas as an adjuvant therapy and how these combinations would benefit glioma patients is left to be explored.

Use of the ALA-PpIX system has been very successful in surgical guidance of brain tumor resection [28, 29]. Preclinical rabbit models were used to test PpIX fluorescence for surgical guidance of brain tumor resection and found to increase the completeness of tumor resection by a factor of 1.4 and decrease the amount of residual tumor by a factor of 16 from the initial tumor volume [26]. Significant success was also seen in the clinic using ALA-PpIX for fluorescence-guided surgery of malignant glioma resection [28]. A phase III randomized, multicenter clinical trial was completed and published in 2006 on the use of PpIX fluorescence for surgical guidance of malignant

glioma resection. Patients were randomly assigned to receive either conventional white light microsurgery or ALA fluorescence-guided tumor resection. Contrast enhancing tumor as measured by MRI was completely resected in 65% of the patients that received ALA fluorescence-guided resection where as only 36% of patients receiving conventional white light microsurgery had completed resections. This increase in resection resulted in higher 6-month progression free survival for the fluorescence guided surgery patients over patients that received conventional resections (41% vs. 21.1%) [29]. Thus, PpIX has been shown to have high tumor selectivity in brain tissue and can be used to improve surgical resection of invasive tumor tissue.

1.2.4. Brain Cancer Therapy Monitoring: Current State & Promising Research

Magnetic resonance imaging (MRI) is the gold standard for noninvasive brain tumor visualization. The main sequences used to visualize anatomic lesions are proton density-weighted images, T2-weighted images, and T1-weighted images. These imaging sequences are normally followed by the injection of a contrast agent, Gadolinium Diethylenetriamine Pentaacetic Acid (Gd-DTPA) and collection of a T1-weighted contrast enhanced imaging set [37-39]. Through use of standard MRI sequences most brain tumors are detected with high sensitivity prior to any intervention, however following conventional treatment differentiation between recurrent tumor and radionecrosis is limited in this anatomical imaging method [39, 40]. Additionally, it has been shown that vast intraobserver variability exists when reading conventional MRI sequences to determine response to therapy [41, 42]. Due to the aggressive nature of gliomas, evaluation of treatment response as early as possible is important for increased

patient survival. Assessment of tumor size may not always be well correlated to survival as progression can occur in a small region of the tumor, but still have a significant effect on the outcome of the patient [43]. For these reasons, functional imaging may prove more useful than anatomical imaging for noninvasive monitoring of treatment efficacy in brain cancer patients.

Along with structural imaging, MRI also offers functional imaging through various sequences that can assess tumor tissue vascularity, architecture and metabolism [38, 39, 44]. Physiologic information about neovascularity and angiogenesis of the entire brain can be attained through dynamic susceptibility contrast perfusion MRI (DSC MRI). DSC MRI is used to calculate the relative cerebral blood volume (CBV), which is usually estimated through acquisition of T2*-weighted images during an intravenous injection of a bolus of Gd-DTPA [44, 45]. CBV has been demonstrated to be closely correlated to microvascular density, and preliminary clinical studies have shown the ability of this metric to predict tumor progression and clinical response [38, 45]. However, some mixed results have been shown in preliminary clinical trials which could be due to the heterogeneity of CBV, requiring further characterization prior to standard practice of this technique [44]. Tumor architecture information can be studied using diffusion weighted MRI which is sensitive to the Brownian motion of intracellular and extracellular water molecules in the tissues [43]. MRI images that have been taken both with and without diffusion encoding can be compared and from these pairs of images the apparent diffusion coefficient (ADC) can be calculated and used as a therapy monitor. Measurements of ADC in the brain have been used to gather information about the changes in cellularity, cell membrane permeability and extracellular space. Similarly to

DSC MRI, diffusion weighted MRI requires additional clinical studies to determine its ability to detect tumor response to therapy, but preclinical studies have shown that ADC measurements are an early indicator of both response to therapy and overall survival [44].

Tumor tissue metabolism can be studied through MR spectroscopic imaging (MRSI), which allows functional imaging of tissue by obtaining information about the composition and spatial distribution of cellular metabolites. Chemical compounds and metabolites commonly detected in brain tissue with MRSI are N-acetylaspartate (NAA), choline containing compounds (Cho), creatine (Cr), lipid (Lip) and lactate (Lac). Spectra of these compounds can be used to interpret information about the tissue depending on the amount of these compounds present and their ratio to one another. NAA signal is a marker of normal neuronal function, its reduction in tumors has been associated with low density of neuronal cells within selected volumes. Cho signal is typically increased in tumor tissue and is thought to represent an increase in cell density and in cell membrane turnover. Cr signal is thought to represent the energy status of the tissue, while Lac is a product of anaerobic metabolism and is thought to represent hypoxic regions of the tissue. Lip signal is thought to correlate to cellular and membrane breakdown corresponding to necrosis [39]. Thus, through the use of these compounds and metabolites MR images and MRSI can be attained in tandem and interpreted together as structural and functional tissue information. Initial studies have shown this technique is quite promising for treatment monitoring, although similar to the other MRI techniques discussed previously, additional clinical experimentation will be required to prove MRSI's validity as a treatment monitoring device [44].

Nuclear medicine is also well suited for functional imaging of tumor tissue with positron emission tomography (PET) and single photon emission computed tomography (SPECT) facilitating assessment of tumor physiology, metabolism and proliferation [46]. A number of tracer molecules have been investigated in both PET and SPECT applications. PET tracers that are the most common and have shown the greatest promise for application to treatment monitoring are [^{18}F]fluorodeoxyglucose (FDG), which tracks glucose uptake, [^{11}C]-L-Methionine (MET), which tracks amino acid uptake and [^{18}F]fluorothymidine (FLT), which tracks nucleoside uptake [1, 46]. FDG is widely used in the PET imaging field, but has not been as useful for treatment monitoring in brain tumors as other tracers due high background uptake in brain tissue as well as its low specificity to tumor growth due to glucose demands of inflammatory cells [46, 47]. C-MET has been more successful at tracking response to therapy as a decreasing uptake during therapy corresponds to stable disease and is able to differentiate recurrent tumor from radiation necrosis. One difficulty with this tracer is its rapid degradation and complex metabolism, making it more difficult to use than [^{18}F] labeled compounds [47, 48]. F-FLT based PET imaging shows promise for treatment monitoring as it is specific for tumor tissue and has higher uptake than C-MET, although trials are still preliminary and additional clinical research is needed to determine its use in monitoring response to therapy [46, 47].

The SPECT tracers that are the most common and have shown the most promise for application to treatment monitoring are Thallium-201 (^{201}Tl), technetium-99m methoxyisobutylisonitrile ($^{99\text{m}}\text{Tc}$ -MIBI) and 123-iodine- α -methyl tyrosine (^{123}I -IMT) [1, 42, 49, 50]. ^{201}Tl has been used heavily for SPECT imaging since the 1970's for various

clinical applications. As a tracer for malignant cells ^{201}Tl is taken up selectively in malignant cells over normal cells which is due to cell membrane ATP-ase pump activity, tumor vascularization and cell proliferation [1, 42]. A few clinical studies have shown ^{201}Tl SPECT imaging able to predict response to therapy better than conventional anatomical imaging [41, 42, 51]. $^{99\text{m}}\text{Tc}$ -MIBI is a newer SPECT tracer and its uptake in brain tumors is driven by metabolic demand. $^{99\text{m}}\text{Tc}$ -MIBI is a tracer for cell viability, which diffuses passively through cell membranes under the control of the transmembrane potential. About 95% of intracellular $^{99\text{m}}\text{Tc}$ -MIBI is found in the mitochondria of the cell with higher uptake in malignant cells than normal cells [50]. $^{99\text{m}}\text{Tc}$ -MIBI SPECT imaging has been studied in the differentiation between tumor recurrence and radionecrosis and found to differentiate between these tissue types [1, 40, 50]. ^{123}I -IMT uptake reflects amino acid transport and is very similar to C-MET PET imaging although more readily available for use than standard PET imaging [1].

1.2.5. Optical Molecular Imaging

The possibility for functional imaging technology currently exists in the clinic in the form of modified MRI sequences, PET and SPECT imaging, although additional research is needed to fully realize the potential of these methods. Optical molecular imaging is unique in the imaging world as it provides an array of contrast mechanisms that can be used to visualize tissue. Endogenous contrasts in the tissue can be imaged through the detection of absorption and scattering properties. Absorption spectra can be used to quantify hemoglobin and water concentrations as well as oxygenation status of the tissue while scattering spectra can be used to quantify the size and density of cellular

components. Both absorption and scattering profiles differ in cancerous tissues as compared to normal tissues providing visible spectral differences between tissue types [52, 53]. Endogenous fluorescence spectroscopy of tissues can also be collected to examine a wide variety of biological molecules with unique spectra including amino acids, structural proteins, enzymes and lipids which also differ in cancerous tissues as compared to normal tissues [54]. Probe development is currently a very active area of research with bioluminescent, near infrared fluorescence and activatable fluorescence probes adding significant capability to optical imaging of diseased tissues [55, 56].

Optical molecular imaging has the potential to greatly impact treatment monitoring and patient health. With the vast array of therapy choices and development of new molecularly targeted therapies it is important to quickly evaluate if the patient is responding to avoid progression of a nonresponsive tumor. Currently there is no reliable way to quickly determine the efficacy of nonsurgical therapies, thus evaluation of therapy response is primarily based on tumor size changes. Typically chemotherapy response is assessed after 8 weeks and radiation response is not assessed until 12 weeks after the initiation of therapy [57]. However, many characterized molecular events have occurred prior to any changes that are seen 8 – 12 weeks following initiation of therapy. Probes to monitor tumor metabolism changes, receptor status and genomic therapies would allow visualization of relevant molecular changes that could impact the course of therapy.

1.3. Thesis Overview

The chapters in this thesis have been organized to describe work performed to characterize the two molecular imaging fluorophores *in vitro*, the imaging systems used

for *in vivo* visualization, data post-processing to enhance signal to background detection and *in vivo* testing following probe and imaging system validation.

Chapter 2 presents *in vitro* studies of Protoporphyrin IX production heterogeneity and correlated cellular morphological features. The methods for *in vivo* brain tumor model development are also outlined.

Chapter 3 introduces the four imaging systems used for *in vivo* fluorescence quantification and monitoring, which are validated through tissue simulating phantom experiments presented in *Chapter 4*. The ability of each system to detect murine intracranial brain tumors will also be discussed.

Chapter 5 deals with the difference seen in tumor tissue morphology and how this affected visualization of the different intracranial brain tumor models using magnetic resonance imaging.

Chapter 6 presents a chronological account of *in vivo* PpIX detection in the three tumor models studied. *In vivo* PpIX production heterogeneity is investigated and the detectability of each tumor type via noninvasive spectroscopy is calculated.

Spectroscopic treatment monitoring is presented in *Chapter 7*. Epidermal growth factor receptor status is monitored via fluorescence spectroscopy measurements in a positive expression model and a negative control group to determine the feasibility of noninvasive Erbitux therapy monitoring.

Chapter 8 presents case studies from animal data presented in both *chapters 6* and *7* to examine fluorescence heterogeneity and cancer as an individual disease.

The concluding remarks and future directions for this work are discussed in *Chapter 9*.

Chapter 2 - *In Vitro* PpIX Studies & *In Vivo* Brain Tumor Models

2.1. Introduction

The Aminolevulinic Acid (ALA) – Protoporphyrin IX (PpIX) system has been studied extensively for Photodynamic Therapy (PDT) and fluorescence imaging applications. ALA is a prodrug which is converted to PpIX via the heme synthesis pathway (Figure 2.1). Low levels of PpIX exist normally in cells prior to its conversion to heme, however the pathway can be overloaded with exogenous ALA to produce fluorescently detectable levels of PpIX [23, 25, 58, 59]. An iron chelator can be administered in combination with ALA to increase the production of PpIX [60]. PpIX production from ALA is widely variable and it has been shown to be dependent on many factors including ALA uptake and PpIX excretion, morphological features of the cells and tissues as well as the cell microenvironment.

The rate limiting enzyme in the heme synthesis pathway is ALA synthase which catalyzes the reaction between glycine and succinyl-CoA to produce endogenous ALA. ALA synthase is subject to feed-back inhibition by the build-up of heme in the system, therefore ALA is only produced when heme levels are low. However, the addition of exogenous ALA bypasses this enzyme and thus the rate-limiting enzyme in the ALA-PpIX pathway is currently under study. A large body of research on this topic is compiled in a review by Collaud, *et al* [24]. Much of past research points to Porphobilinogen Deaminase (PBGD), as the rate limiting enzyme in the ALA-PpIX pathway [25, 61]. However, recent research suggests that PBGD may play a minor role in the accumulation of PpIX in various cells types *in vitro* [62-64]. It has been suggested

that ALA-dehydratase, which converts ALA to Porphobilinogen, may act as the rate limiting step in the ALA-PpIX pathway since its inhibition causes decreased PpIX production [65]. The ferrochelatase enzyme which catalyzes the insertion of iron to convert PpIX to heme is thought to have decreased activity in neoplastic cells, thus allowing for selective accumulation of PpIX in these cells, especially following the administration of exogenous ALA [25, 66]. The importance of the PpIX to heme step in the ALA-PpIX pathway can also be demonstrated via the use of iron chelators, which increase PpIX production when administered to cells *in vitro* [60, 67].

Both cellular ALA uptake and efflux of the formed PpIX are important considerations in the accumulation of PpIX in neoplastic cell lines. Studies using carbon labeled ALA to measure cellular uptake demonstrated that the uptake mechanism of exogenously administered ALA was through passive diffusion [68]. However, other studies suggest that there may be two mechanisms by which ALA is transported into the cells. Passive diffusion is important at short ALA incubation time intervals, while the active transport system becomes more important at the longer incubation intervals [69, 70]. When neoplastic and non-neoplastic cell lines were incubated in media containing serum, the intracellular concentration of PpIX as well as total PpIX production in both cell types was significantly reduced as compared to the PpIX production in serum free media due to efflux of produced PpIX into the serum containing media [71].

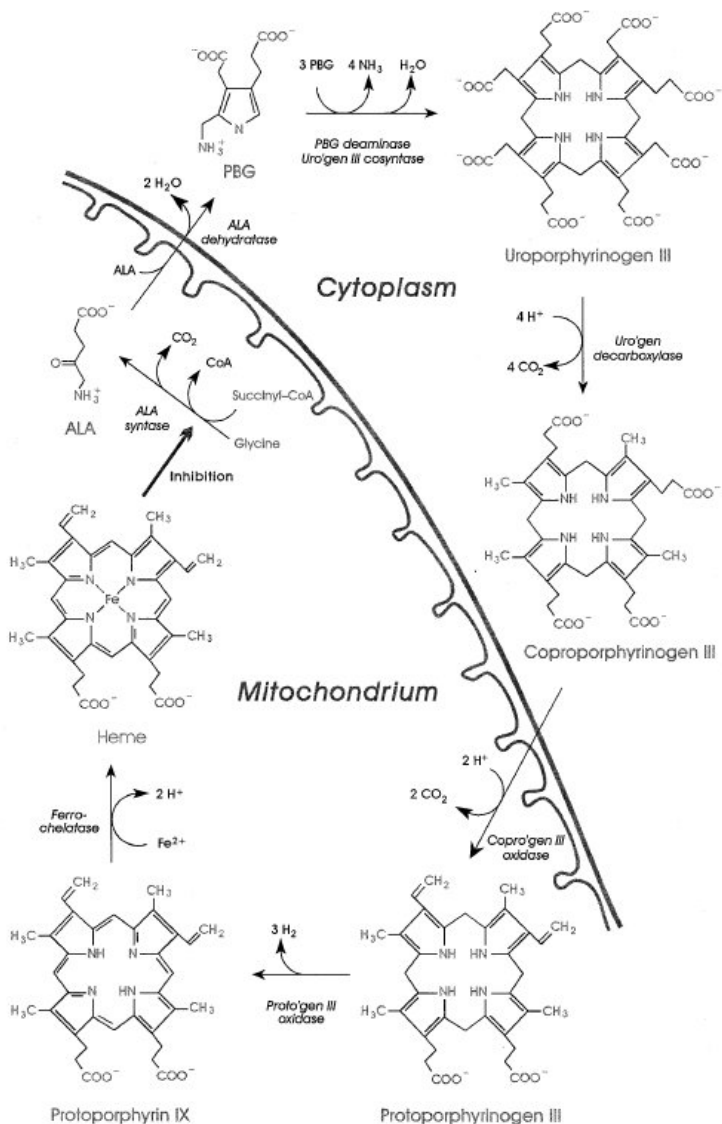


Figure 2.1 – The biochemical steps in the heme synthesis pathway which occurs in and around the mitochondria of all mammalian cells [22].

The enzymatic steps of the heme synthesis pathway occur in and around the mitochondria of the cell and thus cellular mitochondrial contents have been studied in conjunction with PpIX production. Gibson, *et al* demonstrated that varied PpIX production following administration of ALA was correlated to the number of

mitochondria in the cells as measured by Mitotracker Green in four neoplastic cell lines [66]. Liang, *et al* examined the subcellular localization of ALA induced PpIX via fluorescence microscopy and found that the PpIX fluorescence was localized in the mitochondria-rich perinuclear cytoplasm in the two cell lines studied [72]. Cell size was found to have a slight positive correlation to PpIX production with larger cells showing higher production of PpIX in the two cell lines studied [73]. Many environmental factors have also been found to affect PpIX production *in vitro* and are tabulated below (Table 2.1).

	PpIX Production	Reference
Low Glucose	↑	[74]
High Glucose	↓	[74]
Hypoxia	↓	[75, 76]
Normal Oxygen Levels	↑	[75, 76]
Low Incubation Temperature	↓	[24]
High Incubation Temperature	↑	[24]
Acidic pH	↓	[75, 77]
Neutral pH	↑	[75, 77]
Basic pH	↓	[75, 77]
Plateau Growth Phase	↑	[71]
Exponential Growth Phase	↓	[71]
High Plating Density	↑	[73, 76]
Low Plating Density	↓	[73, 76]
G₂ + M Cell Cycle Phase	↑	[73, 78]
G₁ Cell Cycle Phase	↓	[73]
Differentiation Therapy	↑	[79, 80]

Table 2.1 – Environmental factors that affect PpIX production from exogenously administered ALA *in vitro*. PpIX production is shown to increase or decrease with arrow symbols for each environmental factor listed.

The ALA-PpIX pathway has been under much examination with the discovery of many factors that affect the ability of cells to produce PpIX. In this chapter an *in vitro* PpIX production study will be discussed to illustrate morphological factors that can be correlated to PpIX production. The varied PpIX production of the brain tumor cell lines to be studied in this thesis will be illustrated *in vitro*. The brain tumor implantation procedure which was used in all *in vivo* fluorescence studies will also be discussed.

2.2. *In Vitro* PpIX Production Variability

2.2.1. *In Vitro* PpIX Production Variability Materials & Methods

A study was conducted to determine if the PpIX production variability could be correlated with the morphological characteristics of cells. Eight cell lines of varied histological origin were used which included cancers of the brain, breast, prostate and ovary. The DAOY (human medulloblastoma) cell line was cultured in alpha modification of Eagles Medium 1x (MEM) [81]. The Verb/p53 (-/-) (spontaneous mouse oligodendroglioma) cell line and the U-87 (human glioblastoma) cell line were cultured in Dulbecco's modification of Eagle's Medium (DMEM) [82, 83]. The Dunning-MLL (rat prostate carcinoma) cell line and the Du-145 (human prostate carcinoma, ATCC) cell line were cultured in RPMI 1640 1x with L-Glutamine [84, 85]. The Dunning-G (rat prostate carcinoma) cell line was cultured in RPMI 1640 1x with L-Glutamine supplemented with 250 nM Dexamethasone (Sigma-Aldrich, St. Louis, MO) [84]. The Sk-Br-3 (human breast adenocarcinoma) cell line and the Sk-Ov-3 (human ovarian adenocarcinoma) cell line were cultured in DMEM/F12 50/50 Mix with L-Glutamine [86]. All media, PBS and trypsin were obtained from Mediatech Inc., Herndon, VA. The

media for all cell lines was supplemented with 1% penicillin/streptomycin from a stock solution of 10,000 IU penicillin and 10,000 µg/ml streptomycin (Mediatech, Inc., Herndon, VA) and 10% fetal bovine serum (Atlanta Biologicals, Lawrenceville, GA). The cells were incubated at 37° Celsius in 95% air and 5% carbon dioxide humidified environment. All cells were used for experimentation when they were grown to similar confluence to account for growth phase. All cell lines were passed less than 10 times *in vitro* during experiments.

Flow cytometry was used to measure PpIX production prior to ALA administration (Sigma-Aldrich, St. Louis, MO) and at 1, 2 and 4 hours after ALA administration. A FACScan flow cytometer (Becton Dickinson, San Jose, California) with either a 488 nm laser or a 633 nm laser for excitation and either a 650 nm long pass filter or a 661/16 nm band pass filter for emission was used to measure cellular PpIX fluorescence. Mitochondrial content of the cells was examined through staining with Mitotracker Green (Invitrogen – Molecular Probes, Carlsbad, CA) via the FACScan to examine Mitotracker Green fluorescence using a 488 nm laser for excitation and a 530/30 nm band pass emission filter. PpIX production following administration of ALA in combination with an iron chelator 1,2-dimethyl-3-hydroxy-4-pyridone (L1) (Acros Organics, Somerville, NJ) was also examined 4 hours after coadministration of 1 mM ALA and 25 µg/ml L1 in PBS.

Briefly, the procedure for preparation of cells for flow cytometry measurement is explained as follows. The cells were plated in 24-well plates 24 hours prior to the addition of ALA at a concentration of 2.5×10^5 cells in 1 ml volume of the appropriate media. Prior to the addition of ALA the media containing serum was removed and the

cells were washed twice with PBS. Serum free media was then added to the cells to prevent PpIX efflux from the cells into the media [71]. ALA in PBS at a concentration of 1 mM was added to the cells 1, 2 or 4 hours prior to trypsinization followed by PpIX content analysis via flow cytometry. Cells intended for endogenous PpIX production analysis were administered the same volume of PBS without ALA. Mitotracker Green was added to the cells at a concentration of 0.1 μ M 30 minutes prior to trypsinization. For the trypsinization process, the serum free media was removed and the cells were washed once with PBS prior to the addition of 200 μ l of trypsin EDTA (0.05%) to each well. Once the cells had detached from the plate 800 μ l of PBS was added to the well and its contents was placed in a flow cytometer tube and centrifuged at 110 g (Jouan Centrifuge, Model C312) for 5 minutes. The supernatant was removed from the tubes and 0.5 ml PBS was added to each tube. The pellet was then resuspended by vigorous vortexing prior to reading on the FACScan flow cytometer.

The MTS assay was used to assess mitochondrial activity in the eight cell lines. The cells were plated in 96-well plates in triplicate at a concentration of 5.0×10^3 cells in 100 μ l volume of the appropriate media. Triplicate samples of the five types of media were also plated without cells to be used as controls. The 96-well plate was placed in the incubator for two hours following the cell plating to allow the cells to attach to the plate. Fifty μ l PMS reagent, phenazine methosulfate, was added to 1 ml MTS reagent, 3-(4,5-dimethylthiazol-2-yl)-5-(3-carboxymethoxyphenyl)-2-(4-sulfophenyl)-2H-tetrazolium, and mixed well in an Eppendorf tube (CellTiter 96 Aqueous Non-Radioactive Cell Proliferation Assay, Promega Corporation, Madison, WI). Twenty μ l of the PMS and MTS reagent solution was added to each sample in the 96-well plate. The plate was

placed back in the incubator for two hours to allow the bioreduction of the MTS and PMS reagents into the formazan product. Absorbance at 490 nm was read on a MXR Plate Reader (ThermoLabsystems, Chantilly, Virginia). Each cell line's absorbance was normalized for the type of media that was used by reading control blanks containing medium, PMS and MTS reagent solution without cells.

Growth rate of the eight cell lines was measured to determine its relationship with PpIX production. The cells were plated in 60 mm tissue culture dishes at a concentration of 5.0×10^4 cells per dish. Five dishes were plated for each cell line. Each day for five days one dish had the media removed, was washed twice with PBS and trypsinized. The cells were counted in duplicate using a hemacytometer. Growth curves were constructed for each cell line, from which the doubling time for each cell line was calculated.

Cellular size was assessed by two methods including forward scatter via flow cytometry measurements and cellular area measurements performed on fluorescently stained cells. For the cellular area measurements, the cells were plated in 60 mm tissue culture dishes and grown to about 50% confluence. The cells were stained with DiOC₇ (Invitrogen – Molecular Probes, Carlsbad, CA) at a concentration of 1 µg/ml, for 15 minutes. The media was then removed and the cells were washed twice with PBS, trypsinized and resuspended in media. A 10 µl volume of the cell suspension was placed between a slide and cover slip. Images were obtained using a QColor3 camera (Olympus America, Inc., Melville, NY) attached to an inverted fluorescence microscope. The DiOC₇ dye was excited using a 470 – 490 nm filter and the fluorescence emission was seen through a 520 – 560 nm filter. The images obtained at 20x showed rounded fluorescent green cells on a black background and were analyzed using ImageJ (Rasband,

W.S., ImageJ, U. S. National Institutes of Health, Bethesda, Maryland, USA, <http://rsb.info.nih.gov/ij/>, 1997-2005.). Each image was changed from the RGB Color format to an 8-bit format so that the threshold command could be used. Using ImageJ, the images were set to the same threshold and the area of the fluorescent pixels was then analyzed. The area of 50 – 70 cells was averaged to obtain the average cell area in μm^2 for each cell line.

2.2.2. *In Vitro* PpIX Production Variability Results

Endogenous and exogenous PpIX production varied greatly with up to a 13 fold difference seen in endogenous PpIX production while a 10 fold difference in PpIX production was seen following ALA administration (Figure 2.2).

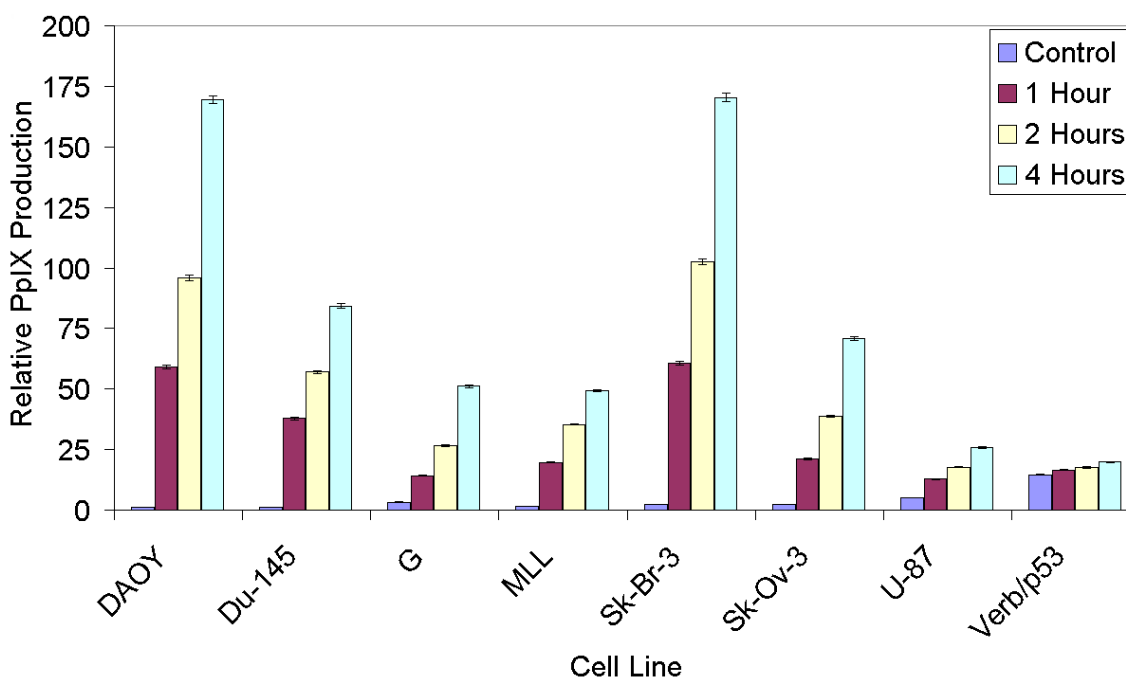


Figure 2.2 – Heterogeneity in PpIX production following 1 mM ALA administration to all cell lines. PpIX content was measured prior to ALA administration (control), then at 1, 2 and 4 hours after ALA administration. The mean PpIX fluorescence intensity for 2000 cells is shown, with the error bars representing the standard error of the mean.

Morphological factors of the cell lines were examined to determine their significance in the heterogeneous production of PpIX both prior to ALA administration and after ALA administration. The heme synthesis pathway occurs in and around the mitochondria, with three of the enzymatic steps occurring in the cytoplasm of the cell, and two of the enzymatic steps occurring in the mitochondria of the cell. A positive correlation was seen between mitochondrial content of the cell line and endogenous PpIX production as measured by Mitotracker Green to examine mitochondrial content ($p = 0.049$) (Figure 2.3(a)). This correlation was further supported by the side scatter measurements obtained via flow cytometry ($p = 0.006$), which physically represent the granularity of the cells and have been loosely correlated to mitochondrial content of the cells in some studies, but are more likely a mixed measure of total intracellular density of small organelles (Figure 2.3(b)) [87]. However, following the administration of exogenous ALA, no correlation was seen between Mitotracker Green fluorescence and PpIX fluorescence ($p = 0.843$) or side scatter and PpIX fluorescence ($p = 0.356$) (Figure 2.3(c) & (d)). The activity of the mitochondria in each cell line was examined via MTS assay, which is frequently used for mitochondrial activity measurement, but may only measure the dehydrogenase activity present in the cell. Mitochondrial activity was not correlated to either endogenous PpIX fluorescence ($p = 0.320$) or exogenous PpIX fluorescence ($p = 0.862$).

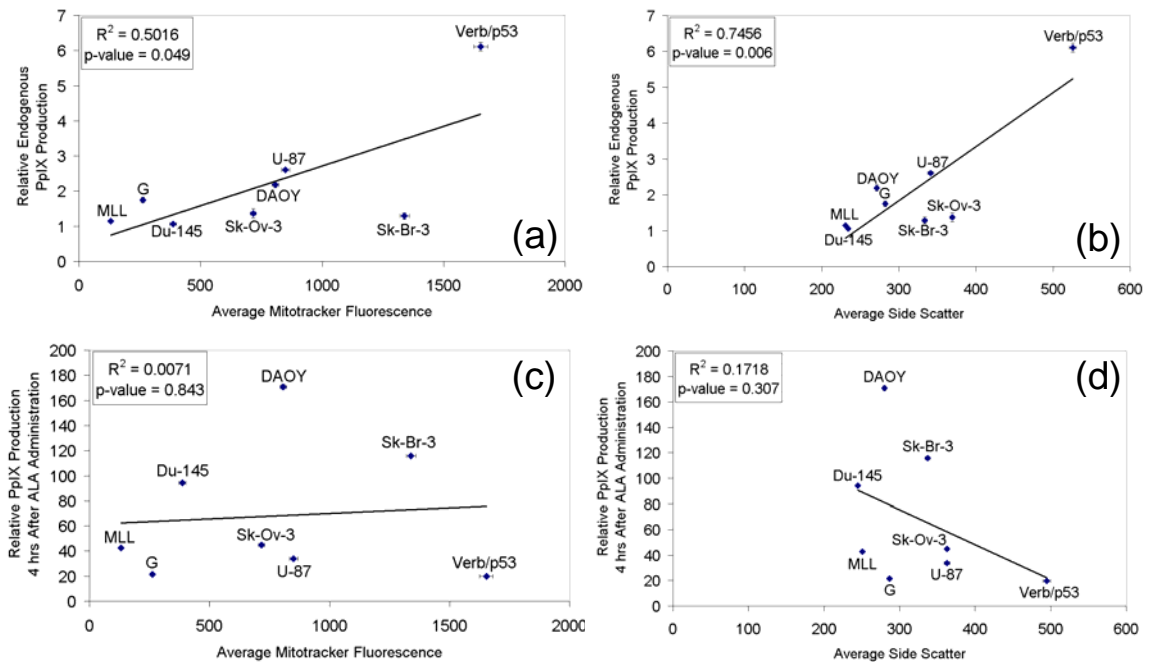


Figure 2.3 – (a) Mitochondrial content as measured by Mitotracker Green showed a positive correlation to the endogenous PpIX fluorescence prior to the administration of ALA. (b) The relative side scatter was well correlated with PpIX production of the eight cell lines prior to ALA administration. (c) Following ALA administration to the eight cell lines no correlation was seen between Mitotracker fluorescence and PpIX production (d) Similarly, when the side scatter measurements from flow cytometry were considered no correlation was seen between relative side scatter and PpIX production following ALA administration.

Both the phase of growth and the phase of the cell cycle at which ALA was incubated with the cells have been shown to affect the PpIX production of the cells [71, 73, 78]. In this study we examined the growth rate of the cells to determine its relationship to cellular PpIX production capacity. No statistically significant correlation was seen between PpIX production and doubling time of the cells ($p = 0.403$). This result was similar to that of Wyld, *et al* in their study of two neoplastic cell lines and four non-neoplastic cell lines where they did not see a correlation between proliferation rate of the cells and generation or accumulation of PpIX [71].

The morphological feature that did show correlation with exogenous PpIX production in this study was cellular area. Cellular area was measured both via fluorescence microscopy of stained cells in suspension and forward scatter as measured by flow cytometry, which is an estimate of cellular size [87]. Both measurements illustrated that cellular area was well correlated to exogenous PpIX production of the cells, with the larger cells showing higher PpIX production at the time of assay (Figure 2.4(a) & (b)). This relationship between cell size and PpIX production held both across the eight cell lines studied as well as within each of the cell lines studied (Figure 2.4(c) & (d)). The correlation between forward scatter and PpIX production as it related to incubation time with ALA can be seen in the DAOY cell line (Figure 2.4(c)) and the U-87 cell line (Figure 2.4(d)). No correlation between forward scatter and PpIX production was seen prior to the administration of ALA in the control samples in either the DAOY or U-87 cell line. However, positive correlation was seen between PpIX production and cellular size following the administration of ALA with the most significant correlation seen at the 4 hour time point. The U-87 cell line had much lower PpIX production than the DAOY cell line (Figure 2.2) and thus the population of cells at the 4 hour time point was not significantly higher than the control population of cells where the PpIX production was measured without ALA administration. However, a positive correlation between forward scatter and PpIX production at 4 hours can still be observed. Our data was in agreement with a study by Moan, *et al* where two neoplastic cell lines were studied and a slight positive correlation between cell size and PpIX fluorescence of the cells was demonstrated via light scatter data from flow cytometry [73]. This finding was also supported by experiments that demonstrate that the most PpIX was produced in the

G₂ + M phase of the cell cycle [73, 78] when the cells would be at their largest size due to their preparation to divide. Therefore, the morphological feature that was most related to exogenous PpIX production was cellular size and thus cytoplasmic content.

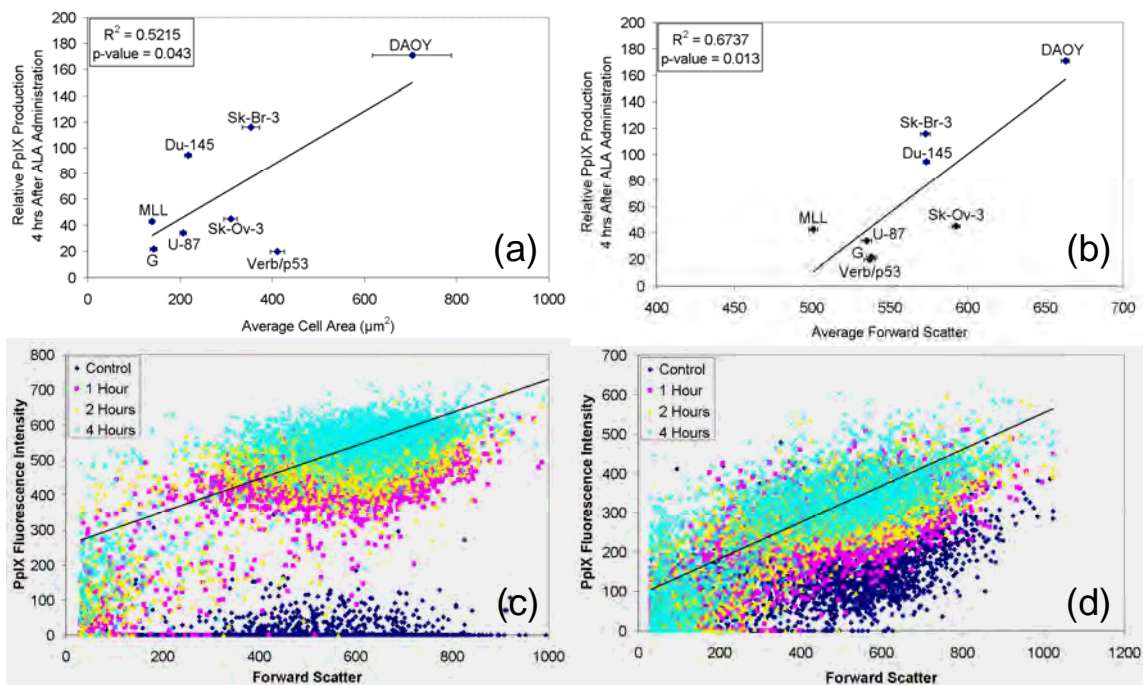


Figure 2.4 – (a) Cell area as measured by fluorescence microscopy on cells in suspension was positively correlated with PpIX production following ALA administration. (b) This relationship was supported by the forward scatter data from flow cytometry which was positively correlated with PpIX production following the administration of ALA. (c) The correlation between forward scatter and PpIX production as it relates to incubation time with ALA can be seen in the DAOY cell line. The black line represents a linear fit to the data at the 4 hour time point to allow visualization of the positive correlation between PpIX production and forward scatter. (d) The correlation between forward scatter and PpIX production as it relates to incubation time with ALA can be seen in the U-87 cell line. A positive correlation between forward scatter and PpIX production at 4 hours was observed, and is represented by the black line that signifies a linear fit to the data.

PpIX production was increased in all of the tested cell lines when an iron chelator, 1,2-dimethyl-3-hydroxy-4-pyridone (L1), was administered in combination with ALA.

This coadministration of ALA and L1 acted to overload the heme synthesis pathway to

produce PpIX and delay the conversion of PpIX to heme, thus increasing the amount of detectable PpIX at the time of measurement (Figure 2.5(a)). Interestingly, following coadministration of ALA and L1 those cell types that had the lowest PpIX production following ALA administration alone showed the largest percentage increase following coadministration of ALA and L1 ($p = 0.027$) (Figure 2.5(b)).

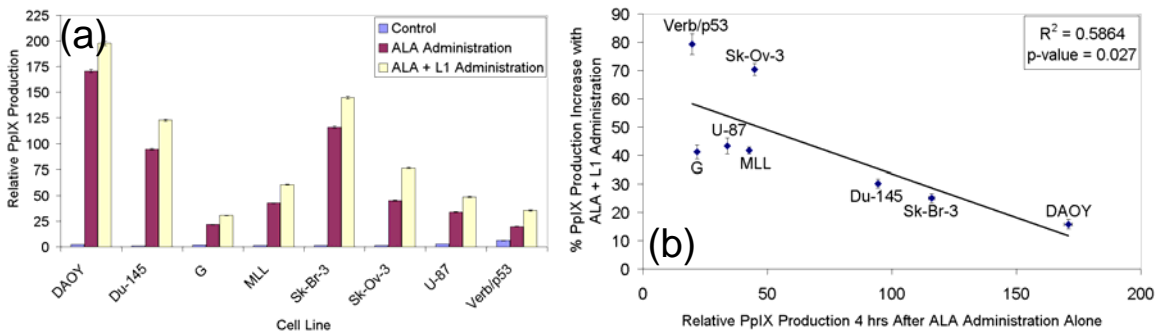


Figure 2.5 – (a) The mean PpIX fluorescence intensity prior to ALA administration (control), 4 hours after ALA administration and 4 hours after ALA + L1 administration is shown, with the error bars representing the standard error of the mean. (b) The cells with the lowest PpIX production following ALA administration alone show the largest percentage increase in PpIX production following ALA + L1 administration. The error bars represent standard deviation of the mean.

2.3. *In Vitro* Variability of PpIX Production in Brain Tumor Cell Lines

Four brain cancer cell lines were examined to determine their PpIX production ability including the U251 (human glioma) cell line, the U251-GFP (human glioma) cell line, the 9L (rat gliosarcoma) cell line and the 9L-GFP (rat gliosarcoma) cell line. The cells were administered 1 mM ALA 1, 2 and 4 hours prior to PpIX content analysis via flow cytometry as described previously. The endogenous, background PpIX production was also examined for cells which were not administered ALA. Figure 2.6 illustrates the PpIX production time course for each of the four cell lines. The PpIX production ability

of the U251 cell line appeared to be unaffected by the GFP transfection process, as the PpIX production of the U251 parent line and the U251-GFP cell line were virtually identical. The PpIX production ability of the 9L cell line did appear to be affected by the GFP transfection as the 9L-GFP cell line had lower PpIX production at each time point shown in Figure 2.6 as compared to the 9L parent line. Four hours after ALA administration the U251-GFP, U251 and 9L-GFP cell lines showed similar PpIX production, however for all *in vivo* PpIX fluorescence measurements the 2 hour time point was examined. The 2 hour time points was chosen for *in vivo* experiments because the skin PpIX fluorescence was lower as will be discussed in chapter 3 and produced PpIX would have less time to efflux from the tissue of interest prior to measurement. Figure 2.6 illustrates that 2 hours after the administration of ALA the U251-GFP cell line had slightly higher PpIX production ability than the U251 cell line, but the two were virtually identical. However, the U251-GFP and the U251 parent line showed considerably higher PpIX production than the 9L-GFP cell line at this time point. The 9L parent cell line was not used for any *in vivo* studies. Its PpIX production 2 hours after ALA administration was very similar to the U251-GFP and U251 cell lines. Interestingly, the PpIX production ability of the 9L parent line 4 hours after ALA administration was the highest of the four brain cancer cell lines tested.

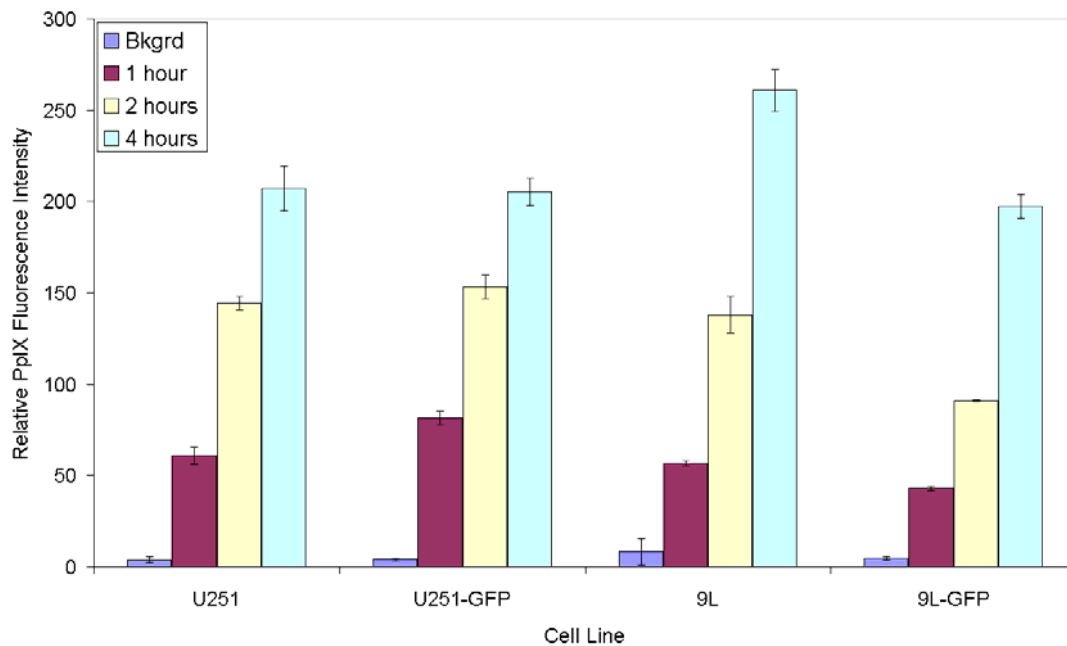


Figure 2.6 – PpIX fluorescence time course for U251, U251-GFP, 9L and 9L-GFP cell lines. Cells were examined for endogenous, background PpIX fluorescence prior to ALA administration (Bkgrd). Exogenous PpIX production was examined following administration of 1 mM ALA to the cells at 1, 2 and 4 hours after administration. Each bar represents the average of three samples. The error bars represent the standard deviation between the averages of the three samples.

2.4. Green Fluorescent Protein Transfection of U251 Human Glioma Line

The U251 cell line was transfected with green fluorescent protein (GFP) for *ex vivo* tumor visualization. The transfection was completed using the pAcGFP1-N1 vector (Clontech), Lipofectin Reagent (Invitrogen, Carlsbad, CA) and Geneticin selective antibiotic (Invitrogen, Carlsbad, CA) at a concentration of 700 $\mu\text{g/ml}$. U251 cell were grown without antibiotics in appropriate growth media (DMEM supplemented with 10% FBS) prior to transfection. For the transfection procedure, the cells were plated in 60 mm dishes at a concentration of 1×10^5 to ensure 30 – 50% confluence at the time of transfection, 24 hours later. Ten μl of Lipofectin solution was mixed with 100 μl of

serum free DMEM media without antibiotics. This mixture was incubated at room temperature for 40 minutes. Two μg of the pAcGFP1-N1 vector was diluted into 100 μl of serum free DMEM. The DNA containing solution was mixed with the Lipofectin solution and incubated at room temperature for 15 minutes, after which 1.8 ml serum free DMEM was added to the DNA-Lipofectin mixture. The media from the U251 cells plated 24 hours prior to the transfection was removed, and the cells were washed twice with PBS. The serum-free DMEM, Lipofectin, DNA mixture was overlaid on the cells. The cells were incubated at 37° C for 18 hours, after which the DMEM, Lipofectin, DNA mixture was removed. DMEM with FBS, but without antibiotics was added to the cells and they were incubated for an additional 24 hours at 37° C. The following day the cells were passed into a T75 flask and Geneticin selection media was added.

Geneticin selection media concentrations were determined via a toxicity study. Three concentrations of cells were plated for each Geneticin concentration tested including 5×10^3 , 1×10^4 and 2×10^4 cells per well. The cells were plated in 6-well plates and allowed to attach for 24 hours prior to the addition of Geneticin containing media. Geneticin media was tested at concentrations of 50, 100 and up to 1000 $\mu\text{g/ml}$ by increments of 100 $\mu\text{g/ml}$ at each cell concentration. The Geneticin media was changed every 48 hours and the cells were monitored for a total of 2 weeks. Following the 2 week Geneticin treatment, the lowest concentration of Geneticin that causes complete toxicity was determined to be between 300 and 400 $\mu\text{g/ml}$. This concentration was doubled resulting in a selection media concentration of 700 $\mu\text{g/ml}$ of Geneticin. The transfected cells were grown in Geneticin selection media during the process of three rounds of selection by flow cytometry via a FACSAria (Becton Dickinson, San Jose, CA).

Following selection, cell cultures were allowed to grow in media without Geneticin and their GFP fluorescence was compared to that of cells grown in selection media to ensure the line was stably transfected. The GFP fluorescence of the U251-GFP cell line was compared to the 9L-GFP cell line, a gift from Alexei Bogdanov [88], and can be seen in Figure 2.7. The U251-GFP cell line had slightly higher fluorescence, than the 9L-GFP cell line. However, the variance in GFP fluorescence was higher in the U251-GFP cell line than the 9L-GFP cell line.

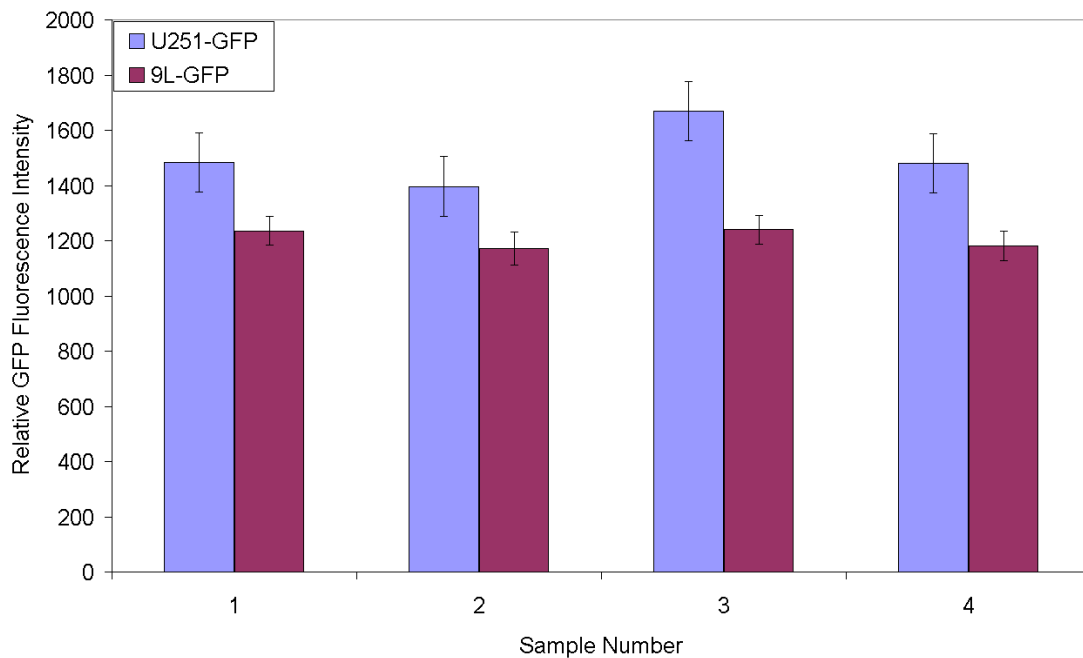


Figure 2.7 – Relative GFP fluorescence intensity of the stably transfected U251-GFP cell line compared to the stably transfected 9L-GFP cell line. Each bar represents the average of three samples. The error bars represent the coefficient of variation (standard deviation/mean expressed as a percentage). Four sets of three samples of each tumor line were measured for mean GFP fluorescence and variation in fluorescence.

2.5. Intracranial Brain Tumor Implantation Procedure

Three cell lines were used for intracranial implantation which included the 9L rat gliosarcoma cell line which had been transfected with green fluorescent protein (9L-GFP), the U251 human glioma cell line and the U251 human glioma cell line GFP transfected variant (U251-GFP). All stable cell lines were cultured in Dulbecco's Modification of Eagle's Medium (DMEM) supplemented with 10% fetal bovine serum and 1% penicillin/streptomycin from a stock solution of 10,000 IU penicillin and 10,000 µg/ml streptomycin. The cells were incubated at 37° Celsius in 95% air and 5% carbon dioxide humidified environment.

The cells were prepared for the implantation procedure as follows. Cells were grown to about 90% confluence in T162 flasks. The growth media was removed and the cells were washed twice with PBS. Five ml trypsin EDTA (0.05%) was added to the flask and allowed to remain on the cells until they detached from the flask. Five ml of DMEM, was added to stop the action of the trypsin. The cell suspension was taken up into a 15 ml tube and vortexed to ensure a homogenous suspension. 100 µl of the cell suspension was placed in a 1.5 ml Eppendorf tube and the remainder was centrifuged at 110 g for 5 minutes. Ten µl of the cell suspension was added to 90 µl of Trypan Blue and live cells were counted via a hemacytometer. Following centrifugation, the supernatant was removed and the cells were resuspended in PBS at 1×10^8 cell/ml.

Male athymic nude mice about 6 weeks of age were used for all intracranial implantations. The mice were anesthetized using ketamine/xylazine in a 90:10 mg/kg ratio. Their body temperature was maintained during anesthesia via use of a heating pad. A small incision was made in the scalp so that the top of the skull was exposed and the

landmarks on the brain were visible (Figure 2.8 (a)). A 1 mm hole was drilled in the mouse skull using a dremel drill 2 mm in front of the bregma and 2 mm to the left of the midline (Figure 2.8 (b) - (d)). A 25 gauge needle was inserted through this hole, 3 mm deep into the brain tissue via guidance from a stereotactic frame (Figure 2.9). Prior to the administration of cells, the needle was retracted 1 mm, so that the cells were implanted at a depth of 2 mm in the brain tissue. The needle was originally inserted deeper into the brain tissue than the implantation depth to make space for the cell suspension to be deposited. 1×10^6 cells in 10 μ l of PBS were injected over 5 minutes using a Hamilton syringe (Figure 2.9). After injection, the needle was slowly removed, the skull was cleaned to ensure cells were not deposited outside the brain and bone wax was used to cover the hole drilled in the skull (Figure 2.10(a)). Finally, the incision in the scalp was closed with a small amount of Vetbond Tissue Adhesive (J.A. Webster, Inc, Sterling, MA) (Figure 2.10(b)). Mice were examined daily following surgery to ensure proper healing of the scalp. Control mice were implanted with 10 μ l PBS without cells to allow similar surgical procedures to be performed on the tumor-bearing and non-tumor-bearing mice.

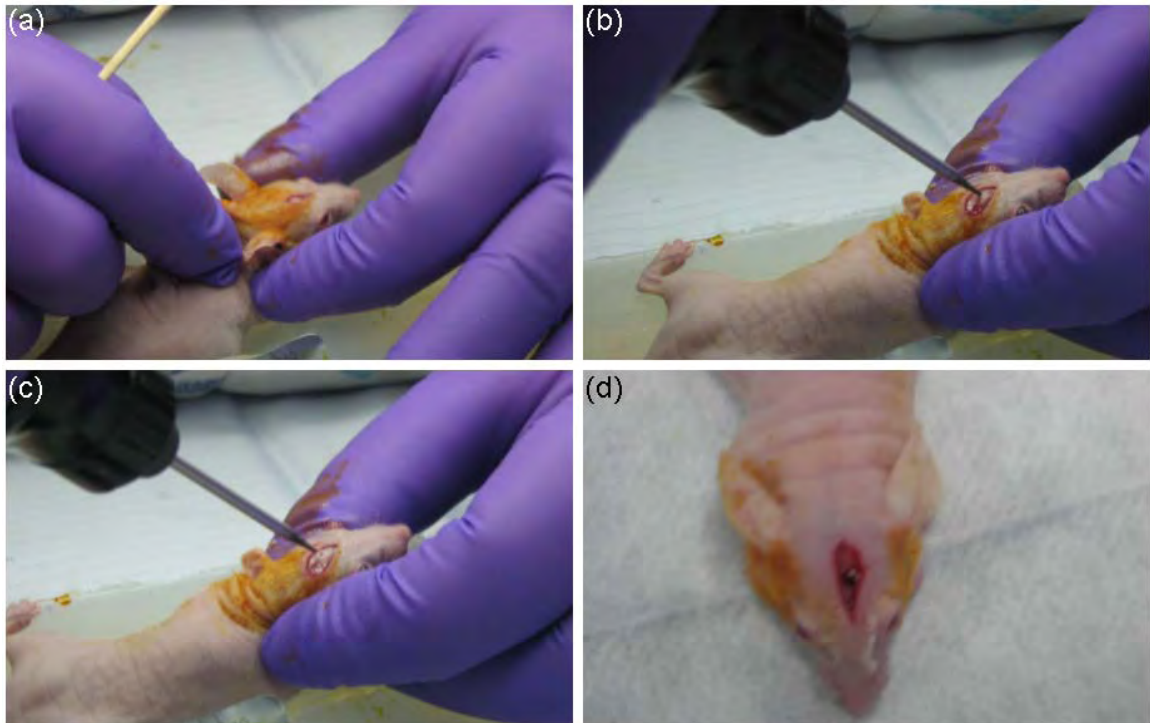


Figure 2.8 – (a) A small incision was made in the scalp using a #10 scalpel, exposing the skull so that landmarks were visible. (b) A dremel drill with a 1 mm drill bit was used to make a hole in the skull. (c) A hole drilled part way through the skull can be seen. (d) A mouse with hole in skull prior to implantation of cells.

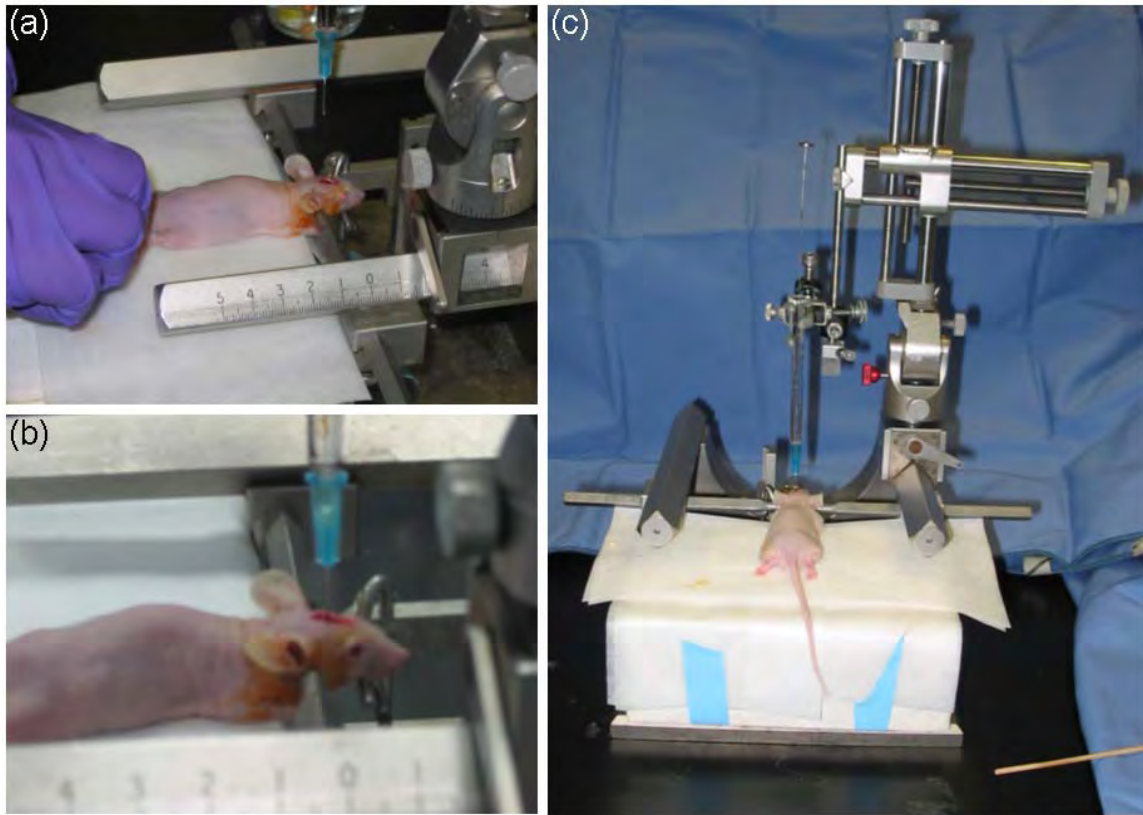


Figure 2.9 – (a) A nude mouse being positioned in the stereotactic frame for tumor implantation. (b) A close-up photograph of the needle being inserted into brain tissue for tumor implantation. (c) The mouse positioned in the stereotactic frame ready for tumor implantation.



Figure 2.10 – (a) Bone wax was used to close the hole drilled in the skull for tumor implantation. (b) The incision in the scalp was closed using VetBond. (c) A top view of the mouse following completion of surgery. (d) A front view of the mouse following completion of surgery.

2.6. Discussion

PpIX production from ALA was highly variable and dependent upon a multitude of factors that have been extensively explored *in vitro*. The studies completed here were focused on correlation of cell line specific morphological factors to PpIX production. Prior to ALA administration, PpIX production was found to be well correlated to mitochondrial content of the cells, however after ALA administration, PpIX production showed no relationship to cellular mitochondrial content (Figure 2.3). Gibson, *et al*

found in their study of four cancer cell lines that the mitochondrial number as measured by Mitotracker did correlate to the PpIX production of the cells following ALA administration [66]. However, in the current study we have demonstrated that upon examination of twice as many cell lines, the relationship of mitochondrial number to PpIX producing capacity is not a general rule for all cancer cell lines. Interpretation of the current data suggests that prior to ALA administration mitochondrial number is a good indicator of PpIX production capacity, but following ALA administration neither the mitochondrial number nor the activity are viable prediction factors for PpIX production capacity of these cells.

Following the administration of ALA, the morphological factor that was found to be most predictive of PpIX production capacity of the cells was cellular size. A positive correlation was found between cell size and PpIX production capacity both between cell lines as well as within a single cell line (Figure 2.4). Consideration of the correlation observed between endogenous PpIX production and mitochondrial number and PpIX production from exogenous ALA and cellular size allowed a possible explanation of the variability seen in PpIX production. Endogenous PpIX production was dependent upon mitochondrial number since it is controlled by feedback inhibition of the enzymes that exist in the mitochondria. Cells that contain more mitochondria have a higher endogenous production of PpIX because more structures that contain a portion of the enzymatic pathway for its production exist in the cell and thus larger amounts of PpIX can be produced in these cells prior to the feedback inhibition of the heme synthesis pathway. When exogenous ALA was administered to the cells however, this situation was drastically changed, as the normal feedback inhibition of the enzymatic pathway was

bypassed, and thus mitochondrial number no longer determined the amount of PpIX the cell would produce. Following exogenous ALA administration cellular size became important where a positive correlation was seen between cell size and PpIX production capacity. Four of the seven enzymes that convert ALA to PpIX exist in the cytoplasm outside of the mitochondria, which include both Porphobilinogen Deaminase (PBGD) and ALA-dehydratase which have been investigated as the rate limiting enzyme in the ALA-PpIX pathway. The morphological correlations found suggest that following ALA administration, the enzymes in the cytoplasm play a more important role in the conversion of ALA to PpIX and PpIX accumulation in the cell than the enzymes in the mitochondria and thus cellular size was positively correlated to PpIX production ability. Additionally, PpIX efflux from the cells into the media was measured in the media that was removed prior to measurement of the PpIX fluorescence of the cells via flow cytometry (data not shown). Minimal PpIX efflux from the cells into the serum-free media was observed which further supports the explanation of the correlation between larger cellular size and higher cytoplasmic enzymatic content in these cells.

PpIX production from exogenously administered ALA was found to be increased by the coadministration of ALA and the iron chelator L1 in all the cell lines studied (Figure 2.5(a)). The cell lines that had the lowest PpIX production from ALA administration alone, showed the largest percentage increase in PpIX production from the coadministration of ALA and L1 (Figure 2.5(b)). This increase in production via the use of iron chelation could prove useful for both increased PDT efficacy and fluorescence imaging purposes.

Four brain tumor cell lines (9L, 9L-GFP, U251 and U251-GFP) were examined for PpIX production capacity over a four hour time course. As can be seen in Figure 2.6 the U251 parent line was largely unaffected by the transfection process as the U251-GFP cell lines showed similar PpIX production following the administration of ALA to the U251 parent line. The U251-GFP and U251 cell line had higher PpIX production ability than the 9L-GFP cell line 2 hours after that administration of ALA, which was the time point examined for *in vivo* studies. The 9L-GFP, U251 and U251-GFP cell lines will be discussed further in chapters 5 – 7 as each line was implanted intracranially for orthotopic brain tumor studies. The intracranial brain tumor implantation procedure was discussed in detail in this chapter (Figure 2.8 - Figure 2.10).

Chapter 3 - Fluorescence Imaging Systems

3.1. Introduction

The ability to accurately quantify the fluorophore concentration in the tissue of interest is of primary importance in studying both murine glioma detection as well as treatment monitoring strategies. Both reflectance geometry and transillumination geometry systems were used in this thesis work, to interrogate *in vivo* fluorophore content. In reflectance geometry based systems the source of excitation and collection of the emitted fluorescence signal occur on the same side of the subject. In contrast, a transillumination/transmission geometry system has the excitation source on the opposite side of the subject from the emission collection instrument. This difference in source-detector geometry affects the ability of both types of imaging system to quantify fluorophore concentration due to the nature of light propagation through tissue. When the excitation light is incident on the tissue, the penetrating photons can interact with the fluorophore of interest or with the tissue itself. Imaging in the NIR range maximizes tissue penetration and minimizes tissue absorption, thus there is a better chance for the photons to penetrate deeper into the tissue, than with light of shorter wavelengths [56]. However, the deeper light penetration creates an environment where photons can be multiply scattered prior to interaction with the fluorophore of interest, before exiting the tissue or both. This causes difficulty for quantification of tissue fluorophore concentration since these multiply scattered photons become convolved with the tissue optical properties [55]. This problem is minimized in the transmission geometry as compared to the reflectance geometry since only photons that travel through the entire

sample are detected, and thus have likely gone through fewer scattering interactions with the tissue.

The reflectance based geometry system can be thought of as a photographic imaging technique where highly sensitive, well-resolved images of the surface fluorescence activity and location can be obtained. Reflectance imaging is highly surface weighted, and thus fluorescence detection sensitivity is rapidly lost as the objects of interest reside beneath the surface or at any depth. This is due to the attenuation of the photons as they propagate to and from the fluorophore within the tissue, while any fluorescent signal detected at the surface is still recorded at full strength [89]. If the object of interest is at depth and any surface background fluorescence or autofluorescence exists, this problem is further magnified as the surface fluorescence can mask the signal from the fluorophore of interest and further reduce sensitivity [55]. The transmission based geometry system is less sensitive to surface fluorescence due to detection of only photons that have penetrated through the entire sample, and thus is better able to quantify fluorophore concentration at depth even when background fluorescence or autofluorescence signals are present. Also, reflectance based imaging is much more sensitive to any bleed-through signal due to imperfect filtering since this would allow for reflected excitation light of maximum intensity to be detected along with the emitted fluorescence. In the transmission based geometry this sensitivity to bleed-through signal due to imperfect filtering causes less detection difficulty since the stray excitation light would be highly attenuated after its propagation through the entire sample [89].

Quantification of fluorophore concentration at depth is also improved by the light penetration through the tissue of interest in the transmission geometry. In the reflectance

geometry it is unclear from sample to sample if the entire volume of interest is investigated for fluorophore concentration, whereas in the transmittance geometry since the light penetrates the sample from one side to the other, the entire volume is interrogated [55].

Both transmission geometry and reflectance geometry fluorescence images can be improved through normalization of the raw fluorescence data to a data set obtained at the excitation wavelength in the same geometry as the raw fluorescence data set.

Normalization of the two data sets to obtain the fluorescence to transmittance ratio decreases the sensitivity to the effects of optical property variation on the signal and can thus improve quantification ability of fluorescence imaging in situations where background optical properties vary such as *in vivo* imaging [89]. Fluorescence normalization to the excitation data also decreases the positional dependence of the fluorescence signal, decreasing signal heterogeneity between measurements of different mice as well as measurements collected at different time points from the same mouse. This strategy was employed in all transmission based imaging systems discussed here.

3.2. Reflectance Fluorescence Imaging

Reflectance fluorescence detection is a common method for sampling the fluorophore content *in vivo* for small animal experiments. In a reflectance geometry fluorescence imaging system, the excitation source and emission detection instrument are on the same side of the subject of interest (Figure 3.1). The most common reflectance fluorescence imaging system is a broad beam geometry system where the excitation source is an expanded light beam that illuminates the entire imaging field during the

emission detection (Figure 3.1(a)). The detection can be optimized by adjusting the camera configurations. However the weakness to this approach for quantitative fluorescence imaging is that the imaged fluorescence signal has traveled through the tissue prior to detection and thus is convolved with the tissue optical properties.

Reflectance imaging systems that sample the subject in a less global manner can limit the convolution of the fluorescence signal with the optical properties of the tissue. One such type of system is a raster scanning system where the light source and the detection system are scanned across the sample, with a small illumination size on the order of 50 – 200 microns (Figure 3.1(b)). By limiting the distance the light travels in the tissue prior to detection, there is less distortion of the fluorescence signal due to interactions with the tissue. A study was completed to compare the ability of a broad beam reflectance imaging system and a raster scanning reflectance imaging system to quantify fluorophore concentration both in tissue phantoms and *in vivo*.

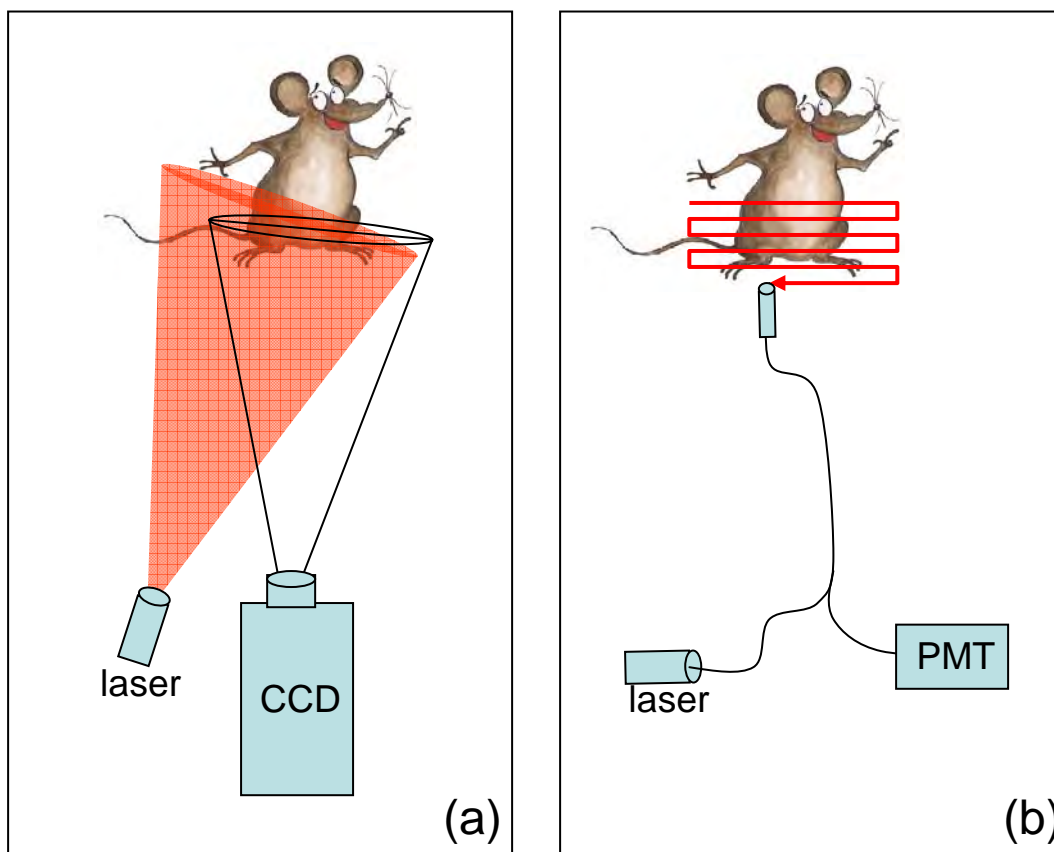


Figure 3.1 – (a) The light path for a broad beam geometry reflectance fluorescence imaging system. The laser source is expanded across the entire imaging field and the whole sample is illuminated simultaneously. (b) The light path for a raster scanning reflectance fluorescence imaging system. The laser source is scanned across the sample so that a small portion of sample is illuminated at a single time point.

3.2.1. *Broad Beam Imaging vs. Raster Scanning*

The photosensitizer aluminum phthalocyanine disulphonate (AlPcS₂) (Frontier Scientific, Logan, UT) was used as the fluorophore of interest in the reflectance imaging comparison study. AlPcS₂ powder was dissolved in 20% dimethyl sulphoxide (DMSO) and 80% sterile saline, at a stock concentration of 10 mg/ml. The stock solution was diluted to concentration of 1 mg/ml for injection into animals and use in tissue phantoms. Between uses the stock solution was kept from light and stored frozen.

The broad beam imaging system used in this study consisted of a 670 nm diode laser excitation source, a SensiCamQE high performance digital CCD camera (The Cook Corp, Auburn Hills, MI), with a 685 nm long pass emission filter over the lens for emission detection. The camera was equipped with a 75 cm focal length lens which had a depth of field measured as 2 cm when the image field was positioned 75 cm above the camera lens. The resolution of the broad beam imaging system in the described configuration was quantified using a USAF test chart [90]. Line pairs no closer than 2.85 per millimeter were able to be resolved and thus the resolution of the broad beam imaging system was found to be 350 microns. The rejection efficiency of the long pass filter was measured at 5 orders of magnitude using a Newport Power meter. The size of the imaging field was fixed at 30 x 30 cm and remained the same throughout the entire imaging system quantification experiment.

The raster scanning system used in this study was a Typhoon 9410 Variable Mode Imager (GE Healthcare Life Sciences). The system was equipped with four lasers for excitation and 8 stock emission filters. Two long pass filters were added to the system including a 685 nm long pass (LP) emission filter to allow imaging of AlPcS₂ and a 650 nm LP emission filter to allow imaging of Protoporphyrin IX. In the current study the 633 nm excitation source and the 685 nm LP filter were used. The collection spot size could be adjusted from 10 – 1000 microns and was set at 200 microns for this study. After collection of the emitted light through the 685 nm LP filter the signal was collected through a photomultiplier tube and the image was built pixel by pixel as the data was acquired. The imaging field was set to just larger than the subject to be imaged, although the maximum size object that could be scanned in the system was 35 x 43 cm.

3.2.2. Reflectance Imaging System Quantification

Tissue simulating phantoms with varied concentrations of AlPcS₂, Intralipid and blood were used to compare the broad beam and raster scanning systems. Two-dimensional (2D) tissue phantoms were prepared containing AlPcS₂, Intralipid to simulate the reduced scattering coefficient of soft tissue, and blood to simulate the absorption coefficient of soft tissue and water. The concentration of AlPcS₂ was serially diluted from 1.95 – 0.0038 µg/ml in a 96-well plate. The Intralipid and blood concentrations were held constant at 1% and 3%, respectively. Phantoms with the concentrations of Intralipid and blood were varied to examine how the background tissue optical properties affected fluorophore quantification. In both sets of phantoms, the AlPcS₂ concentration was held constant at 1 µg/ml. In one set of phantoms, the Intralipid concentration was held constant at 1%, while the blood concentration was varied from 0 – 10% in 1% increments. In a second set of phantoms, the blood concentration was held constant at 3% while the Intralipid concentration was varied from 0.5 – 5% in 0.5% increments.

Both the broad beam and raster scanning imaging systems showed a near linear relationship with increased quantity of fluorophore in the 2D tissue phantom as the images illustrated increased fluorescence intensity (Figure 3.2). There were some differences between the two systems when the Intralipid concentration was varied. In the raster scanning system the AlPcS₂ fluorescence intensity increased in a linear fashion with the concentration of Intralipid. The broad beam system also showed increased fluorescence intensity with increasing concentrations of Intralipid, but not in the same linear fashion as the raster scanning system (Figure 3.3(a)). In the raster scanning system

the AlPcS₂ fluorescence intensity was largely unaffected by the blood plasma concentration, except for a high point at 0% blood plasma. The ability to quantify AlPcS₂ fluorescence intensity in the broad beam system did appear to be correlated to the percentage of blood present in the 2D tissue phantom (Figure 3.3(b)).

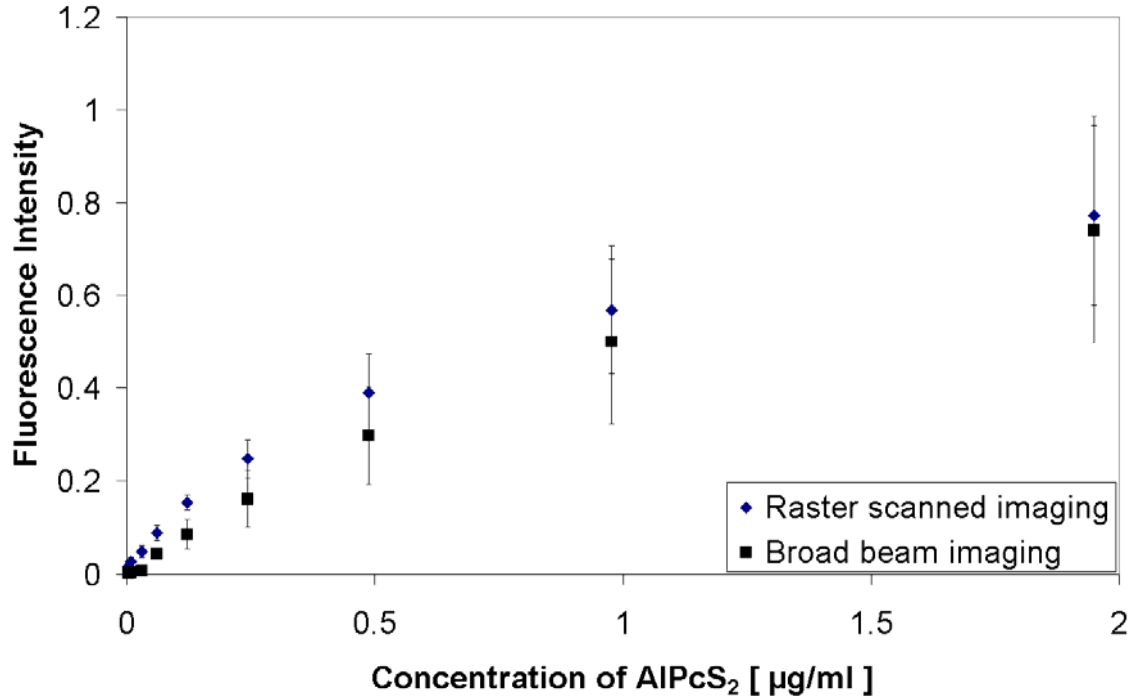


Figure 3.2 – Two-dimensional tissue simulating phantom with 1% Intralipid, 3% blood and varied concentration of AlPcS₂ (1.95 – 0.0038 µg/ml by serial dilution) were constructed. The data represents the mean intensity in appropriate wells of 96-well plate.

Three-dimensional (3D) tissue phantoms of varied sizes were constructed from opaque balloons containing 1% Intralipid, 3% blood and 1 µg/ml AlPcS₂. The phantoms were imaged on both imaging systems, the results of which can be seen in Figure 3.4. The raster scanning system showed that as the size of the phantom increased the fluorescence intensity slightly decreased. In contrast, when the 3D phantoms were

imaged in the broad beam system, the size of the phantom was proportional to the increased fluorescence intensity.

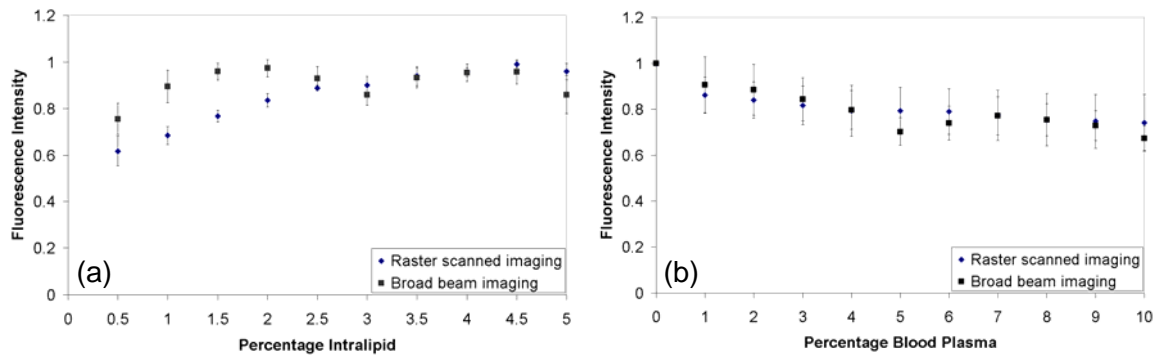


Figure 3.3 – (a) Two-dimensional tissue phantom with 3% blood, 1 $\mu\text{g/ml}$ ALPcS₂ and varied concentrations of Intralipid imaged in both systems and quantified for fluorescence intensity. (b) Two-dimensional tissue phantom with 1% Intralipid, 1 $\mu\text{g/ml}$ ALPcS₂ and varied concentrations of blood imaged in both systems and quantified for fluorescence intensity.

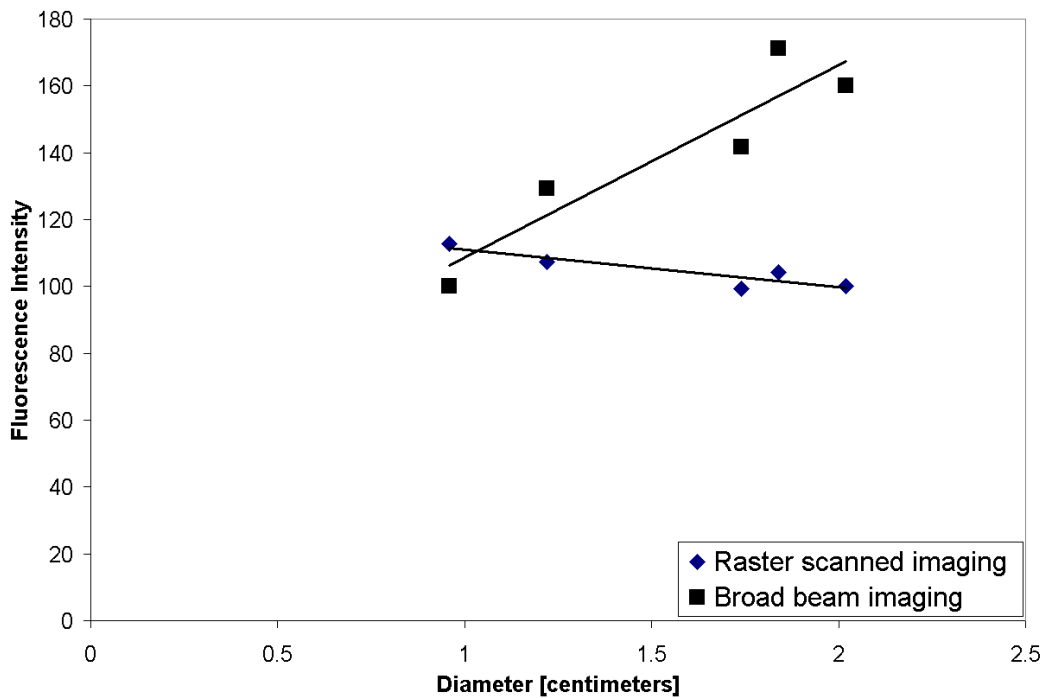


Figure 3.4 – Fluorescence intensity quantification of 3D tissue phantoms constructed from opaque balloons filled with 1% Intralipid, 3% blood and 1 $\mu\text{g/ml}$ ALPcS₂ imaged on both the raster scanning and broad beam imaging system.

C3H/HeJ mice were used for subcutaneous tumor implantation on the mammary fat pad. Mice were shaved on their upper chest area prior to tumor implantation of radiation-induced fibrosarcoma (RIF-1) cells, which were cultured in RPMI 1640 medium supplemented with 10% fetal bovine serum and antibiotics. A subcutaneous injection of 2×10^5 cells in 0.05 ml of PBS produced visible tumors with a surface diameter of 6 – 8 mm about 10 – 14 days after implantation. The animals were anesthetized using ketamine/xylazine in a 90:10 mg/kg ratio injected intraperitoneally. Mice were imaged in both the raster scanning system and the broad beam system to obtain baseline values prior to the administration of AlPcS₂. Following intravenous injection of AlPcS₂ at a concentration of 1 mg/kg the mice were imaged on both systems at 0.5, 1, 2, 4, 6, 24, 48, 72 and 96 hours after injection.

Representative images of the mice can be seen in Figure 3.5(a) for the broad beam imaging system and Figure 3.5(b) for the raster scanning system, where the differences between the two imaging systems were apparent. There was a loss of spatial resolution and inaccuracy in contrast in the broad beam system relative to the raster scanning system. Comparison of Figure 3.5(a) and (b) also illustrates that the intensity of the tumor relative to the normal tissue was significantly higher in the broad beam image as compared to the raster scanned image. Both the tumor tissue and the shaved normal skin were analyzed for fluorescence intensity at the different time points. The ratio of tumor to normal tissue fluorescence was then calculated. Figure 3.5(c) illustrates that the broad beam system showed that the tumor to normal tissue ratio was much higher than shown by the raster scanning system and thus estimated a much higher concentration of AlPcS₂ within the animal than the raster scanning system. This was similar to the relationship

seen when the 3D phantoms were imaged in both the broad beam system and the raster scanning system (Figure 3.4).

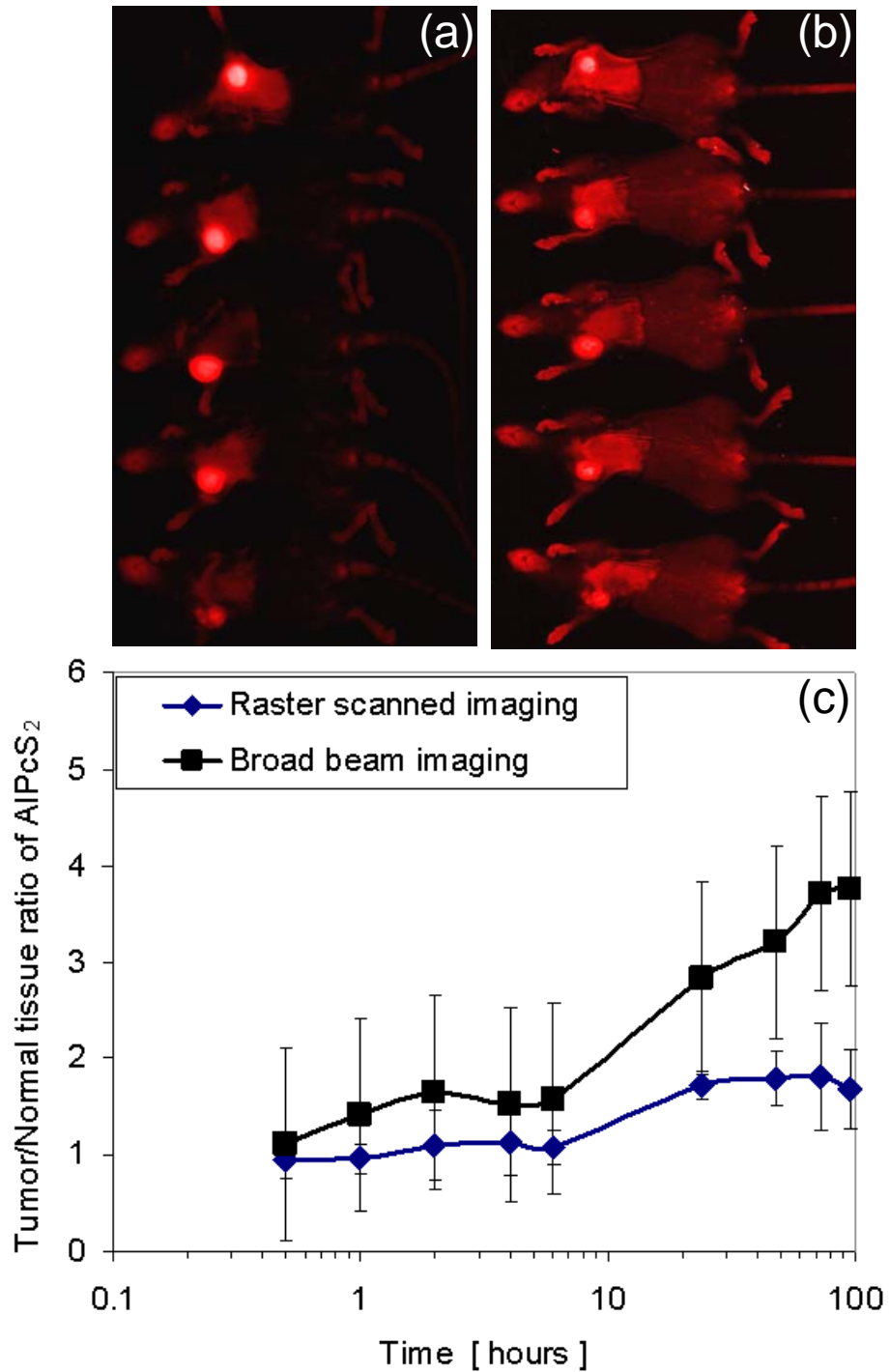


Figure 3.5 – Representative images of five mice 72 hours after intravenous (IV) administration of AlPcS₂ (a) in the broad beam imaging system and (b) the raster scanning system. The approximate field of view was 20 cm x 11 cm. (c) The

fluorescence images generated at each time point in the two imaging systems were used for quantitative estimation of fluorescence in the tumor versus normal tissue. The mean and standard deviation of the tumor to normal tissue ratio is shown for five tumor-bearing mice.

3.3. ALA-Induced PpIX Mouse Skin Fluorescence

Both planar reflectance imaging systems discussed previously were used to image Protoporphyrin IX fluorescence in subcutaneously implanted tumors. Planar imaging studies using PpIX as the fluorophore of interest presented tumor detection problems due to high skin PpIX autofluorescence as well as high PpIX production of the skin following ALA administration. Both the endogenous and exogenous production of PpIX in the skin made it more difficult to use as an imaging contrast agent than other fluorophores that are not naturally occurring and thus have inherently lower systemic or background fluorescence. An example of this difference can be seen in Figure 3.6 where brain tumor cells transfected with GFP (9L-GFP) were implanted subcutaneously on the flank of nude mice. GFP is a perfect fluorophore for tumor detection since it is only present in the tumor tissue and thus has zero background fluorescence. As can be seen in Figure 3.6(a), the mice with the transfected cell line had readily visible tumors by reflectance, raster scanned imaging, while the mice which were injected with the parent line (9L) did not show any fluorescence in the area of the tumor tissue. Figure 3.6(b) illustrates a more clinically relevant case where the fluorophore of interest was AlPcS₂ as discussed above. This fluorophore was injected into the mouse instead of transfected into the cells and thus, background fluorescence does exist, but since this image was collected 72 hours after AlPcS₂ administration, the fluorescence was largely contained within the tumor tissue making the tumors visible by reflectance fluorescence imaging. In contrast, Figure

3.6(c) illustrates the same mice as Figure 3.6(a), however the high skin PpIX fluorescence 6 hours after the administration of ALA masked the tumor PpIX fluorescence making the tumors invisible by reflectance, fluorescence imaging.

The Aminolevulinic Acid-Protoporphyrin IX (ALA-PpIX) system is unique in the imaging world because following administration of the prodrug ALA, which is not fluorescent, the metabolism of the tissues produce PpIX which is fluorescently detectable. Variable levels of PpIX are produced by different cells and tissues when the same amount of ALA is administered, but it is generally the case that the tumor PpIX production is higher than the surrounding normal tissue [24, 25, 58, 59, 91]. The ALA-PpIX system has found extensive use in dermatology as skin cells have very high production of PpIX following the administration of ALA and preferential accumulation in tumor tissues as compared to normal tissues. ALA PDT has been shown to be an effective treatment for actinic keratosis, Bowen's disease, *in situ* squamous cell carcinoma and superficial basal cell carcinomas [92-94]. Although ALA has shown great promise as a photosensitizer, especially for dermatology applications, it has been met with some difficulties in noninvasive imaging applications. More specifically, reflectance based imaging of solid tumors that lie beneath the skin have been largely unsuccessful. This is due to the high background PpIX fluorescence that easily masks the PpIX signal from the tumor tissue in surfaced weighted reflectance imaging geometry. The reflectance geometry raster scanning system discussed previously was used to study the PpIX background fluorescence of the skin and the potential to decrease this fluorescence through modified diet and antibiotics. Broad spectrum antibiotics were

tested to determine if bacteria on the skin was causing the increased PpIX fluorescence, as suggested by Lothar Lilge (Personal communication).

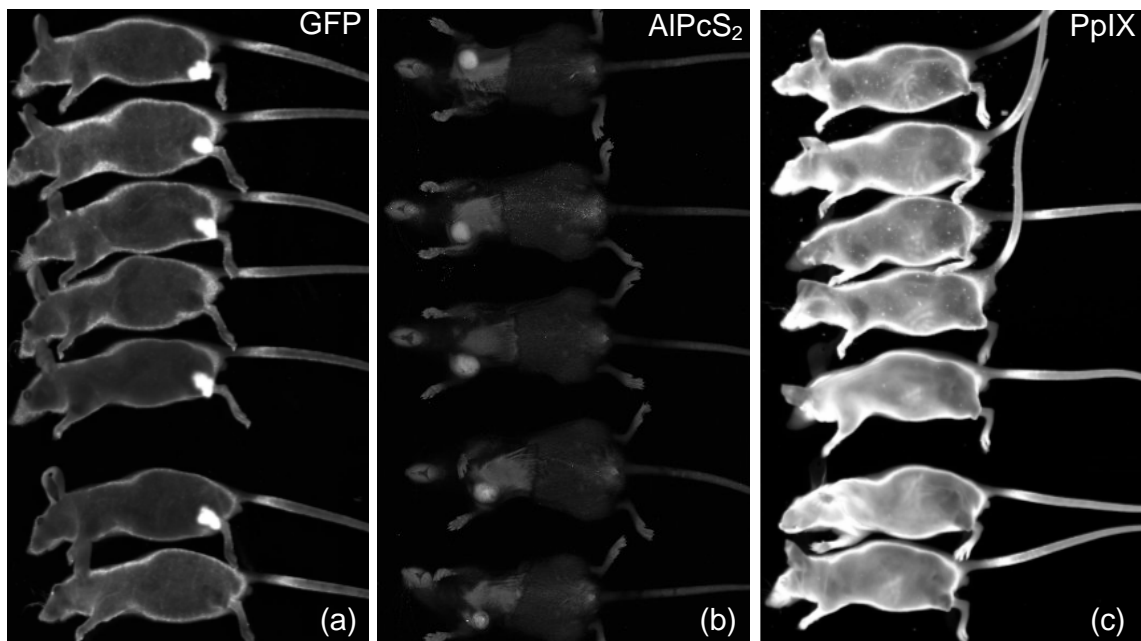


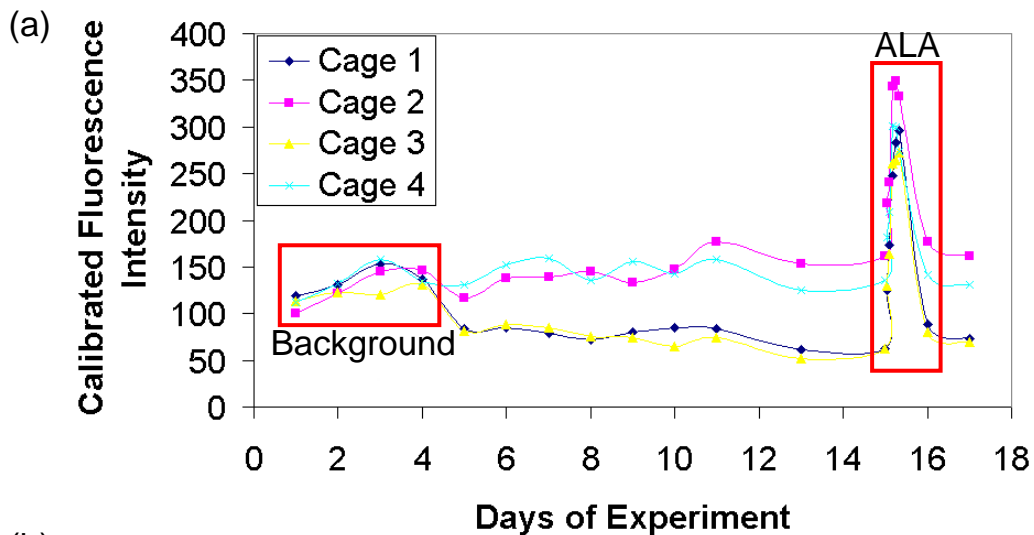
Figure 3.6 – Reflectance, raster scanned images of subcutaneous tumors (a) transfected with green fluorescent protein, (b) with AlPcS₂ as the fluorophore of interest and (c) with PpIX as the fluorophore of interest. The same mice are shown in (a) and (c), with the tumors easily visible by GFP fluorescence in (a), but masked by the PpIX skin fluorescence in (c).

Both a chlorophyll-free purified diet (MP Biomedicals, Solon, OH) and antibiotic (Septra antibiotics) water were tested to determine if their use prior to imaging studies could decrease skin PpIX autofluorescence and PpIX skin fluorescence as induced by ALA administration. The study consisted of eight male nude mice, housed two per cage to allow for administration of varied diet and water regimens. All eight mice were fed standard diet and water during the first four days of the experiment (days 1 – 4). Images of the eight mice (anesthetized with ketamine/xylazine) were obtained on the raster scanning system daily with mice lying on their front, back and side to track PpIX skin

autofluorescence. Following imaging on the 4th day of the study, the food and water combination in cages 1 – 3 were changed, while the mice in cage 4 continued to receive standard food and water. The mice in cage 1 were fed purified diet and standard water, the mice in cage 2 were fed standard diet and antibiotic water, and the mice in cage three were fed both purified diet and antibiotic water. The PpIX skin autofluorescence of the mice was tracked for 10 days following the diet and water change via imaging with the raster scanning system. On the 15th day of the experiment, all the mice were administered 100 mg/kg ALA intraperitoneally (IP) and images of their skin PpIX fluorescence were obtained 1, 2, 4, 6, 8 and 24 hours after administration. An additional imaging session was completed 48 hours after ALA administration to ensure the ALA induced PpIX fluorescence had cleared from the skin. Following clearance of the ALA induced PpIX, on day 17 the mice were sacrificed and the skin, muscle, brain, liver, stomach, kidney and intestine from each mouse were removed and imaged on the raster scanning system to determine the fluorescence of various mouse tissues and organs.

The purified diet was found to significantly decrease PpIX skin autofluorescence and ALA-induced PpIX skin fluorescence. A considerable decrease in mouse skin PpIX fluorescence following change to purified diet from standard diet could be seen after only a single day. The skin PpIX fluorescence continued to decrease for 3 – 4 days after diet change before it plateaued at a much lower level than mice fed the standard diet Figure 3.7(a). The antibiotic water did not show any effect on the level of PpIX skin autofluorescence. Raster scanned images of the mice in the background period of the study when all mice were fed standard diet and water can be seen in Figure 3.8(a). The difference in skin fluorescence could be visualized when the mice fed purified diet (cages

1 & 3) were compared with the mice fed standard diet (cages 2 & 4) 7 days after diet change (Figure 3.8(b)). The mice fed purified diet for 7 days had a 56% lower PpIX skin autofluorescence compared to the mice fed standard diet. The mice fed the purified diet also showed lower PpIX skin fluorescence following the administration of ALA than mice fed standard diet with the largest percentage difference seen 1 hour after ALA administration (Figure 3.7(b)). The smallest percentage difference in mouse skin fluorescence after the administration of ALA between the purified diet group and the standard diet group was seen at the 8 hour time point with only about a 6% difference between the two groups.



(b)

Average	Bkgrd	1 hr	2 hrs	4 hrs	6 hrs	8 hrs	24 hrs	48 hrs
% Difference	55.82	36.19	24.58	20.98	15.58	6.27	41.60	50.59

Figure 3.7 – (a) Skin PpIX autofluorescence prior to diet change (Days 1 - 4), following diet change (Days 5 - 14), after ALA administration (Day 15), and during ALA induced PpIX production and clearance (Day 16 - 17). Mice in Cage 1 were fed purified diet and standard water, mice in cage 2 were fed standard diet and antibiotic water, mice in cage 3 were fed both purified diet and antibiotic water, and mice in cage four were fed standard diet and water. Following ALA administration images were obtained 1, 2, 4, 6, 8 and 24 hours after administration to determine PpIX skin fluorescence. (b) Since little to no effect was seen from the antibiotic water, the data from the mice fed standard diet (Cage

2 & 4) and the mice fed purified diet (Cage 1 & 3) were averaged so that each group contained four mice. The percentage difference in PpIX skin fluorescence was calculated between these two groups.

All mice in the study were sacrificed following clearance of the ALA-induced PpIX skin fluorescence on the 17th day of the study. The skin, muscle, brain, stomach, intestine, liver and kidney were extracted and imaged via the raster scanner for PpIX autofluorescence analysis. The PpIX autofluorescence was highest in the stomach, intestine and skin of the mice, and lowest in the muscle and brain tissue (Figure 3.9(b) & (c)). The PpIX autofluorescence was significantly higher in the stomach and intestine of the mouse fed the standard diet than the mouse fed the purified diet, likely due to contact with the standard diet. All other tissues removed from the mice fed the standard diet appeared to have higher PpIX autofluorescence than the tissues removed from the mice fed the purified diet, although the difference was not as striking as that seen in the organs in contact with the standard diet (Figure 3.9(b) & (c)). Due to the significant decrease in mouse skin PpIX autofluorescence the purified diet was used in all subsequent studies following tumor implantation in the mice.

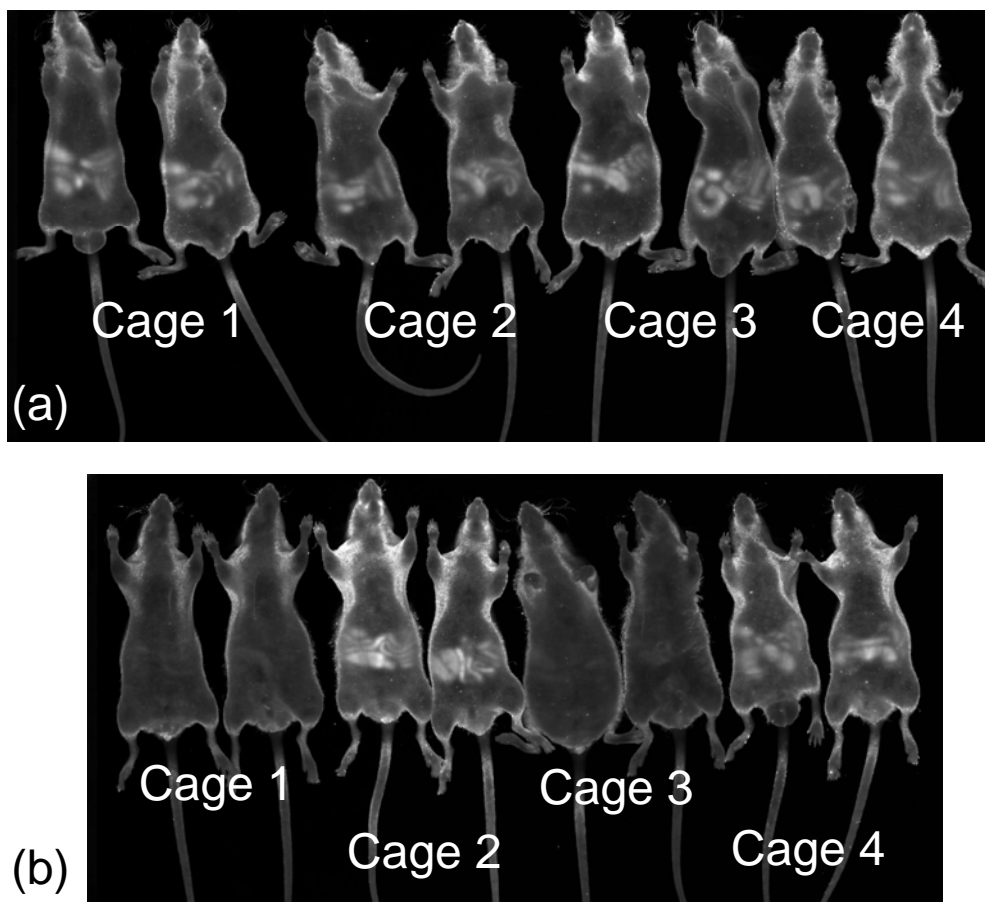


Figure 3.8 – Raster scanned image of eight mice in the skin PpIX fluorescence study (a) during days 1 - 4 when all mice were fed standard diet and water and (b) 7 days after diet change. The mice in cages 1 and 3 received the purified diet, while the mice in cages 2 and 4 received the standard diet.

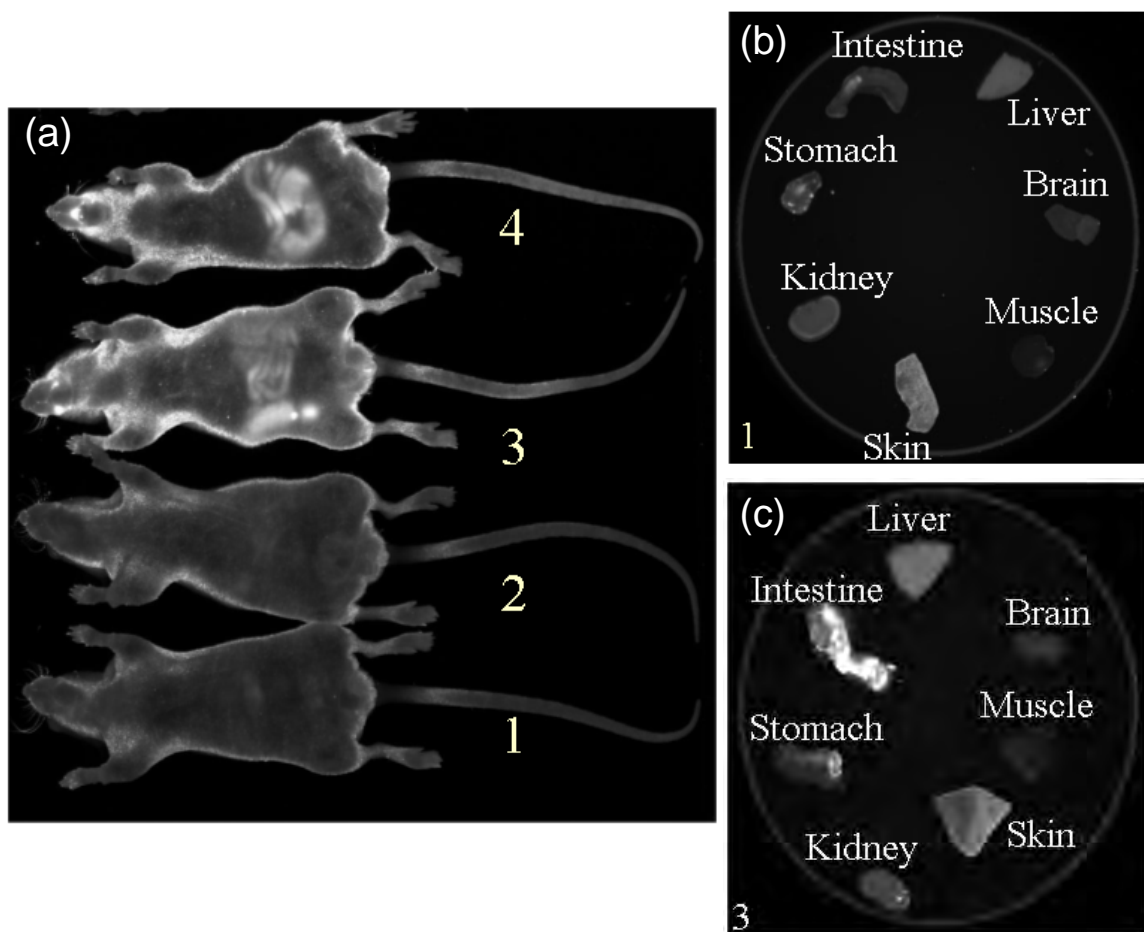


Figure 3.9 – (a) Mouse 1 and 2 were fed purified diet, mouse 3 and 4 were fed standard diet. Following sacrifice the autofluorescence of the skin, muscle, brain, liver, intestine, stomach and kidney were imaged with the raster scanning system. (b) The organs from mouse 1, which was fed purified diet, had lower PpIX autofluorescence than (c) the organs from mouse 3, which was fed standard diet.

3.4. Transmission Fluorescence Imaging

Due to the sensitivity of reflectance imaging techniques to PpIX skin fluorescence, transmission geometry imaging systems were used to image orthotopic tumors, specifically brain tumors which will be further discussed in chapters 6 and 7. Two spectroscopy based transmission imaging systems were used to noninvasively detect murine gliomas *in vivo*. In all transmission imaging studies the fluorescence emission

data was collected using the appropriate laser and filter, then prior to any movement of the mouse or phantom the transmitted excitation data was also collected using the appropriate laser and filter. In all studies the fluorescence to transmittance ratio was calculated and reported. The PpIX detection studies, which will be further discussed in chapter 6, were completed using a single channel transmission spectroscopy system which enabled light transmission measurements directly across the head. The treatment monitoring studies, which will be further discussed in chapter 7, were completed using a multichannel transmission spectroscopy system which enabled light detection at eight positions surrounding the head. Both transmission spectroscopy systems will be described in detail as follows.

3.4.1. Single Channel Transmission Spectroscopy System

A schematic of the single channel spectroscopy transmission system can be seen in Figure 3.10(a) and is explained as follows. A 635 nm helium-neon laser coupled into a collimator was used for excitation by collimating the laser light onto the chin of the mouse. The light transmitted through the mouse head was then collected through a second collimator on top of the mouse head, and passed through a 650 nm LP filter prior to spectrally resolved detection through an Acton Research Spectrometer (1200 l/mm grating, SpectraPro 300, Acton Research, Acton MA) and onto a CCD camera cooled to -90° Celsius (Spec-10:400BR/XTE, Princeton Instruments, Acton MA). Data from the camera was captured and transferred using the commercially supplied software (Winspec, Acton Research). The spectrometer was centered at 705 nm to collect the PpIX fluorescence emission peak and at 615 nm to collect the transmitted intensity from the

635 nm laser. A mouse holder consisted of a bed in a light tight box with holes 180° apart from one another to hold the collimators in contact with the mouse head, which were used in the collection of spectroscopy data (Figure 3.10(b) – (d)).

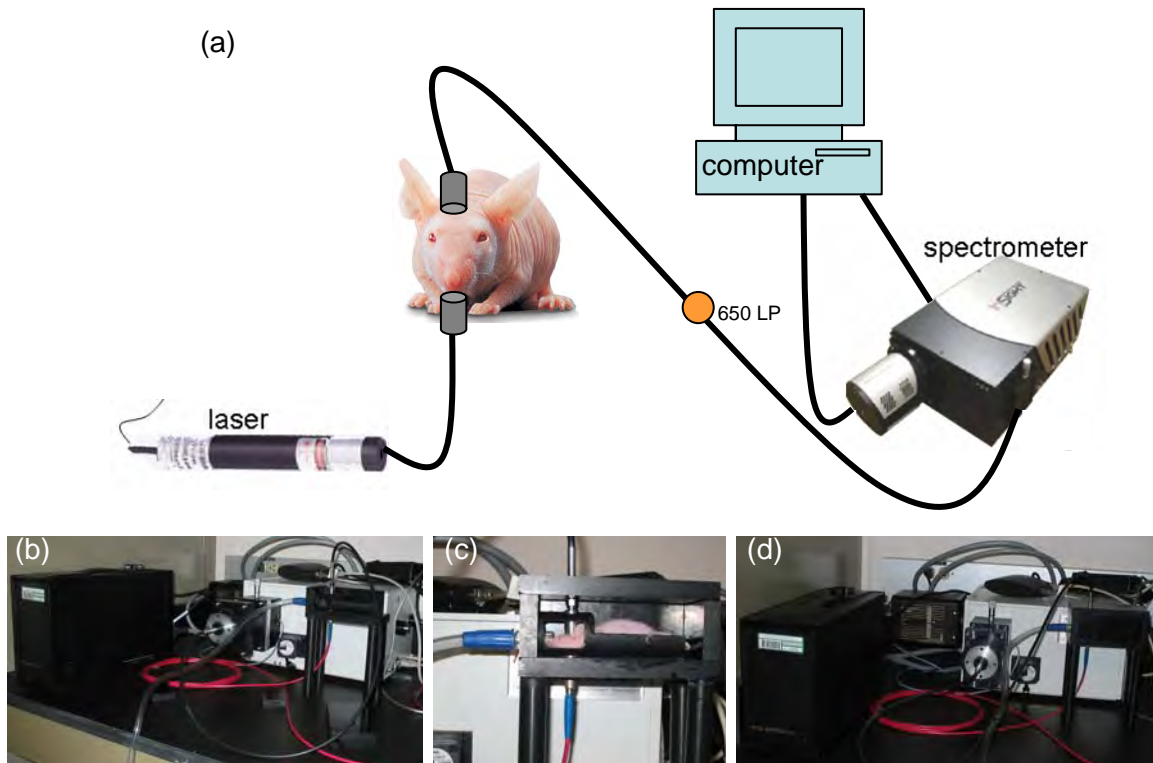


Figure 3.10 – (a) A schematic of the single channel transmission spectroscopy system containing 635 nm laser source, Acton research spectrometer, 650 nm LP filter and computer for detection. (b) A photograph of spectroscopy system containing spectrometer and mouse holder. (c) A photograph of a mouse in the holder, with the collimator on the mouse chin, attached to the laser, and the collimator on top of the mouse head attached to the spectrometer for detection. (d) A photograph of the light-tight box closed-up and ready to obtain measurements.

3.4.2. Multichannel Transmission Spectroscopy System

The multichannel transmission spectroscopy system consisted of two carts, each holding 8 Acton Research Spectrometers and two available laser sources including a

continuous wavelength 635 nm laser and a continuous wavelength 690 nm laser, each of which could be coupled into a rotary stage to obtain measurements (Figure 3.11(a)). Each source fiber was a 400 μm fiber that ran from the rotary stage and was bifurcated into the detector bundle. The detector bundle consisted of 7 additional 400 μm fibers which ran from each of the 16 spectrometers. The appropriate laser source could be coupled sequentially into one of the sixteen source fibers by the precision rotary stage. Each spectrometer had a filter wheel containing a 650 nm LP filter, a 720 nm LP filter, a 1 OD filter and a 2 OD filter. The system was controlled through LabView based software, which allowed control of the number of spectrometers used in the experiment as well as the filter and grating selection. The spectrometers were centered at 705 nm to collect PpIX fluorescence emission data and 620 nm to collect the transmitted intensity for the 635 nm laser. The 650 nm LP filter was used in the collection of both the emission and excitation data sets. The 1200 1/mm grating was used in the collection of the excitation and emission data sets for PpIX. The spectrometers were centered at 820 nm to collect indocyanine green (ICG) and epidermal growth factor (EGF) conjugated IRDye 800CW (EGF-IRDye) emission data and at 690 nm to collect the transmission data for both of these fluorophores. The 720 nm LP filter was used to collect the emission data sets, while the 2 OD filter was used in the collection of the transmission data sets. The 300 1/mm grating was used in the collection of the emission data set for ICG and EGF-IRDye, while the 1200 1/mm grating was used in the collection of the excitation data set for these fluorophores. The LabView control software optimized the exposure time at each fiber optic so that optimal signal from each portion of the head

could be obtained. The optimization program ensured that signals between 20,000 – 60,000 photon counts were collected at each fiber optic around the mouse head.

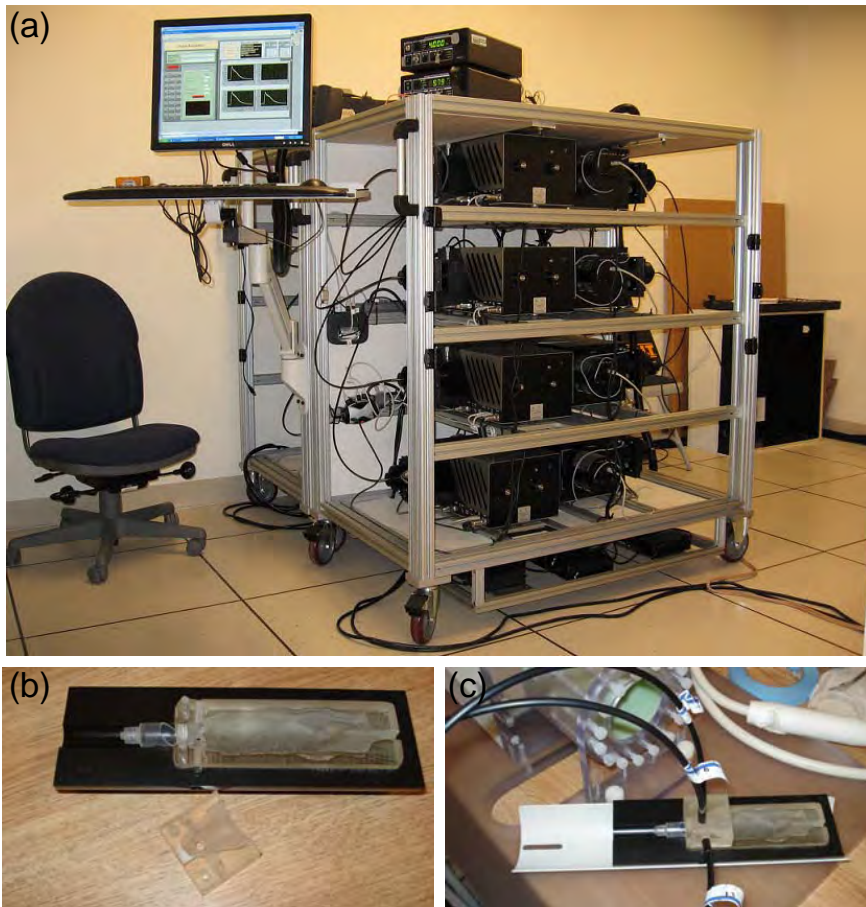


Figure 3.11 – (a) Photograph of multichannel transmission spectroscopy system showing the 2 carts, each containing 8 spectrometers. (b) A photograph of the epoxy/resin mouse holder, with holes drilled for repeatable fiber optics placement. (c) A photograph of the mouse holder with 3 of the possible 8 fiber optics inserted for measurements.

A mouse holder was constructed from liquid epoxy/resin [95] using a silicon mouse prototype to obtain a ‘mouse-shaped’ mold allowing for repeatable fiber placement (Figure 3.11(b)). Two sets of 4 holes 3.5 mm in diameter were drilled in 2 planes 2 mm apart from one another. The 4 holes in each individual plane were 90° apart, which allowed for measurements using 8 of the 16 available spectrometers in the

multichannel transmission spectroscopy system. The fibers were placed through the holes in the mouse holder so that they were in contact with the mouse head (Figure 3.11(c)).

3.4.3. Spectral Data Post-Processing Procedure

The raw spectral excitation and emission data collected using either the single channel or multichannel transmission spectroscopy system (Figure 3.12(a) & (d)) were post-processed by a two step process involving spectral fitting and then normalization. The fluorescence data was spectrally fitted using a MatLab program to perform a linear least squares fit to phantom data from the appropriate fluorophore (Figure 3.12(b) & (e)), so that any bleed through signal could be deconvolved from the fluorescence signal of the fluorophore (Figure 3.12(c) & (f)). The area under the deconvolved fluorescence curve was then calculated and reported as a single number. Both the fluorescence emission data and the transmittance data were normalized to counts/second, to account for differences in exposure time. Then the fluorescence integrated intensity was normalized to the sum of the transmitted laser peak, to help account for positional differences between measurements of a single mouse and for optical property variations.

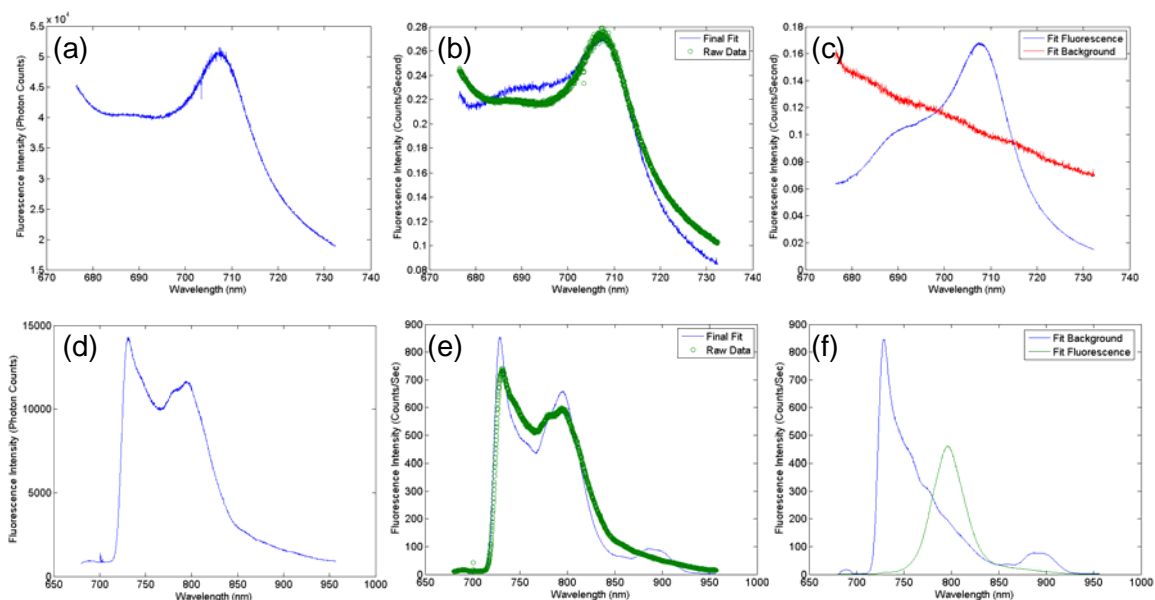


Figure 3.12 – Spectra are shown from (a) *in vivo*, endogenous PpIX fluorescence prior to the administration of ALA; (b) spectrally fitted PpIX phantom data to *in vivo*, endogenous PpIX fluorescence; (c) deconvolved PpIX fluorescence and background bleed-through signal; (d) *in vivo*, EGF-IRDye fluorescence 72 hours after IV administration; (e) spectrally fitted EGF-IRDye phantom data to *in vivo*, EGF-IRDye fluorescence; and (f) deconvolved EGF-IRDye fluorescence and background bleed-through signal.

For the multichannel system, the slight differences in the light path due to multiple fiber optics, spectrometers and filters used to collect measurements should be accounted for and thus additional post-processing steps were completed. Each CCD camera had a baseline offset from zero when a zero second exposure was used. The baseline offset was measured multiple times for each spectrometer and averaged to obtain the baseline offset which would be subtracted from each data set. Similarly, each CCD camera had a dark current which was measured at varied exposure times in a dark room. The average of the dark current spectra was calculated for each CCD camera and subtracted from the measurements obtained using that spectrometer. The slight

difference in filter optical density was accounted for by multiplying the transmitted excitation spectrum by 10, raised to the power of the filter OD. Calibration spectra to account for any inhomogeneities in the CCD array and throughput variability between detector channels were calculated using a cylindrical Teflon phantom. An SMA connector was attached to the top of a Teflon phantom, with the 16 detector bundles circumscribing the phantom. A high powered Tungsten white light source was focused into a fiber connected to the centrally located SMA connector. Multiple spectra were collected with all spectrometers with the same center wavelength and grating using in the imaging study. The spectra were averaged to obtain calibration factors which were used to scale all data from each spectrometer [96].

3.5. Discussion

Reflectance geometry and transmission geometry based systems were both used in the collection of fluorescence data for this thesis. Early studies indicated that the reflectance based geometry systems were not as reliable for fluorophore quantification as the transmission based systems. Phantom and model based comparisons will be discussed in chapter 4 as a more direct comparison of the imaging systems. A study was completed comparing the reflectance raster scanning system with the reflectance broad beam system to quantify fluorophore concentration in two and three dimensional phantoms. This phantom study was compared to *in vivo* imaging with tumors of varied size.

Two dimensional phantoms on both reflectance geometry imaging systems showed relatively small differences between the broad beam imaging system and the

raster scanning system in comparison to imaging three dimensional phantoms or sizeable tumors *in vivo*. When the three dimensional phantoms were imaged on the broad beam system, as the size of the phantom increased the imaged fluorescence intensity also increased, even though the ALPcS₂ concentration remained the same. This increase in detected fluorescence intensity in larger three dimensional objects can be attributed to the geometry of the broad beam system enhancing the multiple scatterings of the light in the three dimensional volume prior to detection. The same relationship between increased size of a three dimensional object and detected increased fluorescence intensity was seen in the mouse imaging experiment. As the tumors became larger during the 96 hour imaging period, the tumor to normal tissue ratio increased significantly with the broad beam system, while the increase was considerably less with the raster scanning system (Figure 3.5(c)).

Thus, reflectance based imaging systems are inherently limited for fluorophore quantification based on the light path which is employed for imaging. The reflectance raster scanning system was better able to quantify fluorophore concentration than the broad beam system and was used in a study of mouse skin PpIX autofluorescence and skin fluorescence following the administration of ALA. Mouse skin PpIX autofluorescence and ALA induced PpIX fluorescence decreased the ability to use PpIX as a contrast agent for imaging and thus diet changes and antibiotics were studied to decrease skin PpIX fluorescence. It was determined that the purified mouse diet significantly decreased mouse skin autofluorescence as well as ALA induced fluorescence (Figure 3.7) and all subsequent experiments were completed using the purified diet following tumor implantation. The antibiotic water did not show any

significant effect on mouse skin PpIX fluorescence and was not used in any further experiments.

Due to the PpIX skin autofluorescence and ALA induced fluorescence in the skin, reflectance geometry imaging system were not useful for solid tumor fluorescence imaging with PpIX as the fluorophore of interest for tumors beneath the skin. The skin fluorescence always masked the fluorescence from the tumor tissue in this surface weighted imaging geometry. In all *in vivo* experiments after this, transmission spectroscopy based systems were used for fluorophore detection. Two systems, including a single channel transmission spectroscopy system and a multichannel transmission spectroscopy system, were used in all further *in vivo* studies. A detailed description of hardware, data acquisition and post-processing for both systems was provided here.

Chapter 4 - Phantom & Model Based Studies

4.1. Introduction

Optical imaging has always had a place in medicine for examining tissue both macroscopically and microscopically. Prior to the development of the wide variety of imaging systems currently available, physicians were dependent upon macroscopic observation and palpation for diagnosis. Since its invention, the microscope has been invaluable for medical diagnosis and microscopy of tissue samples is currently the gold standard for diagnosis [55]. Macroscopic imaging using light to detect abnormalities that lie within the body has been a major area of research for the past two decades [90]. Optical imaging in the near-infrared (NIR) region allows increased depth penetration over the visible range since hemoglobin and water, which are largely responsible for absorption in tissue, have their lowest absorption in the NIR region [56, 97, 98]. However, this also means that the dominant interaction of light with tissue is through scatter, and thus the geometry of the imaged object as well as the way the light is sampled defines the resolution, contrast and detection of anomalies in tissue [90, 99, 100].

Detection of intracranial murine brain tumors via fluorescence imaging requires an imaging system capable of detecting relatively small anomalies, which often lie beneath fluorescent skin. The ideal system for detection of brain tumors would have high sensitivity to detect tumors as small as 1 – 2 mm in diameter, allowing early detection as tumors grow in a population of mice. The murine brain tumors studied in this work ranged in volume from 0.5 – 500 mm³, depending upon the stage of growth, and thus ideally detection of a large range of sizes would be possible. However, this system would need to be relatively insensitive to skin fluorescence, as PpIX fluorescence

increased in both the skin and tumor tissue following ALA administration (chapter 3). Since fluorescence measurements of tumor-bearing mice were collected at multiple time points, a system that was relatively insensitive to mouse positioning would allow for repeatable fluorescence detection of tumors. In this chapter phantom studies conducted on both the reflectance and transmittance imaging systems, discussed in chapter 3, were used to quantify the possibility of murine brain tumor detection using each imaging system.

4.2. Phantom Studies of Reflectance Imaging Systems

Phantom studies were conducted to determine if the reflectance raster scanning and/or broad beam imaging systems could be used to detect murine gliomas. The reflectance imaging systems were compared in a phantom study to quantify the detection of various sized objects at different depths and detection of various sized objects at different contrasts. For both studies liquid phantom stock was made from 1% Intralipid for scattering [101], 3% pig blood for absorption and 5% Tween 20 to keep the PpIX molecules from aggregating. 25 ml of the liquid phantom stock with a concentration of 1 $\mu\text{g}/\text{ml}$ PpIX was used to fill opaque balloons to diameters of 15, 11, 8.3 and 5 mm. The balloons were submerged in a liquid phantom bath, simulating fluorescent brain tissue *in vivo*. For the contrast-size experiment, images of the balloons within the contrast bath were acquired while they were in contact with the imaging surface, to simulate tumors near the tissue surface. The PpIX concentration of the contrast bath was varied from 0 – 1 $\mu\text{g}/\text{ml}$ PpIX by 0.1 $\mu\text{g}/\text{ml}$ increments, while images were acquired at each contrast level. The same phantom was used for the depth-size experiment, where the balloons

were submerged in contrast bath, which did not contain PpIX. The balloons were raised above the imaging plate by 1 mm increments and images were obtained at each depth.

This phantom study was used to quantify the detection ability of both reflectance imaging systems and determine if either system would be suited for the detection of PpIX fluorescence in murine brain tumors. As illustrated in chapter 3, when mice were administered ALA, the PpIX fluorescence of the tumor tissue increased, but the PpIX fluorescence of the skin was also increased. Therefore, the contrast ratio for the tumor tissue to normal tissue was low, with a conservative estimate in the range of 2:1 – 4:1. The size of murine brain tumors varied considerably, depending on the type of tumor and the stage of growth. For the purposes of validating the imaging systems, only the objects with diameters of 5 mm and 8.3 mm were compared to the volume of a murine brain tumor, although these were probably slightly larger than *in vivo* brain tumors. As shown in Figure 4.1(a), when the depth of the object was increased from the imaging surface, the broad beam imaging system was better able to detect larger objects at greater depth than the raster scanning system. Figure 4.1(b) illustrates that the raster scanning system was better able to detect smaller objects at lower contrast ratios than the broad beam imaging system. Contrasts in the 2:1 – 4:1 range were detectable using the raster scanning system, but were largely undetectable by the broad beam system unless the object of interest was larger than sizes possible for a murine brain tumor. However, as can be seen in Figure 4.1(a), when objects around the size of murine brain tumor were imaged at depths greater than 1 mm, they were not detectable by the raster scanning system. Thus, neither the raster scanning system nor the broad beam system would be useful for the detection of murine brain tumors and were not used for intracranial brain tumor studies.

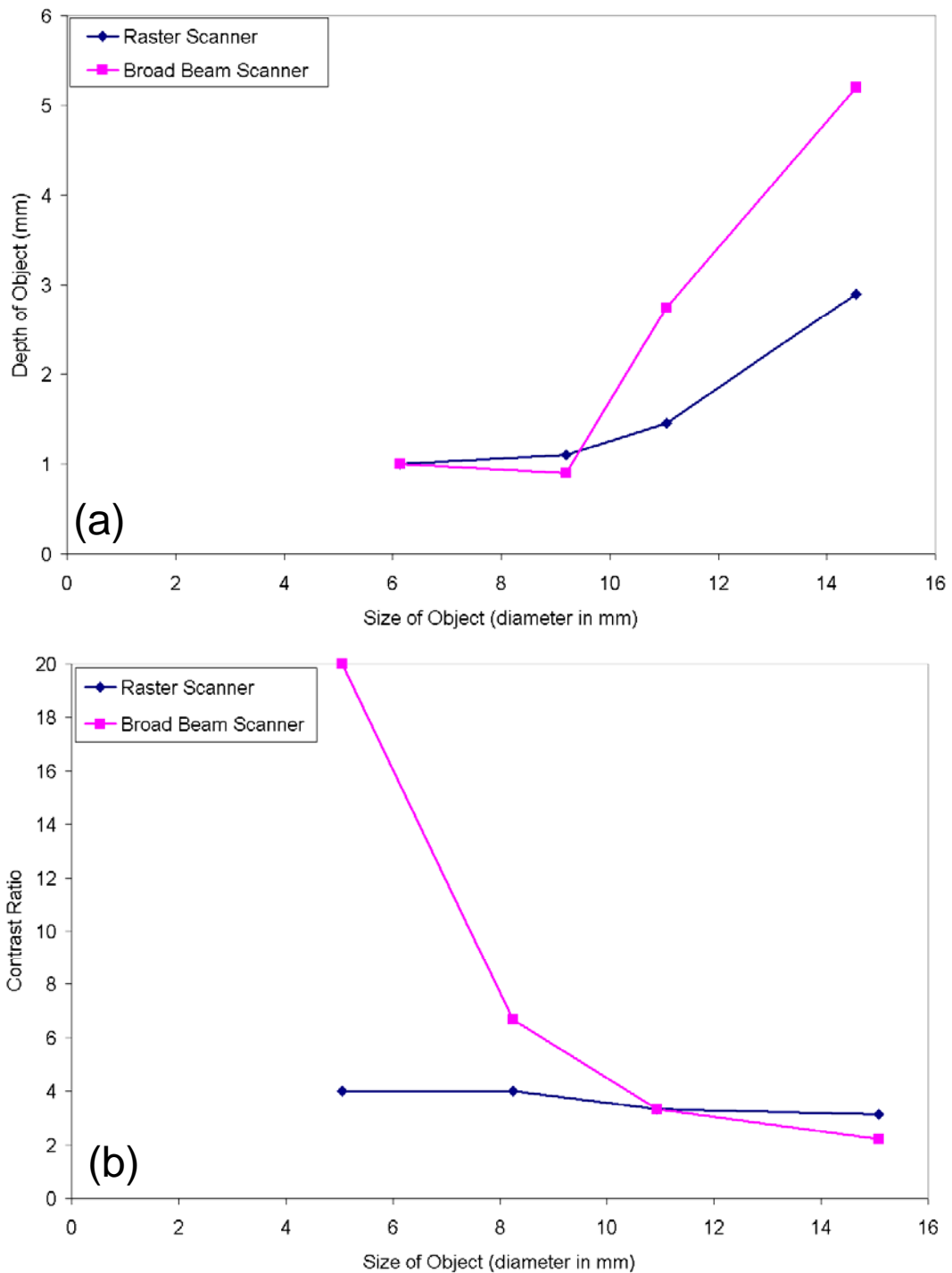


Figure 4.1 – The raster scanning system was compared to the broad beam system to quantify the (a) depth vs. size and (b) contrast vs. size trade-off for detection of three-dimensional phantoms containing 1 $\mu\text{g/ml}$ PpIX. In both plots, any object to the right of the lines would not be detectable by each system; whereas an object to the left of the lines would be detectable by each system.

4.3. Phantom Studies of Transmission Imaging Systems

All *in vivo* detection experiments of murine brain tumors using PpIX were performed with the single channel spectroscopy system. PpIX phantom experiments were completed to determine the size vs. contrast trade-off and positional dependence of these measurements. Phantom experiments were performed to quantify detection by the single channel system of different sized mouse brain tumors beneath varying intensities of PpIX skin fluorescence. The phantom used for this study consisted of a 24 mm thick contrast bath, simulating the mouse head, and anomalies of varied size at the center of the contrast bath simulating a growing brain tumor. The phantom was filled with tissue-simulating liquid phantom comprised of 1% Intralipid, 1 mg/L India ink for absorption and 5% Tween 20. The detection of anomalies with diameters of 1.6, 2.4, 3.2, 4.0 and 6.4 mm was tested using the single channel system. The anomaly contained 1 $\mu\text{g/ml}$ PpIX and the PpIX concentration in the surrounding contrast bath was increased from 0 – 1 $\mu\text{g/ml}$ PpIX by 0.1 $\mu\text{g/ml}$ increments to simulate increasing PpIX skin fluorescence. Measurements were collected at both the excitation and emission wavelengths, after which they were normalized for exposure time. The emission data was spectrally fitted and integrated, followed by normalization to the transmitted laser intensity as described in chapter 3. Figure 4.2 demonstrates that the larger anomalies were easily detected by the single channel spectroscopy system (6.4 and 4.0 mm), while the detection size limit was somewhere in the 2 – 3 mm range. The actual contrast could not to be recovered using this system but enough signal intensity was obtained with the 6.4, 4.0 and 3.2 mm objects at a true contrast of 2:1 to detect the presence of an anomaly. The 2.4 mm object was somewhat difficult to detect while the 1.6 mm object was not detectable using this

system. The results of this phantom experiment indicated that the single channel spectroscopy system would be a useful tool for the detection of brain tumors. Small objects with low contrast could be detected in the center of a 24 mm thick contrast bath, simulating detection of tumor tissue within the mouse brain.

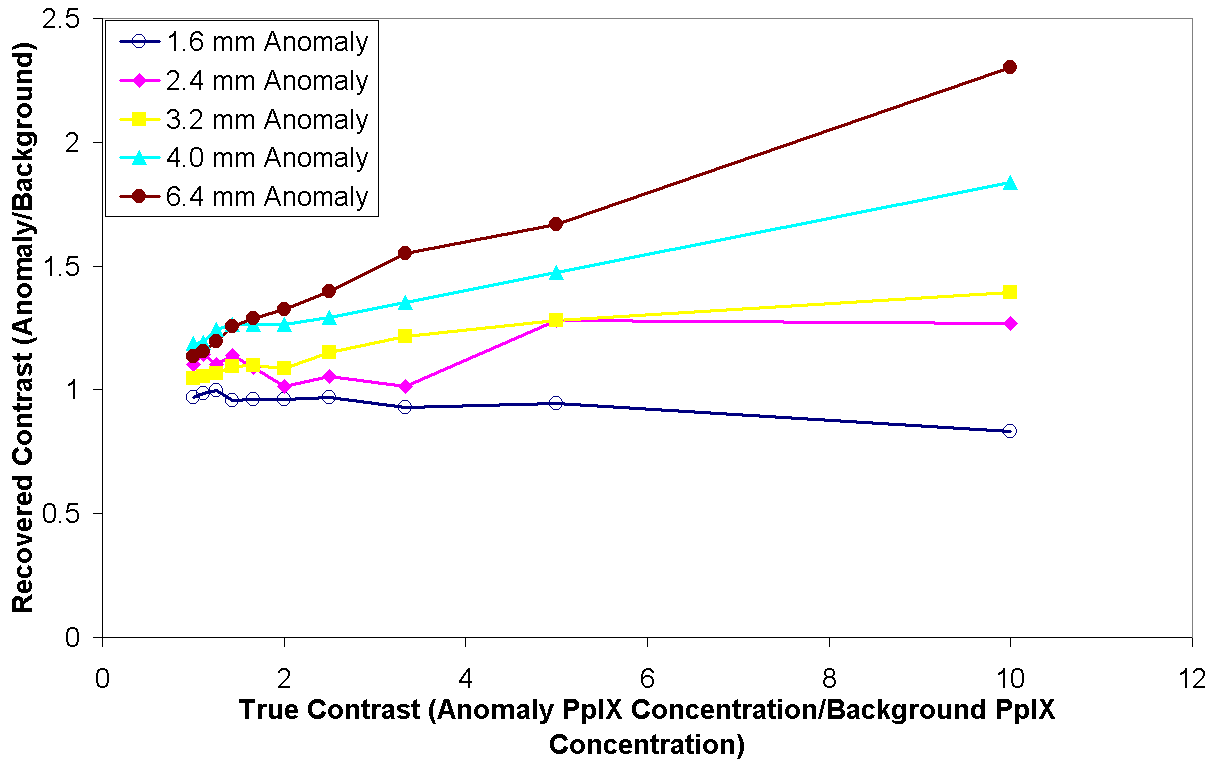


Figure 4.2 – The results of a phantom study with the single channel spectroscopy system to examine size vs. contrast trade-off. The recovered contrast of the anomaly normalized to the background is shown, where recovered contrasts below one are not detectable.

Although transmission based imaging systems were less sensitive to anomaly depth than the reflectance systems, detection with these imaging systems was vastly susceptible to the position of the anomaly in relationship to the fiber optics. The fluorescence detection sensitivity of the transmission system was decreased as the distance between the anomaly and the fiber plane was increased. Phantom experiments

were performed to examine the positional dependence in both the single channel and multichannel systems. The XFM-2 fluorescent phantom (Caliper LifeSciences-Xenogen, Hopkinton, MA), a mouse-shaped phantom made from polyurethane material which included scattering particles and dye to simulate the optical properties of live tissue was used for these experiments (Figure 4.3(c)). The phantom was constructed to accommodate rods with fluorophore embedded in the tip, which could be inserted into the mouse phantom at different depths (Figure 4.3(d) & (e)). For the single channel spectroscopy system the rod containing Alexa Fluor 680 (AF680) fluorophore was used to simulate PpIX fluorescence. AF680 has a broad excitation spectrum with strong absorption at 635 nm and a broad emission peak ranging from 650 – 800 nm. The same center wavelength (705 nm) was used to collect fluorescence emission data for AF680 as was used for PpIX; however due to the broad emission peak the 300 grating was used for emission collection instead of the 1200 grating as was used to collect PpIX emission. The collimators were placed on opposite sides of the mouse with the fluorophore rod inserted into the center of the phantom (Figure 4.3(d)). Fluorescence and excitation data were collected as the fluorophore rod was moved into and out of the fiber plane in 1 mm increments (Figure 4.3(e)). The integrated, spectrally fitted fluorescence to transmittance ratio was calculated for the fluorophore rod at each position to determine the dependence of the fluorescence to transmittance signal intensity on the position of the fluorophore.

The first 6 measurements were collected with the fluorophore below the center of the fiber plane, the 7th measurement was collected with the fluorophore at the center of the fiber plane, and the last 4 measurements were collected with the fluorophore above the fiber plane (Figure 4.3(a) & (b)). As expected, the fluorescence to transmittance ratio

intensity was decreased when the fluorophore was not directly in the plane of the fibers. At a distance of 3 mm from the fiber plane, the detected signal was only 75% of the total signal intensity, and at 7 mm away from the fiber plane the detected signal had decreased by 50% (Figure 4.3(b)).

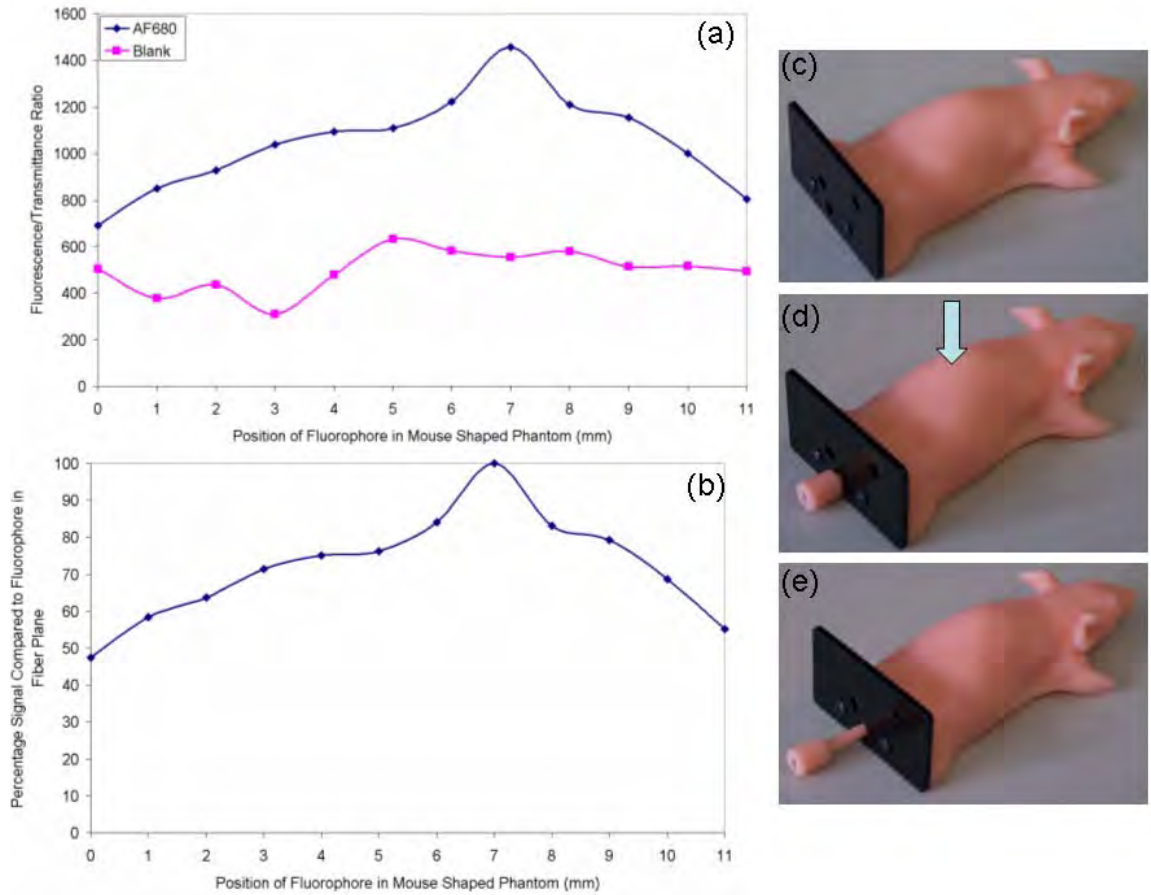


Figure 4.3 – (a) The positional dependence of fluorescence detection in the single channel spectroscopy system was determined using the mouse-shaped phantom and the AF680 fluorescent probe. The first 6 measurements were collected with the probe below the axially positioned fiber plane. The measurement at position 7 was collected when the probe was in line with the fiber plane, and measurements following this were above the fiber plane. (b) The percentage of the fluorescent signal that was detected when the fluorophore was not at the center of the collimators is shown, with 100% signal representing when the fluorophore was directly in the fiber plane. (c) A photograph of the mouse-shaped phantom made to simulate the optical properties of tissue, which could accommodate rods with fluorophore tips, inserted in the holes at the posterior of the phantom. (d) A photograph of the mouse-shaped phantom with rod inserted and arrow

showing approximate location of fluorophore within the phantom. (e) The fluorophore rod was moved caudally out of the axial plane of fibers in 1 mm increments.

The multichannel spectroscopy system was used to detect EGF-IRDye 800CW (LI-COR Biosciences, Lincoln, NE) in mouse brain tumor tissue to study epidermal growth factor uptake and Erbitux treatment monitoring, discussed in chapter 7. Prior to mouse imaging, phantom experiments were performed to determine the linearity of fluorescence detection at physiologically relevant concentrations of EGF-IRDye and to examine the positional dependence of these measurements. A homogeneous Teflon phantom 26.8 mm in diameter, similar to size of a mouse head, was used to hold tissue-simulating liquid phantom which consisted of 1% Intralipid, 1 mg/L India ink, and varied concentrations of EGF-IRDye. Concentrations of EGF-IRDye from 0.5 μM – 0.05 nM were used to determine if fluorescence signal was detectable at physiologically relevant concentrations and if detection of a range of EGF-IRDye concentrations was linear. When the data was plotted on a linear graph it appeared that all concentrations of EGF-IRDye had fluorescence signal greater than zero (Figure 4.4(a)). The data point at 0.5 μM was excluded from the plots in Figure 4.4 because it appeared to be saturated and affected the estimate of the linearity of detection. The data was also plotted on a log-log scale which showed linear detection at concentrations of EGF-IRDye ranging from 0.1 μM to 5 nM (Figure 4.4(b)). For *in vivo* experiments, 1 nmole of EGF-IRDye was administered to the mice intravenously. Mice were estimated to contain approximately 1 – 2 ml of blood volume, thus *in vivo* concentrations of interest would range from 0.5 μM – 1 μM directly following administration and would decrease over the 72 hour monitoring period due to systemic clearance. However, it appeared promising from the

phantom experiment illustrated in Figure 4.4 that *in vivo* detection of EGF-IRDye fluorescent signals would be possible.

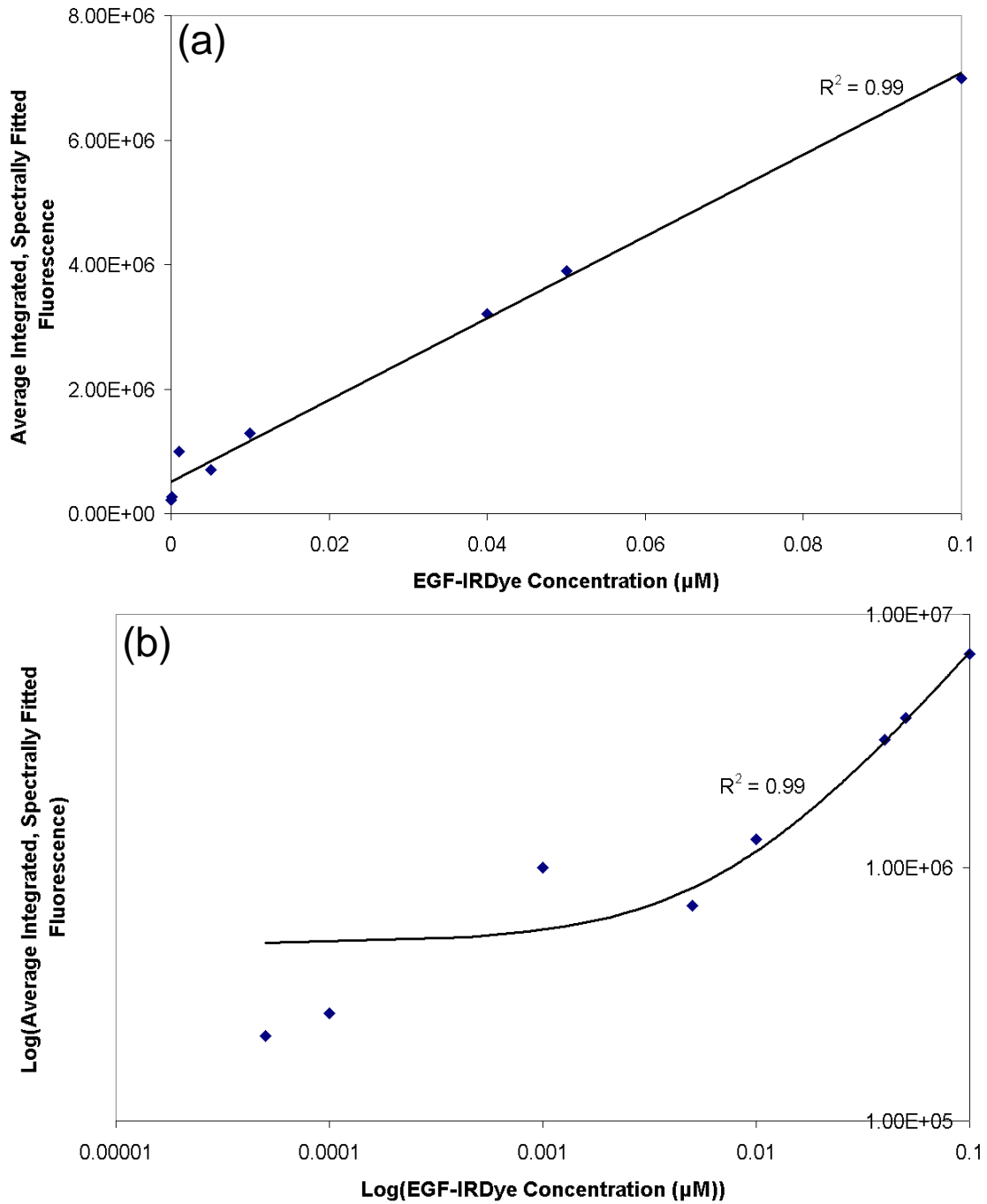


Figure 4.4 – Results of EGF-IRDye homogeneous phantom experiment are shown, to determine detection limits of EGF-IRDye and detection linearity at *in vivo*

concentrations. Liquid phantom containing concentration of EGF-IRDye ranging from 0.5 μM – 0.05 nM were imaged using 8 of the 16 available fiber optics from the multichannel transmission spectroscopy system. The results from the 0.5 μM EGF-IRDye were not included in the graphs due to saturation. Results were plot on (a) a linear scale and (b) a log-log scale.

Similar to the single channel spectroscopy system, the multichannel spectroscopy system was also highly susceptible to position of the anomaly in relation to the plane of fiber optics. A similar phantom experiment to that illustrated in Figure 4.3 was performed using the mouse shaped phantom and a fluorophore rod containing the fluorophore Quantum Dot 800 (QD800) to simulate the fluorescence of EGF-IRDye. Eight of the 16 available fiber optics were positioned axially around the middle of the mouse-shaped phantom (Figure 4.5(c) & (d)). The fiber plane was lined up with the fluorophore at position zero, shown in Figure 4.5. The rod was again moved caudally along the sagittal plane, out of the fiber plane by 1 mm increments up to 1.5 cm away from the plane of fibers. The absorption spectrum for QD800 was broad, but had sufficient absorption at 690 nm, so that the same laser and center wavelength could be used for phantom and *in vivo* experiments. The emission spectrum of QD800 ranged from 700 – 900 nm. The spectrometers were centered at 820 nm and the 720 LP filters were used to collect the emission data to simulate the *in vivo* measurements. The fluorophore rod was imaged in the fiber plane and following movement out of the plane by 1 mm increments. The integrated, spectrally fitted fluorescence to transmittance ratio at each fluorophore rod position is illustrated in Figure 4.5(a). The percentage of signal detected when the fluorophore was moved by 1 mm increments out of the fiber plane is shown in Figure 4.5(b). The detected fluorescence to transmittance ratio was

considerably affected by the position of the fluorophore in relation to the fiber plane, with a large decrease in signal seen when the distance the fluorophore was moved out of the plane was increased (Figure 4.5(a)). When the fluorophore was only 3 mm out of the fiber plane the detected fluorescence to transmittance ratio was decreased by almost half as compared to the detected signal when the fluorophore was directly in line with the fiber plane (Figure 4.5(b)).

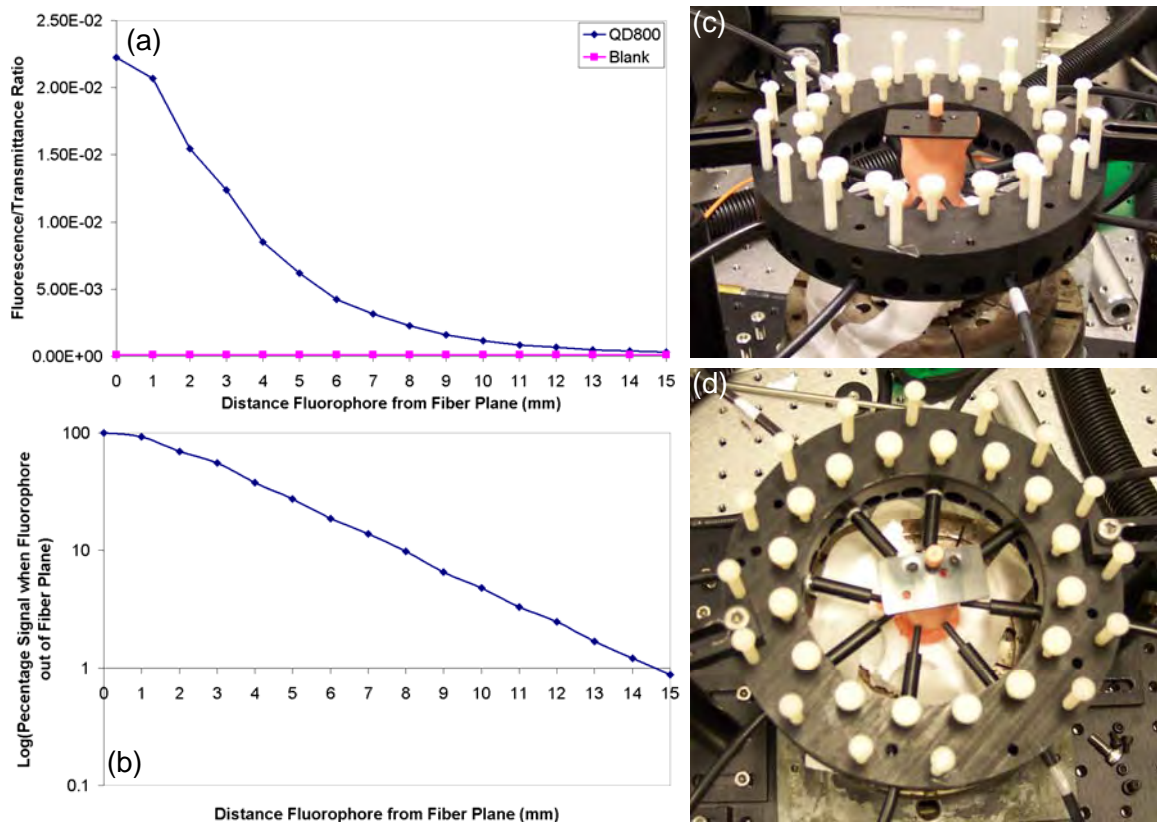


Figure 4.5 – The positional dependence of fluorescence to transmittance ratio as measured by the multichannel transmission spectroscopy system. (a) The integrated, spectrally fitted fluorescence to transmittance ratio of the mouse shaped phantom with the Quantum Dot 800 (QD800) fluorophore rod and with the blank rod which did not contain fluorophore are illustrated. Each rod was imaged in the fiber plane and at 1 mm increments out of the fiber plane up to 1.5 cm away from the fiber plane. (b) The percentage of signal detected as the fluorophore was moved out of the plane of the fibers is graphed on a semi-log scale. When the fluorophore was in the fiber plane (position = 0

mm) the signal was considered to be 100%. The eight fiber optics positioned axially around the center of the mouse can be seen in (c) and (d).

4.4. Modeling Studies of Transmission Imaging Systems

4.4.1. Modeling Materials & Methods

A three-dimensional (3D) modeling study was completed to compare detection of different size tumors, at different contrasts and different positions in the brain by both the single channel and the multichannel transmission spectroscopy system. A 3D mouse head model of a male nude mouse head was constructed from 745 computed tomography (CT) slices, with 0.047 mm resolution, collected using a eXplore Locus Pre-Clinical *In Vivo* MicroCT Scanner (GE Healthcare, Ontario, Canada). This data set was used to create a 3D volumetric mesh through image segmentation, using the medical imaging software MimicsTM (Materialise, Inc), and geometry description. The outer surface of the mouse head as well as the interior regions of brain, bone and skin were segmented using this software (Figure 4.6 (a)). The outer head surface was exported in stereolithography format and meshed into a tetrahedral finite element mesh using the standard meshing software Netgen [102], with a maximum element size of 0.8 mm. The mesh contained 86,927 tetrahedral elements corresponding to 18,662 nodes and was tagged with different material properties for the areas of brain, bone, skin and adipose tissue, which was assumed to be the remaining tissue type in the head (Figure 4.6 (b)). These regions of the mesh were suitably labeled with corresponding optical properties at the excitation and emission wavelengths from literature [103, 104]. This mesh was used for further computation described as follows.

The NIRFAST light diffusion modeling package was used to model the light fluence rate of the excitation source and the emitted wavelength in the tissue [105]. The two fiber optic configurations that were used for *in vivo* experiments were modeled to compare ability to detect tumors of varied sizes, contrasts and positions. Results with two fiber optics, simulating the single channel system (Figure 4.6 (c)) were compared to results obtained with eight fiber optics, simulating the multichannel system (Figure 4.6(d)). In each case, the fiber optic could act as either a source or a detector, but not simultaneously. Thus, for the two fiber optic configuration two measurements were obtained from the model, while for the eight fiber optic configuration, 56 measurements were obtained from the model for each tumor position, size and contrast tested. For control mice an anomaly was not included in the mesh and the light fluence rate of the excitation and the emitted wavelength in the tissue was modeled. A spherical anomaly with a radius of 0.5 – 5 mm increased by 0.5 mm increments was used to simulate a growing tumor. Fluorescence contrast ratios of 2:1, 3:1, 4:1, 5:1, 7:1 and 10:1 tumor tissue to normal tissue were modeled for each tumor size. Five tumor positions for each tumor size and contrast were modeled in this study. The tumor positions included the tumor at the center of the brain (center), the tumor in contact with the top, left edge of the brain (edge), the tumor 1 mm in on all axes from the top, left edge of the brain (1 mm), the tumor 2 mm towards the center on the x-axis from the top, left edge of the brain (2 mm x-axis), and the tumor 2 mm towards the center on the z-axis from the top, left edge of the brain (2 mm z-axis). The area under the curve at the excitation wavelength and the emission wavelength was calculated so that data could be reported as a single number representing the fluorescence to transmittance ratio. The difference in recovered contrast

between a mouse with an anomaly (T) and a control mouse (C) without an anomaly, normalized to the recovered contrast of the control mouse will be reported $((I_T - I_C)/I_C)$.

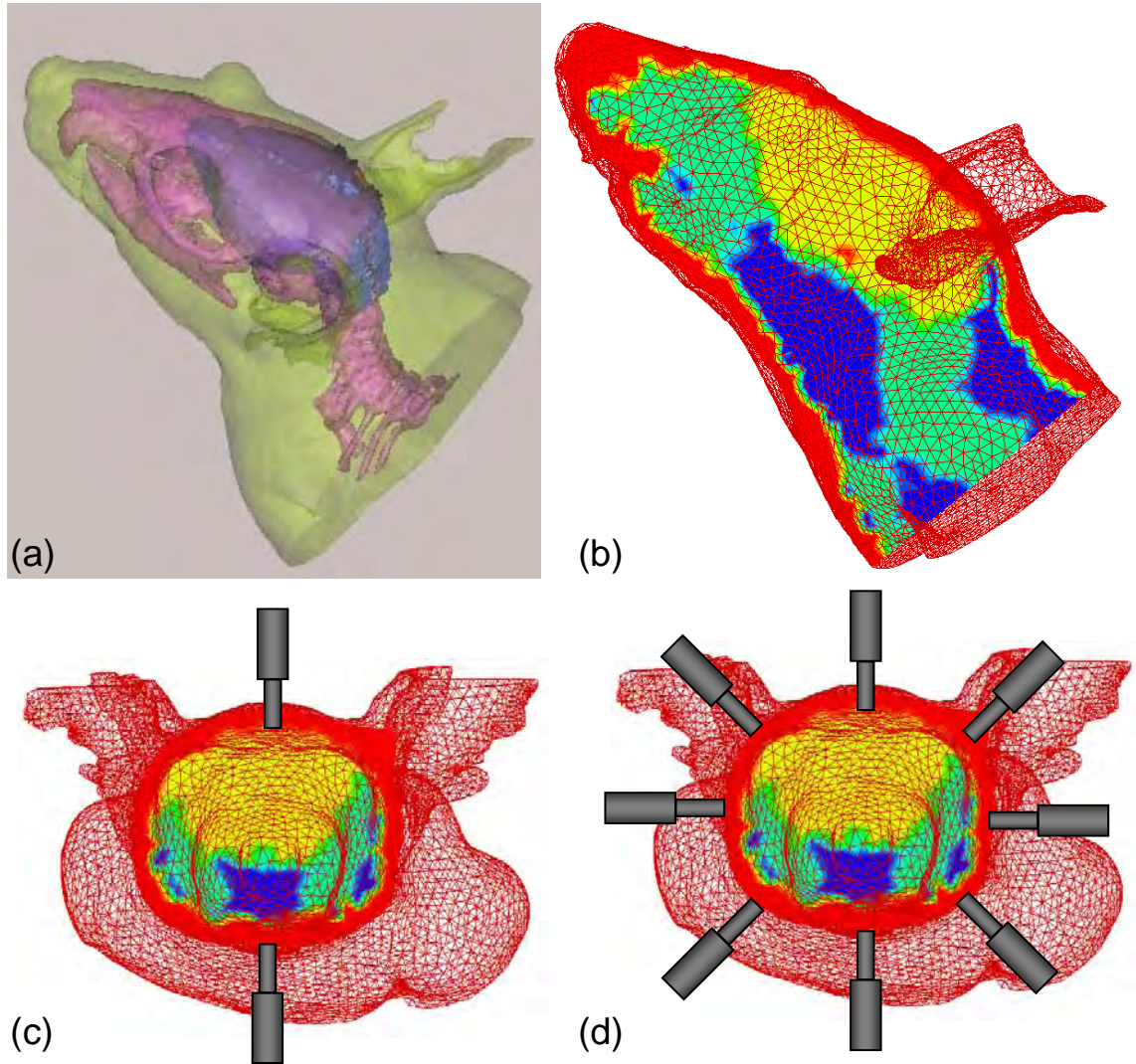


Figure 4.6 – (a) The segmented mouse head boundary with skin, brain and bone regions defined using Mimics was used to construct (b) a three-dimensional mouse head mesh with regions segmented from the volume representing the skin (red), brain (yellow), bone (green) and adipose (blue) tissues. (c) The positions of the two fibers used to model the single channel spectroscopy system. (d) The positions of the eight fibers used to model the measurements collected with the multichannel spectroscopy system.

4.4.2. Model of Single Channel System vs. Multichannel System

The difference in recovered contrast for each tumor position, contrast and size as compared to the control mouse can be seen in Figure 4.7 for the two fiber optics, where signal was collected at the top of the head from light input into the chin of the mouse. This fiber configuration had the highest recovered contrast when the tumor was at the center of the brain (Figure 4.7(a)), directly between the two fibers. The recovered contrast was decreased considerably when the tumor was out of plane with the fiber optics (Figure 4.7(b) - (d)). These results were comparable to the positional phantom experiment where the signal detection was highest when the fluorophore was directly in line with the fiber plane and decreased by 15% when the fluorophore was only 1 mm out of plane (Figure 4.3). The modeled tumor position which most closely simulated the *in vivo* situation was when the tumor tissue was at the 1 mm position (Figure 4.7(e)), as this was closest to the implantation site used for intracranial tumors, described in chapter 2. The recovered contrast of tumors at this position was greater than zero for tumors of all sizes modeled, indicating that tumor-bearing mice could be detected over control mice. However, a tumor to normal tissue contrast of 3:1 or higher was necessary to detect recovered contrast greater than zero with the two fiber optic configuration. These results indicated that the sizes and contrasts detectable by this fiber optic configuration were relevant for *in vivo* imaging.

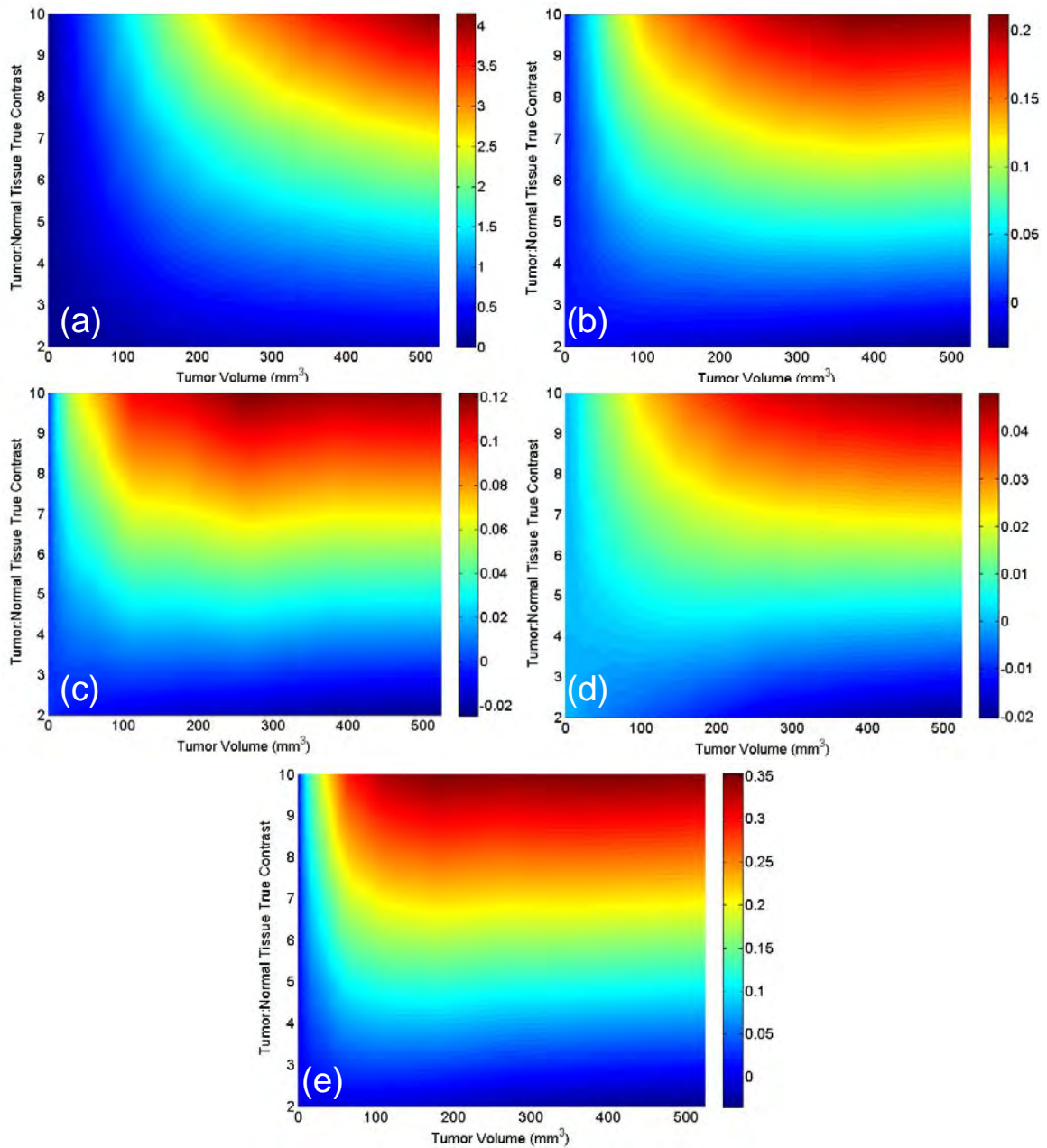


Figure 4.7 – The effect of the tumor volume and contrast on the recovered contrast of the model using two fibers is plotted as the color scale in each figure, with different tumor positions shown as separate figures. The tumor modeled (a) at the center of the brain, (b) at the top, left edge of the brain, (c) 2 mm towards the center from the top, left edge of the brain on the x axis, (d) 2 mm towards the center from the top, left edge of the brain on the z axis and (e) 1 mm towards the center from the top, left edge of the brain on the x, y and z axes.

An important difference between this model-based data and the phantom data for the single channel system was the size of the collimators used for illumination and collection of light. The single channel spectroscopy system was equipped with collimators that had 11 mm diameter lenses. By contrast sources and detectors in NIRFAST are modeled as small point sources, so although the trend of the model data was similar to phantom data it does not simulate the exact detection limits of the single channel system. The model data was most useful to compare recovered contrast on exactly the same tumor positions, sizes and contrasts when either two or eight fiber optics were used for data collection.

The same tumor positions, sizes and contrasts were modeled using eight fibers to compare the recovered contrast of the tumor tissue with the same parameters, but additional measurements around the mouse head. The source was rotated through each of the fiber optics enabling a total of 56 measurements per tumor position, size and contrast to be collected. The signal intensity shown in Figure 4.8 represents the recovered contrast when the 56 measurements were averaged into a signal number that was normalized to the appropriate model control mouse. A similar pattern of recovered contrast from the different tumor positions was seen using eight fibers as when two fibers were used. The recovered contrast was highest when the tumor was at the center of the brain since it was directly in line with the fiber plane (Figure 4.8(a)). The worst recovered contrast was seen when the tumor was out of the fiber plane as can be seen in Figure 4.8(b) – (d).

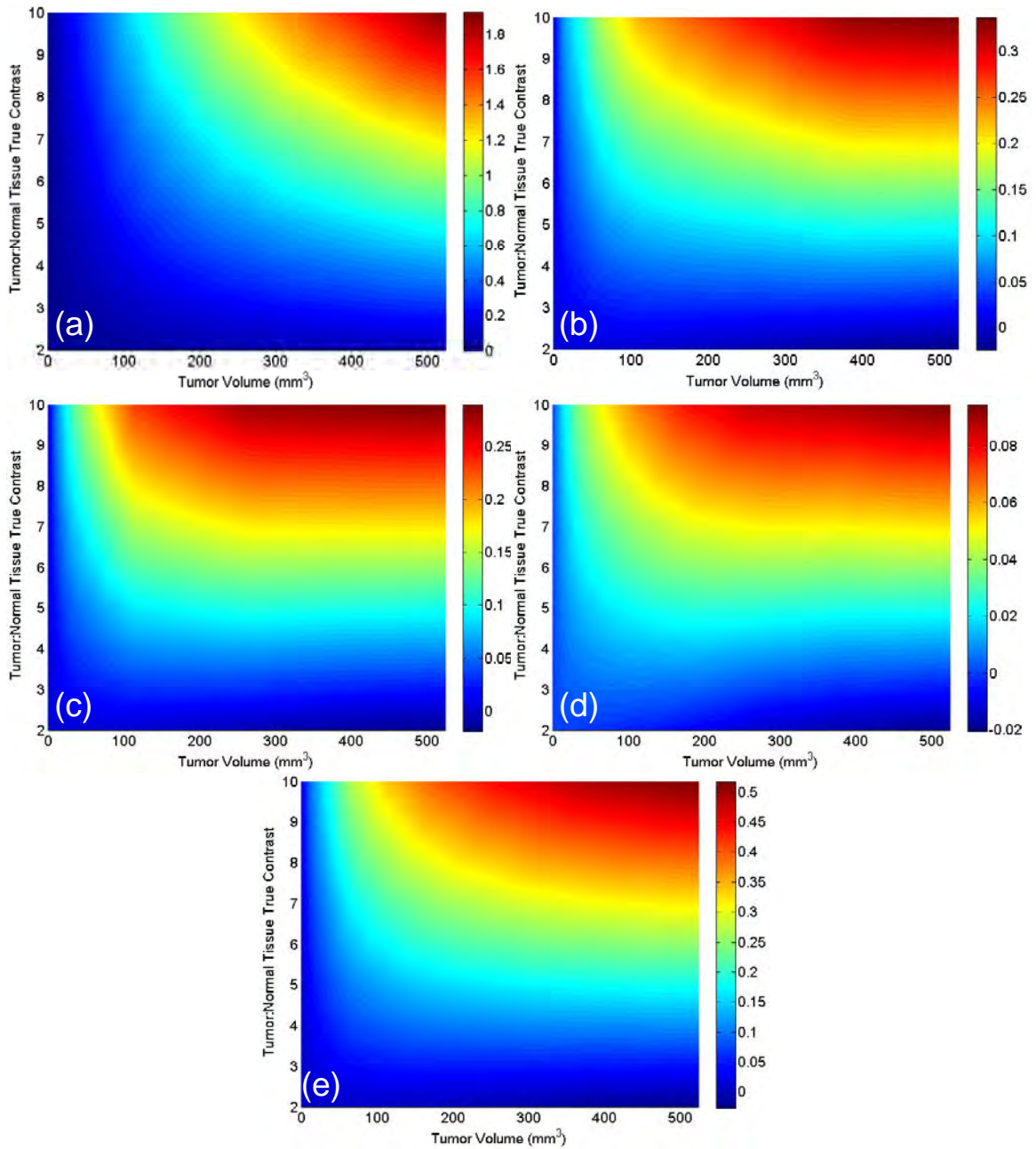


Figure 4.8 – The effect of the tumor volume and contrast on the recovered contrast of the model using eight fibers is plotted as the color scale in each figure, with different tumor positions shown as separate figures. The tumor modeled (a) at the center of the brain, (b) at the top, left edge of the brain, (c) 2 mm towards the center from the top, left edge of the brain on the x axis, (d) 2 mm towards the center from the top, left edge of the brain on the z axis and (e) 1 mm towards the center from the top, left edge of the brain on the x, y and z axes.

The most realistic case modeled, when the tumor was at the 1 mm position, showed that the recovered contrast for all modeled tumor sizes was greater than zero, indicating tumor-bearing mice could be detected over normal control mice (Figure 4.8(e)). Similar to the results seen when two fibers were used for measurement, a tumor to normal tissue contrast of at least 3:1 was necessary to detect recovered contrasts greater than zero with the eight fiber optic configuration. These results indicated that the sizes and contrasts able to be detected by this fiber optic configuration were also relevant for *in vivo* imaging.

4.4.3. Optimal Light Paths for Tumor Detection with the Multichannel System

The recovered contrasts were compared for the measurements collected which simulated the single channel system and the multichannel systems. Interestingly, when the tumor was at the center of the brain the single channel system showed much higher recovered contrast than the multichannel system (Figure 4.7(a) & Figure 4.8(a)), even though the multichannel system provided 55 additional measurements of fluorescence intensity from around the head. The multichannel system showed better recovered contrast for the other four tumor positions as compared to the single channel system; however the recovered contrast was only slightly better using the multichannel system as compared to the single channel system (Figure 4.7 & Figure 4.8). Following this result, select groups of measurements were considered to determine if averaging all 56 measurements actually decreased the recovered contrast, since some of the light paths would not pass through the fluorescent tumor tissue. The light paths between the eight fibers were divided into four groups, which will be referred to as transmission, semi-

transmission, semi-reflectance and reflectance (Figure 4.9).

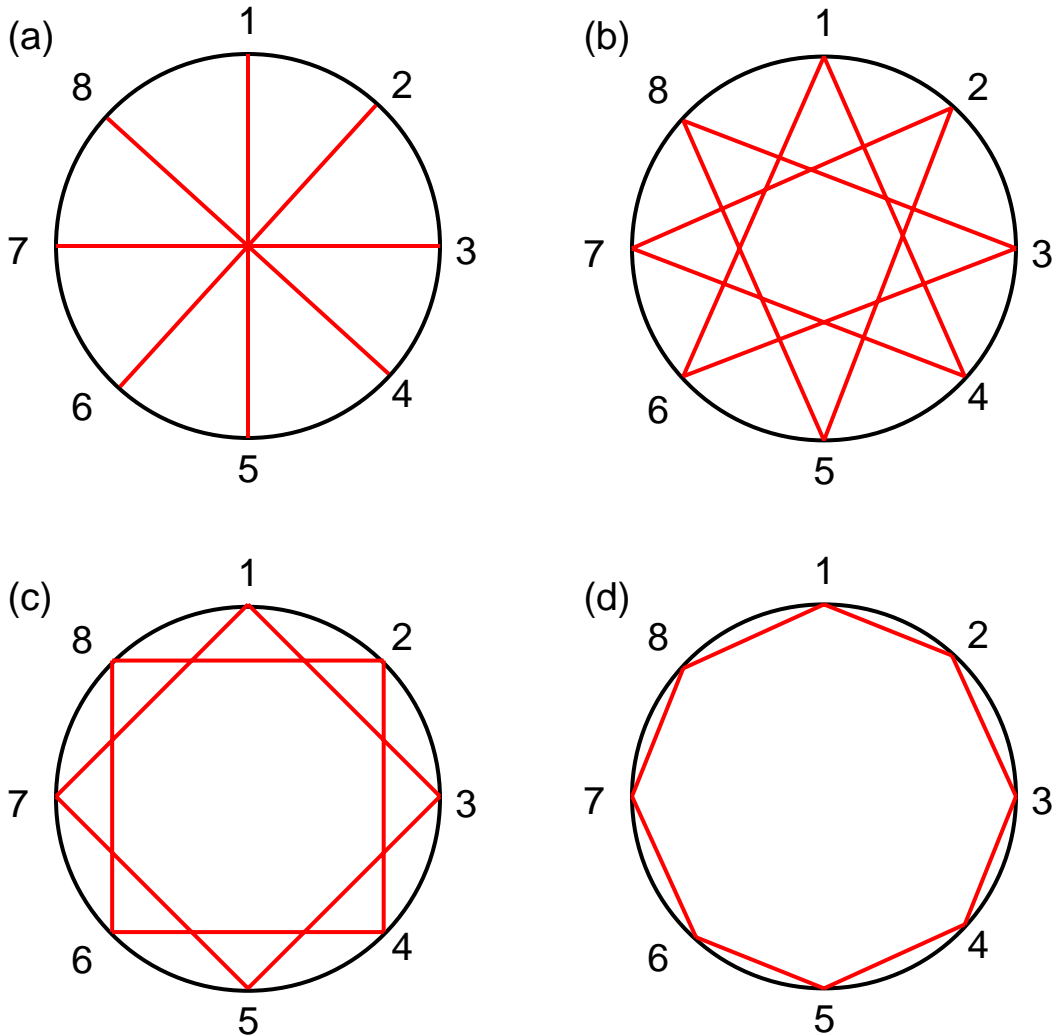


Figure 4.9 – The light paths from source-detector pairs in the model of the multichannel spectroscopy system. The fiber optics were numbered 1 - 8 and are illustrated around a circle which represents a coronal section of the mouse head. Each red line represents the light path between the two fiber optics, and thus two measurements, since each fiber can be both a source and a detector. The light paths which represent (a) transmission measurements, (b) semi-transmission measurements, (c) semi-reflectance measurements and (d) reflectance measurements from around the mouse head are illustrated.

Using these groups, the model data for the multichannel system with the tumor at the center of the brain and at the 1 mm position were considered to determine if recovered

contrast could be improved by averaging only a portion of the 56 collected measurements. Averaging groups of light paths instead of all 56 measurements was also considered using the mouse shaped phantom data to determine if the detected fluorescence to transmittance ratio would be increased in phantom data.

Groups from the 56 measurements were systematically analyzed and compared to the average of all measurements. When only the transmission measurements (Figure 4.9(a)) were averaged the recovered contrast for the tumor at the center of the brain and at the 1 mm position was improved (Figure 4.10(a) & (b)). The improvement over the average of all measurements was illustrated by normalizing the average of the transmission data to the average of all the data at each tumor tissue size and contrast. The recovered contrast of the tumor at the center of the brain was improved most significantly for low tumor to normal tissue contrasts, specifically less than 3:1 contrast (Figure 4.10(c)). The recovered contrast for the tumor at the 1 mm position showed considerably more improvement than the tumor at the center of the brain, as the recovered contrast of all tumor sizes and contrasts were improved except when the tumor was of appropriate size to pass directly through the fiber plane (Figure 4.10(d)).

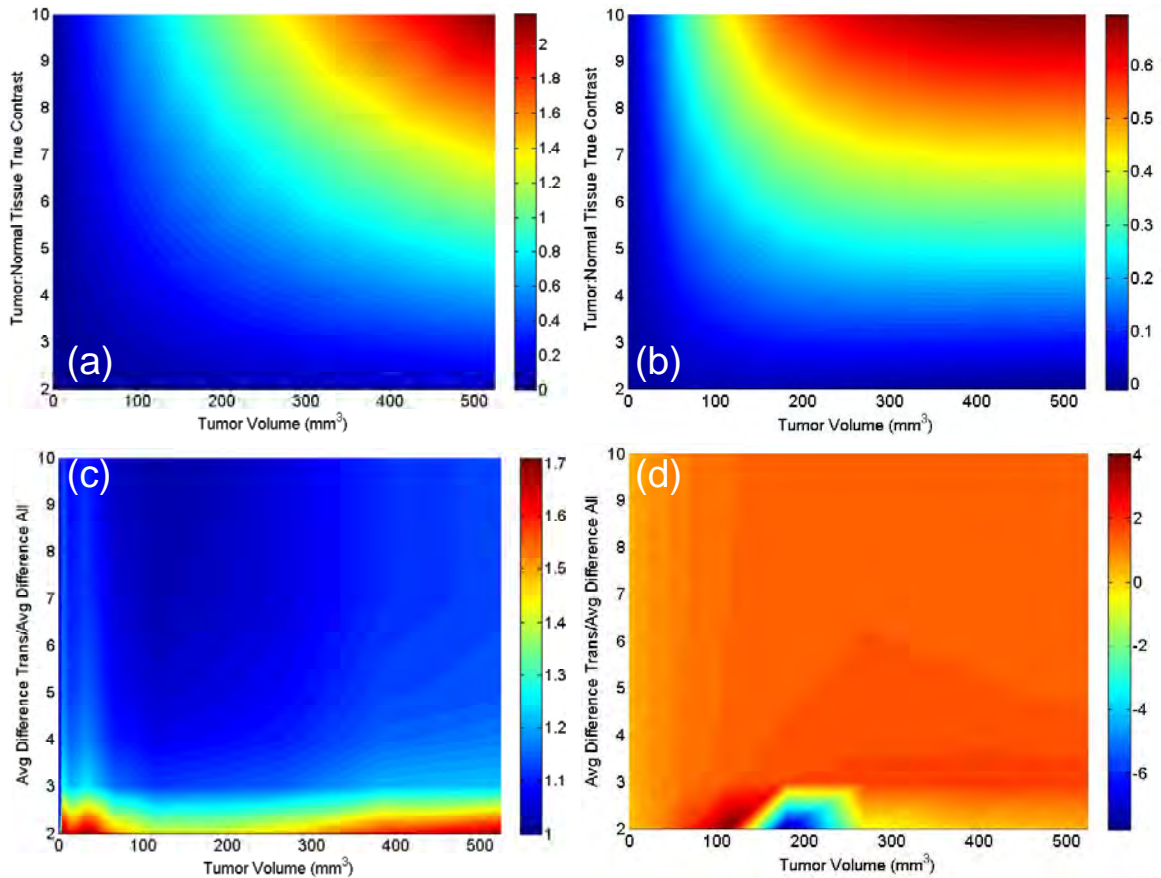


Figure 4.10 – The transmission measurements illustrated in Figure 4.9(a) were averaged for the tumor (a) at the center of the brain and (b) at the 1 mm position. These results were compared to those seen when all 56 measurements were averaged by normalizing the average transmission data at each contrast and tumor volume to the same data when all 56 measurements were averaged. The normalization of the transmission data to the average of all 56 measurements for the tumor (c) at the center of the brain and (d) at the 1 mm position are illustrated.

When the transmission and semi-transmission measurements (Figure 4.9(a) & (b)) were averaged, the recovered contrasts for the tumor at the center and 1 mm positions in the brain were similar to that seen when the average of only the transmission measurements were considered (Figure 4.11(a) & (b)). The improvement over the average of all measurements is shown in Figure 4.11(c) and (d). The recovered contrast for a tumor at the center of the brain was improved most for tumors with low tumor to

normal tissue contrast. Although there was not as much improvement in the recovered contrast for tumors of low contrast, there was improvement in the recovered contrast for small tumors, about 50 mm^3 in volume and smaller, which was not seen when only the transmission measurements were averaged (Figure 4.11(c)). The recovered contrast was also increased for tumors at the 1 mm position when the transmission and semi-transmission measurements were averaged as compared to the average of all 56 measurements, although the improvement was less than that seen when only the transmission measurements were averaged (Figure 4.10(d) & Figure 4.11(d)). A similar decrease in recovered contrast was seen when the tumor was of the appropriate size to be directly in the plane of the fibers as was seen in Figure 4.10(d).

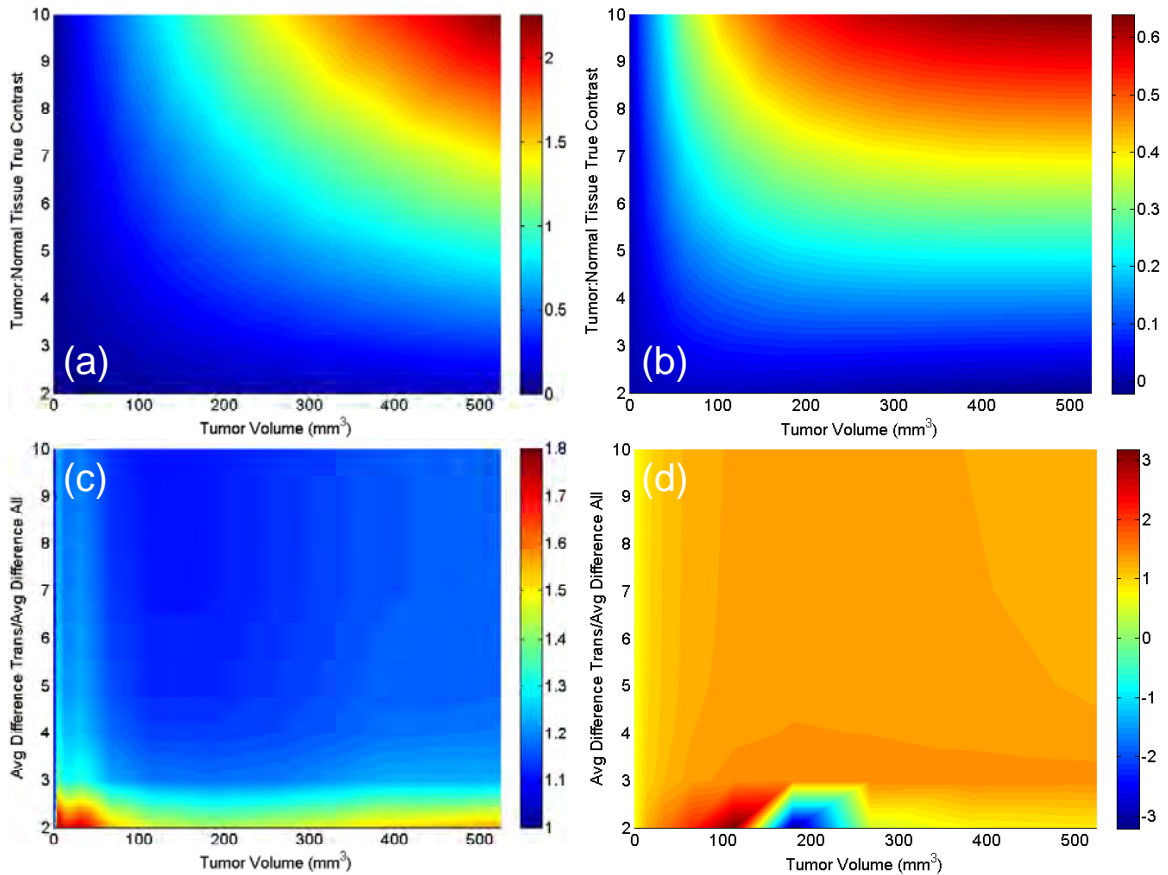


Figure 4.11 – The recovered contrast when the transmission measurements and semi-transmission measurements (Figure 4.9(a) and (b)) were averaged for the tumor (a) at the center and (b) 1 mm position in the brain. These results were compared to those seen when all 56 measurements were averaged by normalizing the average transmission and semi-transmission data at each contrast and tumor volume to the same data when all 56 measurements were averaged. The normalization of the transmission and semi-transmission data to the average of all measurements for the tumor (c) at the center and (d) 1 mm position in the brain are illustrated.

The multichannel system data was also considered when the transmission, semi-transmission and semi-reflectance measurements were averaged and thus only the reflectance measurements were excluded (Figure 4.9). Both tumor positions showed improved recovered contrast as compared to the average of all 56 measurements (Figure 4.12(a) & (b)). The recovered contrast for the tumor at the center of the brain was most

improved for small, low contrast tumors (Figure 4.12(c)). The recovered contrast for the tumor at the 1 mm position showed a similar pattern of improvement to that shown when the previous groups of measurements were averaged (Figure 4.12(d)). The recovered contrast for both tumor positions considered was only slightly improved when the reflectance measurements were excluded from the average in comparison to averaging all of the measurements.

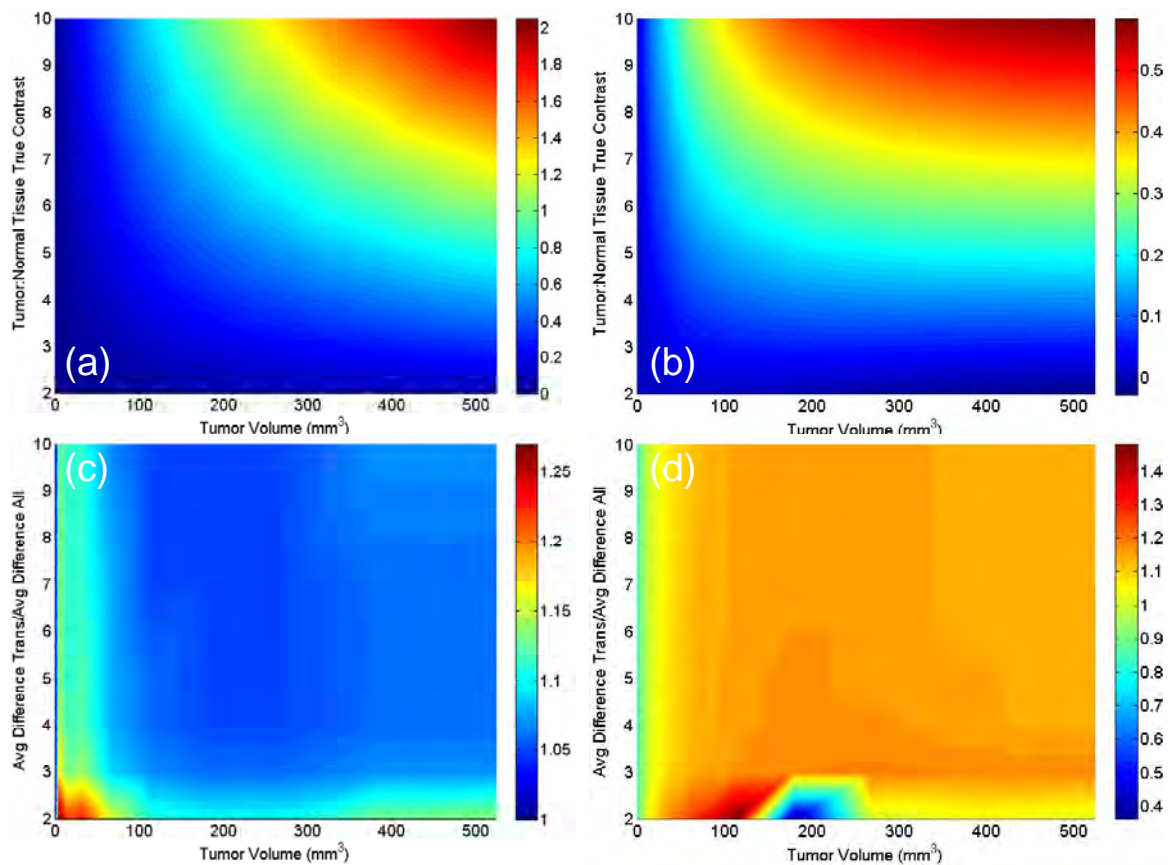


Figure 4.12 – The recovered contrast for the average of all measurements except reflectance measurements (Figure 4.9(d)) for the tumor (a) at the center and (b) 1 mm position in the brain. These results were compared to those seen when all 56 measurements were averaged by normalizing the data at each contrast and tumor volume. The normalization of the average of all measurements except the reflectance measurements to the average of all 56 measurements for the tumor (c) at the center and (d) at 1 mm position in the brain are illustrated.

The same groups of measurements which were averaged and illustrated in Figure 4.10 – Figure 4.12, were tested on the phantom data obtained from the mouse shaped phantom illustrated in Figure 4.5. The integrated, spectrally fitted fluorescence to transmittance ratio of each group of measurements at each position is illustrated in Figure 4.13(a). As was seen in the modeled data, the average of the transmission measurements gave the highest fluorescence to transmittance ratio, while the average of all the measurements gave the lowest fluorescence to transmittance ratio. When the transmission and semi-transmission measurements were averaged the fluorescence to transmittance ratio was very similar to that detected when only the transmittance measurements were averaged (Figure 4.13(a)). The natural log of the data was calculated to determine the distance the fluorophore was moved from the fiber plane before the signal decreased by more than $1/e$. Distances from the fiber plane that caused a decrease in signal less than $1/e$ were considered to be within the ‘effective sampling region’ as little effect would be seen from positional dependence of the measurements. All measurement groups tested showed signal decrease less than $1/e$ when the fluorophore was 1 mm out of the fiber plane. However, when the fluorophore was 2 mm out of the fiber plane only the average of all measurements showed a signal decrease less than $1/e$, demonstrating that the average of all 56 measurements provided more robust signal detection than the average of a smaller subset of these measurements. When the fluorophore was 3 mm out of the fiber plane the decrease in signal intensity was greater than $1/e$ for all measurement groups illustrating that the effective sample region was ± 3 mm from the fiber plane when the average of all 56 measurements was considered.

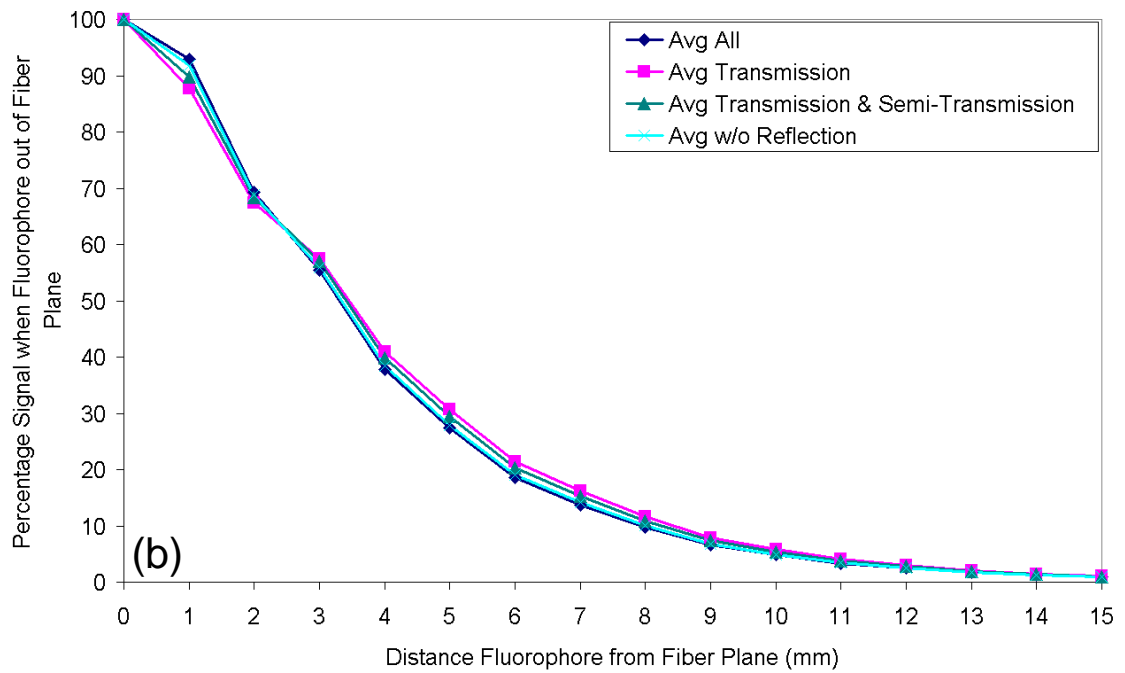
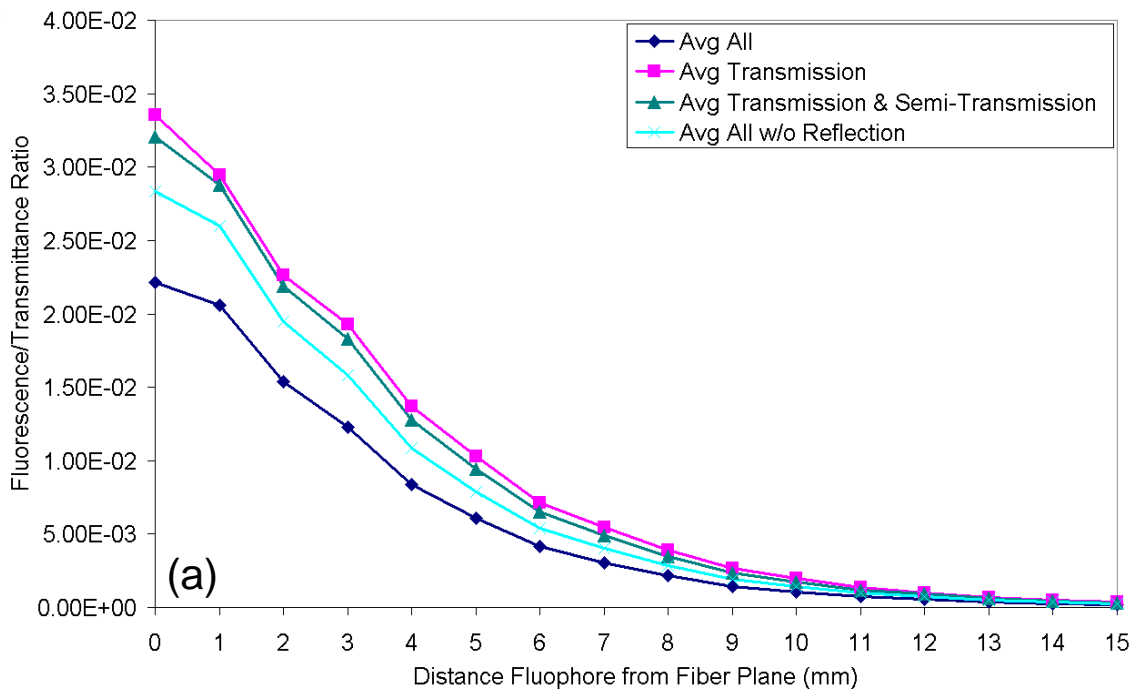


Figure 4.13 – (a) The average of the groups of measurements at each fluorophore position are illustrated for the mouse-shaped phantom imaged in the multichannel system. (b) The percentage difference from the average of all measurements when the fluorophore was in the fiber plane is shown for each group of measurements.

4.5. Discussion

Model and phantom studies were completed for the reflectance and transmittance geometry based imaging systems to assess feasibility of intracranial brain tumor detection with each system. Phantom studies showing the size limit for anomaly detection when different contrasts and depths were considered were completed to compare the reflectance raster scanning and broad beam systems. Interpretation of these studies indicated that neither reflectance imaging system would be useful for detection of intracranial brain tumors. The raster scanning system was able to detect anomalies with low enough contrast to simulate the *in vivo* situation, but had little depth resolution. In contrast, the broad beam system was able to detect anomalies at depths sufficient for the *in vivo* application, but could not detect small, low contrast anomalies (Figure 4.1).

The single channel and multichannel transmission spectroscopy systems were much less sensitive to object depth in a mouse sized geometry, but were quite sensitive to positioning. The size limit for anomaly detection with varied contrasts was quantified using the single channel spectroscopy system (Figure 4.2). The system could detect anomalies 2 – 3 mm in diameter with sufficiently low contrast to be relevant to the *in vivo* case when the anomaly was in the center of the mouse sized geometry, similar to an intracranial brain tumor. However, this phantom experiment was run when the anomaly was in the fiber plane, a much different detection ability of both the single channel and multichannel systems was encountered when the anomaly was out of plane with the fibers. A phantom experiment was conducted to systematically test the positional dependence of both systems as the fluorophore was moved by 1 mm increments from the fiber plane. The detected signal intensity was decreased by 15% when the fluorophore

was 1 mm out of the fiber plane, 25% when the fluorophore was 3 mm out of plane and up to 50% when the fluorophore was 7 mm out of plane using the single channel spectroscopy system (Figure 4.3(b)). The multichannel spectroscopy system had a steeper decrease in signal intensity when the fluorophore was out of plane with the fibers (Figure 4.5(a)). The signal intensity as measured by the multichannel system decreased by 8% when the fluorophore was 1 mm out of plane, 30% when the fluorophore was 2 mm out of plane and almost 50% when the fluorophore was 3 mm out of plane with the fibers (Figure 4.5(b)).

The multichannel system was more affected by positioning than the single channel system due to the size of the fiber interface with the tissue. The single channel system was equipped with large collimators that had 11 mm lenses and allowed for greater light collection from the tissue surface than the smaller tissue interface on the multichannel system. The fiber bundles used for light collection on the multichannel system were constructed from eight 400 μm fibers, which together had a diameter of about 1.2 mm. This significant difference in the size of the fiber at the tissue interface allowed the single channel spectroscopy system to collect signal from the fluorophore even when it was not at the center of the collimator. In fact, the fluorophore in the phantom experiment was still in the path of the detection collimator when it was up to 5 mm away from the center of the fiber plane. In contrast, when the fluorophore was only 2 mm out of the fiber plane in the multichannel system, it was no longer in the light path and detected signal was reduced by 30%. For the purposes of brain tumor detection, the lens size on the single channel system provided tissue sampling with reduced positional

dependence. A more significant positional dependence would most likely be seen using this system if a larger *in vivo* model system such as a rat or rabbit were considered.

A model study was also completed to compare the single channel and multichannel systems. The model study did not take the tissue-fiber interface size into account and thus was most useful for comparison of a single measurement vs. 56 measurements from around the mouse head of the same tumor sizes, positions and contrasts. Similar to the phantom results, the highest recovered contrast was seen when the tumor was directly between the fibers in both the two and eight fiber models (Figure 4.7 & Figure 4.8). Interestingly, the recovered contrast from the single measurement was much higher than the average of the 56 measurements from the eight fibers, when the tumor was directly between them. Tumor positions that were not directly between the fibers were also considered and the eight fiber positions showed increased recovered contrast as compared to the single measurement, however this increase was modest. It was hypothesized that averaging the 56 measurements together might decrease the recovered contrast because not all of the measured light paths would pass directly through the tumor, especially if it were at the center of the domain (Figure 4.9).

Groups of light paths were considered to determine if some of the measurements collected with the eight fibers should be excluded from the average to increase the recovered contrast from the tumor. Averaging the transmission measurements (Figure 4.9(a)) or both the transmission and semi-transmission measurements (Figure 4.9(b)) showed similar increase in recovered contrast over the average of all measurements. Tumor positions at the center of the mouse head and at a position closer to the site of implantation were considered when these two groups were averaged and compared to the

average of all measurements. The tumor that was located near the *in vivo* implantation site showed the largest improvement in recovered contrast when only the transmission and semi-transmission measurements were considered (Figure 4.10 & Figure 4.11). An average of all measurements except the reflection measurements (Figure 4.9(d)) was also considered, but did not show much improvement over the average of all measurements (Figure 4.12). Averaging these groups of measurements instead of all 56 measurements was tested on the positional phantom data to determine if positional dependence could be reduced by using a subset of measurements. The natural log of the data was compared to determine which fluorophore positions had signal intensity decrease less than $1/e$ and thus could be considered in the 'effective sampling region'. The average of all 56 measurements provided more robust signal detection than averaging smaller subgroups of measurements. When the fluorophore was less than 3 mm away from the fiber plane it was still within the effective sampling region using the average of all measurements. By comparison, when the fluorophore was 2 mm out of plane using any of the measurement subgroups it was not within the effective sampling region (Figure 4.13). This was important for *in vivo* analysis, as the average of all measurements was used to examine EGF-IRDye fluorescence since it provided the most robust signal detection even if the tumor tissue was not directly in the fiber plane.

In conclusion, the transmission geometry based systems would be more useful for the detection of intracranial brain tumors than either of the reflectance based systems. The transmission systems could detect anomalies with physiologically relevant depths and contrast for *in vivo* detection of intracranial tumors. However, positioning of the tumor tissue within the fiber optic plane was critical, as both systems showed significant

decrease in signal detection when the fluorophore was not in the fiber plane. Due to the size of the tissue-fiber interface the single channel system was less affected by positional differences than the multichannel system for sizes relevant to the detection of murine glioma. To address the positional difficulty, the multichannel system was constructed with the capability to collect simultaneous magnetic resonance images and spectroscopy data, enabling structural guidance of the spectroscopy measurements [96].

Chapter 5 - Magnetic Resonance Imaging for the Visualization of Murine Glioma

5.1. Introduction

Magnetic Resonance Imaging (MRI) was used in this thesis work as a means to detect tumor presence, to verify signals collected via fluorescence spectroscopy. It was determined that although a multitude of MRI sequences were used, not all model tumors were able to be detected and visualized by the MRI. Both the 9L-GFP and U251 tumor models were easily detected by various MRI sequences. However, the U251-GFP tumor model did not always illustrate the same growth morphology, which was found to vastly affect the ability to detect and visualize the tumor by MR imaging. In this chapter, a summary of the contrast of the tumor tissue over the normal brain tissue for each tumor model is presented, along with receiver operating characteristic (ROC) analysis, followed by specific examples from each tumor model. Some possible explanations for the differences in MRI detection and visibility will also be discussed.

MRI and computed tomography (CT) are commonly used to detect brain abnormalities, including primary diagnosis of brain tumors. MR imaging is often superior to CT due to its increased soft tissue contrast and its ability to provide additional information about tumor complexity and heterogeneity through additional imaging sequences [37, 38]. Standard T1 and T2 spin echo imaging sequences are most commonly used for brain tumor detection. Brain tumors normally appear hypointense by T1 MRI and hyperintense by T2 MRI, which are used in combination to determine tumor size and location [106]. Rapidly proliferating brain tumors, such as glioblastomas, often cause break down of the blood brain barrier (BBB) [37], that can be visualized through

the use of the intravenous contrast agent gadolinium DTPA which provides hyperintense contrast in T1 weighted images. Additional information about the presence of edema, hemorrhage and necrosis in the tumor tissue can be obtained through specialized MRI sequences [37, 38] and biochemical information may be gained with localized MR spectroscopy.

MRI sequences which permit additional evaluation of tumor tissue characteristics and are often used to evaluate brain tumors including T2 fluid attenuated inversion recovery (FLAIR), proton density weighted, diffusion and T1 inversion recovery (IR) sequences [37, 38, 107]. The T2 FLAIR imaging sequence reduces signal from the cerebral spinal fluid permitting better evaluation of anatomy containing significant fluids [107], such as tumors which appear hyperintense, due to portions of edema, hemorrhage and necrosis. Proton density weighted imaging highlights differences in the number of magnetized protons per volume [107]. Brain tumors usually appear hyperintense by proton density weighted MRI, as rapidly proliferating tumor tissue is generally more cellular than normal brain tissue. Diffusion MRI is based on measurement of Brownian motion of water molecules contained within the tissue [43]. Regions of high tissue water mobility have greater signal loss than tissues where water mobility is inhibited. Images with varied diffusion weighting can be acquired so that the apparent diffusion coefficient (ADC) can be calculated, where low ADC corresponds to regions of increased density of structures that impede water movement. ADC images can be used as a measure of cellularity of the tissue, so similar to proton density images ADC images would show increased contrast in the region of the tumor tissue due to increased cellular density [106, 108, 109]. T1 IR MR imaging enables increased contrast to be seen between tissues with

different T1 relaxation times [107]. Since brain tumors usually appear hypointense by T1 spin echo images, changing the inversion time used could increase the contrast seen between the normal brain and the tumor tissue.

5.2. Magnetic Resonance Imaging Methods

Most of the MR imaging for this thesis was completed using a Philips 3T MRI scanner, with a research rodent coil insert designed specifically for imaging mice and rats (Figure 5.1). Various MRI sequences were used, which evolved in complexity over time as difficulty with brain tumor visualization was encountered. T1 turbo spin echo (TSE) contrast enhanced (CE) with gadolinium DTPA and T2 TSE sequences were routinely used to visualize brain structure and vascular volume changes due to tumor growth. T1 TSE images were collected before and after gadolinium administration via an IP catheter, allowing T1 difference images to be calculated and used to increase the ability to visualize gadolinium uptake. Additional sequences were adapted for mouse imaging from those provided as standard sequences in the Philips software. The most successful of these sequences included T2 fluid attenuated inversion recovery (FLAIR), T1 inversion recovery (IR), proton density weighted turbo spin echo (PDW) and T1 fast field echo (FFE). Parameters such as slice thickness, field of view and the size of the reconstruction matrix were varied and tested to allow acquisition of the qualitatively best images.

Analysis of MRI visibility of the three brain tumor models (9L-GFP, U251 and U251-GFP) discussed in chapter 2 was completed by measuring the intensity in a region of interest in the tumor and a similar region of interest in the normal, contralateral side of

the brain. The tumor to normal tissue contrast was calculated using this analysis for at least 5 MRI slices per imaging sequence. The tumor to normal tissue ratio intensity was used to calculate ROC curves so that tumor detection could be compared between different tumor lines and between difference MRI sequences. All MR images were compared to *ex vivo* H+E sections and GFP scans when available, to examine the relationship between *in vivo* and *ex vivo* visualization. Where MRI visualization was difficult *ex vivo* H+E sections and GFP scans were carefully examined for the presents of tumor tissue and to determine if any subtle abnormalities seen by MRI could be correlated to tumor location and/or size.

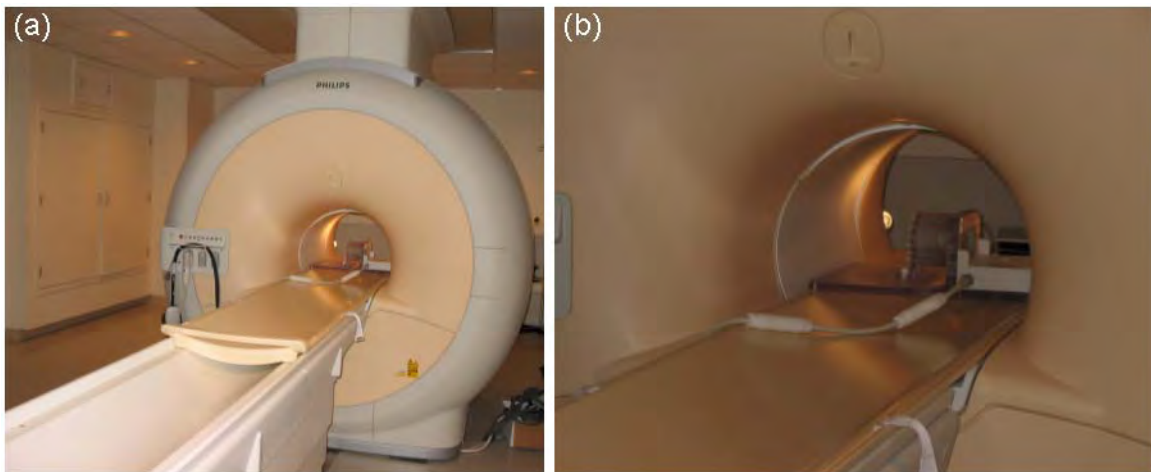


Figure 5.1 – (a) A photograph of the Philips 3T magnetic resonance imaging system with research rodent coil insert in magnet bore. (b) A close-up photograph of research rodent coil in magnet bore.

5.3. Magnetic Resonance Imaging Contrast & Tumor Detection

Conventional T1 TSE CE and T2 TSE imaging sequences were used routinely for tumor visualization as they were found to readily highlight the 9L-GFP and U251 brain tumor models (mean tumor to normal tissue contrast T1 TSE CE: 9L-GFP = 1.41, U251

= 1.30, Control = 0.98, mean tumor to normal tissue contrast T2 TSE: 9L-GFP = 1.26, U251 = 1.46, Control = 0.97) as compared to control mice (p-values ≤ 0.001).

Interestingly, when the U251 cell line was stably transfected with GFP, as described in chapter 2, it had three *in vivo* growth morphologies, two of which were largely invisible by T1 TSE CE or T2 TSE MRI (Figure 5.2(a) & (b)). The three growth morphologies of the U251-GFP tumor model were diffuse growth in one hemisphere of the brain, growth in the ventricle space and growth as a bulk tumor at the bottom of the brain invading the cranium. The U251-GFP tumor growing as a bulk mass at the bottom of the brain was easily visible by T1 TSE CE and T2 TSE MRI as can be see in Figure 5.2(a) and (b), where this growth morphology was labeled U251-GFP bulk (mean tumor to normal tissue contrast U251-GFP bulk: T1 TSE CE = 1.34, T2 TSE = 1.24). Two sample t-tests yielded p-values ≤ 0.001 , illustrating a statistically significant difference between the control mice and the U251-GFP mice with bulk tumor growth for both T1 TSE CE and T2 TSE MRI. However, when the U251-GFP tumor grew either diffusely in one hemisphere of the brain or in the ventricle space it became difficult to visualize *in vivo* and could only be readily quantified when compared with *ex vivo* H+E sections and GFP images. These two growth morphologies were grouped into a single bar in Figure 5.2, labeled U251-GFP diffuse. Aside from a few animals with slightly higher than average contrast the U251-GFP mice with these two growth morphologies had very similar tumor to normal tissue contrast as compared to the control mice by T1 TSE CE and T2 TSE MRI (mean tumor to normal tissue contrast U251-GFP diffuse: T1 TSE CE = 1.04, T2 TSE = 1.00).

The difference in visibility was more easily assessed by ROC curves (Figure 5.2(c) & (d)) which were constructed using different intensity threshold levels on the tumor to normal tissue contrasts for each tumor type. As the intensity threshold is changed the true positive fraction (TPF) and the false positive fraction (FPF) can be calculated, where TPF is synonymous with the sensitivity of the imaging modality and FPF is representative of 1 minus the specificity of the imaging modality. The area under the curve (AUC) for each tumor type and imaging sequence can be calculated and used as a direct measure of sensitivity and specificity of the imaging modality. An AUC of 1 indicates that the imaging modality has 100% sensitivity and specificity for tumor detection while an AUC of 0.5 indicates there is only 50% sensitivity and specificity for detection, which is equivalent to random guessing of tumor status. The TPF and the FPF values were plotted for both T1 TSE CE and T2 TSE MR images. T1 TSE CE and T2 TSE MRI had perfect ROC curves for the 9L-GFP, U251 and U251-GFP tumors growing as a bulk mass where the AUC was equal to one indicating that tumors could be detected with 100% specificity and sensitivity at all thresholds (Figure 5.2(c) & (d)). In contrast, the U251-GFP tumors growing either diffusely or in the ventricle space were difficult to detect by both T1 TSE CE and T2 TSE MRI, as illustrated by the ROC curves in Figure 5.2(c) and (d). T1 TSE CE MRI provided slightly better detection (AUC = 0.80) than T2 TSE MRI (AUC = 0.67) of diffusely growing U251-GFP tumors.

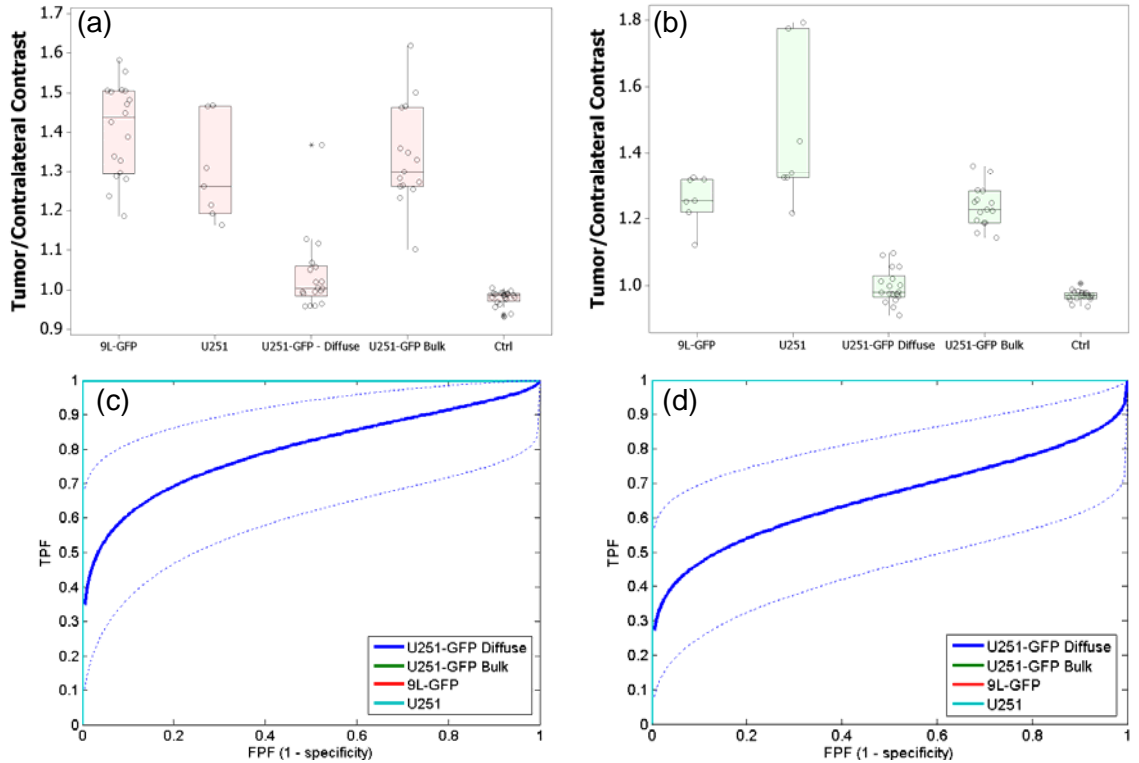


Figure 5.2 – Tumor to contralateral normal tissue contrast values are shown for (a) T1 TSE CE MRI and (b) T2 TSE MRI of the 9L-GFP, U251 and U251-GFP tumors, which grew either diffusely in the brain or as a bulk tumor. Control mice left brain hemisphere to right brain hemisphere ratio values are shown for comparison. Receiver operator characteristic (ROC) curves are shown for (c) T1 TSE gadolinium enhanced MRI and (d) T2 TSE MRI of 9L-GFP, U251 and both the diffuse and bulk tumor growth pattern of the U251-GFP tumor model. TPF is defined as the true positive fraction and FPF is defined as the false positive fraction.

After difficulty with MRI detection of the U251-GFP tumors growing diffusely in one hemisphere of the brain or growing in the ventricle space, additional MRI sequences were tested to try to increase the ability to detect these tumors *in vivo*. A number of MR sequences were experimented with on multiple mice growing these two morphologies of U251-GFP tumors. The tumor to normal tissue contrast of the most successful sequences can be seen in Figure 5.3, where the two morphologies of the U251-GFP which were

difficult to visualize by conventional MRI were grouped into a single bar in the graphs, labeled U251-GFP diffuse. T1 difference imaging was used for better visualization of gadolinium uptake, and readily illustrated contrast in the U251-GFP bulk tumors, as can be seen in Figure 5.3(a). A few of the mice in the U251-GFP diffuse group had tumor to normal tissue contrast greater than that seen in the control group (mean tumor to normal tissue contrast: U251-GFP diffuse = 1.41, Control = 1.08) using T1 difference imaging, however there was not a statistically significant difference between the two groups (p-value = 0.09). T2 FLAIR imaging was used to examine T2 signal with the signal from the cerebral spinal fluid suppressed, allowing for better visualization of any fluid signal caused by the tumor tissue. Similar to T1 difference imaging, T2 FLAIR MRI showed significant tumor to normal tissue contrast (mean tumor to normal tissue contrast: U251-GFP diffuse = 1.05, U251-GFP bulk = 1.32, Control = 0.98) between the control group and the U251-GFP bulk tumor group (p-value < 0.0001), while there was not a significant difference between the control group and the U251-GFP diffuse group (p-value = 0.146) (Figure 5.3 (b)). T1 inversion recovery (IR) sequences can be used to increase contrast between tissues which have different T1 relaxation times. T1 IR sequences were examined with varied inversion recovery times of 100, 200, 400 and 800 ms, with 200 and 400 ms providing the best qualitative contrast. Similar to the previous sequences, the U251-GFP bulk tumor was readily visible by T1 IR over the control mice (p-value < 0.0001) while the U251-GFP diffuse tumor was not significantly different (mean tumor to normal tissue contrast: U251-GFP diffuse = 0.98, U251-GFP bulk = 1.15, Control = 0.99) from the control (p-value = 0.946) (Figure 5.3(c)). However, unlike the previous sequences the variance in the U251-GFP diffuse group was large compared to

that seen in Figure 5.3(a) and (b) even though the mean was similar to that of the control. Proton density weighted (PDW) TSE MRI was examined to determine if proton density could be used to measure contrast between tumor tissue and normal tissues. As seen with the previous sequences, the U251-GFP bulk tumor was significantly different from the control mice (p -value < 0.0001), while the U251-GFP diffuse tumor was not (p -value = 0.408) (mean tumor to normal tissue contrast: U251-GFP diffuse = 1.04, U251-GFP bulk = 1.20, Control = 1.02).

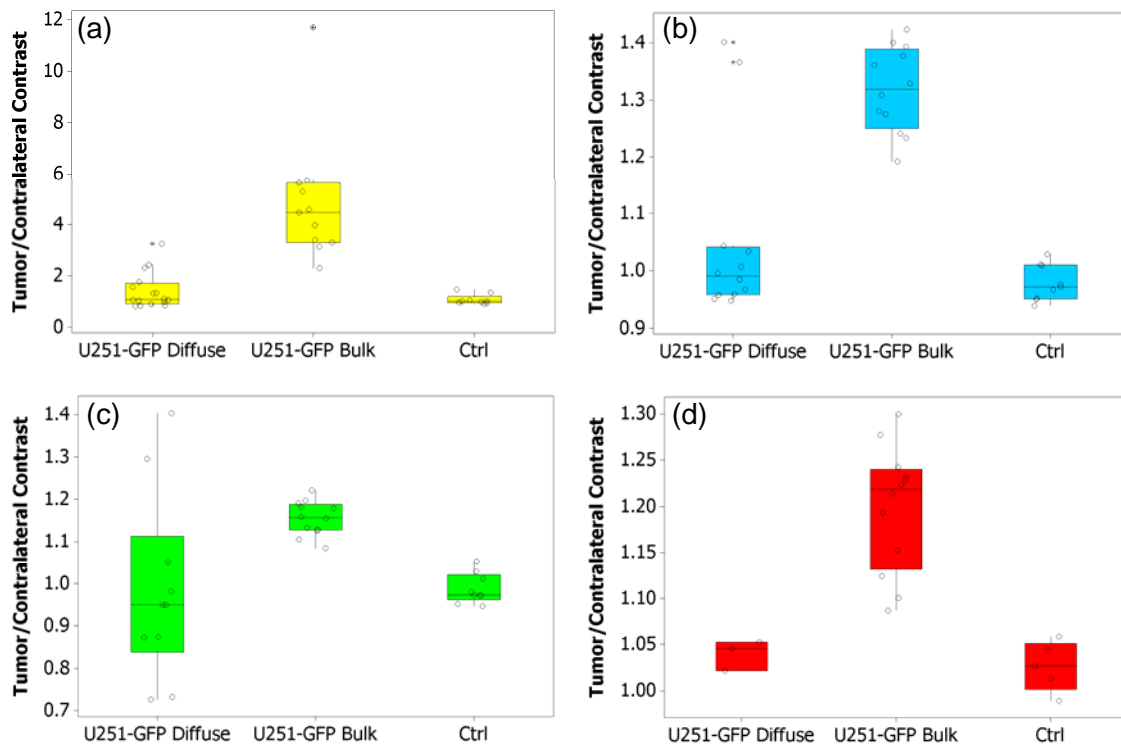


Figure 5.3 – Additional MRI sequences were used to detect the U251-GFP diffuse growing tumors which were not readily visible by conventional MRI, including (a) T1 difference imaging, (b) T2 FLAIR (fluid attenuated inversion recovery), (c) T1 IR (inversion recovery), and (d) PDW (proton density weighted) TSE. For each type of imaging sequence the U251-GFP tumors growing diffusely in one hemisphere or in the ventricle space (labeled U251-GFP Diffuse) and the U251-GFP tumors growing as a bulk mass towards the bottom of the brain (labeled U251-GFP Bulk) were compared with one another as well as with sham surgery implanted control mice.

As shown in Figure 5.2 and Figure 5.3, MR imaging could be used for tumor identification for the 9L-GFP and U251 brain tumor models as well as the bulk tumor growth morphology of the U251-GFP tumor. However, conventional MRI as well as more complicated sequences including T1 difference imaging, T2 FLAIR, T1 IR and PDW TSE did not provide significantly different tumor to normal tissue contrast between control mice and the U251-GFP tumor growing diffusely or in the ventricle space. This data was compiled in Figure 5.4(a), where a ratio of 1 for tumor to normal tissue contrast indicated zero contrast between tumor tissue and normal tissue. Some MRI sequences showed better tumor to normal tissue contrast than others, however none of the sequences were able to identify tumor tissue in every mouse imaged, even though all mice shown in Figure 5.4(a) had tumors present by *ex vivo* analysis. An ROC curve was constructed to compare the sensitivity and specificity of each of the MRI sequences. Figure 5.4(b) illustrates that the T1 TSE CE (AUC = 0.80) and T1 fast field echo (FFE) MRI (AUC = 0.81) had the best sensitivity and specificity of the MRI sequences used, while the T1 IR (AUC = 0.38) had the worst sensitivity and specificity. Due to the continued difficulty with MRI identification of the diffuse U251-GFP tumors, multiple MRI sequences were run on each animal and used together to determine if tumors were present, although *ex vivo* verification was often required for assurance of tumor presence.

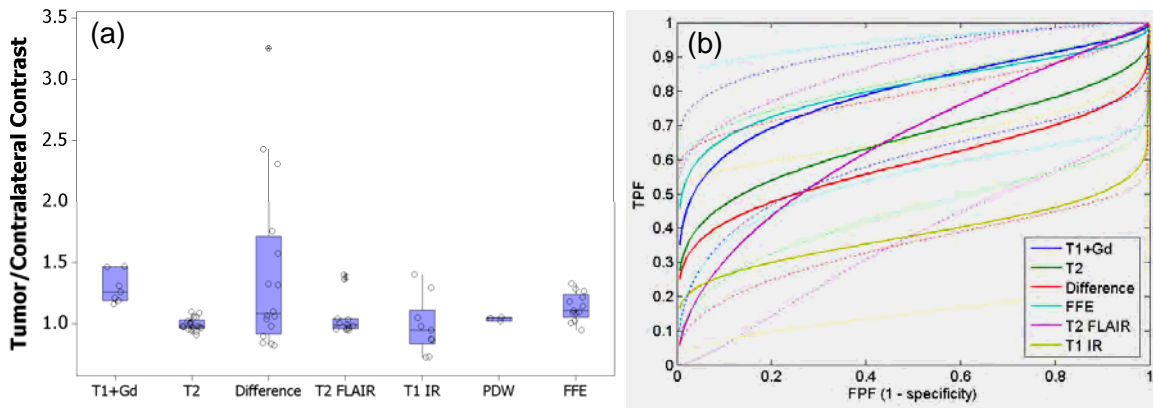


Figure 5.4 – (a) Tumor to normal tissue contrast for the U251-GFP tumor growing in the ventricle space or diffusely in one hemisphere of the brain for T1 TSE CE, T2 TSE, T1 difference imaging, T2 FLAIR, T1 IR, PDW TSE and T1 fast field echo (FFE) MRI. (b) ROC analysis for the U251-GFP tumor morphologies with low MRI visibility as compared to control mice is shown for all imaging sequences illustrated in (a).

5.4. Case Studies: Sample MRI & *Ex Vivo* Verification

Representative MR images from the 9L-GFP, U251 and different growth morphologies of the U251-GFP were compared to H+E sections as well as any available GFP images. 9L-GFP tumor-bearing mice were scanned with some of the additional MRI sequences tested on the U251-GFP mice to determine how tumor tissue contrast would appear in a mouse with a tumor that was readily visible by MRI. A Varian small bore 7T MRI was also used to compare images of 9L-GFP tumors with diffusely growing U251-GFP tumors to determine if higher field strength and smaller bore size could provide better tumor contrast resolution. Images from the 7T were not included in the quantification shown in Figure 5.2 - Figure 5.4, because a similar difficulty to that seen with the 3T was found in detection of the diffusely growing U251-GFP tumor morphology. The 7T MRI was also used to collect diffusion images and T2 images at multiple echo times so that T2 maps could be constructed. However, these imaging

sequences did not illustrate better qualitative contrast than any of the imaging sequences used on the 3T MRI. *Ex vivo* H+E images were compared to the MR images to determine if a pathological explanation for this difference seen in MRI visibility was possible. Example *in vivo* and *ex vivo* images of representative mice with 9L-GFP, U251 and the different growth morphologies of the U251-GFP tumors will be shown and discussed as follows.

5.4.1. 9L-GFP Tumor-Bearing Mice

5.4.1.1. Case 1: T1 TSE CE MRI for 9L-GFP Tumor Detection

All intracranially implanted 9L-GFP tumors grew in large masses in the mouse brain and were easily distinguishable from normal tissue by MRI as well as by *ex vivo* H+E and GFP images. Figure 5.5 illustrates the correlation between *in vivo* T1 TSE gadolinium enhanced MRI and *ex vivo* H+E and GFP images of the corresponding brain slice. At higher magnification it was evident that the tumor was rapidly proliferating, illustrated by mitotic figures (Figure 5.5(f) and (h)). Some edema was noticeable at 40x magnification, but overall the tumor tissue and surrounding normal brain tissue appeared healthy.

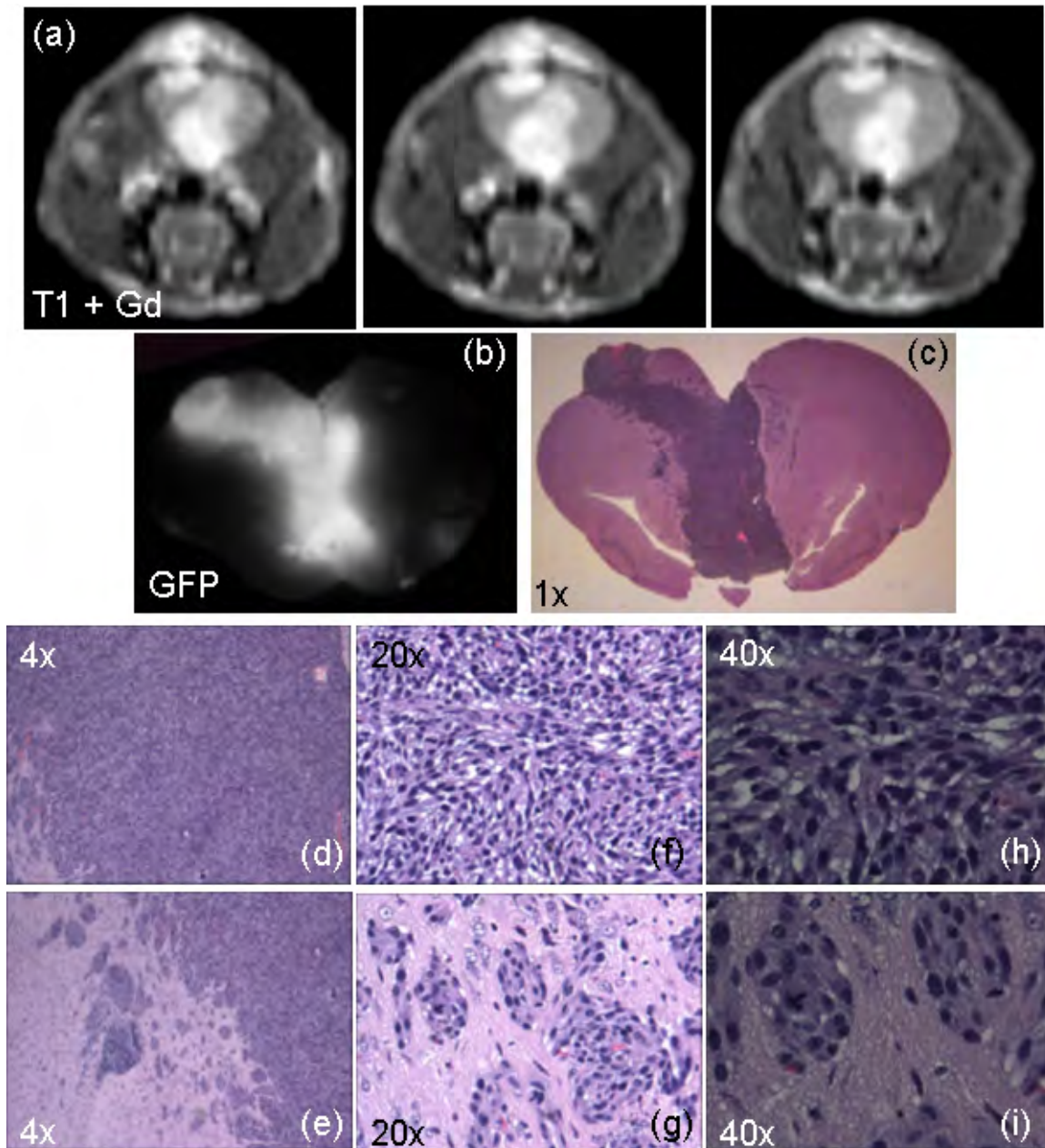


Figure 5.5 – *In vivo* and *ex vivo* images of a representative 9L-GFP tumor-bearing mouse with healthy tumor tissue and surrounding brain tissue are shown. (a) T1 TSE CE MRI of the three slices most representative of the brain slice shown in the *ex vivo* (b) GFP image and (c) H+E 1x magnification image. Images at (d) 4x, (f) 20x and (h) 40x magnification of the center of the tumor illustrated healthy cells. Images at (e) 4x, (g) 20x and (i) 40x of the periphery of the tumor illustrated both healthy tumor tissue and adjacent normal brain tissue.

5.4.1.2. Case 2: T2 TSE MRI Correlation to 9L-GFP Tumor Edema

Some of the 9L-GFP tumor-bearing mice had all healthy tumor tissue, as seen in Figure 5.5, however many of the 9L-GFP tumor-bearing mice had tumors that could be divided into a healthy, rapidly proliferating, invasive portion and a slow growing portion with significant edema. A representative example of this type of 9L-GFP tumor is illustrated in Figure 5.6, where the proliferative, healthy tumor tissue was growing at the periphery of the tumor and significant edema was visible at the center of the tumor (Figure 5.6(g) & (h)). The three T2 TSE and T1 TSE CE MRI slices that most closely correspond to the *ex vivo* brain slice showed enhancement in the area of the tumor tissue. However, in the T1 TSE images the gadolinium uptake was not homogeneous, with the center of the tumor showing less enhancement than the edges of the tumor. This observation was correlated to the growth pattern seen in the H+E sections where the center of the tumor had significant edema in comparison to the periphery of the tumor (Figure 5.6(a) & (g) – (j)). The T2 TSE images, which derive their contrast from tissue fluid content, had increased contrast at the center of tumor as compared to the T1 TSE CE MR images. Figure 5.6(a) and (b) also showed that some of the 9L-GFP cells were growing in the ventricle space, which was not visible by T1 TSE CE MRI, but was readily visible by T2 MRI, where the ventricles showed considerable enlargement as well as bright enhancement on both sides of the brain. The growth of the 9L-GFP tumor cells in the ventricle space was verified by *ex vivo* GFP and 1x magnification H+E images which can be seen in Figure 5.6(c) and (d).

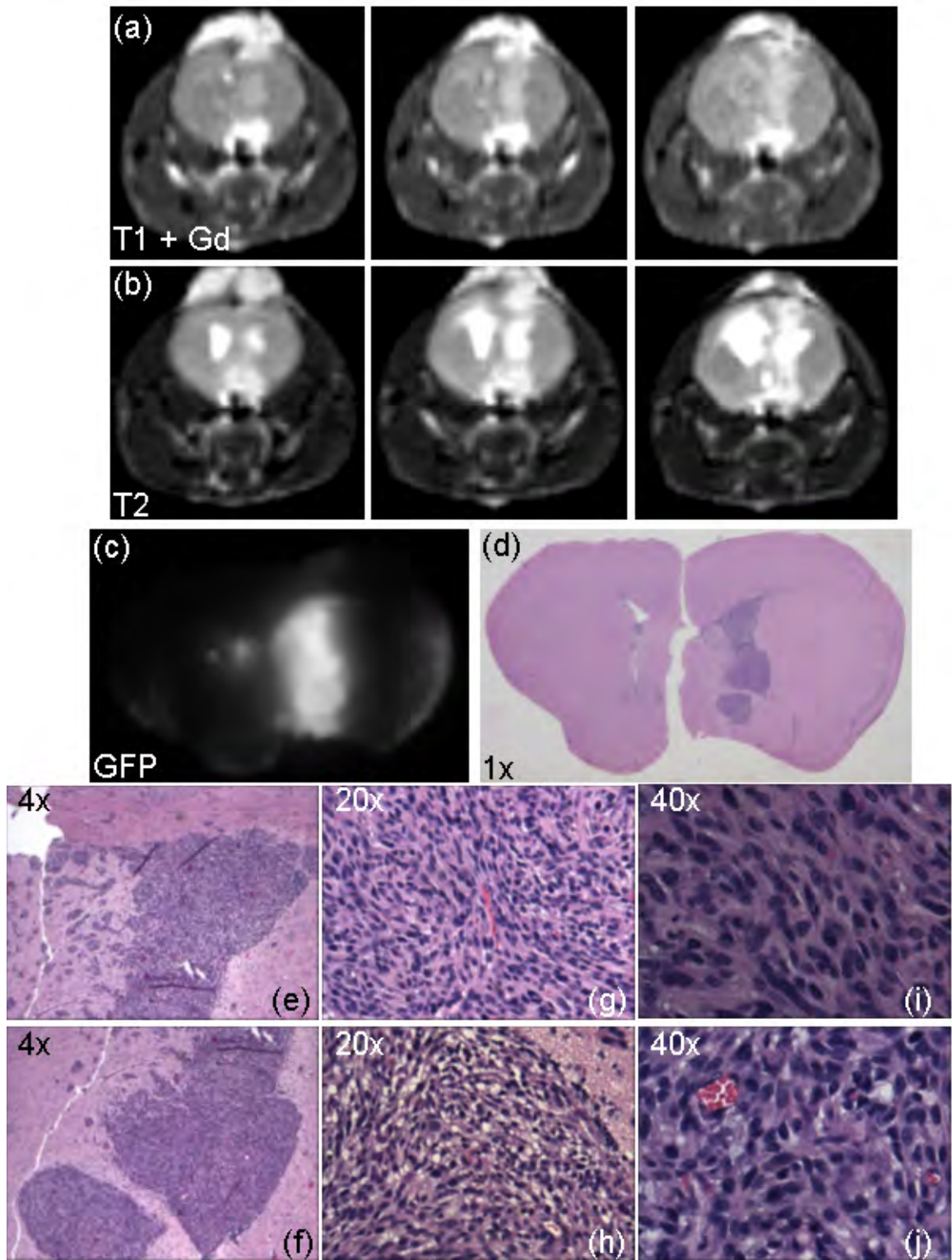


Figure 5.6 – *In vivo* and *ex vivo* images of a representative 9L-GFP tumor-bearing mouse with both proliferative and slow growing tumor tissue shown. Three representative slices

of (a) T1 TSE CE and (b) T2 TSE MRI, which most closely matched the *ex vivo* (c) GFP and (d) H+E 1x magnification brain slice are shown. Images at (e) 4x, (g) 20x and (i) 40x magnification of the quickly proliferating edge of the tumor are shown. Images at (f) 4x, (h) 20x and (j) 40x magnification of the slower growing center of the tumor are shown.

5.4.1.3. Case 3: 9L-GFP Visibility by T1 IR, T2 FLAIR & T1 Difference MRI

9L-GFP tumor-bearing mice were imaged with T1 IR, T2 FLAIR, T1 FFE and T1 difference imaging to ensure that these MR imaging sequences allowed for tumor visualization, since they were used to try to increase the tumor to normal tissue contrast of the diffusely growing U251-GFP tumors. Representative sample T1 IR and T2 FLAIR MR images from a 9L-GFP tumor-bearing mouse can be seen in Figure 5.7(a) and (b), where the three slices that were most representative of the *ex vivo* brain slice shown in Figure 5.7(c) and (d) by GFP and 1x magnification H+E. The 9L-GFP tumor had bright contrast in the T2 FLAIR image, corresponding to increased fluid in the tumor tissue over the normal brain tissue (Figure 5.7(a)). This 9L-GFP tumor tissue also had a different T1 relaxation time than the normal brain tissue as can be seen in Figure 5.7(b), where the tumor tissue had bright contrast compared to the normal brain tissue. Thus, both the T2 FLAIR and T1 IR sequences were able to delineate tumor tissue from normal tissue when a bulk tumor such as intracranial 9L-GFP was examined. The pathology of this tumor was similar to that illustrated in Figure 5.6, where two regions of the tumor were visible including an edema containing region and a region of proliferative tumor. In this example, there was not as much spatial distinction between these two regions, as regions with and without edema existed throughout the tumor tissue (Figure 5.7(g) – (j)).

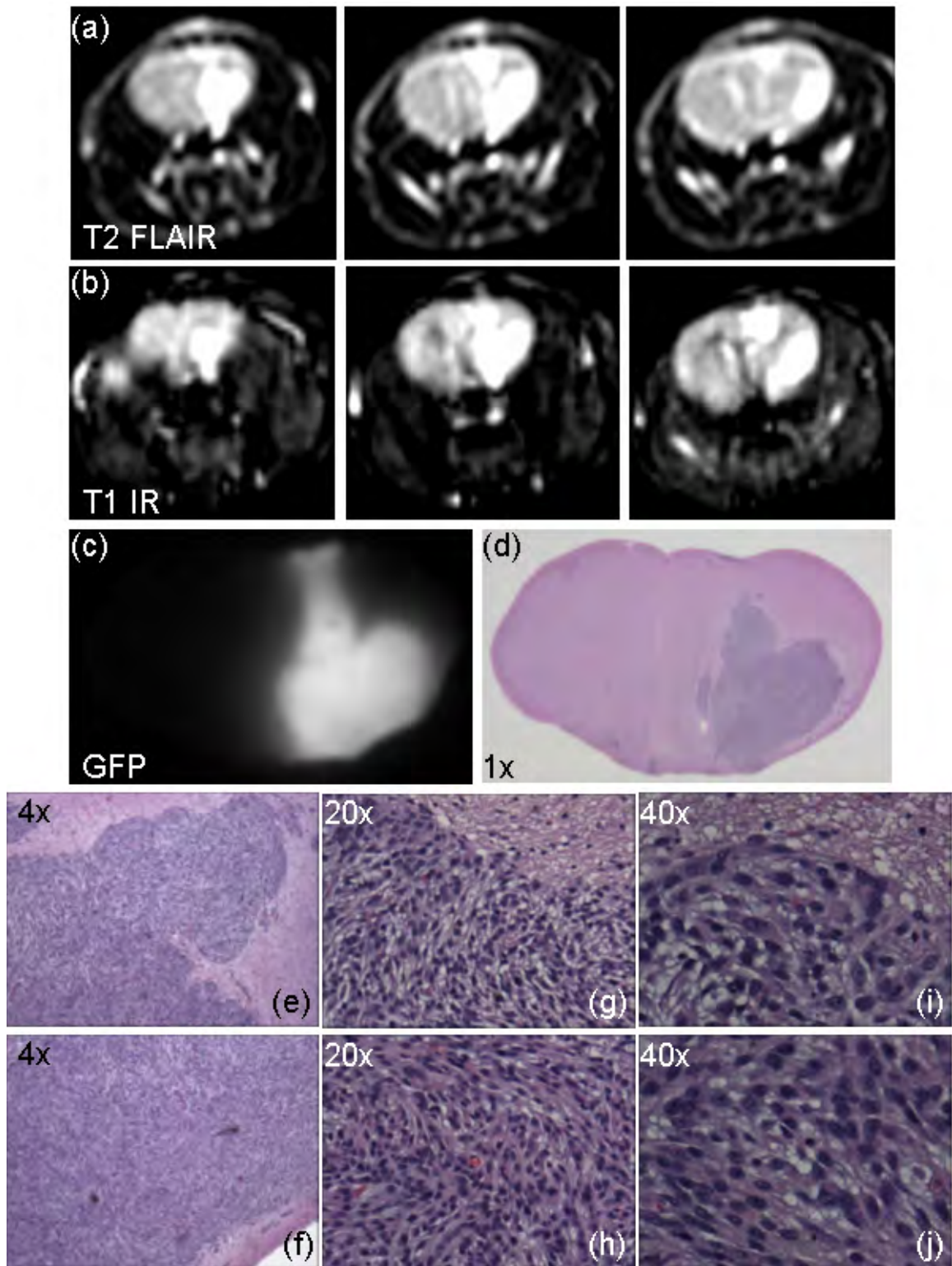


Figure 5.7 – *In vivo* and *ex vivo* images of a representative 9L-GFP tumor-bearing mouse are shown. Three representative slices of (a) T2 FLAIR and (b) T1 IR MRI, which most

closely correlate to the *ex vivo* (c) GFP and (d) H+E 1x magnification brain slice. Images of the periphery of the tumor are shown at (e) 4x, (g) 20x and (i) 40x magnification. Images of the center of the tumor are shown at (f) 4x, (h) 20x and (j) 40x magnification.

5.4.1.4. Case 4: 3T vs. 7T MRI for 9L-GFP Tumor Detection

A final example 9L-GFP mouse is illustrated in Figure 5.8 to allow for direct comparison of 3T and 7T MR images of the same mouse. The pathology of this mouse also showed an edema containing region, which corresponded to the region growing in the normal brain tissue (Figure 5.8(k), (m) & (o)) and a proliferative region which corresponded to the region growing beneath the brain (Figure 5.8(j), (l) & (n)). In the proliferative region of the tumor mitotic figures and vessels were visible at 20x and 40x magnification (Figure 5.8(l) & (n)). The growth pattern of healthy tumor beneath the brain and edema containing tissue within the normal brain tissue was well correlated to enhancement seen in the 3T MR images. The corresponding T1 TSE CE MRI slice showed gadolinium uptake at the base of the brain, but not in the center of the brain (Figure 5.8(a)). The T2 TSE MR image showed heterogeneous fluid contrast enhancement, with bright contrast in the region of the tumor growing within normal brain, corresponding to the edema seen by H+E (Figure 5.8(b)). The T2 FLAIR image showed bright contrast throughout the tumor tissue (Figure 5.8(c)) as was seen in the previous example (Figure 5.7(a)). MR images collected on the 7T were examined to determine if tumor tissue contrast resolution would be improved by the increased field strength and smaller bore size. However, as can be seen by comparing T1 and T2 images from both magnets, the tumor was more easily visualized by the 3T than the 7T MRI. Diffusion and T2 maps were also reconstructed from data collected on the 7T and are

illustrated in Figure 5.8(f) and (g) in black and white as well as false color. The intensity scale for ADC maps ranged from 0 – 0.1 with black or blue for the false color scale representing the low ADC values and white or red for the false color scale representing the high ADC values. The intensity scale for the T2 maps ranged from 20 – 50 with black or blue for the false color scale representing the low intensities and white or red for the false color scale representing the high intensities. Due to significant noise in the images, all but the brain was windowed from these images for display purposes. The image reconstructions of ADC and T2 maps for the 7T MRI did not appear to provide increased ability to visualize tumor tissue as compared to images collected on the 3T MRI.

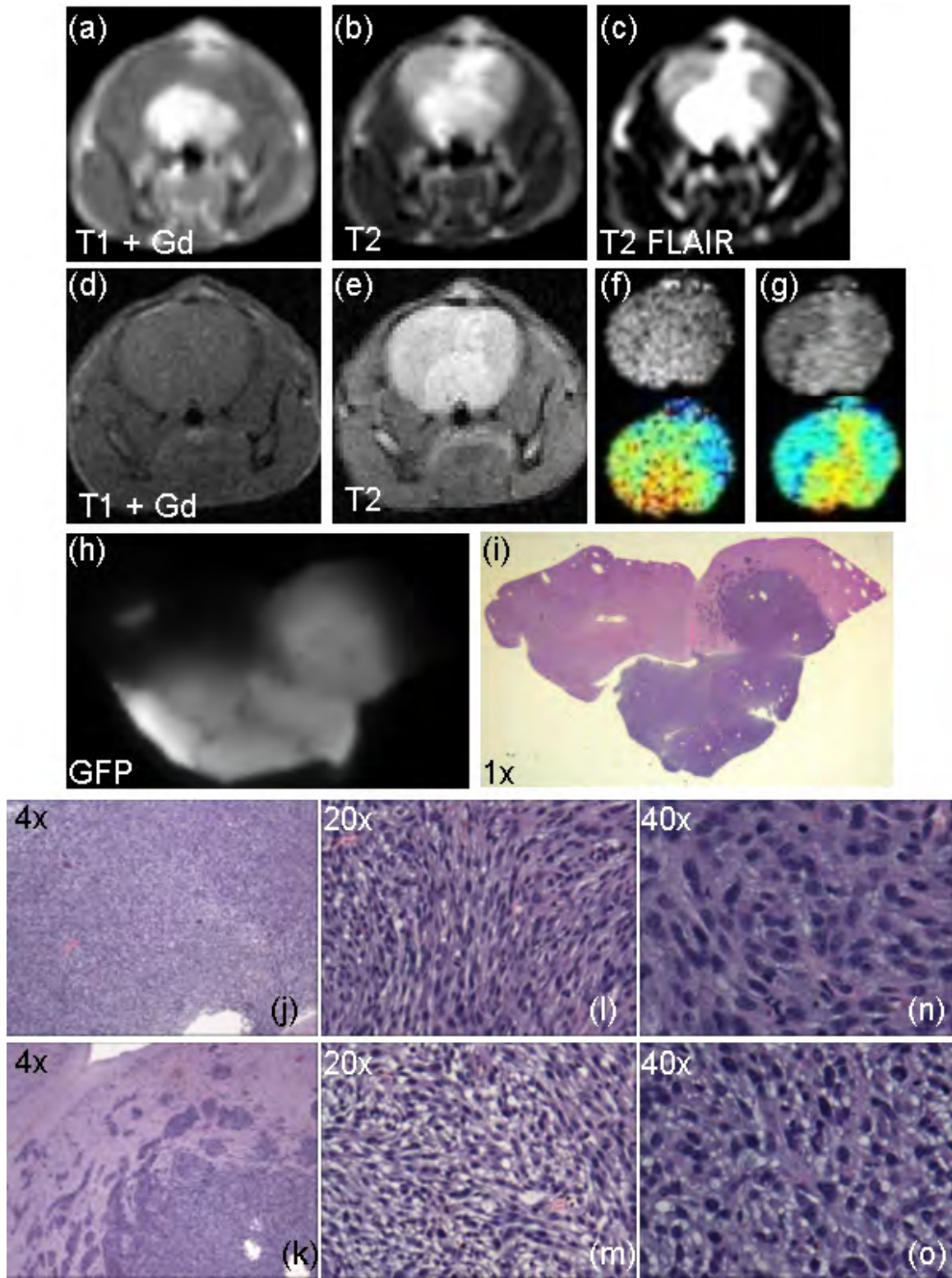


Figure 5.8 – *In vivo* and *ex vivo* images of a representative 9L-GFP tumor-bearing mouse with slow growing tumor tissue within the normal brain and proliferative tumor tissue

growing beneath the brain. 3T MRI (a) T1 TSE CE, (b) T2 TSE and (c) T2 FLAIR are illustrated. For comparison 7T MRI (d) T1 TSE CE, (d) T2 TSE, (e) T2 map and (f) diffusion images in black and white as well as false color. Due to the noise in the T2 maps and diffusion images all but the brain was windowed from image. For all MR images, the image slice that most closely correlated to the *ex vivo* (h) GFP and (i) H+E 1x magnification brain section was shown. H+E images of the tumor growing beneath the brain are shown at (j) 4x, (l) 20x and (n) 40x magnification. H+E images of the tumor tissue growing within the normal brain are shown at (k) 4x, (m) 20x and (o) 40x magnification.

5.4.2. U251 Parent Line Tumor-Bearing Mice

U251 parent line tumors were also easily visualized via T2 TSE and T1 TSE CE MRI, as will be shown in two representative U251 example mouse image sets. Border delineation was more difficult for the U251 tumors by MRI as compared to the 9L-GFP tumors, which illustrated sharp borders between enhancing regions and normal brain tissue (Figure 5.5 – Figure 5.8). Many of the U251 tumor-bearing mice had tumor tissue which grew in a bulk mass towards the bottom of the brain, as will be illustrated in one of the examples shown here. The U251 tumors showed considerably more hemorrhage than the 9L-GFP tumors, which corresponded to heterogeneous contrast by T2 TSE MRI. The tumor pathology of the U251 tumors was also significantly different from that of the 9L-GFP tumors and its relationship to MRI visibility will be examined in detail as follows.

5.4.2.1. Case 1: T1 TSE CE & T2 TSE MRI Necessary to Characterize U251 Tumors

The U251 tumor-bearing mouse illustrated in Figure 5.9, had two distinct portions to its tumor which included a portion growing towards the outside of the normal brain tissue (Figure 5.9(c)) and a portion growing invasively within the normal brain (Figure

5.9(d)). These two regions are illustrated as two separate H+E images at 1x magnification because the portion of the tumor growing outside the brain was invading the cranium and was inadvertently detached from the brain tissue upon removal from the cranium. Both of these tumor regions were visible by T1 TSE CE MRI, as a region of bright enhancement was visible on the right side of the brain corresponding to the bulk tumor tissue and a less intense region of enhancement was visible towards the center of the brain corresponding to the tumor growing invasively in the brain (Figure 5.9(a)). The T2 TSE MR images showed the tumor invading the normal brain contained more fluid than the bulk tumor invading the cranium, since higher contrast was visible toward the center of the brain (Figure 5.9(b)). The border of the bulk tumor was well defined by the T1 TSE gadolinium enhanced images; however it was more difficult to determine the border of the portion invading the normal brain tissue. T2 TSE images also showed tumor presence, but delineation of tumor borders was similarly difficult.

The H+E slice of the tumor tissue invading the normal brain showed a significant hemorrhage visible on the right side of the brain slice (Figure 5.9(d)), corresponding to the increased fluid seen by T2 TSE MRI. Magnified images of this section illustrated considerable vasculature and many mitotic figures which were visible at 20x magnification (Figure 5.9(g)). Some edema was present in this portion of the tumor as can be seen at 40x magnification of the H+E slice (Figure 5.9(j)); although much less edema was present than seen in the 9L-GFP tumors (Figure 5.6 – Figure 5.8). The bulk tumor which grew at the base of the brain and invaded the cranium shown at 1x and 4x magnification where the sample was entirely tumor tissue except the pink portions, which

were bone that had been infiltrated by the tumor (Figure 5.9(c) & (e)). H+E images at 20x and 40x magnification of the bulk tumor illustrated the invasion of the tumor into the cranium (Figure 5.9(g) & (i)).

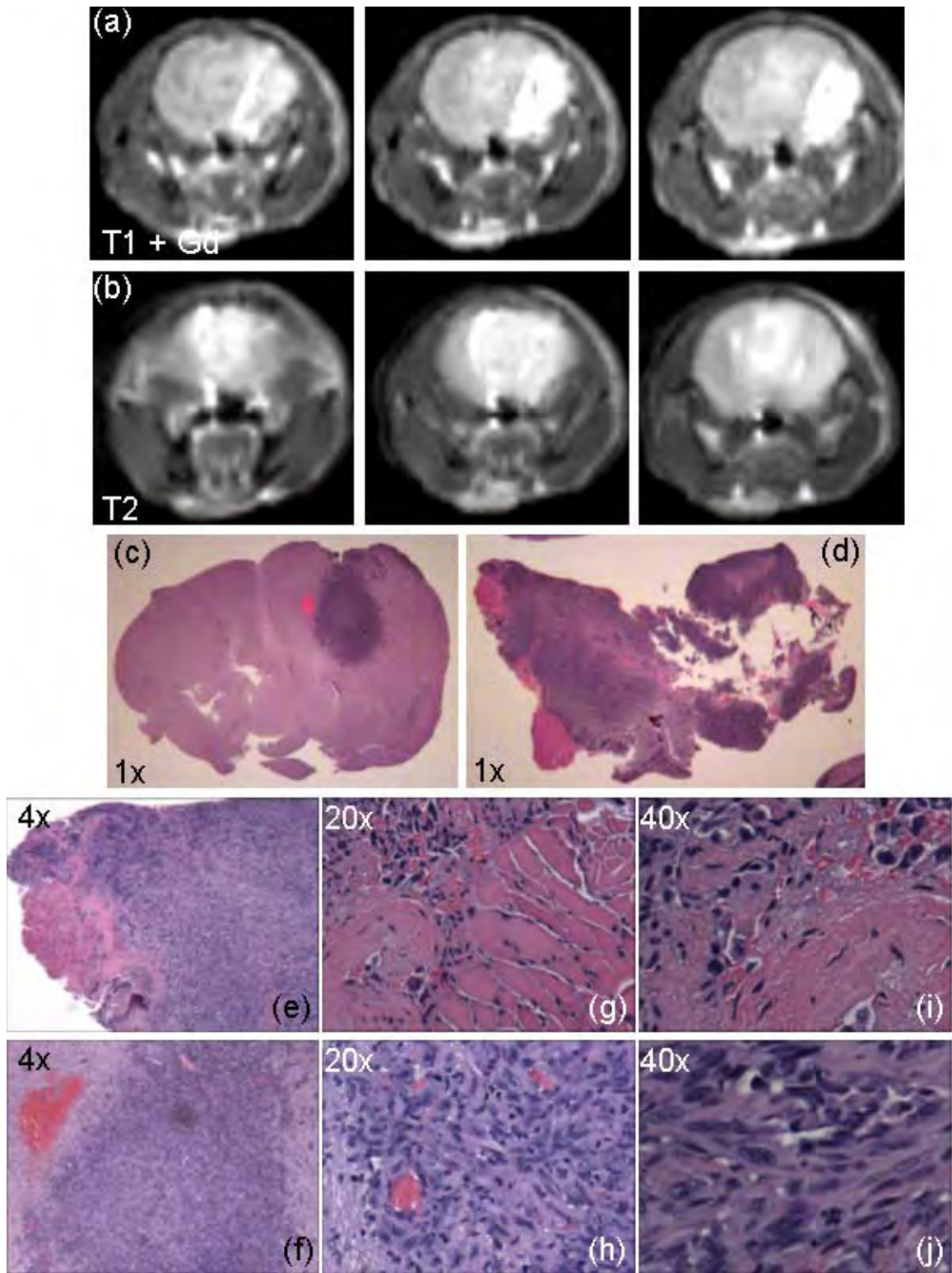


Figure 5.9 – *In vivo* and *ex vivo* images of a representative U251 tumor-bearing mouse with tumor tissue growing within the normal brain and beneath the brain, invading the

cranium. Three representative slices of a (a) T1 TSE CE and (b) T2 TSE MRI are shown which most closely correlate to the *ex vivo* H+E 1x magnification brain slices shown for (c) the tumor tissue invading the normal brain and (d) the bulk tumor which was separated from the brain upon removal from the cranium. H+E images of the bulk tumor are shown at (e) 4x, (g) 20x and (i) 40x magnification. H+E images of the tumor invading the normal brain are shown at (f) 4x, (h) 20x and (j) 40x magnification.

5.4.2.2. Case 2: U251 Tumor Border Delineation Difficult by MRI

The 9L-GFP tumor-bearing mice had little visible immune response by the normal brain to the tumor tissue, in contrast, the U251 tumor-bearing mice showed a significant immune response to the tumor tissue which was visualized through the presence of lymphocytes and macrophages in the H+E images. An example U251 tumor-bearing mouse is shown in Figure 5.10, where significant immune response was visible when the H+E image was examined at 20x and 40x magnification in the form of lymphocytes (Figure 5.10(f), (g), (i) & (j)), which were even visible in the cross section of a blood vessel (Figure 5.10(i)). This U251 tumor grew as an infiltrative mass, which was invading the normal brain tissue (Figure 5.10(c)). The vasculature supporting the tissue was readily visible by H+E staining and can be seen in both the 1x and 4x magnification images (Figure 5.10(c) & (d)). Similar to the previous example (Figure 5.9), this tumor also had a large area of hemorrhage. The T1 TSE CE MRI of this U251 tumor was more homogeneous than that seen in Figure 5.9, which was supported by the increased vasculature visible in the H+E image. Similar to the example seen in Figure 5.9, the tumor borders were not as clearly delineated as in the 9L-GFP tumor-bearing mice. The T2 TSE images showed contrast in the area correspond to the contrast enhancing portion of the T1 TSE images, with bright contrast in a similar region to that of the hemorrhage seen by H+E.

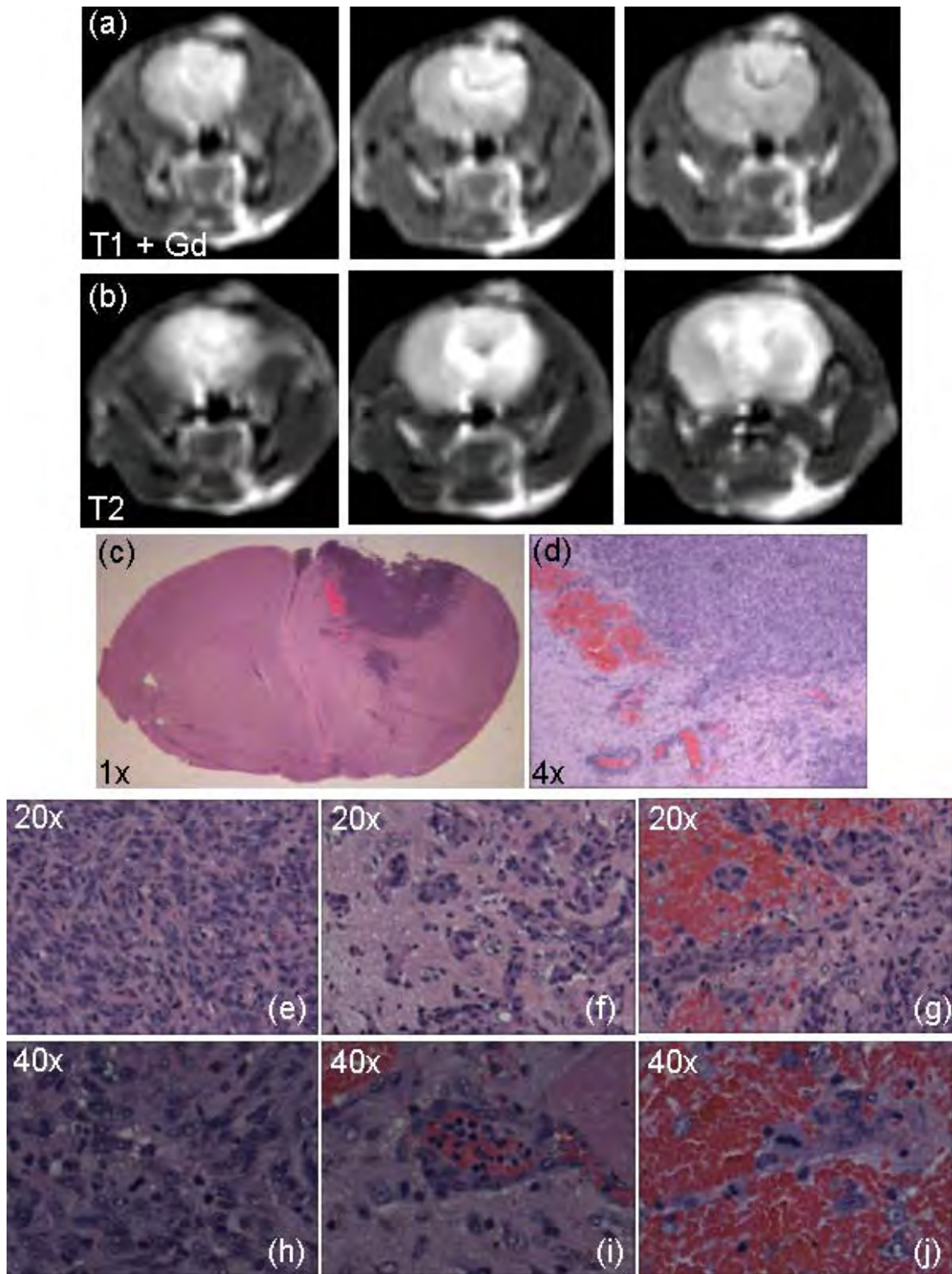


Figure 5.10 – *In vivo* and *ex vivo* images of a representative U251 tumor-bearing mouse with tumor tissue growing within the normal brain. Three representative slices of a (a)T1

TSE CE and (b) T2 TSE MRI are shown which most closely correlate to the (c) *ex vivo* H+E 1x magnification brain slice. (d) An image at 4x magnification of the area of the tumor containing vasculature and hemorrhage is shown. Images at 20x magnification of the (e) center and (f) periphery of the tumor and the (g) hemorrhage next to the tumor are illustrated. Images at 40x magnification of the (h) center of the tumor, (i) tumor periphery with a blood vessel containing lymphocytes and (j) hemorrhage next to the tumor are illustrated.

5.4.3. U251-GFP Tumor-Bearing Mice

Following stable GFP transfection of the U251 parent line, the U251-GFP tumor line grew in three distinct morphologies in the brain. These included diffuse growth in one hemisphere of the brain, growth in the ventricle space and growth as a bulk mass towards the bottom of the brain similar to the parent line (Figure 5.9). Any U251-GFP tumors that grew as a bulk mass toward the bottom of the brain were easily visible by MRI; however the other two growth morphologies were much more difficult to identify *in vivo*. U251-GFP tumors growing in the ventricle space were largely MRI invisible and only became visible when they had caused sufficient swelling of the ventricle space for ventricle enlargement to be visible by MRI. U251-GFP tumors growing diffusely in one hemisphere of the brain were virtually invisible by MRI even though the mice had physical symptoms consistent with brain tumor presence including significant weight loss, hunching of the spine and involuntary shaking. Representative example images of U251-GFP tumors growing in these three morphologies will be shown, with greater focus on the ‘MRI invisible morphologies’.

5.4.3.1. Case 1: U251-GFP Diffuse Tumor Invisible by MRI

A representative example of a U251-GFP tumor-bearing mouse with the tumor growing diffusely in one hemisphere of the brain is illustrated in Figure 5.11. The tumor was undetectable by T1 TSE CE, T2 FLAIR and T1 FFE MR imaging (Figure 5.11(a) – (c)). Slight enlargement of the ventricle space was visible, although in comparison to control mice (data not shown) the size difference was very minor. A single image of each mouse brain is illustrated in Figure 5.11 for each MRI sequence because all images appeared to show normal, healthy mouse brains. Even though no tumor was visible by MRI, the mice presented with all the standard physical symptoms of brain tumors mentioned previously. Following sacrifice, the brain was sectioned coronally at the point of needle insertion for greatest chance at *ex vivo* tumor detection. The coronal sections were imaged for GFP fluorescence, which was present in both the front and middle portion of the brain (Figure 5.11(d) & (e)). Corresponding H+E stained images confirmed the presence of tumor tissue infiltrating the normal brain (Figure 5.11(f) & (g)), however no tumor mass was present as was seen in all examples of the 9L-GFP and U251 mice. The H+E images shown at 1x magnification have a slightly purple hue to their right hemisphere, but it was difficult to visualize the tumor tissue without further magnification of the image. Representative 4x magnification images showed nests of tumor cells of varying size growing diffusely over the hemisphere (Figure 5.11(h), (i) & (l)). When these tumor nests were examined at higher magnification the vasculature and mitotic figures that were visible in both the 9L-GFP and U251 tumors did not appear to be present in this example (Figure 5.11(j), (k) & (m)). Logically, a similar immune response by the normal brain was visible in response to the U251-GFP tumors as

compared to the parent U251 tumors, as a few lymphocytes were visible at higher magnification of the H+E images (Figure 5.11(k) & (m)).

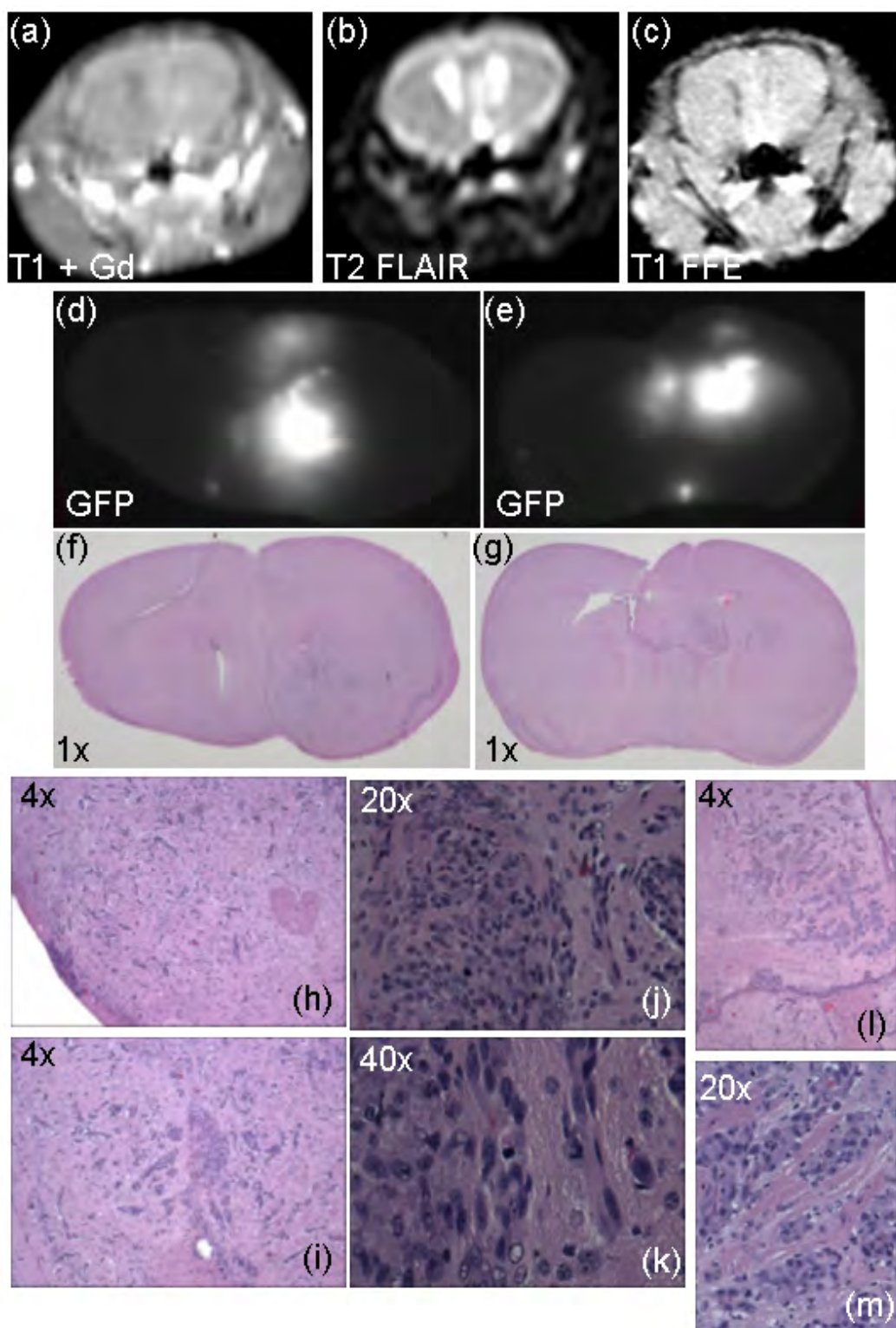


Figure 5.11 – *In vivo* and *ex vivo* images of a representative U251-GFP tumor-bearing mouse with tumor tissue growing diffusely in the right hemisphere of the brain. A

representative slice of a (a) T1 TSE CE, (b) T2 FLAIR and (c) T1 FFE MRI are shown. Due to the difficulty with MRI visibility, it was difficult to discern which MRI slice most closely corresponded to the *ex vivo* data, so brain size and shape were used to guide selection. *Ex vivo* GFP fluorescence images of the (d) front and (e) middle of the brain are illustrated with their corresponding H+E image, where the (f) front of the brain and the (g) middle of the brain are shown at 1x magnification. Images at (h) & (i) 4x, (j) 20x and (k) 40x magnification of the front brain section are illustrated. Images at (l) 4x and (m) 20x magnification of the middle brain section are illustrated.

5.4.3.2. Case 2: U251-GFP Diffuse Tumor Subtle Gadolinium Uptake Not Detectable

T1 difference imaging was experimented with to determine if subtle gadolinium uptake was present which would only be visible following subtraction of the precontrast T1 TSE image. Representative T1 TSE CE, T1 FFE and T1 difference MR images of an example U251-GFP tumor-bearing mouse with the diffusely growing tumor morphology are illustrated in Figure 5.12(a) – (c). Similar to the MR images shown in Figure 5.11, little difference was seen between the MR images of this tumor-bearing mouse and a sham surgery implanted control mouse. Some enhancement was seen corresponding to the ventricle space in the T1 TSE CE MR image (Figure 5.12(a)), and a similar pattern of contrast was seen in the T1 difference image (Figure 5.12(c)). However, a similar pattern of ventricle enhancement was also seen in the control mice (data not shown). Tumor presence was confirmed through *ex vivo* GFP fluorescence images of the front (Figure 5.12(d)) and middle sections (Figure 5.12(e)) of the brain as well as the corresponding 1x magnification H+E sections (Figure 5.12(f) & (g)). Examination of higher magnification H+E images showed larger tumor nests than those seen in the previous example (Figure 5.12(h) – (m)) as well as the presence of some mitotic figures as illustrated in Figure 5.12(m).

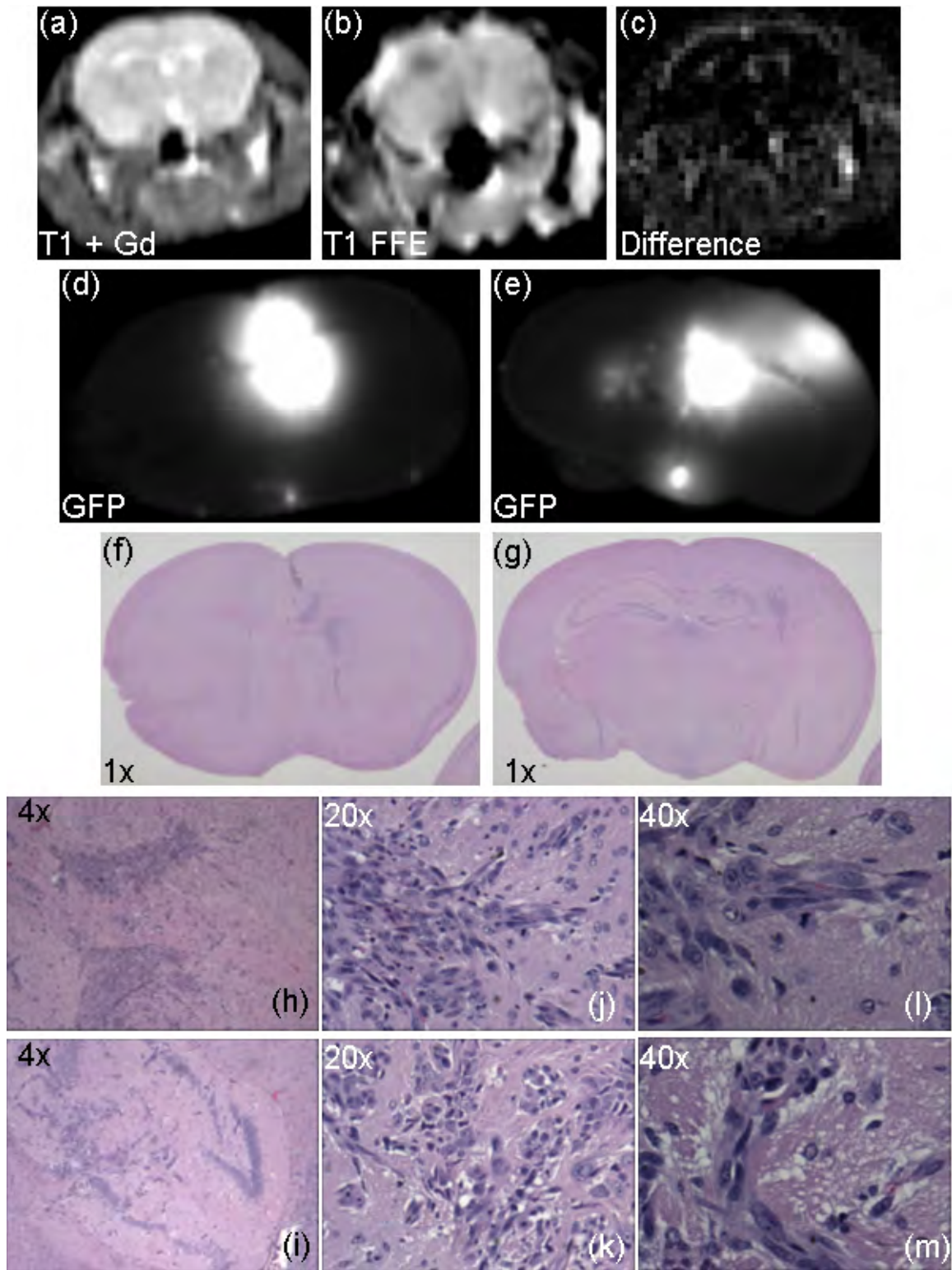


Figure 5.12 – *In vivo* and *ex vivo* images of a representative U251-GFP tumor-bearing mouse with tumor tissue growing diffusely in the right hemisphere of the brain. An MR

image showing (a) T1 TSE CE, (b) T1 FFE and (c) T1 difference sequences with the slice shown that most closely correlated to the *ex vivo* data. Tumor presence was confirmed through *ex vivo* GFP fluorescence images of the (d) front and (e) middle of the brain and their corresponding 1x magnification H+E image, where the (f) front and (g) middle of the brain are also shown. Images of the front brain section at (h) 4x, (j) 20x and (l) 40x magnification are shown. Images of the middle brain section at (i) 4x, (k) 20x and (m) 40x magnification are shown.

5.4.3.3. Case 1: U251-GFP Ventricle Growth Visible by Asymmetric Ventricle Swelling

U251-GFP tumors that grew in the ventricle space were only visible by MRI when the growth was large enough to cause significant swelling of the ventricle space. The swelling was visible as a structural change by T1 based MRI and as bright contrast on T2 based MRI. Tumor presence in the ventricle space prior to the increased size of the ventricles was largely undetectable by MRI. A representative mouse with a U251-GFP tumor large enough to cause swelling of the ventricle space is illustrated in Figure 5.13, where the structural size change of the ventricle was visible by both T1 FFE and T1 TSE CE MRI, however no contrast enhancement in the tumor tissue was detected (Figure 5.13(a) & (b)). The T1 relaxation time of the ventricle containing tumor cells was different from that of the normal ventricle on the contralateral side of the mouse as bright contrast was visible by T1 IR MRI in the tumor containing ventricle (Figure 5.13(c)). Tumor presence was confirmed by *ex vivo* GFP fluorescence (Figure 5.13(d)) and the corresponding H+E stained slice (Figure 5.13(e)). The tumor tissue was healthy and proliferating illustrated through presence of mitotic figures and lack of edema (Figure 5.13(h) and (k)). The tumor growth was also supported by a blood supply illustrated by the cross section of vessels shown at 20x and 40x magnification (Figure 5.13(g), (j) &

(k)). The immune response of the normal brain was detectable via the presence of lymphocytes adjacent to proliferating tumor tissue (Figure 5.13(l) & (m)).

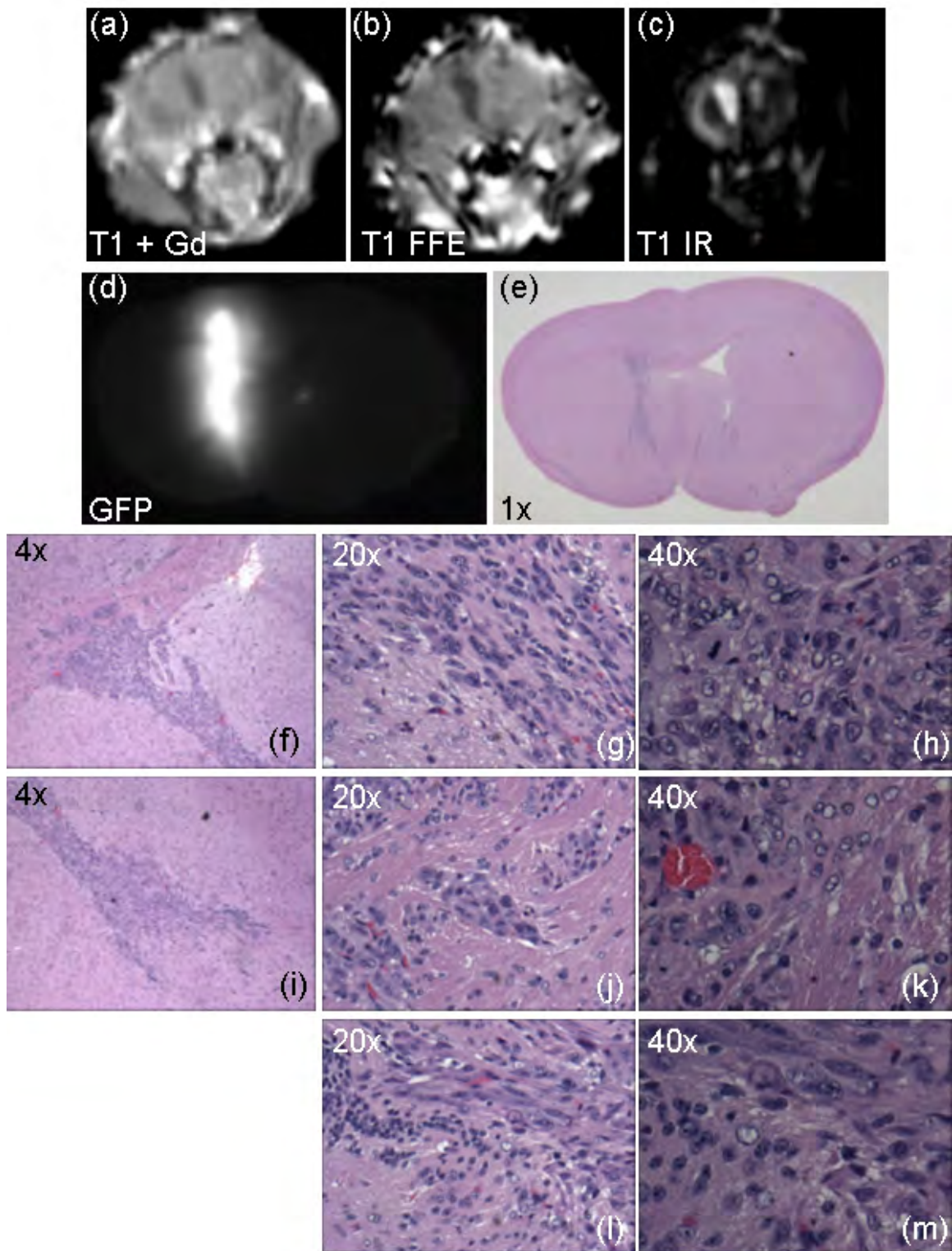


Figure 5.13 – *In vivo* and *ex vivo* images of a representative U251-GFP tumor-bearing mouse with tumor tissue growing in the left ventricle space are shown. An MR image

showing (a) T1 TSE CE, (b) T1 FFE and (c) T1 IR sequences with the slice that most closely correlated to the *ex vivo* data are shown. Tumor presence was confirmed through *ex vivo* (d) GFP fluorescence image and the corresponding (e) 1x magnification H+E image of the front of the brain. Images of both ends of the ventricle tumor at 4x magnification are illustrated in (f) and (i). Images of the center of the tumor at (g) 20x and (h) 40x magnification are shown. Images of the periphery of the tumor at (k) 20x and (m) 40x magnification are illustrated. The immune response of the normal brain was detectable through the presence of lymphocytes illustrated at (l) 20x and (m) 40x magnification.

5.4.3.4. Case 2: U251-GFP Symmetric Ventricle Growth Invisible by 3T or 7T MRI

A second example of a U251-GFP tumor-bearing mouse with tumor cells growing in the ventricle space is illustrated in Figure 5.14, however this tumor was not large enough to cause significant swelling of the ventricle space and thus was not visible by MR imaging. Similar to the example U251-GFP mice discussed previously this mouse had significant tumor burden as it exhibited physical symptoms consistent with tumor presence including a decrease in weight from 29.5 g to 20 g over 3 weeks of tumor growth. The U251-GFP cells were growing in both sides of the ventricle as can be seen in the *ex vivo* GFP and 1x magnification H+E images (Figure 5.14(h) & (i)). It was difficult to visualize tumor presence in the 1x H+E image, however upon magnification the small tumor nests growing in both the right (Figure 5.14(j) – (l)) and left (Figure 5.14(m) – (o)) side of the ventricles were readily visible, and showed healthy tumor cells. It was very difficult to identify this tumor by MRI due to its small size as well as its symmetry in both ventricles. In the previous example the MR images illustrated structural changes due to ventricle swelling on the left, while the right ventricle was of normal size, showing a structural abnormality caused by the tumor (Figure 5.13). However, in this example the ventricles were not swollen and did not show increased

enhancement via T2 TSE, PDW or T1 IR 3T MR images (Figure 5.14(a) – (c)). Images were also collected on the 7T MRI, similar to those shown for the 9L-GFP mouse in Figure 5.8, to determine if the increased field strength and decreased bore size would improve tumor tissue contrast resolution. When Figure 5.14(a) and (d) are compared it appears that the resolution of the 7T MR images was higher than that of the 3T, however this higher field strength did not show any improved ability to detect the U251-GFP tumor cells in the ventricle space by either T2 or T1 CE MRI. Data was also collected so that diffusion images and T2 maps could be reconstructed from images collected at multiple echo times. Due to the noise in the reconstructed images, everything except the brain was windowed from the image. T2 maps and diffuse images are shown in both black and white and false color in Figure 5.14(f) and (g). The T2 map (Figure 5.14(f)) showed similar enhancement to that seen in the T2 TSE image from the 3T MRI (Figure 5.14(a)). Both images showed only slight enhancement, which was symmetric in the ventricle space, making *in vivo* tumor identification difficult. The 7T diffusion images were of lower resolution than the T2 maps, but showed similar enhancement in the ventricle space (Figure 5.14(g)). However, these images also showed a significant area of increased contrast towards the bottom of the brain which was not confirmed through *ex vivo* images. Thus it appeared that increased contrast did not always correspond to the presence of tumor cells in the diffusion MR images. The *ex vivo* GFP image did show some tumor nodules at the base of the brain, but not the extent illustrated by diffusion 7T MRI.

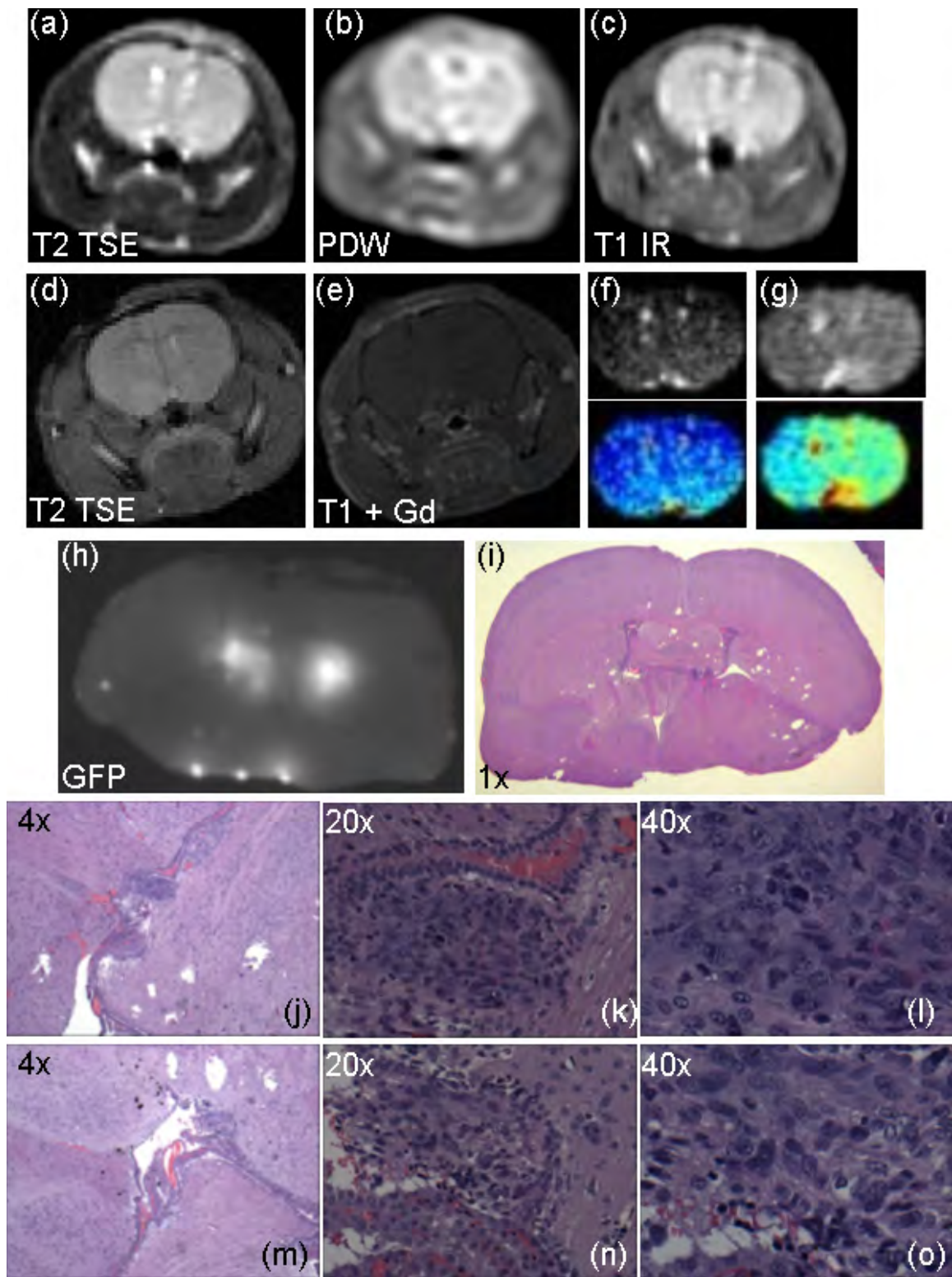


Figure 5.14 – *In vivo* and *ex vivo* images of a representative U251-GFP tumor-bearing mouse with tumor tissue growing in both ventricles is shown. 3T MRI (a) T2 TSE, (b)

PDW TSE and (c) T1 IR are illustrated. For comparison 7T MRI (d) T2, (e) T1 CE, (f) T2 map and (g) diffusion image in black and white and false color. Due to the noise in the T2 maps and diffusion images all but the brain was windowed from image. For all MR images, the image slice that most closely correlated to the *ex vivo* (h) GFP and (i) H+E 1x magnification brain section was shown. H+E images of the tumor tissue in the right ventricle are shown at (j) 4x, (k) 20x and (l) 40x magnification. H+E images of the tumor tissue in the left ventricle are shown at (m) 4x, (n) 20x and (o) 40x magnification.

5.4.4. U251-GFP Bulk Tumor Growth

5.4.4.1. Case 1: U251-GFP Bulk Tumor Growth Detectable by All MRI Sequences

In contrast to the U251-GFP example mice discussed in the previous four examples, when the tumor tissue grew as a bulk mass towards the bottom of the brain the tumors were easily detectable by all MRI scans tested. The U251-GFP tumor illustrated in Figure 5.15 had a growth pattern similar to the U251 parent line shown in Figure 5.9. *Ex vivo* the tumor tissue was shown in two GFP (Figure 5.15(h) & (j)) and two 1x magnification H+E images (Figure 5.15(g) & (i)) because the tumor grew at the base of the brain invading both the normal brain tissue and the cranium. The bulk tumor tissue that was invading the cranium was inadvertently detached from the brain tissue during extraction. The tumor invading the normal brain tissue was highly proliferative and had recruited blood supply (Figure 5.15(j), (l) & (n)), while the bulk tumor tissue appeared healthy, but did not contain as many mitotic figures or vessels (Figure 5.15(k), (m) & (o)). Different MR sequences were used to collect images of the tumor which are illustrated in Figure 5.15(a) – (f). The tumor tissue had increased uptake of gadolinium which was seen in the T1 TSE CE image and confirmed by the T1 difference image. The tumor also contained more fluid than the normal brain as can be seen by T2 TSE and T2 FLAIR images. The PDW TSE image illustrated a higher proton density in the tumor

tissue as compared to the normal tissue. Contrast was also easily visualized in the T1 IR image as the tumor T1 relaxation time was significantly different from the normal tissue.

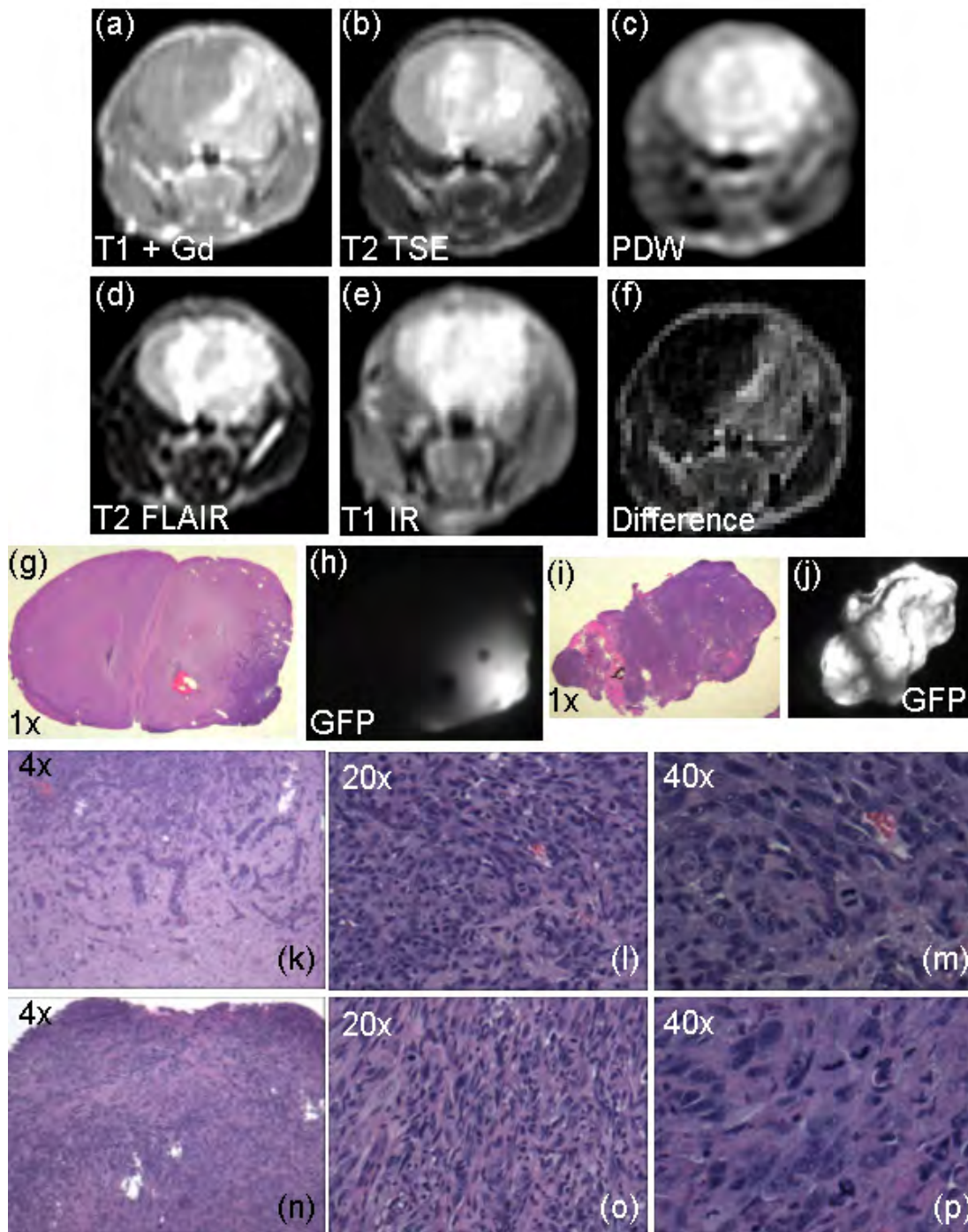


Figure 5.15 – *In vivo* and *ex vivo* images of a representative U251-GFP tumor-bearing mouse with tumor tissue growing at the base of the brain invading the normal brain and

the cranium. An MR image showing (a) T1 TSE CE, (b) T2 TSE, (c) PDW TSE, (d) T2 FLAIR, (e) T1 IR and (f) T1 difference sequences with the slice that most closely correlated to the *ex vivo* data are shown. *Ex vivo* (g) 1x magnification H+E and (h) GFP images of the tumor invading the normal brain are illustrated. *Ex vivo* (i) 1x magnification H+E and (j) GFP images of the bulk tumor which was invading the cranium are shown. Images at (k) 4x, (l) 20x and (m) 40x magnification of the tumor tissue invading the normal brain are shown. Images at (n) 4x, (o) 20x and (p) 40x magnification of the bulk tumor tissue growing at the base of the brain are shown.

5.5. Discussion

The focus of this thesis was not on visibility of different brain tumor models by MRI; rather MRI was used as a tool for validation of tumor presence for comparison to spectroscopy measurements. However, during data collection it was observed that some tumor models were more readily detectable by MR imaging than others. The goal of this chapter was to examine the MR detection and visibility differences seen between the brain tumor models studied in this thesis and propose a possible explanation for these observed differences.

Both the 9L-GFP and U251 tumor models were detectable with 100% sensitivity and specificity by both T1 TSE CE and T2 TSE MR imaging (Figure 5.2(c) & (d)), although tumor border delineation was more difficult for U251 tumor-bearing mice than for 9L-GFP tumor-bearing mice. Following stable GFP transfection, the U251-GFP tumor had three distinct growth patterns in the brain, which showed varied ability to be detected via MR imaging. U251-GFP tumors which grew diffusely as nests of tumor cells in one hemisphere of the brain (Figure 5.11 & Figure 5.12) were very difficult to detect via MRI, even though the use of multiple MRI sequences highlighting different features of brain tumors (Figure 5.4(b)). U251-GFP tumors which grew in the ventricle space were only visible by MRI when their size was large enough to cause detectable

swelling of the ventricle space. Large tumor masses in the ventricle space were visible by T1 TSE CE MRI due to structural change in the brain; gadolinium administration did not show increased contrast in these images. T2 TSE, T2 FLAIR and T1 IR MR images illustrated contrast in the ventricle space of all mice including sham surgery implanted control mice. Thus, even though contrast was visible by T2 TSE, T2 FLAIR and T1 IR, without ventricle size change it was not possible to determine if tumor tissue was present in the ventricles. Tumors growing in the ventricle space were easiest to identify when the growth was asymmetric, as illustrated in Figure 5.13, but could also be visualized when growing symmetrically if the tumor-bearing mice appeared to have hydrocephalus. As shown in Figure 5.14, mice with U251-GFP tumors growing in the ventricle space did not always show enlarged ventricles prior to the presence of nearly fatal tumor burden. Mice with tumors in the ventricles that did not show enlargement were virtually undetectable by MR imaging. The U251-GFP tumor cells also grew as large masses at the base of the brain as was seen in many of the U251 parent line tumors, an example of which is shown in Figure 5.9. When the U251-GFP tumor grew as a bulk mass it was detected with 100% sensitivity and specificity (Figure 5.2(c) & (d)). An example mouse with a U251-GFP bulk tumor was illustrated in Figure 5.15, where tumor tissue was easily visualized by T1 TSE CE, T2 TSE, PDW, T2 FLAIR, T1 IR and T1 difference MR imaging sequences illustrating that all MRI sequences were able to detect tumor tissue when enough cells were present.

A possible explanation for the MRI detection difficulty observed was determined through examination of the corresponding H+E slides. All 9L-GFP tumors and U251 tumors grew as large masses of cells within the cranium and were detected with 100%

sensitivity and specificity. When the U251-GFP tumors grew as a large mass of cells, it was also detectable with 100% sensitivity and specificity. However, when the U251-GFP tumor grew diffusely in the brain as small nests of tumor cells it was not visible. U251-GFP tumors growing in the ventricle space were only visible when enough cells had grown to cause structural changes. Thus, it appears that density of the tumor cells was well correlated to the ability to detect and visualize tumor presence by MR imaging. This is also supported by the fact that the U251 parent line tumors had a more infiltrative growth pattern into the normal brain tissue than the 9L-GFP tumors, and thus more projections growing off of the main tumor mass were present. This made tumor border delineation in the U251 tumor-bearing mice more difficult than in the 9L-GFP tumor-bearing mice. All U251-GFP tumors used to study detection via PpIX and EGF-IRDye uptake fluorescence spectroscopy grew either diffusely in the brain or in the ventricle space. Thus, tumor tissue presence of the U251-GFP tumors for all *in vivo* spectroscopy studies had to be confirmed through *ex vivo* analysis of H+E sections and GFP fluorescence.

Chapter 6 - *In Vivo* PpIX Studies

6.1. Introduction

Interest in Aminolevulinic Acid induced Protoporphyrin IX (ALA-PpIX) production for oncology applications has significantly increased over the past thirty years, with a seminal review paper on this subject published in 1996 by Kennedy, *et al* [23]. ALA-induced PpIX has been extensively investigated as a photosensitizer for photodynamic therapy (PDT) in the treatment of many types of cancer. ALA-induced PpIX has found widespread use in dermatology to treat various malignant and non-malignant skin conditions including actinic keratosis, squamous cell carcinoma, basal cell carcinoma, psoriasis, and others [91, 110]. ALA-induced PpIX PDT treatment has been found to be most successful for cancers of hollow organs where the cancerous cells proliferate on the wall of the organ as opposed to tumors that grown in solid masses, mainly because of the ease of use in topical applications and also because of the high specificity which can be observed in abnormal squamous tissues. ALA-PpIX based PDT for bladder carcinoma, Barrett's esophagus, colon carcinoma and others have been investigated [25, 58].

Due in large part to its success as a tumor margin demarcation tool in neurosurgical resection of human gliomas, a large body of research on ALA-induced PpIX fluorescence of brain tumor cells and tissues currently exists. Conventional therapy for malignant gliomas involves surgical resection, fractionated radiotherapy and adjuvant chemotherapy to eradicate the tumor tissue which may remain following attempted surgical resection [6, 7]. The infiltrative nature of glioma tumors make them very difficult to fully resect, however survival following treatment is linked to completeness of

tumor removal [111]. A randomized Phase III multicenter clinical trial was conducted in Germany using ALA-induced PpIX fluorescence as the tumor tissue contrast agent for neurosurgical guidance. PpIX fluorescence was found to be specific for the glioma tumor tissue showing bright red fluorescence, while the normal brain tissue had little porphyrin fluorescence [28, 111]. The Phase III clinical trial showed improved ability to have full resection of the contrast-enhancing tumor as determined by post operative MR. The conclusion of the study showed 65% of patients that received ALA-PpIX guided surgery had complete resections by MRI, in comparison to only 36% that received conventional white light surgery. This translated into higher 6 month progression free survival for the ALA-PpIX guided surgery group where 41% of patients that received ALA-PpIX guided surgery had 6 month progression free survival as compared to only 21.1% of patients that received conventional white light surgery [29].

This specific accumulation of PpIX in brain tumor tissue was examined further in this work as a tool for *noninvasive* detection of the tumor presence. Three models of glioma were studied in this work including a rat gliosarcoma (9L-GFP), a human glioma (U251), and a variant of the U251 cell line that was transfected with green fluorescent protein (U251-GFP). The latter two (U251 & U251-GFP) had different growth properties, indicating they should be treated as different cell lines. These tumor types were tested for their ability to be spectroscopically detected over normal, healthy mice. Since PpIX fluorescence has been found to be significantly lower in normal brain tissues and cells than in brain tumor tissues and cells, mice with brain tumors should show higher bulk PpIX fluorescence than normal control mice following the administration of ALA. However, it has been observed that PpIX fluorescence of various types of

experimental tumors is heterogeneous both in our lab, as discussed in chapter 2, as well as by other researchers [112, 113]. This variability was examined across the three cell lines *in vivo* and skin photobleaching was studied to increase the contrast between tumor-bearing mice and normal, healthy mice for better brain tumor detection.

6.2. Pilot Studies for Tumor Detection & Skin Photobleaching

The single channel spectroscopy system, described in chapter 3, was used in the studies discussed here to examine PpIX fluorescence for murine glioma detection. The single channel spectroscopy system was used to collect bulk measurements of PpIX fluorescence both *in vivo* and *ex vivo*. The general brain tumor implantation procedure, described in chapter 2, was used to form groups of tumor-bearing and non-tumor-bearing control mice for all studies. Pilot studies were performed using 9L-GFP tumor-bearing mice to test brain tumor detection over non-tumor-bearing mice using the single channel spectroscopy system. In the first study sham surgery was not performed on the control mice, as was described in chapter 2, in order to compare to normal controls without any surgical damage to 9L-GFP tumor-bearing mice. All mice were measured for bulk PpIX fluorescence prior to ALA administration, which was termed the background PpIX fluorescence. Following background PpIX measurements, 100 mg/kg ALA was administered IP and measurements of each mouse were obtained 2 hours after ALA administration *in vivo*. The mice were then sacrificed, and their brains were extracted to be placed back in the spectroscopy system for bulk *ex vivo* PpIX fluorescence measurements. The fluorescence to transmittance ratio was calculated as described in chapter 3. Figure 6.1(a) illustrates that the mean PpIX fluorescence prior to ALA

administration was the same for non-tumor-bearing control mice and the 9L-GFP tumor-bearing mice. The mean PpIX fluorescence was increased 2 hours after the administration of ALA, however little difference in PpIX fluorescence was seen between the tumor-bearing group and the control group (Figure 6.1(b)). A considerable difference in PpIX fluorescence intensity between the control group and the tumor bearing group could only be seen in the *ex vivo* measurements of the bulk brain (Figure 6.1(c)).

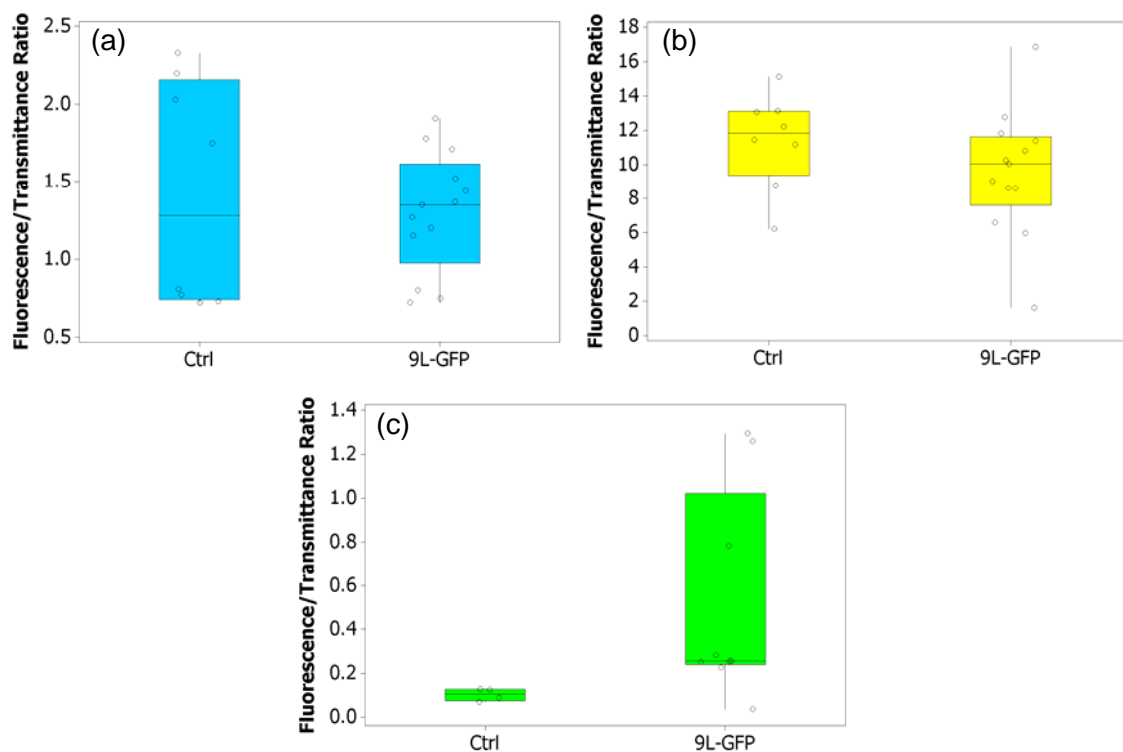


Figure 6.1 – Box and whisker plots of the first pilot PpIX brain tumor detection study results. (a) The fluorescence to transmittance ratio of background PpIX fluorescence in 9L-GFP tumor-bearing mice and non-tumor-bearing mice which had not received sham surgery. (b) *In vivo* PpIX fluorescence 2 hours after the administration of 100 mg/kg ALA IP. (c) *Ex vivo* PpIX fluorescence of extracted brain tissue, 2 hours after the administration of ALA.

Since *in vivo* measurements collected with the single channel spectroscopy system were bulk PpIX measurements of the mouse head, the skin PpIX fluorescence was

included in the measurement. Even though the PpIX fluorescence in the tumor-bearing mouse brains was higher than that in the control mouse brains, as can be seen from the *ex vivo* measurements (Figure 6.1(c)), this difference was masked by the skin PpIX fluorescence. To ensure any measured skin PpIX fluorescence in the control group would be the same as that measured in the tumor-bearing group a second pilot experiment was completed where the control mice received sham surgery, which was described in chapter 2. The sham surgery enabled the same wound healing process to occur in both the tumor-bearing group and the control group accounting for fluorescence differences from the scalp as well as any damage inflicted on the brain and the blood-brain-barrier.

The second pilot study also compared PpIX fluorescence between the 9L-GFP tumor-bearing mice and non-tumor-bearing control mice. The same measurements of background PpIX fluorescence, *in vivo* and *ex vivo* PpIX fluorescence 2 hours after ALA administration were collected. As can be seen in Figure 6.2(a) the mean background PpIX fluorescence measurements appeared to be significantly affected by the sham surgery. The tumor-bearing mice had a higher mean PpIX fluorescence than the control mice prior to the administration of ALA. This trend continued 2 hours after administration of 100 mg/kg ALA IP, as the mean PpIX fluorescence in the tumor-bearing group was appreciably higher than in the control group (Figure 6.2(b)).

Verification of the higher content of PpIX in the brain of the tumor-bearing mice over the control mice can be seen in the *ex vivo* bulk measurements of the brain, where the mean PpIX fluorescence of the 9L-GFP group was higher than the mean PpIX fluorescence of the control group (Figure 6.2(c)). Due to the significant differences between the two pilot studies shown in Figure 6.1 and Figure 6.2, all control mice for studies completed after

the second pilot study had sham surgery to ensure that brain tumor detection via PpIX fluorescence would not be skewed by difference in skin PpIX fluorescence due to wound healing following tumor implantation. Further PpIX brain tumor detection studies were completed using additional tumor cell lines and will be discussed later in this chapter.

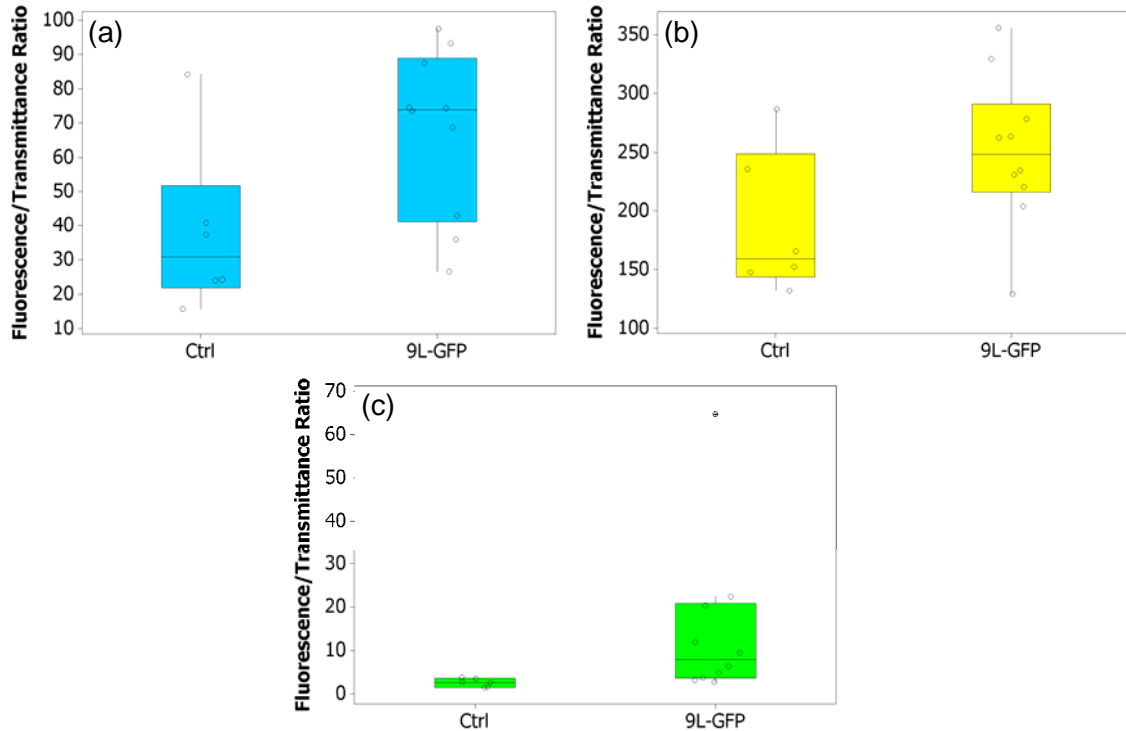


Figure 6.2 – The results of the second pilot study of PpIX brain tumor detection is shown as box and whisker plots, using control mice with sham surgery, to have the same level of scaring and damage from implantation. (a) The fluorescence to transmittance ratio of background PpIX fluorescence in 9L-GFP tumor-bearing mice and non-tumor-bearing control mice which had received sham surgery. (b) *In vivo* PpIX fluorescence 2 hours after the administration of 100 mg/kg ALA IP. (c) *Ex vivo* PpIX fluorescence of extracted brain tissue 2 hours after ALA administration.

PpIX molecules are bleached by exposure to light, which is well documented in the ALA-PpIX PDT literature [114-117]. PpIX is readily photobleached by laser light during PDT treatment, and this phenomenon has been studied extensively both *in vitro*

and *in vivo*, including a study which illustrated that blue light was much more effective at producing PpIX photobleaching than red light [118]. A small pilot study was completed to determine if photobleaching the mouse skin PpIX fluorescence could increase the PpIX fluorescence contrast seen between the tumor-bearing group and the control group. A small cohort of 9L-GFP tumor-bearing mice was compared to control mice that had received sham surgery. The single channel spectroscopy system was used to measure PpIX fluorescence prior to ALA administration, 2 hours after ALA administration, following photobleaching of one side of the mouse head, and then following photobleaching of both sides of the mouse head. The photobleaching dose was delivered through the same collimators that were in contact with the mouse head for spectroscopy measurements using a 405 nm laser. A photobleaching dose of 8 J/cm^2 was delivered sequentially through both of the collimators in contact with the mouse head. Due to the small number of control animals used in this study, the variance in the PpIX fluorescence measurements were very large and thus the mean PpIX fluorescence prior to ALA administration as well as 2 hours after ALA administration was very similar for both the tumor-bearing group and the non-tumor-bearing control group (Figure 6.3(a) and (b)). However, administration of blue light skin photobleaching significantly affected the ability to differentiate between the control mice and the tumor-bearing mice. After photobleaching of one side of the mouse head the mean PpIX fluorescence was still very similar between the control mice and the tumor-bearing group (Figure 6.3(c)). Following photobleaching of both sides of the mouse head the mean PpIX fluorescence was considerably higher for the tumor-bearing group than the control group (Figure 6.3(d)). The total detected PpIX signal decreased, due to the administration of the 8 J/cm^2 blue

light photobleaching dose to both sides of the mouse head, but the PpIX contrast increased as less of the measured bulk PpIX fluorescence was from extraneous PpIX skin fluorescence.

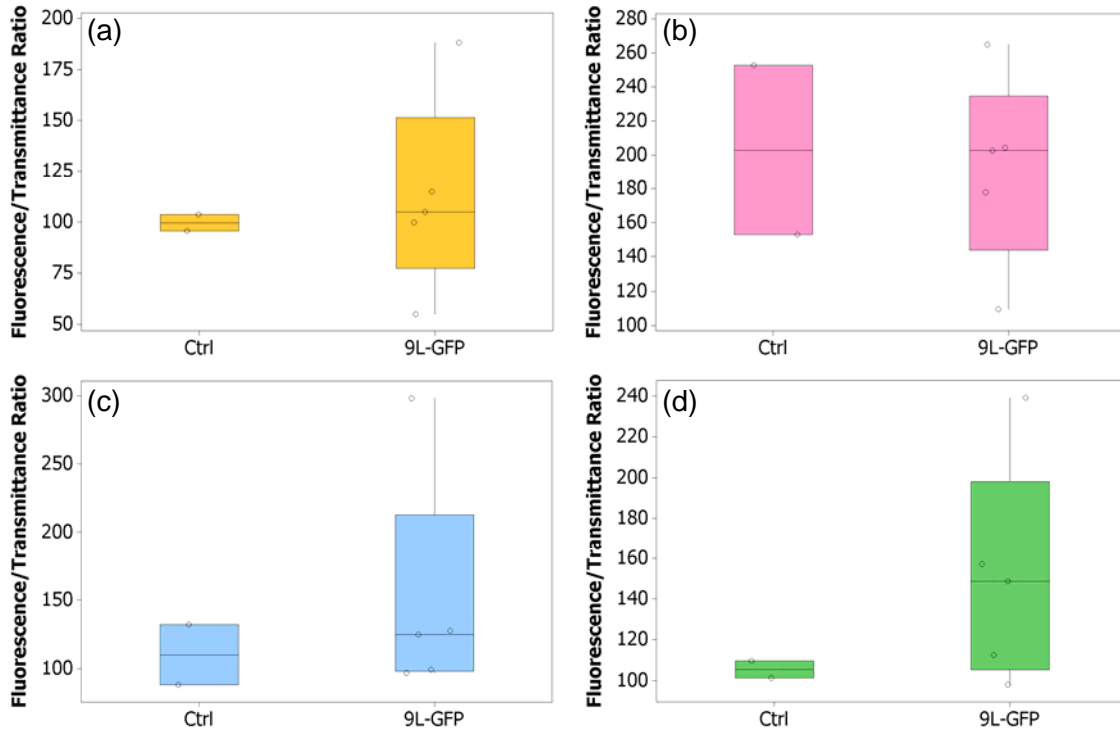


Figure 6.3 – The pilot PpIX skin fluorescence photobleaching study results are shown in box and whisker plots. The PpIX fluorescence to transmittance ratio (a) prior to ALA administration, (b) 2 hours after 100 mg/kg ALA administration, (c) after 8 J/cm² photobleaching dose was administered to one side of the head, and (d) after 8 J/cm² photobleaching dose was administered to both sides of the head.

6.3. Skin PpIX Photobleaching Studies

Skin PpIX photobleaching studies were completed to determine if a protocol to increase PpIX fluorescence difference between non-tumor-bearing control mice and tumor-bearing mice could be established. The same 635 nm laser that was used for spectroscopy measurements was used in a time course photobleaching experiment, where

spectroscopy measurements were collected throughout administration of the photobleaching dose. A blue light photobleaching experiment was performed on normal, healthy mice which had not undergone sham surgery to compare different photobleaching doses for their ability to bleach PpIX skin fluorescence. A second blue light photobleaching study was completed comparing tumor-bearing mice to non-tumor-bearing control mice. The lowest effective blue light photobleaching dose determined from the healthy mouse study was administered to all mice following their spectroscopy measurement 2 hours after ALA administration to examine PpIX contrast between the groups. These skin photobleaching experiments will be discussed in detail as follows.

6.3.1. Time Course Red (635 nm) Photobleaching

Two types of tumor-bearing mice were used in this study including 9L-GFP tumor-bearing mice, used in the pilot studies, and U251 tumor-bearing mice. Single channel spectroscopy measurements were obtained on all mice prior to ALA administration to determine background PpIX levels in the non-tumor-bearing control group, 9L-GFP group and U251 group. The mean PpIX fluorescence of the non-tumor-bearing control group and the two tumor bearing groups were similar prior to the administration of ALA (Figure 6.4(a)). All mice were administered 100 mg/kg ALA IP and measured for *in vivo* PpIX fluorescence 2 hours after administration. Both tumor-bearing groups had significantly higher mean PpIX fluorescence than the control group (mean PpIX fluorescence: control = 25.02, 9L-GFP = 43.20, U251 = 41.50), however the 9L-GFP group had much larger variance than the U251 group (variance: 9L-GFP = 312.02, U251 = 89.26) (Figure 6.4(b)). The same 250 mW, 635 nm laser which was used

for excitation in the spectroscopy measurements was used to administer red light photobleaching. The laser was left on between measurements which were acquired over a 32 minute period. The red light photobleaching cumulative dose administered to each mouse over the 32 minute measurement period can be seen in Table 6.1.

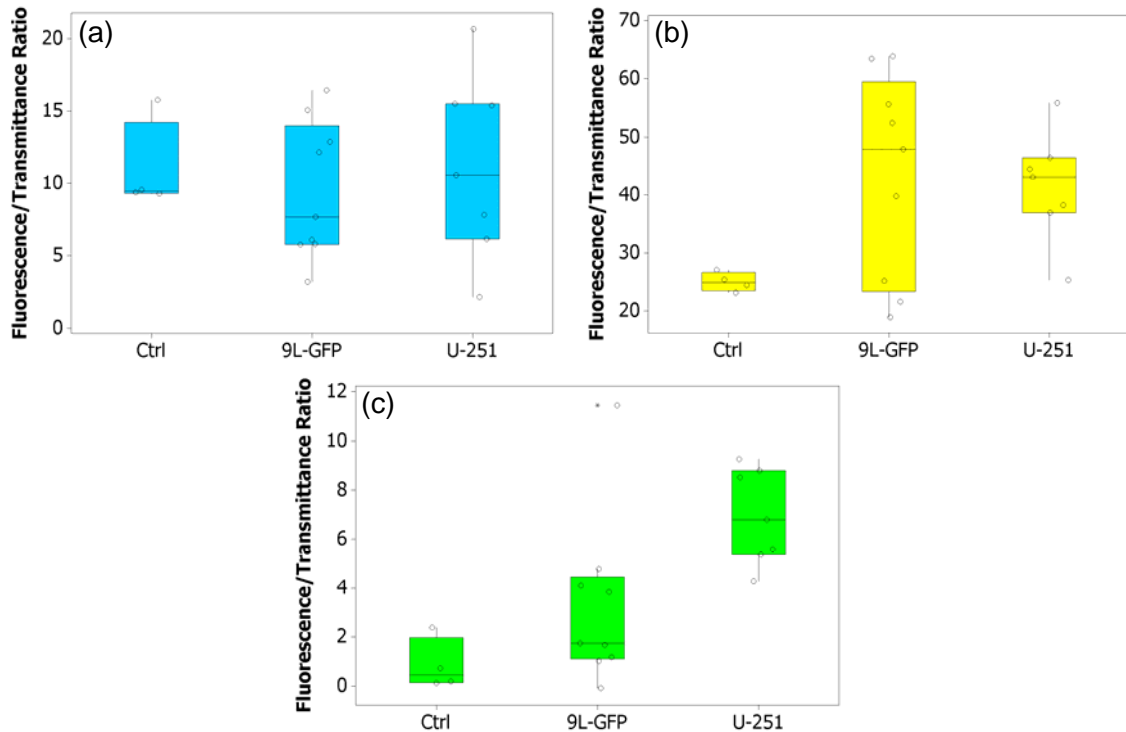


Figure 6.4 – Spectroscopy measurements are summarized (a) prior to the administration of ALA, (b) *in vivo* 2 hours after the administration of ALA and (c) *ex vivo* 2 hours after the administration of ALA. The PpIX fluorescence at each time point was compared between sham surgery implanted control mice, 9L-GFP and U251 tumor-bearing mice.

Light Administration Time (minutes)	Cumulative Photobleaching Dose (J/cm ²)
1	37
2	74
4	148
8	296
16	591
24	887
32	1183

Table 6.1 – The red light (635 nm) photobleaching dose is tabulated in J/cm². A 250 mW, 635 nm laser was used for photobleaching dose administration. All photobleaching doses are rounded to the nearest whole number.

The mean PpIX fluorescence measurements acquired 2 hours after ALA administration showed a different relationship between the control group and the tumor bearing groups, as compared to that seen in the bulk *ex vivo* PpIX measurements. Specifically, the 2 hour *in vivo* measurements showed the 9L-GFP group with higher mean PpIX fluorescence than the U251 group, while the *ex vivo* measurements illustrated that the mean PpIX fluorescence of the U251 group was almost twice that of the 9L-GFP group. The time course photobleaching measurements were examined to determine if the red light photobleaching facilitated *in vivo* visualization of the same PpIX fluorescence contrast seen in bulk *ex vivo* measurements. Measurements of PpIX fluorescence were obtained at each of the time points listed in Table 6.1. Figure 6.5 shows the PpIX fluorescence decreased during the photobleaching dose administration, where each line represents the average of all mice in each group. At low red light photobleaching doses the mean PpIX fluorescence of the 9L-GFP group was slightly higher than the U251 group. The measurement obtained after 8 minutes of red light photobleaching had

administered a cumulative photobleaching dose of 296 J/cm^2 showed the mean PpIX fluorescence of the U251 group was higher than the 9L-GFP group, which was the same relationship that was seen in the *ex vivo* measurements (Figure 6.6). After 296 J/cm^2 of photobleaching the mean PpIX fluorescence of the 9L-GFP group was decreased by nearly twice as much (37%) as the U251 group (20%) when compared to the mean PpIX fluorescence 2 hours after ALA administration, prior to any photobleaching.

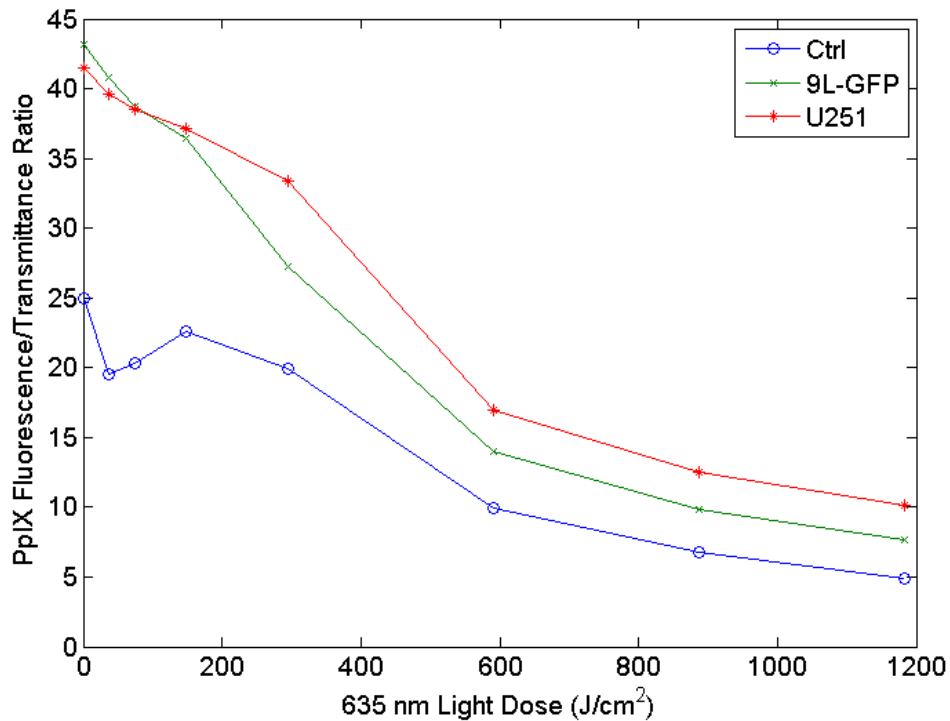


Figure 6.5 – PpIX fluorescence to transmittance ratio of each group of mice during red light photobleaching administration. The cumulative red light dose is shown on the x-axis and corresponds to measurements obtained at the time points listed in Table 6.1, where 0 J/cm^2 corresponds to the measurements 2 hours after the administration of ALA, prior to any photobleaching. Each line represents the average of all mice in each group. (Control $n = 4$, 9L-GFP $n = 9$, U251 $n = 7$).

Additional cumulative photobleaching dose was administered to all mice in the study following the mean PpIX fluorescence change that was seen after 296 J/cm^2 dose.

The difference in mean PpIX fluorescence between the 9L-GFP group and the U251 group was slightly smaller following 591 J/cm² photobleaching dose. The difference between the mean PpIX fluorescence of the control group, the 9L-GFP group and the U251 group appeared constant at higher cumulative red light photobleaching doses (Figure 6.5). Therefore, additional red light photobleaching after the 296 J/cm² dose, or following 8 minutes of red light photobleaching did not increase the PpIX contrast between the groups.

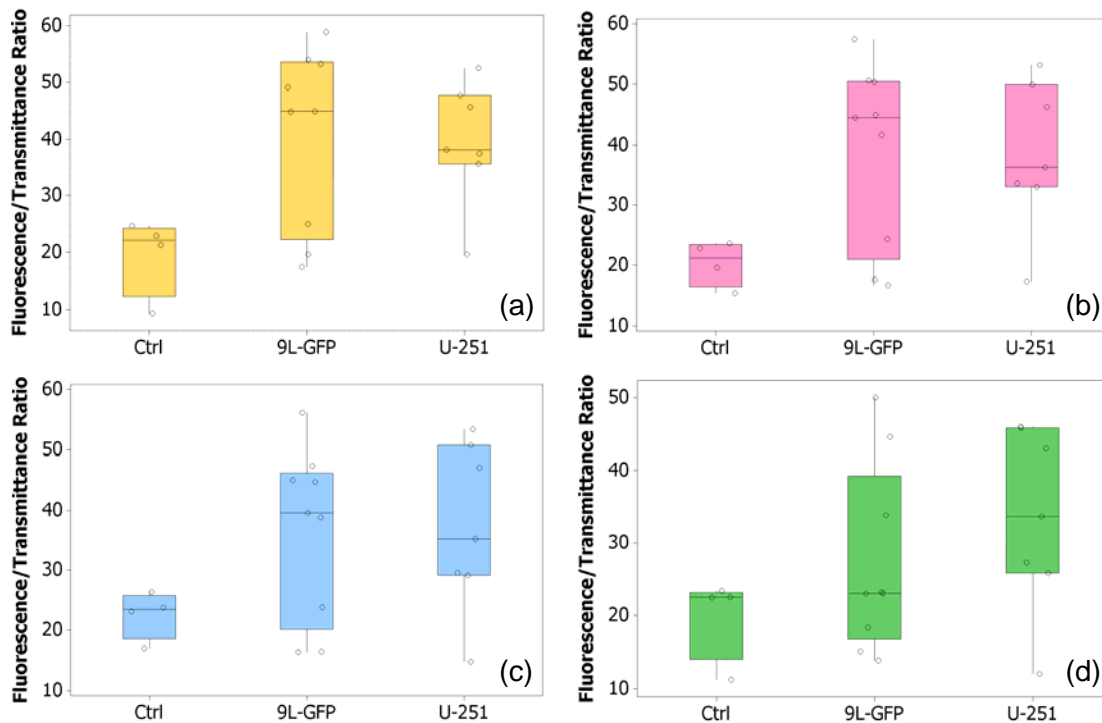


Figure 6.6 – Box and whisker plots illustrating the individual mice following (a) 1 minute of photobleaching (37 J/cm²); (b) 2 minutes of photobleaching (74 J/cm²); (c) 4 minutes of photobleaching (148 J/cm²); and (d) 8 minutes of photobleaching (296 J/cm²).

6.3.2. Blue Light (400 +/- 5 nm) Photobleaching

The red light photobleaching experiment was completed so that photobleaching could be studied in a time dependent manner, however blue light photobleaching might provide better contrast enhancement. The penetration depth of blue light in comparison to red light in tissue is significantly less, due to absorption of hemoglobin in the blue wavelength range. Theoretically, the use of blue light photobleaching would only photobleach the skin and thus using this technique would spare all PpIX fluorescence which was accumulated in the brain tissue for spectroscopic measurement.

The pilot study measurements shown in Figure 6.3 were collected using a 405 nm laser and a photobleaching dose of 8 J/cm² delivered to each side of the mouse head through collimators. A photobleaching box was designed, which consisted of two 35 mW blue light emitting diodes (LED), with wavelength centered at 400 nm and a 5 nm spectral width, and a plate positioned between them to hold the mouse during photobleaching treatments (Figure 6.7(a) & (b)). Three photobleaching doses were tested including 4, 8 and 12 J/cm² on normal mice that had not received sham surgery. The amount of skin photobleaching caused by these doses was monitored to determine if larger photobleaching doses caused decreased skin PpIX fluorescence. The mice were monitored for 32 minutes following the completion of the photobleaching dose to detect any PpIX re-accumulation in a sufficient window of time for future brain tumor spectroscopy measurements. There were 7 mice tested in the 4 J/cm² group, 7 mice tested in the 8 J/cm² group and 8 mice tested in the 12 J/cm² group. All three photobleaching doses caused similar skin fluorescence decrease. There was large variability in mouse skin PpIX production in each of the three groups at all measured

time points including prior to the administration of ALA (Figure 6.7(c)). Since increased photobleaching dose did not cause decreased PpIX skin fluorescence, the lowest photobleaching dose tested, 4 J/cm^2 , was used in all subsequent experiments. The 4 J/cm^2 photobleaching dose did not cause any visible skin toxicity to the mice at the time of photobleaching or during the days following the experiment. However, in the case of the higher photobleaching doses used, 8 and 12 J/cm^2 , considerable skin erythema was seen just after the delivery of the light dose and during the days following the experiment significant skin toxicity was observed.

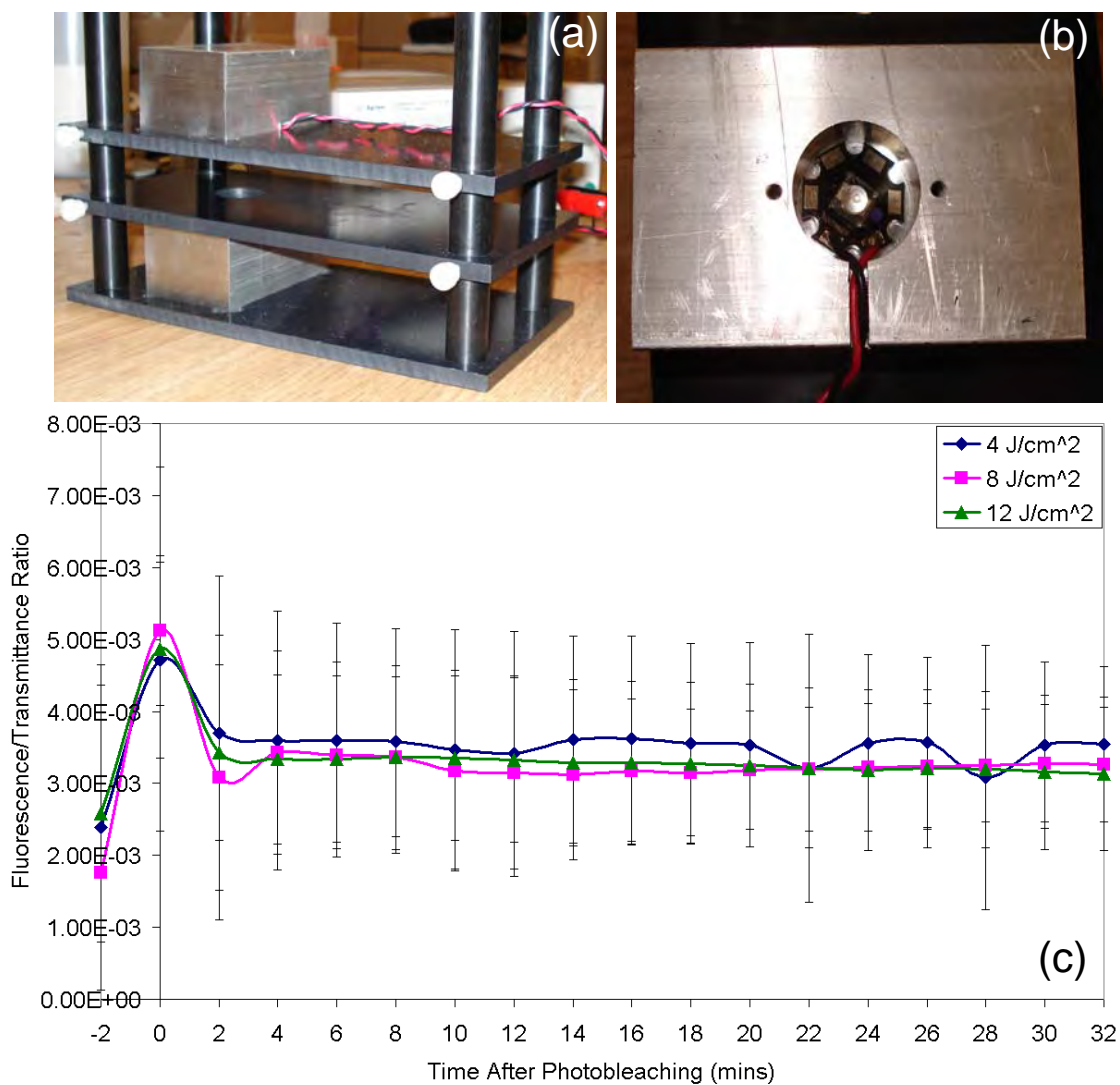


Figure 6.7 – (a) The mouse photobleaching box is shown with blue LEDs contained within large aluminum heat sinks. Holes were drilled to allow the light from each LED to hit the mouse skin, while the mouse was positioned on the plate in the center of the device. (b) A close-up photograph of the LED in the aluminum heat sink, as shown in (a). (c) The results from photobleaching of healthy nude mice are shown, where photobleaching doses of 4, 8 and 12 J/cm² were compared. The point at time = -2 represents the background PpIX measurement prior to the administration of ALA. The point at time = 0 represents the PpIX measurement 2 hours after the administration of ALA. Mouse numbers per group where: n=7 at 4 J/cm²; n=7 at 8 J/cm²; and n=8 at 12 J/cm². The points represent the mean of the mice in each group while the error bars show the standard deviation in each group.

Blue light photobleaching was tested on 9L-GFP and U251-GFP tumor-bearing mice to determine if PpIX contrast would be improved between non-tumor-bearing control mice and tumor-bearing mice. All mice in the study were measured for background PpIX fluorescence prior to the administration of ALA and then again at 2 hours after ALA administration. The photobleaching box shown in Figure 6.7(a) was used to administer 4 J/cm^2 photobleaching dose to all mice, after which PpIX fluorescence was again measured via the single channel spectroscopy system. After completion of the *in vivo* measurements, the mice were sacrificed; their brains extracted and measured in the spectroscopy system for bulk *ex vivo* PpIX fluorescence. The results of this experiment can be seen in Figure 6.8.

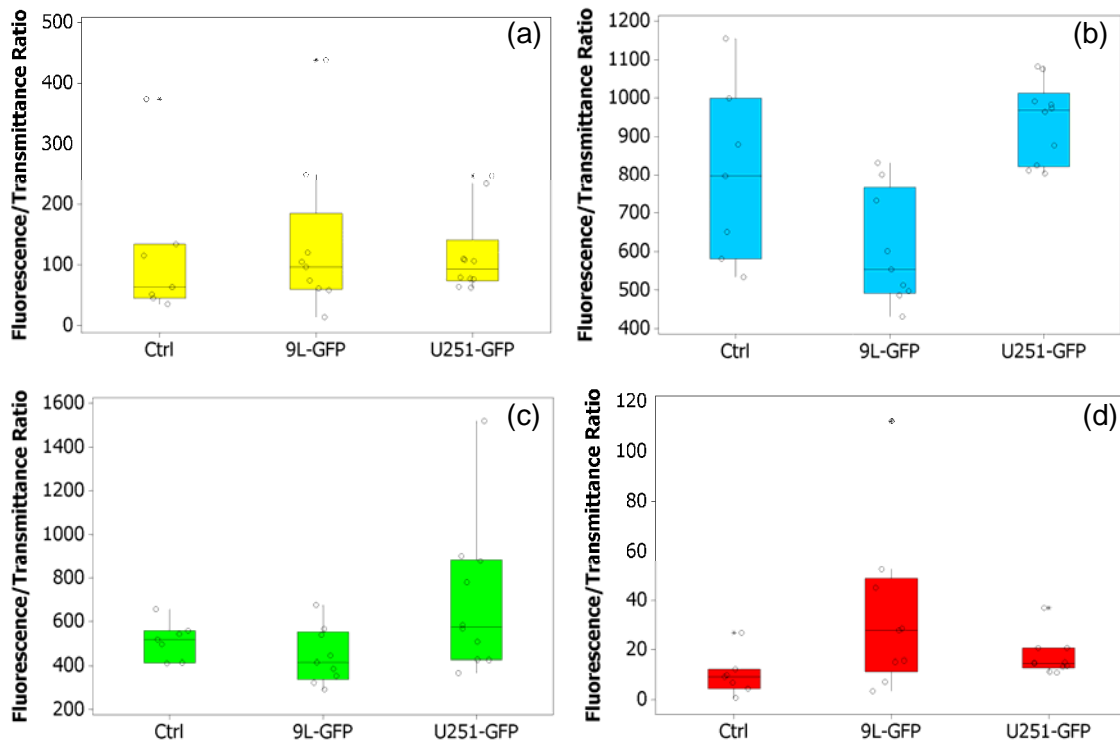


Figure 6.8 – The summary of the single channel spectroscopy measurements from the blue light photobleaching study, (a) prior to the administration of ALA, (b) 2 hours after

the administration of ALA, (c) following administration of 4 J/cm² blue light and (d) *ex vivo*.

As seen in previous PpIX fluorescence experiments, prior to the administration of ALA, the background PpIX fluorescence was similar between non-tumor-bearing control mice and tumor-bearing mice (Figure 6.8(a)). Interestingly, 2 hours after the administration of ALA, the average PpIX fluorescence of the control mice was higher than seen in previous experiments and thus more similar to that of the tumor-bearing mice. In fact, the mean PpIX fluorescence of the U251-GFP mice was higher than the control mice, but the mean PpIX fluorescence of the 9L-GFP mice was actually lower than the control mice (Figure 6.8(b)). After the photobleaching dose was administered the mean PpIX fluorescence decreased in all three groups, but was still similar between the control group and the tumor-bearing groups (Figure 6.8(c)). A more substantial difference between the control group and the tumor-bearing groups could only be seen in the *ex vivo* measurements. Upon examination of the tumors *ex vivo*, a considerable difference in size between the two tumor types was apparent. The PpIX fluorescence data at each time point was normalized to tumor size, the results of which can be seen in Figure 6.9. The percentage of the brain that was tumor tissue was calculated and used to normalize the PpIX fluorescence to transmittance ratio. Prior to the administration of ALA, there was a slight difference in the average PpIX fluorescence of the 9L-GFP group and the U251-GFP group (Figure 6.9(a)). However, 2 hours after the administration of ALA the U251-GFP group had higher PpIX fluorescence than the 9L-GFP group (Figure 6.9(b)) and this same result was seen after the photobleaching dose was administered (Figure 6.9(c)). *Ex vivo* measurements did show higher PpIX

fluorescence in the U251-GFP group, but not at the significant levels seen *in vivo* (Figure 6.9(d)).

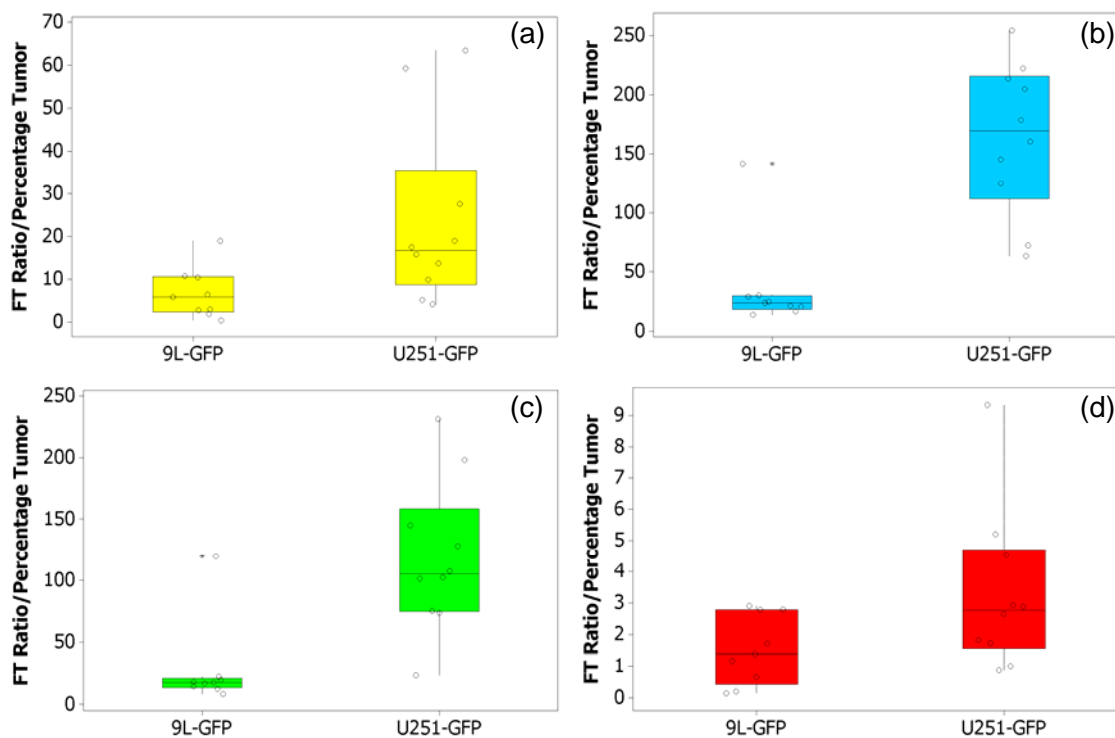


Figure 6.9 – A summary of the blue light photobleaching experiment, with the PpIX fluorescence to transmittance ratio (FT Ratio) normalized to the tumor size. The normalized FT ratio is shown (a) prior to the administration of ALA, (b) 2 hours after ALA administration, (c) following the 4 J/cm^2 photobleaching dose and (d) *ex vivo*.

6.4. PpIX Tumor Detection by Transmission Spectroscopy Summary

The data from each of the above studies was normalized to the average of the control mice in that study, allowing the three tumor lines studied to be directly compared. As was seen in previous studies, prior to the administration of ALA, PpIX fluorescence was not detectably different for non-tumor-bearing control mice as compared to tumor-bearing mice (Figure 6.10(a)). Two hours after the administration of ALA a significant PpIX fluorescence difference between each of the tumor-bearing groups and the control

group was seen (Figure 6.10(b)). The PpIX fluorescence difference between the tumor-bearing groups and the control group could also be visualized through *ex vivo* measurements (Figure 6.10(c)).

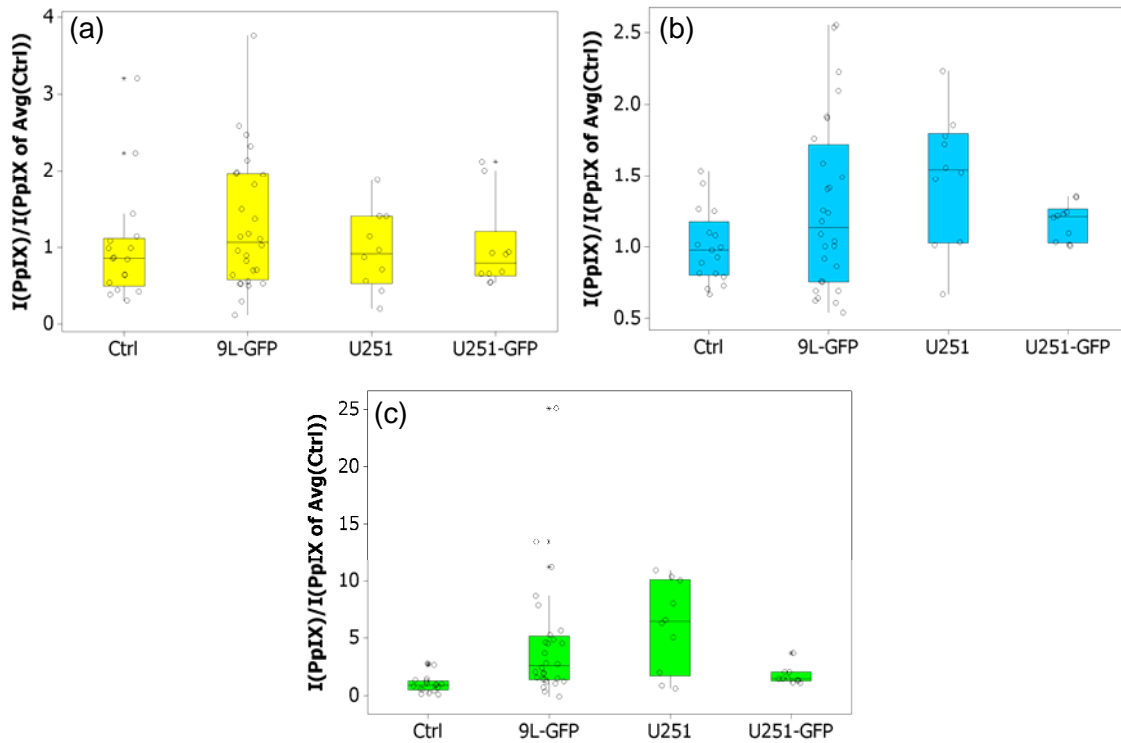


Figure 6.10 – Summary PpIX fluorescence data normalized to the average controls mouse from each study are shown. The normalized PpIX fluorescence to transmittance ratio is shown (a) prior to the administration of ALA, (b) 2 hours after the administration of ALA and (c) *ex vivo*.

Each of the brain tumor types were able to be detected over the control mice *in vivo*, following the administration of ALA. The normalized mean PpIX fluorescence 2 hours after that administration of ALA was 1.0 for the non-tumor-bearing control group, 1.28 for the 9L-GFP group, 1.49 for the U251 group and 1.17 for the U251-GFP group. The variation in PpIX production in each of the tumor-bearing groups was significantly different, as can be illustrated through the coefficient of variance (CV), which is defined

as the ratio of the standard deviation to the mean expressed as a percentage. The CV for the control group was 25% illustrating the normal PpIX production variation in healthy mice. The CV was largest for the 9L-GFP group, 47%, while the CV was 31% in the U251 group. Interestingly, the CV was smallest in the U251-GFP group, only 11%, significantly less than either of the other tumor-bearing groups or the control group. Student's t-tests were performed to calculate p-values to determine the statistical significance of the PpIX fluorescence difference between the tumor-bearing groups and the non-tumor-bearing control group at each measurement time point. As can be seen in Table 6.2, the p-values of the PpIX fluorescence difference between the control group and the tumor-bearing groups prior to the administration of ALA were not statistically significant. Following the administration of ALA, the p-values for the PpIX fluorescence difference between the control group and each of the tumor-bearing groups were statistically significant both *in vivo* and *ex vivo*.

Tumor Model	Background	2 hours after ALA	<i>Ex Vivo</i>
9L-GFP	0.24	0.037	0.002
U251	0.86	0.010	0.003
U251-GFP	0.99	0.027	0.031

Table 6.2 – p-value calculation using Student's t-test for PpIX fluorescence difference between the tumor-bearing group and the non-tumor-bearing control group at the time points shown.

ROC analysis was performed to determine the ability to detect each tumor type using the single channel spectroscopy system prior to ALA administration as well as *in vivo* and *ex vivo* 2 hours after ALA administration. Each ROC curve in Figure 6.11

shows the relationship between the false positive fraction (FPF) and true positive fraction (TPF) based on different fluorescence intensity thresholds for the 9L-GFP, U251 and U251-GFP tumor-bearing mice as compared to the non-tumor-bearing control mice. Prior to the administration of ALA, there was little detectable difference between the control mice and any of the tumor bearing groups, as the ROC curves for each tumor-bearing group were nearly linear which indicates a 50/50 chance of detecting tumor tissue when it is present Figure 6.11(a). The area under the curve (AUC) was calculated from the ROC curve and normalized to one. An area of 1 indicates 100% sensitivity and specificity of detection, while an area of 0.5 indicates 50% specificity and sensitivity, or random guessing. The AUC for each tumor line prior to ALA administration was nearly 0.5, indicating no specificity or sensitivity of detection (Table 6.3). Two hours after ALA administration the single channel spectroscopy system detection of the U251 and U251-GFP tumor-bearing mice was better than detection of the 9L-GFP tumor-bearing mice *in vivo* (Figure 6.11(b)). The AUC for the U251 and U251-GFP mice were very similar and considerably higher than the AUC for the 9L-GFP mice (Table 6.3). The *ex vivo* detection results were better than the *in vivo* detection results for all three tumor lines (Figure 6.11(c)). The AUC was similar for the three brain tumor types *ex vivo*, with substantial improvement over *in vivo* detection for the 9L-GFP tumors and modest improvement over *in vivo* detection for the other two tumor types (Table 6.3).

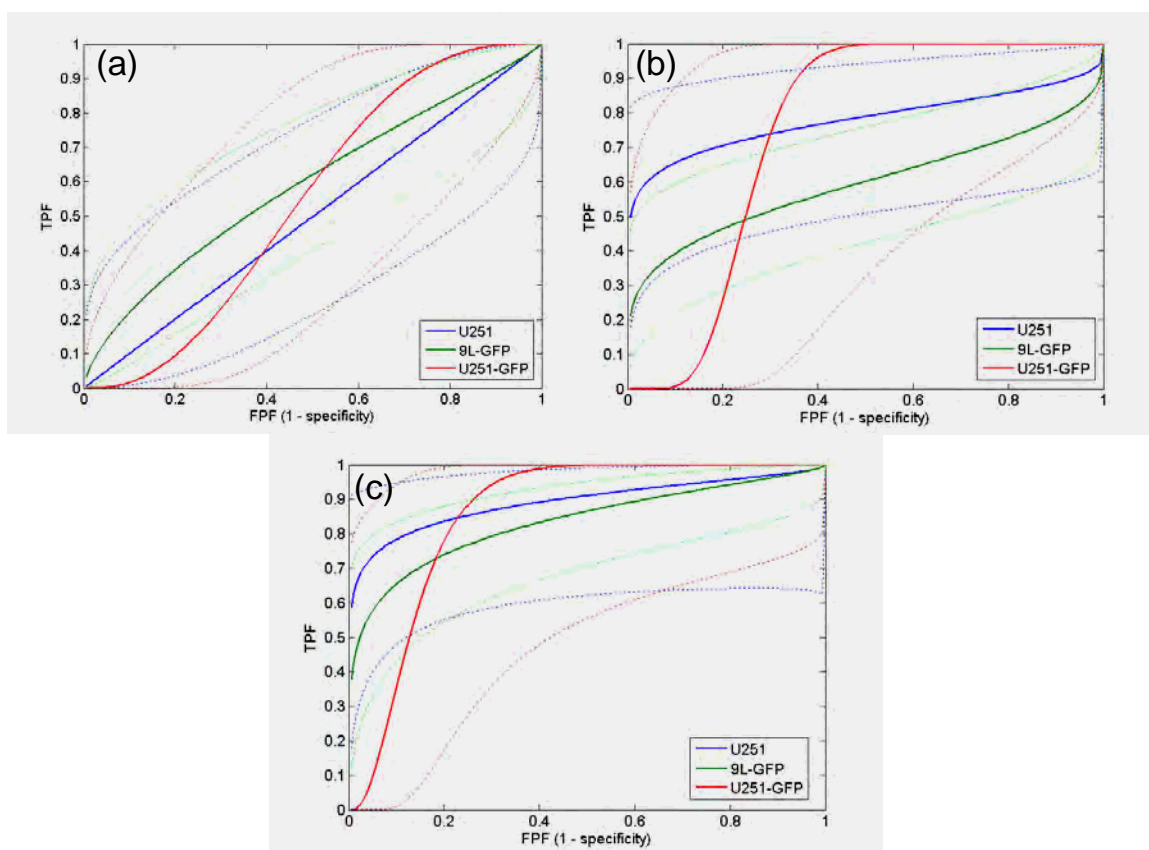


Figure 6.11 – ROC curves constructed from the PpIX summary data shown in Figure 6.10 to quantify the ability of the single channel spectroscopy system to detect 9L-GFP, U251 and U251-GFP tumor bearing mice over non-tumor-bearing control mice (a) prior to ALA administration, (b) *in vivo* 2 hours after ALA administration and (c) *ex vivo* 2 hours after ALA administration.

Tumor Model	Background	2 hours after ALA	<i>Ex Vivo</i>
9L-GFP	0.59	0.59	0.83
U251	0.50	0.78	0.89
U251-GFP	0.54	0.75	0.86

Table 6.3 – The area under the curve normalized to 1 as calculated from ROC curves shown in Figure 6.11. An area of 1 indicates detection with 100% specificity and sensitivity. An area of 0.5 indicates detection with 50% specificity and sensitivity.

6.5. PpIX Production Pattern Heterogeneity: *Ex Vivo* Analysis

The variance seen in the *in vivo* PpIX spectroscopy measurements was quite large in the 9L-GFP group and considerably smaller in the U251 and U251-GFP groups (Figure 6.10(b)). A similar pattern of variance was seen in the *ex vivo* bulk PpIX spectroscopy measurements where the 9L-GFP tumor line had the largest CV, 118%. The CV for the control group was 77%, which was higher than that seen in the U251 group (CV = 64%) or the U251-GFP group (CV = 45%). Following the *ex vivo* spectroscopy measurements, the brain tissue was further examined to determine PpIX production patterns. The brain was extracted and sectioned into quarters coronally; enabling *ex vivo* slices to be qualitatively matched to the *in vivo* MRI. The reflectance raster scanning system discussed in chapter 3 was used to scan the coronal brain sections. For the 9L-GFP and the U251-GFP tumors PpIX fluorescence scans were collected followed by GFP fluorescence, while the tumor tissue remained in the same orientation for direct comparison. All brain tissues were sent for H+E staining following measurement by the reflectance raster scanner.

When the *ex vivo* PpIX fluorescence measurements collected from the reflectance raster scanning system were examined a different PpIX production pattern was seen in the three tumor lines grown *in vivo*. Upon examination of the PpIX production pattern in the *ex vivo* 9L-GFP brain tumor tissue, a possible explanation of the large variance seen in spectroscopy measurements was possible. The example mouse illustrated in Figure 6.12(a) showed the PpIX production pattern that would be expected, where the increased PpIX fluorescence was seen in the bulk tumor. This can be seen via a comparison between the PpIX, GFP and H+E images shown in Figure 6.12(a). However, in

comparison to the population of 9L-GFP tumor-bearing mice examined via spectroscopy measurement, the example mouse shown in Figure 6.12(a) was anomalous. Most of the mice in the 9L-GFP population had PpIX production patterns which were more similar to those shown in Figure 6.12(b) and (c), where high PpIX production was not seen in the bulk tumor. Upon examination of Figure 6.12(b) and (c), it can be seen that the PpIX production in the two example mice shown, was primarily at the periphery of the tumor tissue when the PpIX image was compared to the corresponding GFP and H+E images. When the corresponding MRI images were examined, a low vascular density in the tumor did not seem to be the reason for the low PpIX production, as T1 turbo spin echo (TSE) images that had been enhanced with Gadolinium (Gd) show high contrast in the bulk tumor area. Since Gd is a vascular contrast agent, these images illustrated that the tumor was well vascularized and thus, a different explanation must exist for the PpIX production pattern.

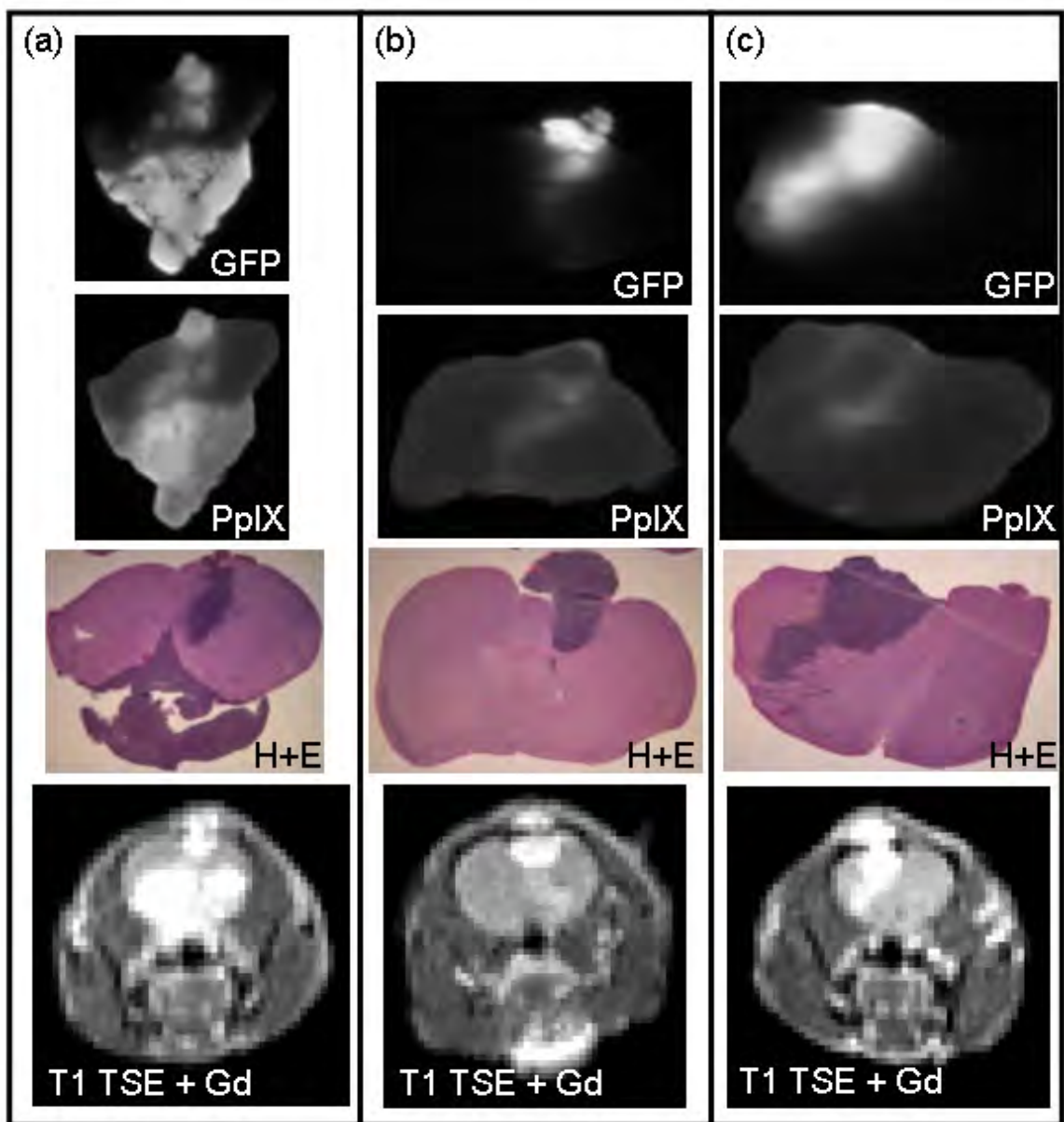


Figure 6.12 – Images from three example mice from the 9L-GFP tumor-bearing group are shown, one in each column, where *ex vivo* GFP fluorescence, PpIX fluorescence and the corresponding H+E staining are shown in the first three rows. The T1 TSE CE MR image which was qualitatively most similar to the *ex vivo* measurements was included for comparison.

A similar set of images for example U251 tumor-bearing mice were examined to determine if the PpIX production pattern was different from that seen in the 9L-GFP

tumors, since the variance seen in the spectroscopy measurements was less than that seen in the 9L-GFP tumor group. As can be seen in Figure 6.13, the PpIX production pattern for the U251 tumor tissue was substantially different from that seen in the 9L-GFP tumor line. The PpIX production was mostly confined to the bulk tumor tissue as can be seen when the *ex vivo* PpIX fluorescence images obtained on the reflectance raster scanning system were compared to the corresponding H+E images. The three examples shown in Figure 6.13 were representative of the U251 tumor-bearing population examined via the single channel spectroscopy, and all showed PpIX production contained within the bulk tumor instead of just around the periphery of the tumor as in the case of the 9L-GFP tumors. Interestingly, when the corresponding MRI images were examined the tumor borders were not as well delineated by T1 TSE CE MRI as seen in the 9L-GFP tumors (Figure 6.12 & Figure 6.13). T2 TSE MRI sequences were collected in addition to T1 TSE CE MRI on the U251 tumor-bearing group, in an attempt to obtain better tumor tissue contrast and tumor border delineation (Figure 6.13). The T2 TSE image did not increase the ability to differentiate the tumor margins over the T1 TSE CE MRI images.

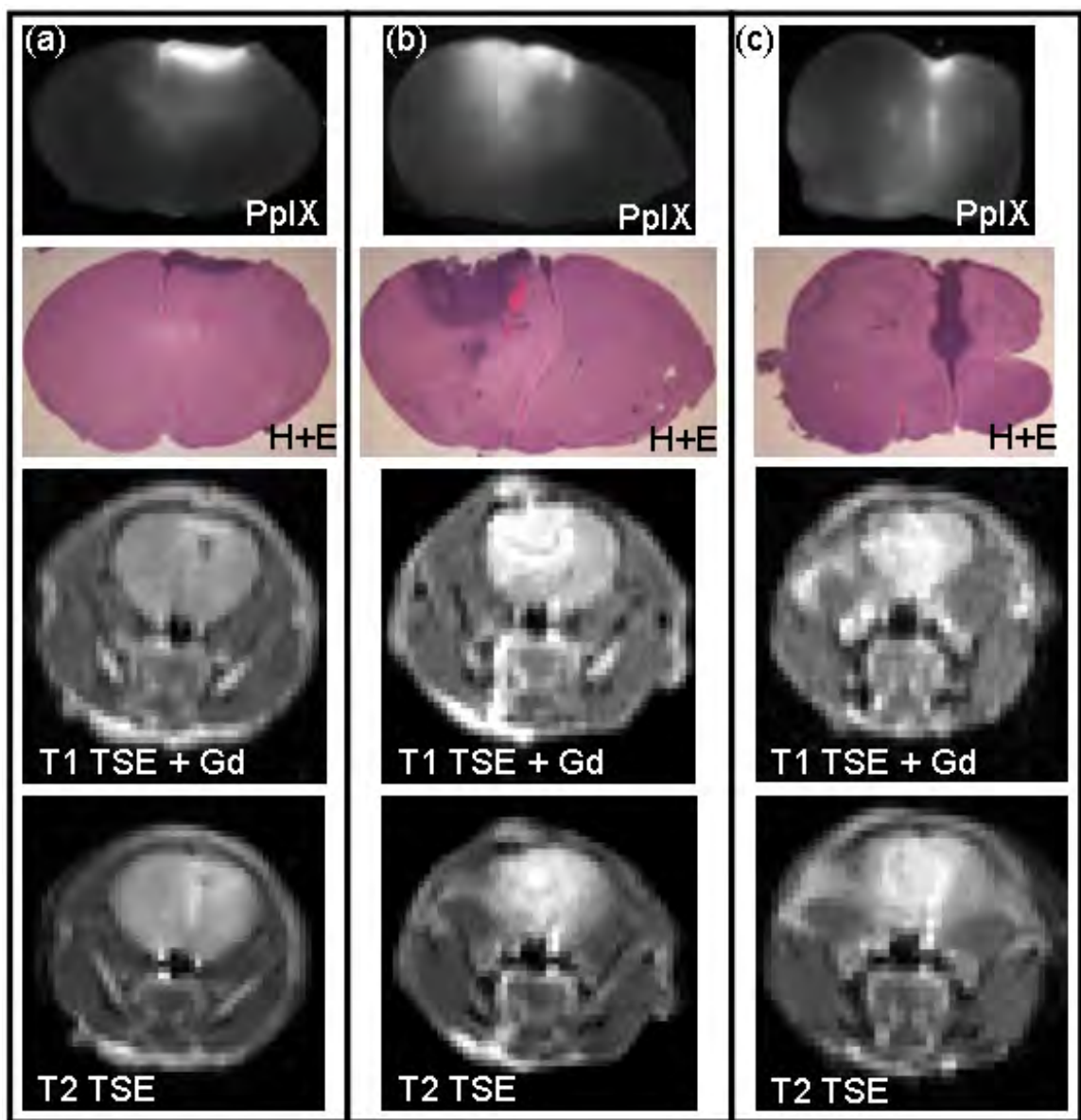


Figure 6.13 – Three representative examples of U251 tumor-bearing group are shown in the three columns, where the *ex vivo* PpIX fluorescence and corresponding H+E image are shown in the top rows. The U251 tumor line was not GFP transfected and thus, GFP images are not shown. The MRI slices which qualitatively corresponds to the *ex vivo* image are shown for both T1 TSE CE images (3rd row) as well as T2 TSE images (bottom row).

The U251-GFP tumor-bearing group had the smallest PpIX production variability by spectroscopy both *in vivo* and *ex vivo*. A similar set of images of the U251-GFP

tumor-bearing mice were examined to determine if the low PpIX variability could be explained by the PpIX production pattern seen via *ex vivo* reflectance raster scanning images. Similar to the examples shown of the U251 tumor-bearing group, the PpIX fluorescence of the U251-GFP tumor-bearing group was largely confined to the bulk tumor tissue (Figure 6.14). This production pattern was illustrated in the three representative examples of the U251-GFP tumor when compared to the GFP fluorescence images and the corresponding H+E images (Figure 6.14). The three example mice shown in Figure 6.14 were representative of the U251-GFP population on which single channel spectroscopy measurements were collected. The growth pattern of the U251-GFP tumor was quite different from either the 9L-GFP or the U251 tumor line which could be seen when the H+E images were examined. The U251-GFP tumor did not grow as a large mass of cells in the population of the U251-GFP tumors examined. Instead most of the U251-GFP tumors grew diffusely in the hemisphere of the brain in which they were implanted. Figure 6.14(a) shows an example U251-GFP tumor that grew as a mass in the brain, while Figure 6.14(b) and (c) illustrate the more common diffuse growth pattern of the U251-GFP tumor. This difference in growth pattern did not seem to affect the PpIX production pattern as all three example mice shown in Figure 6.14 had similar PpIX production patterns. Interestingly, when the MRI images were examined, the tumor tissue contrast was considerably different than that seen in the U251 or 9L-GFP images. Only the example shown in Figure 6.14(a) was easily visible via T1 TSE CE MRI while the other two examples, which were more representative of the U251-GFP population, did not have tumors that were easily visible by T1 TSE CE. Discussion of MRI visibility of these tumors can be found in chapter 5.

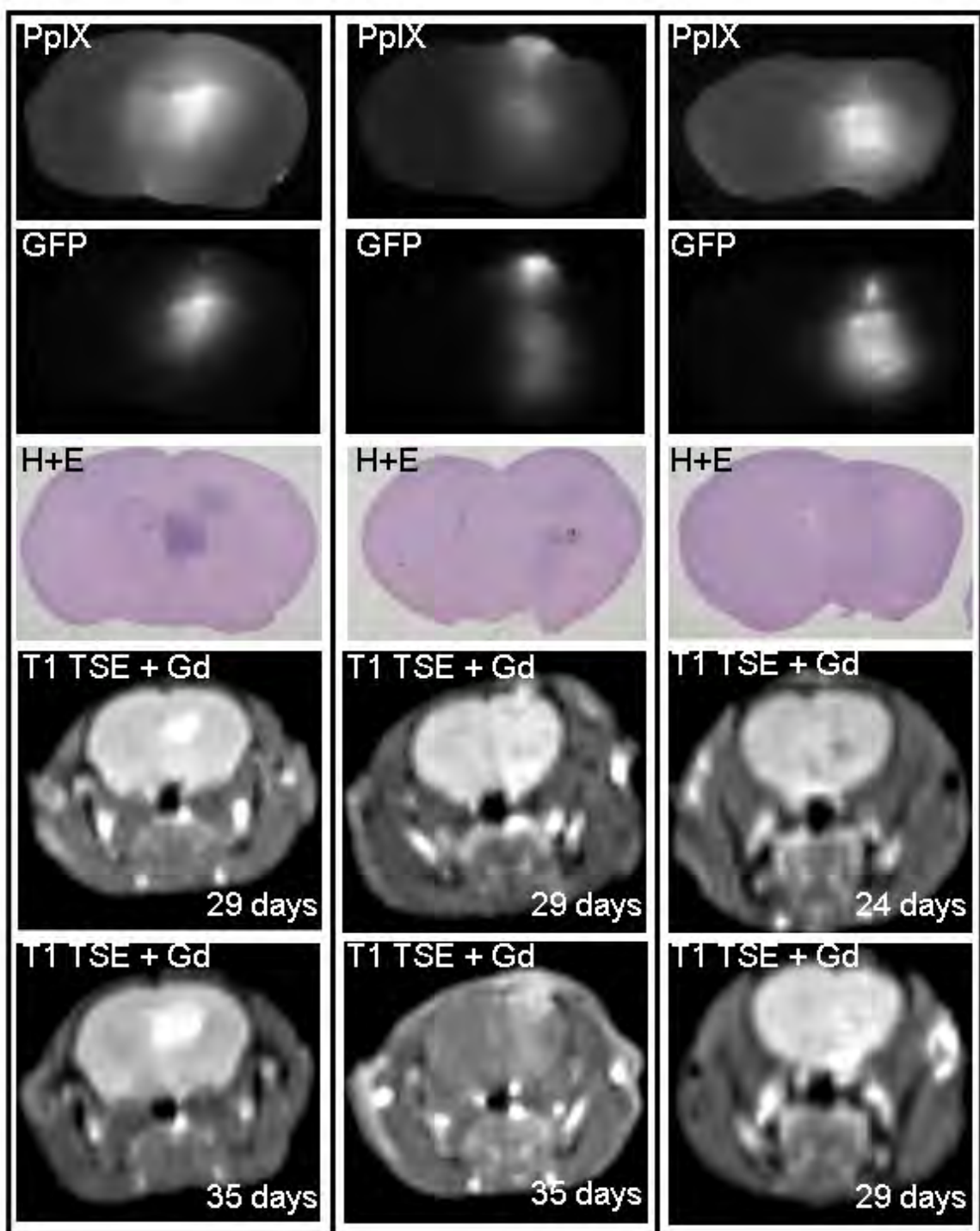


Figure 6.14 – Three examples of the U251-GFP tumor-bearing group are shown one per column, where the *ex vivo* GFP fluorescence, PpIX fluorescence and corresponding H+E slices are shown in successive rows. T1 TSE CE MRI images 29 days and 35 days

following tumor implantation are also shown. The MRI slices shown qualitatively corresponded to the *ex vivo* images.

The PpIX and GFP fluorescence contrast measured via the reflectance raster scanning system in the tumor tissue compared to the contralateral normal tissue in the same brain slice was quantified. The average PpIX fluorescence was higher in all tumor-bearing groups than in the control group (mean = 0.99), with the highest average fluorescence seen in the U251 group (mean = 3.66), and the lowest average PpIX fluorescence seen in the 9L-GFP group (mean = 1.65). The average PpIX fluorescence of the U251-GFP group (mean = 1.82) was slightly higher than the 9L-GFP group (Figure 6.15(a)). The 9L-GFP group and U251-GFP group were examined for tumor to contralateral normal tissue GFP contrast. As can be seen in Figure 6.15(b) GFP contrast of both tumor-bearing groups was considerably higher than the average GFP fluorescence in the control group (mean = 0.99). The average GFP contrast was higher in the 9L-GFP group (mean = 22.34) than in the U251-GFP group (mean = 7.47), although the variance in the U251-GFP group (CV = 63%) was smaller than that seen the 9L-GFP group (CV = 101%).

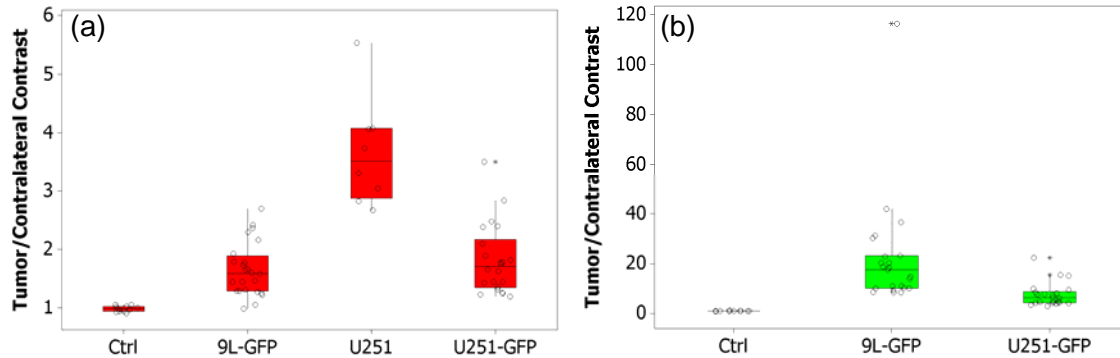


Figure 6.15 – Tumor tissue to contralateral normal tissue PpIX fluorescence measured in the control group and each of the tumor-bearing groups via the reflectance raster scanner is plotted for (a) PpIX fluorescence and (b) GFP fluorescence. The U251 parent line was not included in the GFP contrast graph since it was not a GFP transfected tumor line.

6.6. Discussion

Three brain tumor lines were studied *in vivo* which had very different tissue PpIX production patterns. The three tumor lines were examined for the ability to detect the brain tumor presence, *noninvasively* via spectroscopic measurements of PpIX fluorescence. Prior to the administration of ALA, tumor-bearing mice were not able to be distinguished from non-tumor-bearing control mice via *in vivo* PpIX spectroscopy measurements (Figure 6.10(a)). Two hours after that administration of 100 mg/kg ALA, the average PpIX fluorescence in each of the tumor-bearing groups was higher than in the control group (Figure 6.10(b)). This difference in PpIX fluorescence level was confirmed by *ex vivo* bulk spectroscopy measurements, which illustrated a similar pattern to that seen *in vivo*, where the PpIX fluorescence was higher on average in each of the tumor-bearing groups as compared to the control group of animals (Figure 6.10(c)). The reflectance raster scanner was also used to quantify PpIX fluorescence *ex vivo* and showed higher average PpIX fluorescence in the tumor bearing mice over the control

mice (Figure 6.15(a)). ROC analysis revealed that brain tumor detection via PpIX spectroscopy was better for the U251 and U251-GFP tumor-bearing groups than for the 9L-GFP tumor-bearing group *in vivo* 2 hours after ALA administration. *Ex vivo* detection via PpIX spectroscopy was improved for all three groups over *in vivo* detection 2 hours after ALA administration. *Ex vivo* detection was similar for the U251, U251-GFP and 9L-GFP tumor-bearing mice (Figure 6.11).

Skin photobleaching was examined for its ability to increase PpIX contrast between the tumor-bearing mice and the non-tumor-bearing control mice. A small pilot study was completed using blue light for skin photobleaching with promising results that indicated a photobleaching dose delivered to both sides of the mouse head improved the PpIX fluorescence different between tumor-bearing and control animals (Figure 6.3(d)). Both red light and blue light skin photobleaching were considered in larger studies. Time course, red light photobleaching was used in a study comparing the 9L-GFP and U251 tumor-bearing mice to non-tumor-bearing control mice. The PpIX fluorescence difference between the tumor-bearing groups and the control mice was largest 2 hours after the administration of ALA, prior to any skin photobleaching (Figure 6.5). However, prior to any skin photobleaching the average PpIX fluorescence of the 9L-GFP group was higher than the U251 group, which was not seen in *ex vivo* PpIX measurements (Figure 6.4 (b) & (c)). The red light photobleaching improved the ability to quantify the PpIX fluorescence which was contained in the brain tumor tissue. The relationship seen between the average PpIX fluorescence of the two tumor-bearing groups and the control group was very similar to that seen *ex vivo* following 296 J/cm² of red light photobleaching delivered over 8 minutes (Figure 6.5 & Figure 6.6). Additional PpIX

photobleaching was delivered and decreasing PpIX contrast was seen between the three groups as the cumulative photobleaching dose was increased (Figure 6.5).

Due to the penetration depth of red light during photobleaching, the use of blue light was investigated to selectively bleach the skin PpIX fluorescence, theoretically sparing any brain PpIX fluorescence. A study was completed on healthy mice to determine the minimum dose required to induce skin PpIX fluorescence decrease 2 hours after ALA administration. Three blue light photobleaching doses were considered and the smallest dose studied, 4 J/cm^2 , was found sufficient to cause skin PpIX fluorescence photobleaching (Figure 6.7(c)). The 4 J/cm^2 blue light dose was used in a study of 9L-GFP and U251-GFP tumor-bearing mice in comparison to a control group of mice to determine if PpIX fluorescence contrast was improved via blue light skin bleaching. Interestingly, in this experiment the PpIX fluorescence of the control mice appeared to be higher than in previous single channel spectroscopy experiments, where 2 hours after the administration of ALA, the average PpIX fluorescence of the control mice was higher than the 9L-GFP tumor bearing group and only slightly lower than the U251-GFP tumor-bearing group (Figure 6.8(b)). However, in *ex vivo* measurements, the average PpIX fluorescence of both the tumor-bearing groups was higher than that seen in the control group (Figure 6.8(d)). Although it would appear that skin PpIX fluorescence was causing this disparity in intensity of *in vivo* PpIX detected signal and skin photobleaching would improve the ability to detect the tumor-bearing group over the control group, this did not seem to be the case as photobleaching did not improve the contrast between the three groups (Figure 6.8(c)). Upon examination of the tissue slices *ex vivo*, it was determined that the U251-GFP tumors were significantly smaller than the 9L-GFP tumors. This

difference was quantified by determining the percentage of the brain tissue that was tumor using GFP images collected from the reflectance raster scanner. When the PpIX fluorescence to transmittance ratio obtained from spectroscopy measurements was normalized to the tumor size the average PpIX fluorescence in the U251-GFP group was much higher than in the 9L-GFP group at all time points measured (Figure 6.9).

Summary analysis was performed by normalizing all spectroscopy measurements to the average control mouse measurements, so that the data sets could be combined and the three tumor types could be directly compared (Figure 6.10). The combined data set showed prior to ALA administration the average PpIX fluorescence was similar for the control group and the three tumor bearing groups (Figure 6.10(a)). The difference between the non-tumor-bearing control group and each of the tumor-bearing groups was not significant prior to ALA administration (Table 6.2). Two hours after ALA administration the average PpIX fluorescence of each of the tumor bearing groups was higher than the control group which can be seen by both *in vivo* and *ex vivo* spectroscopy measurements (Figure 6.10(b) & (c)). A statistically significant difference in PpIX fluorescence was seen between the control group and each tumor-bearing group both *in vivo* and *ex vivo* (Table 6.2).

However, on a mouse by mouse basis, the PpIX fluorescence of tumor-bearing mice was not always higher than with the control mice. There was large variation in PpIX production ability of different tumor lines, as discussed extensively in chapter 2, as well as within a single tumor line. A large variance in PpIX production of normal mice was also seen as was illustrated in the skin photobleaching experiment of healthy mice, as well as the control mice in all tumor detection experiments both before and after

administration of ALA (Figure 6.7(c) and Figure 6.10). An explanation for the PpIX production difference was examined *in vitro* in chapter 2, and determined to be related to tumor cell size. Tumor cells grown *in vivo* also show varied ability to produce PpIX as can be examined via PpIX production patterns illustrated in Figure 6.12 – Figure 6.14. This varied PpIX production capacity of different tissues may help to explain the inability to determine tumor status on a mouse by mouse basis. Methods to increase tumor tissue production of PpIX could be further explored such as iron chelation [60, 67], however methods to decrease PpIX production heterogeneity would perhaps be more useful for *in vivo* detection of brain tumors on a mouse by mouse basis. Differentiation therapy applied for a short time periods prior to the administration of ALA has been shown *in vitro* to increase overall PpIX production, as well as decrease the fraction of cells in the population that contain low levels of PpIX [80]. Additional experimentation with *in vitro* and/or *in vivo* differentiation therapy to decrease PpIX production heterogeneity could be completed in the future to improve brain tumor detection on a mouse by mouse basis. Case studies of mouse PpIX fluorescence *in vivo* and *ex vivo*, pathology and MRI visibility will be further discussed in chapter 8. The different imaging modalities will be examined together to determine if tumor morphology can be related to PpIX production and heterogeneity.

Chapter 7 - Epidermal Growth Factor Uptake & Erbitux Therapy Monitoring

7.1. Introduction

Malignant gliomas account for a relatively small number of cancer patient diagnosed yearly, with less the 19,000 cases diagnosed in the United States in 2005. However, patients diagnosed with malignant gliomas have a very poor prognosis as nearly 100% are lethal. Even with aggressive therapy which typically includes surgical resection, radiation and temozolomide chemotherapy, glioblastoma multiforme patient survival is typically 9 – 12 months following diagnosis [14]. Substantial research has been completed on molecularly targeted therapies for all different types of cancer. Glioblastoma multiforme (GBM) is well suited for treatment via targeted molecular therapy because it has a defined set of ‘molecular lesions’ as well as identified signaling pathway interruptions that provide clear targets [18]. One such target is epidermal growth factor receptor (EGFR) which is overexpressed in 40 – 50% of all GBMs [18, 119].

EGFR is a transmembrane protein with three domains which include an extracellular ligand-binding domain, the transmembrane region and an intracellular protein tyrosine kinase domain [20]. EGFR is overexpressed on many types of cancers and has been shown to promote development and progression of malignancy because it is associated with proliferation, angiogenesis, metastasis and apoptosis inhibition [16]. Different methods to shutdown EGFR activation have been investigated, including blocking binding of the extracellular domain to its ligands, transforming growth factor α (TGF α) and epidermal growth factor (EGF), and methods at inactivating signaling

cascades via tyrosine kinase [19]. Anti-EGFR monoclonal antibodies were developed to target the extracellular domain of the receptor and have been shown to successfully inhibit EGFR activation. One such antibody, IMC-C225/cetuximab has been commercially developed by ImClone as the molecularly targeted therapy Erbitux.

Erbitux binds competitively to the extracellular domain of human EGFR with a two-log higher affinity than either TGF α or EGF. Once Erbitux is bound to EGFR, the antibody-receptor complex is internalized and inactivated. Thus, signaling from EGFR through the tyrosine kinase is blocked by both downregulation of the cell surface receptors as well as competitive binding between Erbitux, EGF and TGF α for EGFR. Decreased EGFR activation is associated with inhibition of cell growth, induction of apoptosis and a decrease in matrix metalloproteinase and vascular endothelial growth factor production [19, 20]. The FDA approved Erbitux therapy in 2004 for the treatment of patients with advanced colorectal cancer that did not respond to irinotecan and in 2006 as a monotherapy for head and neck cancer or in combination with radiation therapy [19]. Clinical trials for GBMs are still in preliminary stages although preclinical data showed that systemic treatment with Erbitux decreased proliferation and increased apoptosis in xenografts models of GBM grown both subcutaneously and orthotopically, when the cell line overexpressed EGFR [17]. These results are encouraging due to concern about restricted delivery of high molecular weight monoclonal antibodies across an intact or only partially impaired blood brain barrier [14, 17].

In the current study, Erbitux was used as a monotherapy to treat two types of brain tumors, a positive expression model with high EGF uptake and a negative control with low EGF uptake. The brain tumor with high EGF uptake was assumed to have

higher EGFR expression than the brain tumor with low EGF uptake and thus was expected to show more response to Erbitux therapy than the brain tumor with low EGF uptake and thus lower EGFR expression. The goal of this molecular imaging study was two-fold. First, to determine if EGF uptake could be detected *in vivo*, using a fluorescently labeled EGF and second to determine if use of this fluorescently labeled EGF would enable fluorescence detection of treatment efficacy. The ability to noninvasively detect high EGF uptake *in vivo* would allow for tumors to be stratified into groups that would potentially respond to Erbitux therapy and groups that would not. By comparing the positive expression model to the negative control, it was possible to monitor the efficacy of Erbitux therapy through EGF uptake in a responsive and unresponsive model.

7.2. Epidermal Growth Factor Uptake & Erbitux Therapy Monitoring *In Vitro*

A panel of brain cancer cell lines that included 9L-GFP (rat gliosarcoma), U251 (human glioma), CNS-GFP (rat glioma), F98 (rat glioma) and C6-GFP (rat glioma) were tested for epidermal growth factor (EGF) uptake. Each cell line was plated in 60 mm dishes at a concentration of 1×10^5 in triplicate and allowed to attach for 24 hours prior to EGF uptake measurements. A 4th 60 mm dish was also plated for each cell line to examine background fluorescence at the excitation and emission wavelength of the bound dye. EGF conjugated to Alexa Fluor 647 (Molecular Probes, Eugene, OR) was used to determine the *in vitro* EGF uptake of the 5 cell lines tested via flow cytometry. A 633 nm laser was used for excitation and a 661/16 nm band pass filter was used to collect the emission. Each sample was incubated with 5 $\mu\text{g/ml}$ EGF-Alexa Fluor 647 (EGF-

AF647) in media containing 1% fetal bovine serum for 30 minutes prior to trypsinization and preparation for measurement via flow cytometry. A similar procedure to that described in chapter 2 for the PpIX flow cytometry experiments was used to prepare the cells for EGF uptake measurements. Briefly, the dye containing media was removed from the cells and the cells were washed once with PBS prior to trypsinization. The trypsin was diluted with PBS and the cells were centrifuged for 5 minutes, after which the supernatant was removed, and the cells were resuspended in 500 μ l of PBS for measurement via flow cytometry.

The cell lines tested showed varied EGF uptake as can be seen in Figure 7.1. The 9L-GFP, CNS-GFP, F98 and C6-GFP cell lines all had similar magnitudes of EGF uptake, while the U251 cell line showed significantly higher EGF uptake (mean EGF-AF647 fluorescence: 9L-GFP = 72.3, U251 = 1388.3, CNS-GFP = 52.7, F98 = 24.9, C6-GFP = 107.3). The U251 cell line was selected as the positive expression model for comparison with the 9L-GFP cell line, the negative control. The EGF uptake of the U251 cell line was about 20-fold higher *in vitro* as compared to the 9L-GFP cell line. Higher EGF uptake was hypothesized to correspond to higher EGFR expression and thus, Erbitux therapy administered to the U251 cell lines was expected to decrease EGF uptake corresponding to effective therapy. Since the 9L-GFP cell line had 20-fold less EGF uptake and presumably therefore less EGFR expression, Erbitux therapy was expected to be ineffective against this model.

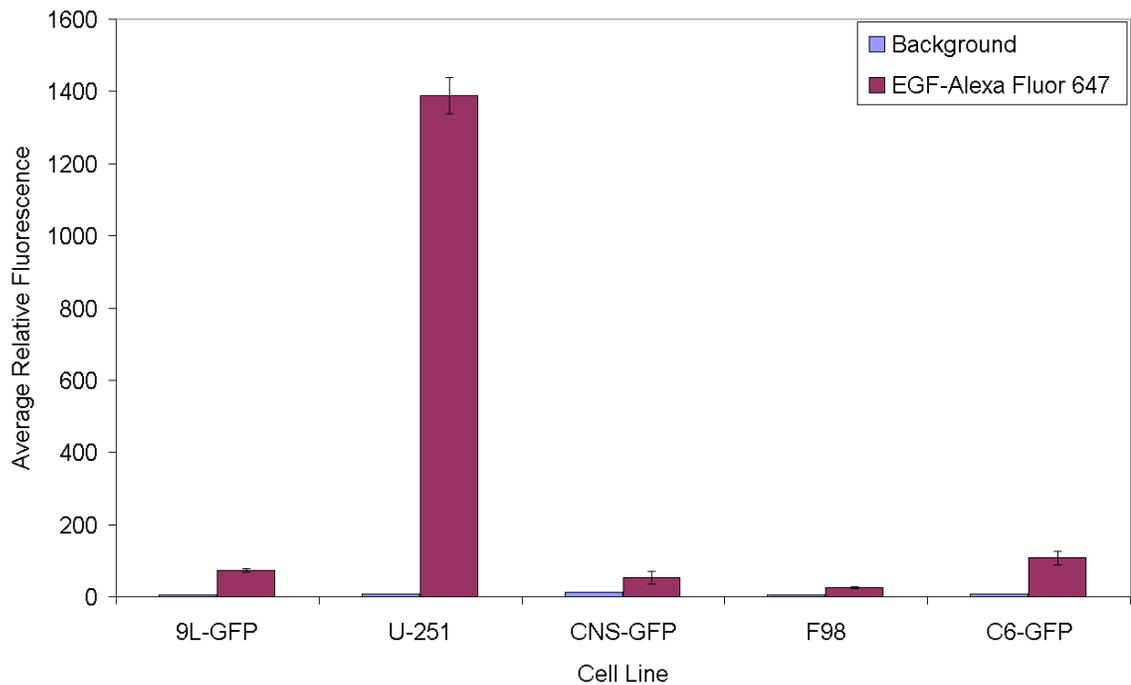


Figure 7.1 – The EGF uptake of a panel of brain cancer cell lines as measured via flow cytometry quantification of fluorescently labeled EGF. The blue bars represent the endogenous fluorescence of each cell line at the excitation and emission wavelengths of Alexa Fluor 647. The purple bars represent mean fluorescence from three samples for each cell line incubated with EGF-AF647, with error bars showing the standard deviation of the mean.

An *in vitro* study was completed to determine if a fluorescence difference in EGF uptake via flow cytometry could be visualized between treated and untreated cells with varied concentrations of Erbitux (ImClone, Bristol-Myers Squibb Co, Princeton, NJ). Following the results of the EGF uptake experiment (Figure 7.1), a fluorescence difference corresponding to EGF uptake after Erbitux therapy was expected to be seen in the U251-GFP cell line, but not in the 9L-GFP cell line. Each cell line was plated at a concentration of 5×10^4 in triplicate for each drug concentration and time point tested. Both Erbitux therapy concentration and administration time were varied to determine

when the largest fluorescence difference could be seen in EGF uptake between Erbitux treated and untreated cells. EGF-AF647 was used as previously described to determine the EGF uptake difference between treated and untreated cells at all Erbitux therapy concentrations and administration times. Erbitux therapy was administered to the cells at concentrations of 0, 0.01, 0.1, 1, 10 and 100 $\mu\text{g/ml}$ as was previously used by Eller, *et al* for viability studies on brain tumor cell lines isolated from human tumor tissue removed during surgery [120]. For the U251-GFP cell line Erbitux therapy was administered for 6, 12, 24, 48 or 72 hours prior to staining with EGF-AF647 to examine EGF uptake of the cells. For the 9L-GFP cell line Erbitux therapy was administered for 12, 24, 48 or 72 hours prior to staining with EGF-AF647. The same procedure described previously was used for cell preparation and fluorescence reading via flow cytometry. It should be noted that the time points shown in Figure 7.2 corresponded to the amount of time the Erbitux therapy was incubated with the cells prior to the addition of EGF-AF647 for 30 minutes before flow cytometry measurements.

EGF uptake of the U251 cell line was not affected by the GFP transfection, as the transfected line also had about a 20-fold higher EGF uptake than the 9L-GFP cell line (Figure 7.1 & Figure 7.2). As can be seen in Figure 7.2, the EGF uptake of the U251-GFP cell line was highly effected by Erbitux therapy, even a the lowest dose tested (0.01 $\mu\text{g/ml}$), while the EGF uptake of the 9L-GFP cell line was largely unaffected by the Erbitux therapy, even at the highest concentration tested (100 $\mu\text{g/ml}$). Different incubation times of Erbitux therapy on the U251-GFP cell line had varied affect on the EGF uptake of the cells especially at the lower concentrations of Erbitux therapy. The U251-GFP cell line showed increased EGF uptake after incubation with 0.01 $\mu\text{g/ml}$

Erbitux therapy for 48 and 72 hours as compared to the EGF uptake after 6, 12 and 24 hours incubation. The EGF uptake increased by about four-fold at the longer time points (48 and 72 hours) of Erbitux therapy incubation. The lowest EGF uptake, and thus the lowest EGF-AF647 fluorescence, for the U251-GFP cell line was seen 12 hours after Erbitux administration. Since the largest fluorescence difference was seen between treated and untreated cells after 12 hours of Erbitux incubation this time point was chosen for all *in vivo* studies. The fluorescence difference was especially apparent at the lower Erbitux concentrations (0.01, 0.1 and 1 $\mu\text{g/ml}$), which were assumed to be more physiologically relevant for tumor tissue concentration based on an exploratory pharmacokinetics study in mice by Luo, *et al* [121]. This study was conducted on GEO human colon cancer implanted subcutaneously in nude mice. Pharmacokinetic analysis was conducted for plasma concentrations of Erbitux as well as tumor concentrations following a single IP administration of Erbitux at varied doses including 1, 0.25 and 0.04 mg/dose. The mice were monitored for 72 hours following Erbitux administration and the plasma concentration was found to be relatively constant during this period. The tumor concentration was about 30 times lower than the plasma concentration and also relatively constant during the 72 hours following Erbitux administration [121].

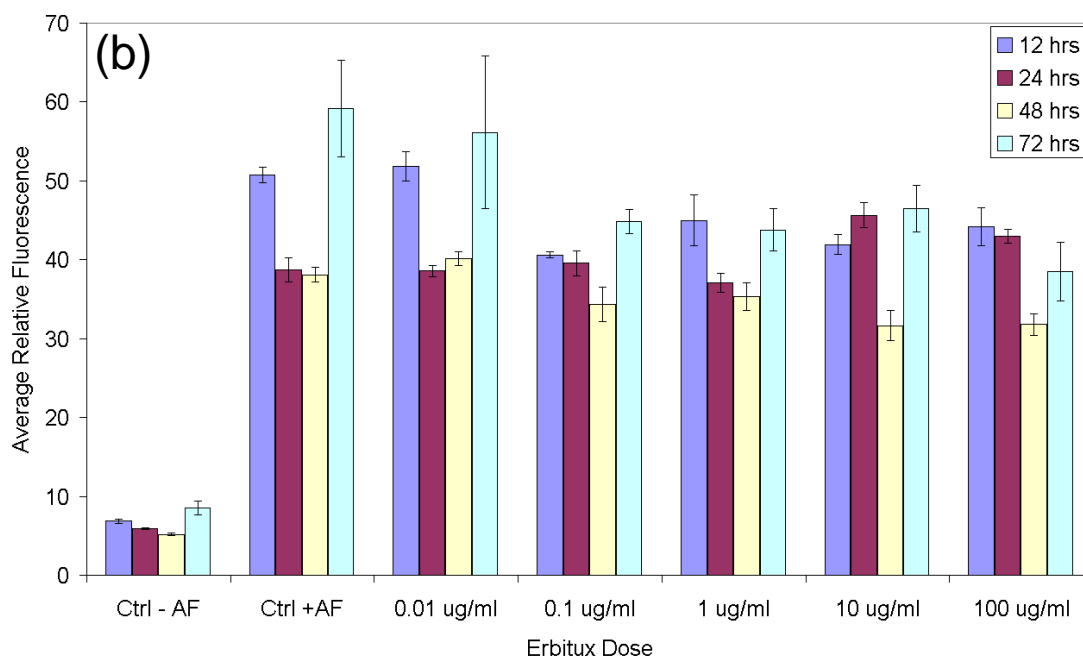
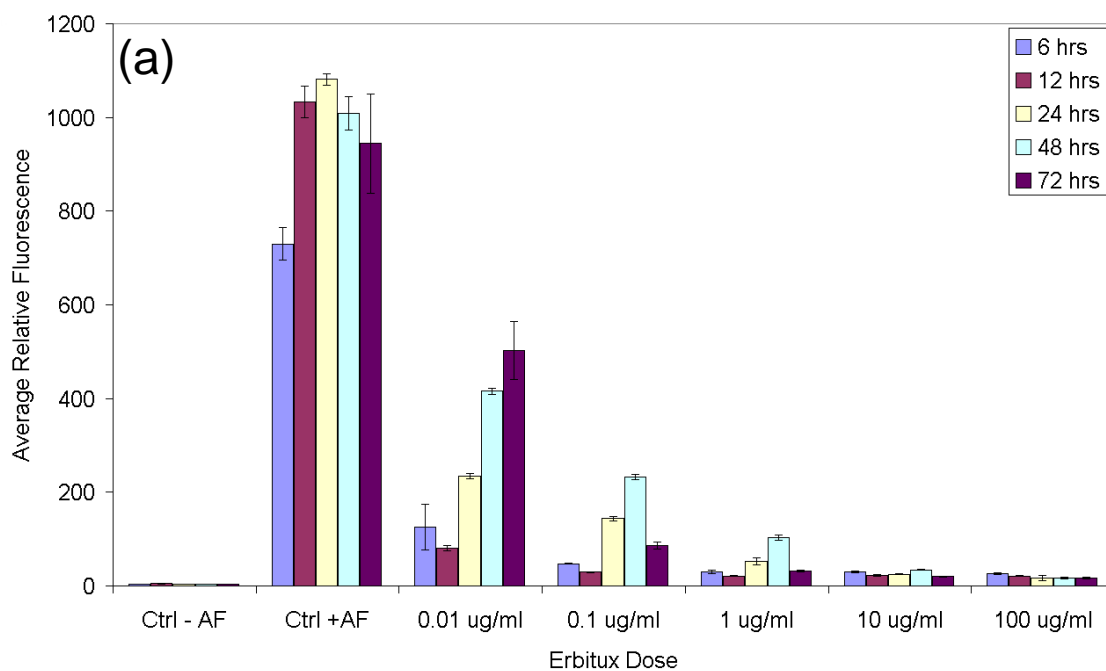


Figure 7.2 – The EGF uptake of U251-GFP cells (a) and 9L-GFP cells (b) as measured by EGF-AF647 fluorescence, following varied incubation times with different Erbitux concentrations. The bars labeled Ctrl –AF represents the background, endogenous fluorescence of the cell line at the excitation and emission wavelengths of Alexa Fluor 647. The point labeled Ctrl +AF represents the fluorescence from EGF uptake of untreated cells. Each bar represents the average of three samples, and the error bar shows the standard deviation.

7.3. Erbitux Therapy Monitoring *In Vivo*

7.3.1. Erbitux Therapy Monitoring *In Vivo* Materials & Methods

An *in vivo* treatment monitoring study was performed to compare intracranially implanted U251-GFP and 9L-GFP brain tumors. A similar fluorescence monitoring technique to that used *in vitro* where fluorescently labeled EGF was administered following Erbitux therapy, was used *in vivo* and monitored via the multichannel fluorescence spectroscopy system (chapter 3). The EGF-IRDye 800CW Optical Probe (LI-COR Biosciences, Lincoln, NE) was used for *in vivo* monitoring of EGF uptake because it had more optimal excitation (broad absorption band centered at 775 nm, 690 nm used here) and emission wavelengths (centered at 805 nm) for *in vivo* detection than EGF-AF647. From *in vitro* experimental results, the U251-GFP brain tumors were expected to show decreased EGF uptake following Erbitux therapy which would be detectable via fluorescence decrease as compared to untreated animals. The 9L-GFP brain tumors were expected to be unaffected by the Erbitux therapy and thus fluorescence of treated and untreated animals would be the same. The procedure described in chapter 2 was used for brain tumor implantation of 18 9L-GFP tumors and 17 U251-GFP tumors. Sham surgeries were also performed on 8 mice which acted as the control in the experiment. Mice from each of the tumor-bearing and control groups were stratified into either an Erbitux treated or an untreated group. There were 9 mice in both the 9L-GFP treated and untreated groups, 9 mice in the U251-GFP treated group and 8 mice in the U251-GFP untreated group. The control group was divided so that half the animals received Erbitux treatment and the other half did not (4 treated and 4 untreated).

A timeline of the Erbitux treatment monitoring study can be seen in Figure 7.3 and is explained as follows. All mice had surgery on day 0 and were either implanted with intracranial brain tumors or received sham surgery in the case of the control mice. On the 12th day of the experiment, MRI was performed to identify tumor presence. Following MRI on the 12th day, Erbitux was administered to all treatment groups (9L-GFP, U251-GFP and control) IP in the evening to allow circulation for 12 hours prior to EGF-IRDye administration (Figure 7.3). Erbitux was administered at a dose of 1 mg/mouse by IP injection as this was the most frequently administered dose for *in vivo* mouse studies in literature [21, 120-123]. Some studies administered the drug IP, while other studies administered the drug IV, but efficacy was seen with both administration routes. On the 13th day of the experiment, 1 nmole of EGF-IRDye in 75 μ l of PBS was injected intravenously via the tail vein according to manufactures instructions [124]. The EGF-IRDye fluorescence of the mice was monitored using the multichannel fluorescence spectroscopy system with a 690 nm laser for excitation and a 720 LP filter to collect emission data. Prior to the Erbitux treatment monitoring experiment, a pilot experiment was performed with intracranially implanted 9L-GFP and U251-GFP cells where tumor-bearing mice were administered EGF-IRDye IV and sacrificed 24, 48, 72 and 96 hours following dye injection. At each time point the brains were extracted and scanned for EGF-IRDye fluorescence on the Odyssey Infrared Imaging System (LI-COR Biosciences, Lincoln, NE) which is a reflectance raster scanner optimized to detect the LI-COR dyes. These time points were modeled after previous experiments performed by Kovar, *et al* using the EGF-IRDye to examine molecular mechanisms in prostate cancer progression. In these studies the mice were imaged every 24 hours for up to 8 days after

IV administration of the EGF-IRDye with the best signal to noise ratios obtained 72 to 96 hours after injection [124]. In the pilot study, the EGF-IRDye fluorescence was localized in the brain tumor tissue as compared to the normal brain at each of the time points tested and showed decreasing fluorescence signal over the 96 hour period (data not shown).

For the Erbitux treatment monitoring study, EGF-IRDye fluorescence was monitored 24, 48 and 72 hours following administration (Figure 7.3). Since EGF-IRDye fluorescence was observed in the brains of the pilot study mice at up to 96 hours following administration of the fluorophore, it was hypothesized that *in vivo* monitoring at 24 hour intervals would allow for visualization of the pharmacokinetics of the drug clearance as well as delineation of the optimal time point for brain tumor signal detection.

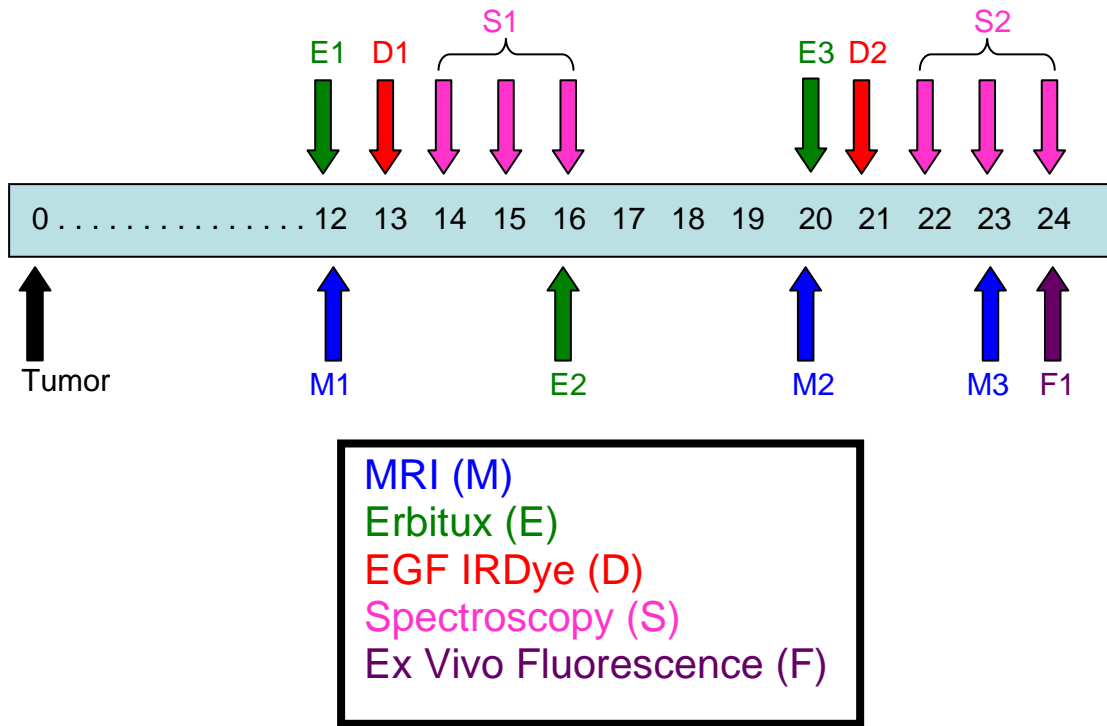


Figure 7.3 – The timeline for the Erbitux therapy monitoring experiment is shown. The experiment started on day 0, with tumor implantation. Each mouse in the study received MRI, EGF-IRDye and fluorescence monitoring via spectroscopy on the days as shown.

Only the mice in the treatment groups received the Erbitux therapy on the appropriate days.

Following the first round of spectroscopy measurements, the mice in the treated groups were administered a second dose of Erbitux therapy (1 mg/mouse IP) on the 16th day of the study to keep the plasma concentration of the Erbitux constant in the treated group [121]. MR images were collected on the 20th day of the experiment to monitor any visible tumor size changes. Following MRI, the treated groups were again administered Erbitux therapy in the evening. On the 21st day a second dose of EGF-IRDye was administered intravenously and the second round of fluorescence spectroscopy measurements were obtained 24, 48 and 72 hours following administration. Following the 72 hour fluorescence spectroscopy measurement, corresponding to the 24th day of the experiment, the mice were sacrificed and their brains were extracted (Figure 7.3). The brains were scanned on the Odyssey system for *ex vivo* quantification of EGF-IRDye fluorescence. Following scanning on the Odyssey system the brains were imaged on the reflectance raster scanning system for GFP fluorescence to visualize tumor size and growth pattern. All brains were preserved in 10% formalin for standard H+E staining.

7.3.2. Erbitux Therapy Monitoring In Vivo Results

7.3.2.1. Transmission Spectroscopy Measurements Week 1

MR images on the 12th day of the experiment showed tumor presence in all implanted 9L-GFP tumor-bearing mice. In contrast, tumor visualization in the U251-GFP group was largely not possible via MRI, as discussed in chapter 5. However, due to the success rate of previous brain tumor implantation procedures, all mice implanted with

brain tumors were stratified into either the treated or untreated groups. Spectroscopy was performed using the multichannel fluorescence spectroscopy system 24, 48 and 72 hours after administration of the EGF-IRDye. Data was collected at both the excitation and emission wavelengths, which was postprocessed as described in chapter 3, to obtain the integrated, spectrally fitted fluorescence to transmittance ratio of *in vivo* EGF-IRDye. Data from the first week of spectroscopy measurements can be seen in Figure 7.4 where box and whisker plots show the mean and interquartile range of the groups, with each open circle representing an individual animal. The animals in the control group were averaged to obtain the mean fluorescence to transmittance ratio at each source-detector position. All mice were normalized to this average measurement on a point by point basis including the 8 control mice. Thus, the y-axis on the graphs in Figure 7.4 represents the average of the 56 measurements after normalization of each individual source-detector measurement to the average control measurement at that source-detector pair. This normalization scaled the data so that anything with a mean around zero was considered the same as the control animals. The normalization also provided better visualization of the fluorescence relationship between the groups without showing the fluorescence decrease due to pharmacokinetic clearance of the EGF-IRDye.

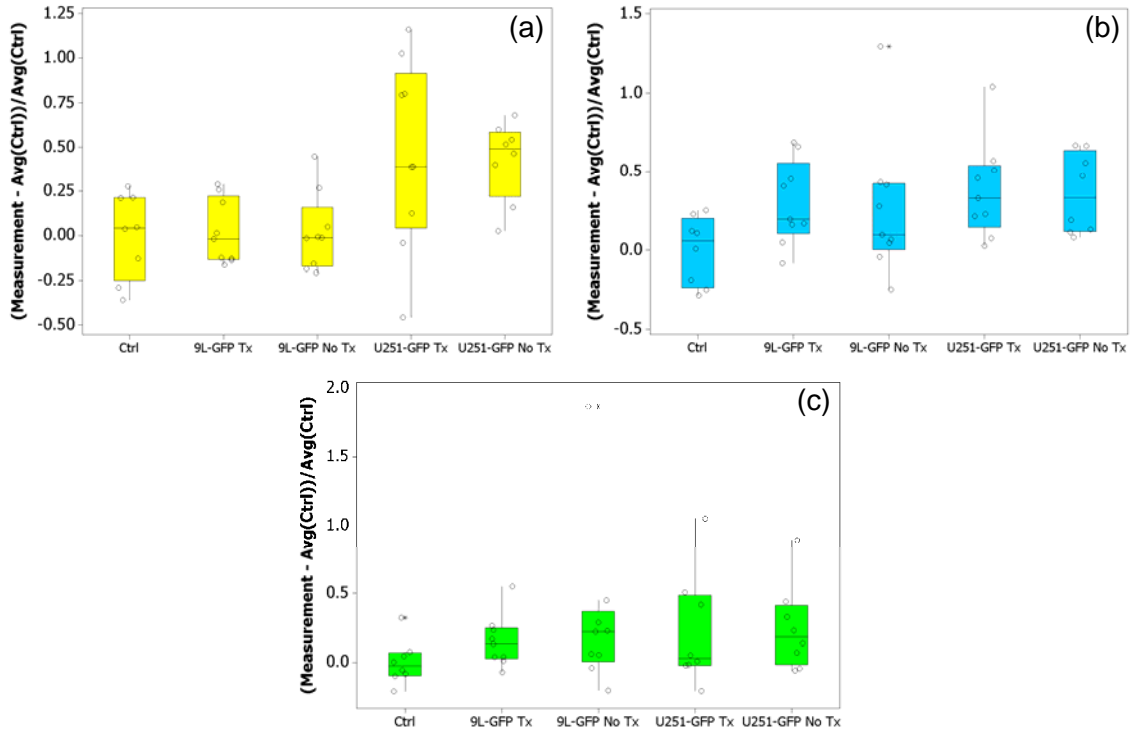


Figure 7.4 – Integrated, spectrally fitted fluorescence to transmittance ratio normalized to the average control mouse of EGF-IRDye fluorescence at each source-detector point for the first week of spectroscopy measurements, obtained on days 14 – 16 of the experiment. The treated and untreated groups for the 9L-GFP and U251-GFP tumor-bearing mice, and a mixed treated and untreated control group are illustrated in the graphs. *In vivo* EGF-IRDye fluorescence (a) 24 hours, (b) 48 hours and (c) 72 hours after administration.

The 9L-GFP treated and untreated groups had similar mean EGF-IRDye fluorescence to one another as well as to the control group 24, 48 and 72 hours after EGF-IRDye administration (Figure 7.4). The mean U251-GFP EGF-IRDye fluorescence in both the treated and the untreated groups was higher than that seen in either of the 9L-GFP tumor bearing groups or the control group 24 hours after EGF-IRDye administration. The mean EGF-IRDye fluorescence of the U251-GFP untreated group was higher than the U251-GFP treated group, although the variance in both groups was

quite large (Figure 7.4(a)). Although, a statistically significant difference was not visible between the U251-GFP treated and untreated groups, the relationship between the control mice and the treated and untreated groups displayed the expected trend. The 9L-GFP treated and untreated tumor-bearing mice did not illustrate different EGF-IRDye fluorescence which was expected from the low EGF uptake seen in the *in vitro* experiments as well as the similar fluorescence seen in treated and untreated cells. The U251-GFP tumor-bearing mice had higher EGF-IRDye fluorescence than either of the 9L-GFP groups or the control group, as would be expected from the *in vitro* experiment that illustrated twenty-fold higher EGF uptake (Figure 7.2). A statistically significant difference was visible between the U251-GFP untreated group and the control mice (p-value = 0.003), illustrating significant EGF uptake of the U251-GFP tumor *in vivo*. The U251-GFP untreated group also had significantly higher EGF-IRDye fluorescence than the 9L-GFP untreated group at the 24 hour time point (p-value = 0.002).

The EGF-IRDye fluorescence was also examined by individual source-detector pairs instead of by averaging over all the source-detector pairs. As expected, some source-detector pairs showed higher fluorescence to transmittance ratio, corresponding to measurements of light from opposite sides of the brain, while other source-detector pairs showed relatively lower fluorescence to transmittance ratio, corresponding to measurements of light from the same side of the brain. Interestingly, there was a distinct pattern in the source-detector measurements that was repeatable between all animals, as can be seen in Figure 7.5. All spectroscopy measurements collected 24 hours after EGF-IRDye administration (Figure 7.4(a)) are shown as individual source-detector pairs in Figure 7.5(b) and (c). A statistically significant difference was seen between the average

of the control mice and the U251-GFP untreated group when all source-detector pair measurements were averaged (p-value = 0.003), as seen in Figure 7.4. When the individual source-detector measurements were examined, it could be seen that all but one of the source-detector pairs, measurement number 24, showed higher fluorescence to transmittance ratio in the average of the U251-GFP untreated group than in the average of the control group (Figure 7.5(b)). When the 9L-GFP treated and untreated groups were examined on a point-by-point basis in comparison to the control, the fluorescence to transmittance ratio was nearly identical at most source-detector measurements, and thus the fluorescence to transmittance ratio of the 9L-GFP untreated group and the control group were the same (p-value = 0.867). There was not a statistically significant difference between the U251-GFP treated and untreated groups, although the mean fluorescence to transmittance ratio was higher in the U251-GFP untreated group as compared to the treated group (Figure 7.4(a) & (c)). Figure 7.5(a) also illustrated that the U251-GFP untreated group had higher EGF-IRDye fluorescence as compared to the U251-GFP treated group at many, but not at all source detector pairs. Figure 7.5(c) showed virtually no fluorescence difference between the 9L-GFP treated and untreated groups even when the data was examined on a point by point basis.

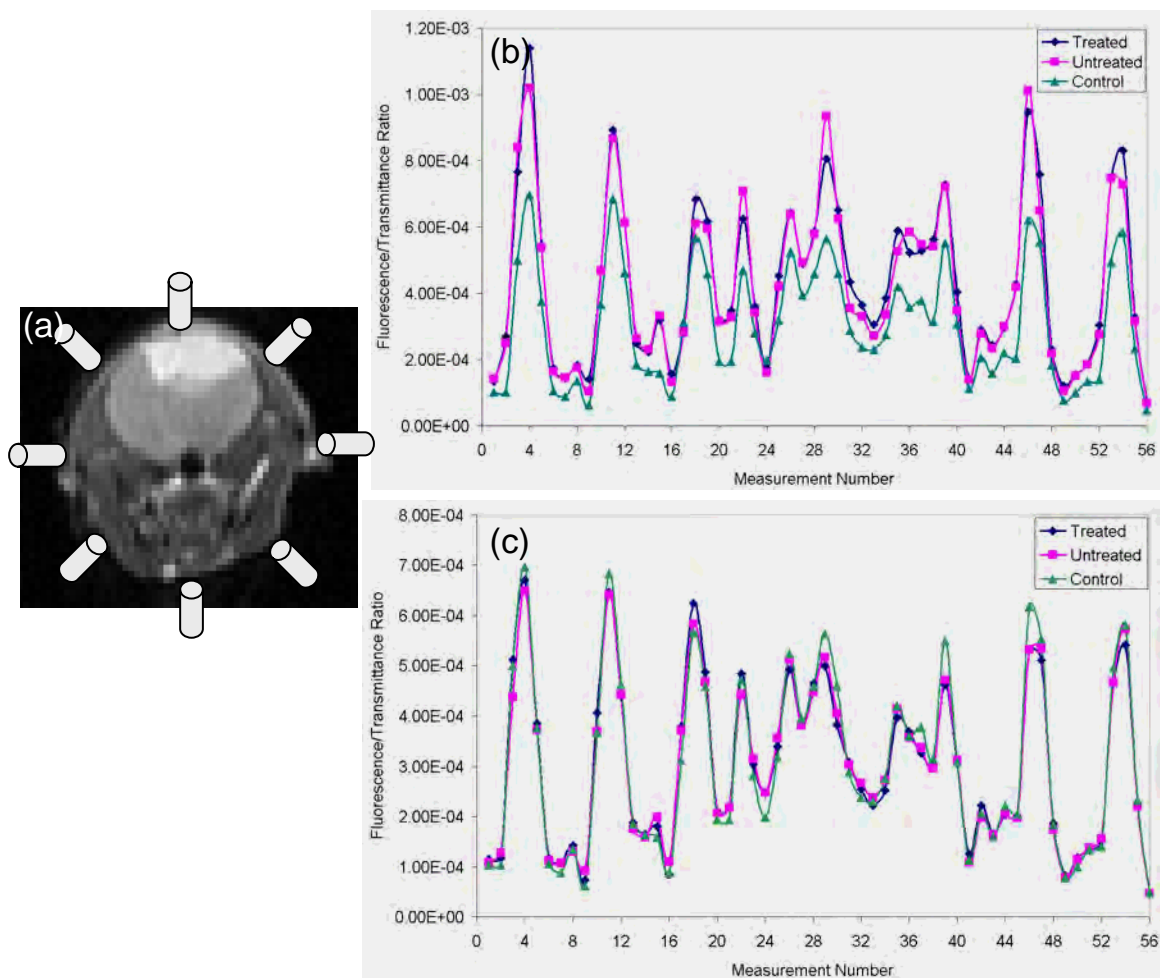


Figure 7.5 – (a) A coronal slice of a T1 TSE CE MRI showing a brain tumor was used to illustrate the positioning of the fiber optics around the mouse head. Each fiber could act as both a source and a detector, but not simultaneously. The source was rotated sequentially through the 8 fiber optics, while the remaining 7 fiber optics took measurements and thus, 56 total measurements were obtained. The integrated, spectrally fitted fluorescence to transmittance ratio of each source-detector pair for the average values at 24 hours after EGF-IRDye administration are shown for the (b) U251-GFP and (c) 9L-GFP tumor-bearing mice compared to the average of the control mice.

7.3.2.2. Transmission Spectroscopy Measurements Week 2

Following completion of the first week of spectroscopy measurements, the treated groups were administered a second dose of Erbitux therapy (1 mg/mouse IP), which circulated for three days before the second round of MRI and spectroscopy

measurements. A similar difficulty was encountered with MR images on the 20th day of the experiment as when images were collected on the 12th day of the experiment. The 9L-GFP tumors were easily visible by MR imaging, however, the U251-GFP tumors were not readily detectable with conventional MRI scans. The mice in the U251-GFP tumor-bearing group illustrated physical symptoms of brain tumors, including substantial weight loss, hunching of the spine and some involuntary shaking, but nothing of note was visible by MRI. The mice in the treated U251-GFP group were less symptomatic than the mice in the U251-GFP untreated group; although it appeared that only some mice in the U251-GFP treated group responded to Erbitux therapy. The presence of brain tumors was easily detectable in both the treated and untreated U251-GFP groups, with the average fluorescence to transmittance ratio significantly higher in the treated (p-value = 0.008) and the untreated groups (p-value = 0.001) over the control group, 24 hours after EGF-IRDye administration (Figure 7.6(a)).

The mean EGF-IRDye fluorescence was significantly higher in the U251-GFP untreated group as compared to the U251-GFP treated group (p-value = 0.035), while there was not a statistically significant difference in fluorescence between the 9L-GFP treated and untreated groups (p-value = 0.19) (Figure 7.6(a)). In fact, the 9L-GFP treated group had higher mean EGF-IRDye fluorescence as compared to the 9L-GFP untreated group illustrating that Erbitux therapy was not correlated to fluorescence intensity for the 9L-GFP tumor-bearing mice. In contrast, the fluorescence in the U251-GFP tumor-bearing groups did appear to be correlated with Erbitux therapy, with the untreated U251-GFP group showing higher mean EGF-IRDye fluorescence than the treated group, as would be expected from *in vitro* experiments shown in Figure 7.2(a). When the

spectroscopy measurements at 48 hours following EGF-IRDye administration were examined it could be seen that the same relationships between the U251-GFP treated and untreated groups and the control group were visible with significantly higher fluorescence seen in both the treated (p-value = 0.003) and the untreated (p-value = 0.002) as compared to the control group (Figure 7.6(b)). Similar to the 24 hour time point, the fluorescence of the 9L-GFP tumor-bearing mice was not significantly different from the control mice (p-value 9L-GFP: treated = 0.28 and untreated = 0.12). A statistically significant difference between the U251-GFP treated and untreated groups was only visible at the 24 hour time point (Figure 7.6); showing noninvasive fluorescence treatment monitoring was possible when the pharmacokinetics of the Erbitux and EGF-IRDye were measured at the appropriate time point. The mean fluorescence of the 9L-GFP treated and untreated groups were the same 24, 48 and 72 hours after EGF-IRDye administration due to low EGF uptake, confirming the use of this model as the negative control for the treatment monitoring experiment.

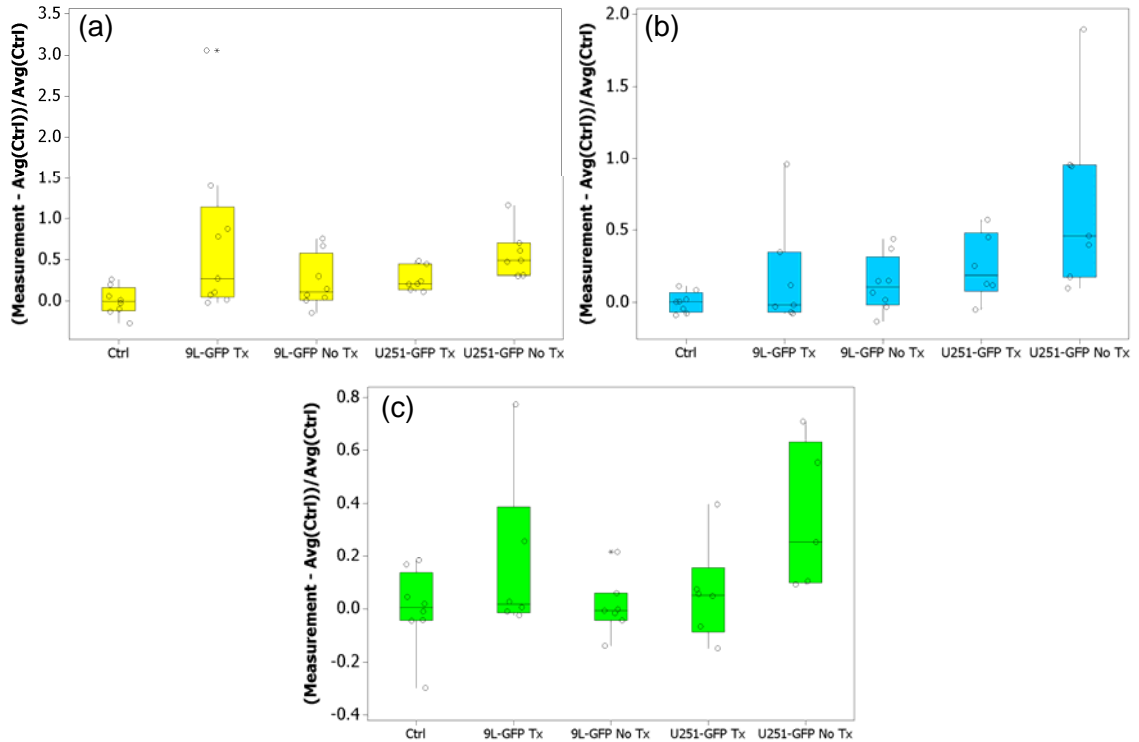


Figure 7.6 – The integrated, spectrally fitted fluorescence to transmittance ratio normalized to the average control mouse for EGF-IRDye fluorescence values at each source-detector point (obtained on days 21 – 24 of the experiment). The treated and untreated groups for the 9L-GFP and U251-GFP tumor-bearing mice, and a mixed treated and untreated control group are illustrated in the graphs. *In vivo* EGF-IRDye fluorescence (a) 24 hours, (b) 48 hours and (c) 72 hours after administration.

The EGF-IRDye fluorescence was also examined on a point-by-point basis instead of averaging all source-detector positions for the U251-GFP treated and untreated groups for the second week of spectroscopy measurements (Figure 7.7). The EGF-IRDye fluorescence was higher in the untreated U251-GFP group as compared to the U251-GFP treated group at every source-detector point at both the 24 hour time point and the 48 hour time point (Figure 7.7(a) and (b)). However, a statistically significant difference was only seen between the U251-GFP treated and untreated groups at the 24 hour time

point when all measurements were averaged. Less fluorescence difference was seen between the U251-GFP treated and untreated groups at the 72 hour time point, as the EGF-IRDye was cleared from systemic circulation (Figure 7.7(c)).

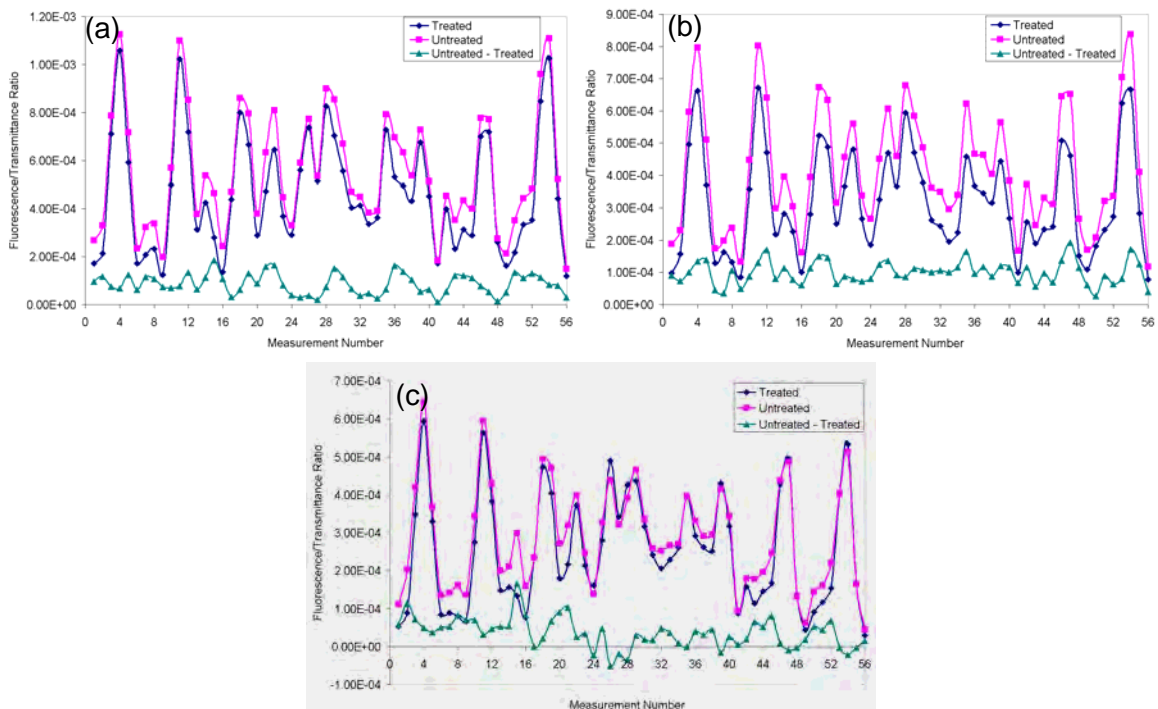


Figure 7.7 – The integrated, spectrally fitted fluorescence to transmittance ratio of each source-detector pair for the U251-GFP treated and untreated mice (a) 24 hours, (b) 48 hours and (c) 72 hours after EGF-IRDye administration. The difference between the untreated and treated groups at each source detector point is also graphed at each time point in green.

7.3.2.3. Optimal Light Paths for Multichannel System In Vivo

The spectroscopy measurements collected 24 hours after EGF-IRDye administration during the second cycle of spectroscopy were further examined to determine if averaging select measurements together increased the statistical significance as compared to averaging all measurements together (Figure 7.8). The same light paths that were considered in chapter 4 for the model and positional phantom study were used

here (Figure 4.9). For all groups of measurement there was a statistically significant difference between the U251-GFP tumor-bearing animals and the control animals, regardless of treatment status (Table 7.1). A statistically significant difference was seen between the U251-GFP treated and untreated group when all 56 measurements were averaged, as shown in Figure 7.6, however when the average of a portion of the measurements was calculated the fluorescence difference between the mean of the treated and untreated group was not significant (Table 7.1). The only metric that showed improved ability to differentiate between the U251-GFP treated and untreated groups was when the maximum of the 56 data points was considered for each mouse (Figure 7.8(c)).

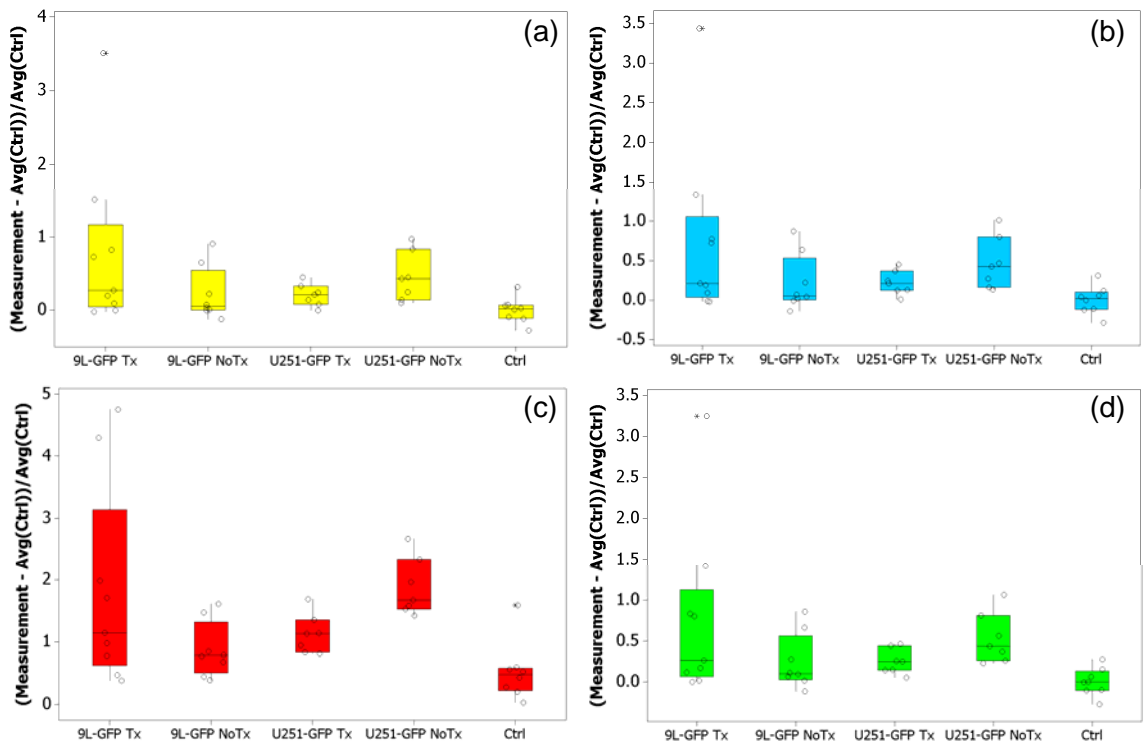


Figure 7.8 – The relative average difference 24 hours after EGF-IRDye administration during the second week of spectroscopy measurements. Groups of fiber measurements were considered to determine if an optimal measurements set could be determined. The average of the (a) transmission only (b) transmission and semi-transmission (c) maximum point and (d) transmission, semi-transmission and semi-reflectance data is shown for each

group of mice. The light paths corresponding to each of these groups are shown in Figure 4.9.

The model study, discussed in chapter 4, indicated that improved signal intensity was detected when only the transmission measurements were averaged if the anomaly was in very close proximity to the fiber plane. However, when positional phantom data was considered it indicated that the average of all 56 measurement points was more robust than the average of a subset of these measurements when the anomaly was not directly in the fiber plane. A similar result was illustrated here for *in vivo* data collected with the multichannel system. The data presented in this analysis was collected with simultaneous MRI, to ensure proper positioning of the fiber plane. However, *in vivo* tumor tissue does not create a spherical anomaly as used in the modeling study. Even though some of the tissue was in the plane of the fiber, some tissue was not and thus, the average of all measurements provided better fluorescence detection than the average of a subset of measurements. When the maximum data point out of the 56 measurements was considered an increased difference in the mean of the U251-GFP treated and untreated groups was seen. Although the same measurement point was not compared for each mouse this method could be considered to examine treatment monitoring on an individual basis.

Measurements	Ctrl vs. U251-GFP Tx	Ctrl vs. U251-GFP No Tx	U251-GFP Tx vs. No Tx
Average	0.008	0.001	0.035
Transmission	0.013	0.031	0.117
Trans & Semi-Trans	0.025	0.010	0.108
w/o Reflection	0.011	0.003	0.061
Maximum Point	0.008	<0.0001	0.005

Table 7.1 – The 56 measurements collected from the multichannel system were considered to determine if an optimal measurement group could be averaged to increase the statistical significance between treatment groups over averaging all measurements. The p-values calculated between the control group, U251-GFP treated and U251-GFP untreated groups during the second cycle of spectroscopy measurements 24 hours after EGF-IRDye administration for different measurement groups measurements are shown. (Tx = treated group, No Tx = untreated group)

7.4. EGF-IRDye Fluorescence: *Ex vivo* Analysis

After the second 72 hour EGF-IRDye *in vivo* spectroscopy measurement, the mice were sacrificed and their brains extracted for *ex vivo* quantification via the Odyssey system. These images were used to quantify the fluorescence intensity in the tumor tissue normalized to the fluorescence intensity in a region of interest from the normal brain tissue (Figure 7.9). The mean fluorescence in the 9L-GFP untreated group was slightly higher than the mean fluorescence in the 9L-GFP treated group, however, the variance in both groups was considerably larger than in either of the U251-GFP tumor bearing groups or in the control group. The mean fluorescence in the U251-GFP untreated group was not significantly higher than that in the treated group similar to the fluorescence measured *in vivo* (p-value = 0.668) (Figure 7.9(a)). Given that *in vivo* data was collected at multiple time points, the 24 hour *ex vivo* data was not available; although based on the results seen here, there would likely be a statistically significant difference

between the U251-GFP treated and untreated groups *ex vivo* 24 hours after EGF-IRDye administration.

Following *ex vivo* examination of the brain tumor tissue, it was clear that the 9L-GFP tumors were significantly larger than the U251-GFP tumors, which can be seen in Figure 7.10 – Figure 7.13. The *ex vivo* fluorescence measurements were normalized to the tumor area that was obtained during region of interest analysis on the images.

Normalization of the *ex vivo* fluorescence intensity to tumor area showed an interesting relationship which can be seen in Figure 7.9(b). The variance in the U251-GFP tumor bearing groups was considerably increased and the mean fluorescence of the treated group was higher than that of the untreated group. Since the opposite relationship was seen between the mean EGF-IRDye fluorescence prior to normalization to tumor area, it appears that the U251-GFP tumors in the treated group were significantly smaller than those in the untreated group, illustrating that Erbitux therapy decreased the growth rate of the U251-GFP tumors.

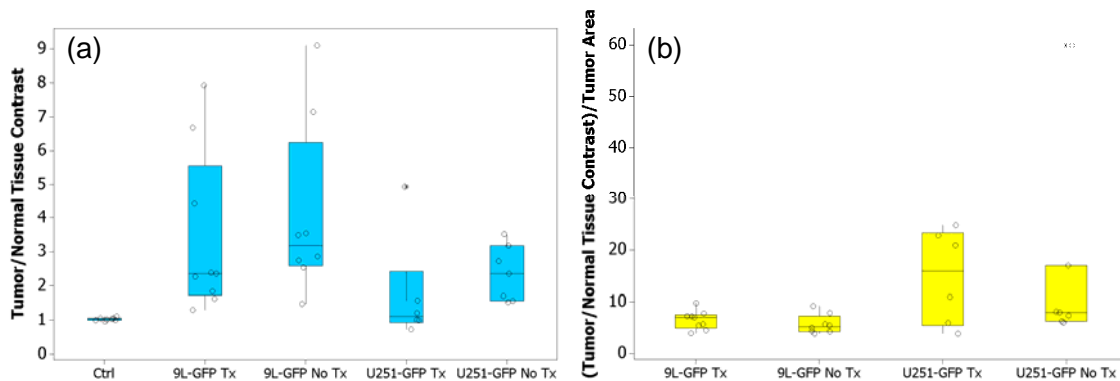


Figure 7.9 – (a) *Ex vivo* EGF-IRDye tumor tissue fluorescence intensity normalized to healthy brain tissue fluorescence intensity. (b) *Ex vivo* fluorescence intensity normalized to healthy brain tissue fluorescence intensity divided by tumor area.

7.4.1. 9L-GFP Tumor-Bearing Mice

The EGF-IRDye fluorescence was examined in *ex vivo* brain slices and compared to the GFP fluorescence and H+E stained slides to determine if higher fluorescence could be seen in the tumor tissue over the normal tissue. The U251-GFP treated brains were compared to the U251-GFP untreated brains to determine if the decrease in fluorescence could be visualized qualitatively. When the 9L-GFP tumor bearing mice were examined the EGF-IRDye fluorescence was mostly confined to the tumor tissue as could be visualized when the EGF-IRDye fluorescence *ex vivo* images were compared to the GFP fluorescence images and the corresponding H+E stained images (Figure 7.10 & Figure 7.11).

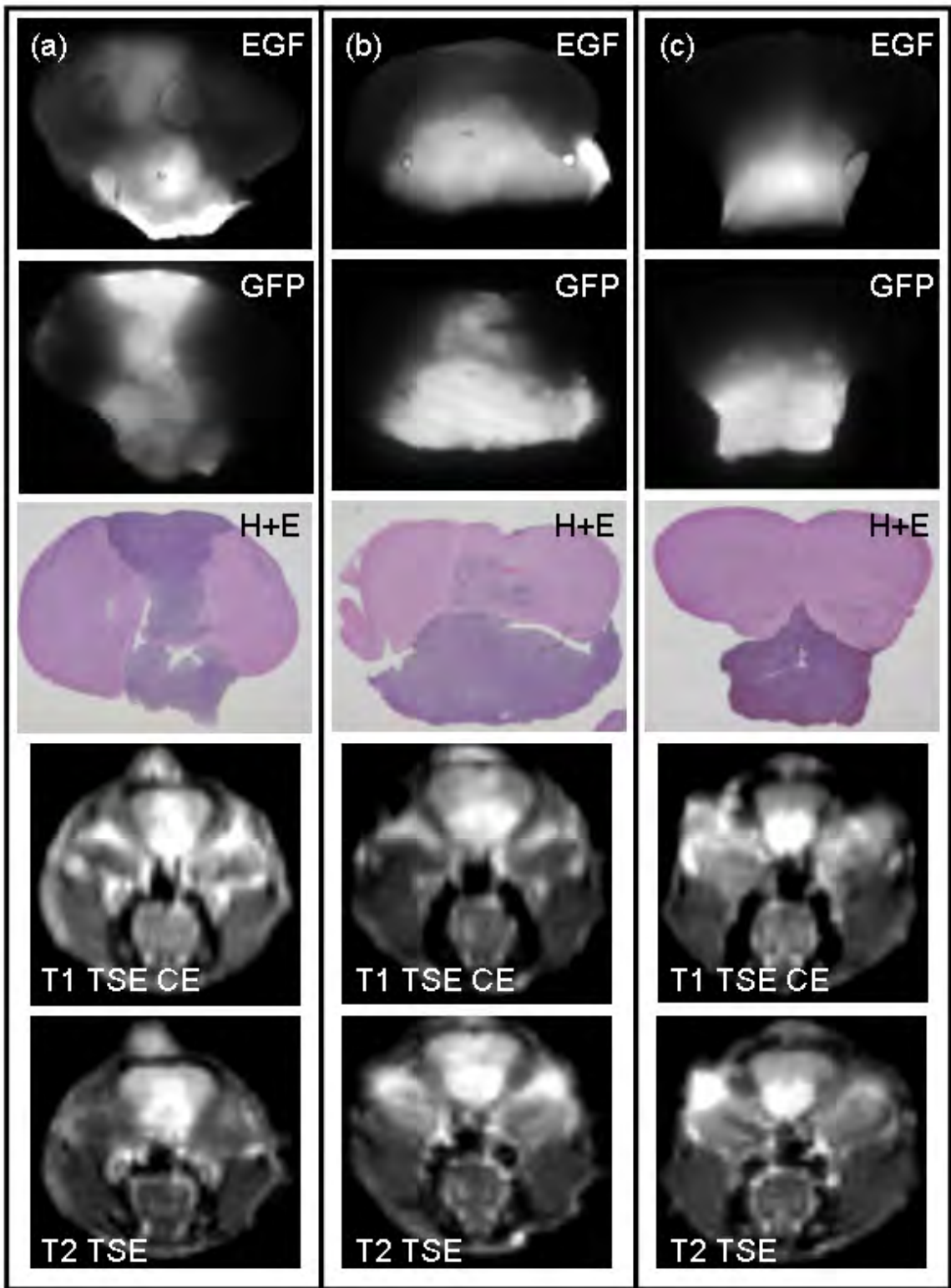


Figure 7.10 – The *ex vivo* images showing the EGF-IRDye fluorescence (1st row), which can be compared to the GFP fluorescence (2nd row) as well as the corresponding H+E

section (3rd row) for three example mice in the 9L-GFP treated group. The *in vivo* MR image that qualitatively matched the *ex vivo* brain slice is shown for comparison. T1 TSE CE and T2 TSE MR images are illustrated in the bottom two rows of the figure. A different mouse is shown in each column with (a) – (c) illustrating three representative mice in the 9L-GFP Erbitux treated group.

The EGF-IRDye fluorescence in both the treated and the untreated 9L-GFP mice was highly heterogeneous, as some areas that corresponded to high fluorescence in the GFP image illustrated bright fluorescence in the EGF-IRDye image, while other areas show quite low fluorescence. The highly fluorescent areas most likely correspond to regions of the tumor which were proliferating quickly and had higher levels of EGFR than areas of the tumor which exhibit relatively low fluorescence. Little difference in uptake of the fluorescently labeled EGF was seen between the 9L-GFP treated and untreated animals as can be seen in the representative examples shown in Figure 7.10 and Figure 7.11. This corresponds to the relationship seen during *in vivo* spectroscopy measurements, where little difference in mean fluorescence was observed between the two groups at any of the time points tested during either the first or second week of spectroscopy measurements (Figure 7.4 & Figure 7.6). However, it does appear from the uptake of the EGF-IRDye that the 9L-GFP tumor tissue did have more epidermal growth factor receptors than when the cells were tested in culture during the *in vitro* flow cytometry experiments (Figure 7.1 & Figure 7.2). The MRI images for the 9L-GFP mice in both the treated and untreated groups illustrated that the tumor tissue was readily visible by T1 TSE CE, T2 TSE and T2 FLAIR MR imaging.

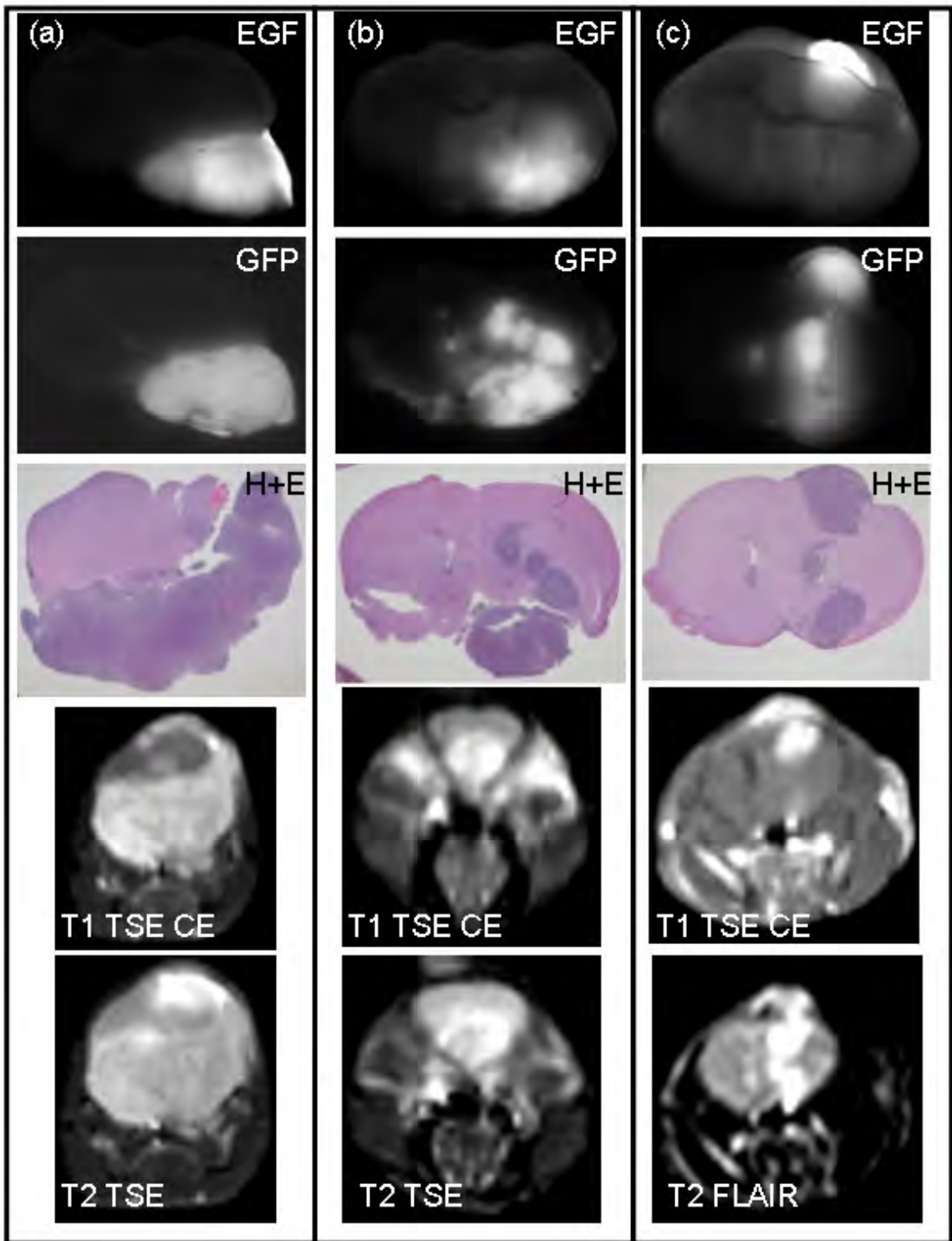


Figure 7.11 – The *ex vivo* images illustrating the EGF-IRDye fluorescence (1st row), which can be compared to the GFP fluorescence (2nd row) as well as the corresponding H+E section (3rd row) for three example mice in the 9L-GFP untreated group. The *in*

vivo MR image that qualitatively matched the *ex vivo* brain slice is shown for comparison. T1 TSE CE and T2 TSE MR images are illustrated in the bottom two rows of the figure. A different mouse is shown in each column with (a) – (c) illustrating three representative mice in the 9L-GFP untreated group. For mouse (c), all images are the same except a T2 FLAIR MR image is shown in the bottom row, instead of a T2 TSE image.

7.4.2. U251-GFP Tumor-Bearing Mice

Similar *ex vivo* image sets were examined for the U251-GFP treated and untreated groups. A much different EGF-IRDye fluorescence pattern was seen in these treated and untreated groups than in the 9L-GFP animals. The U251-GFP treated animals had low EGF-IRDye fluorescence in the tumor tissue as could be seen when the images of the *ex vivo* brain slices were compared to the GFP images and the corresponding H+E images (Figure 7.12). In contrast, the U251-GFP untreated group showed higher EGF-IRDye fluorescence in the tumor tissues as compared to the treated animals (Figure 7.12 & Figure 7.13). This corresponds to the relationship seen during *in vivo* spectroscopy measurements where the mean fluorescence of the U251-GFP untreated group was higher than that seen in the U251-GFP treated group, confirming that the EGF-IRDye uptake was decreased in response to Erbitux therapy, and thus allowing for noninvasive *in vivo* treatment monitoring.

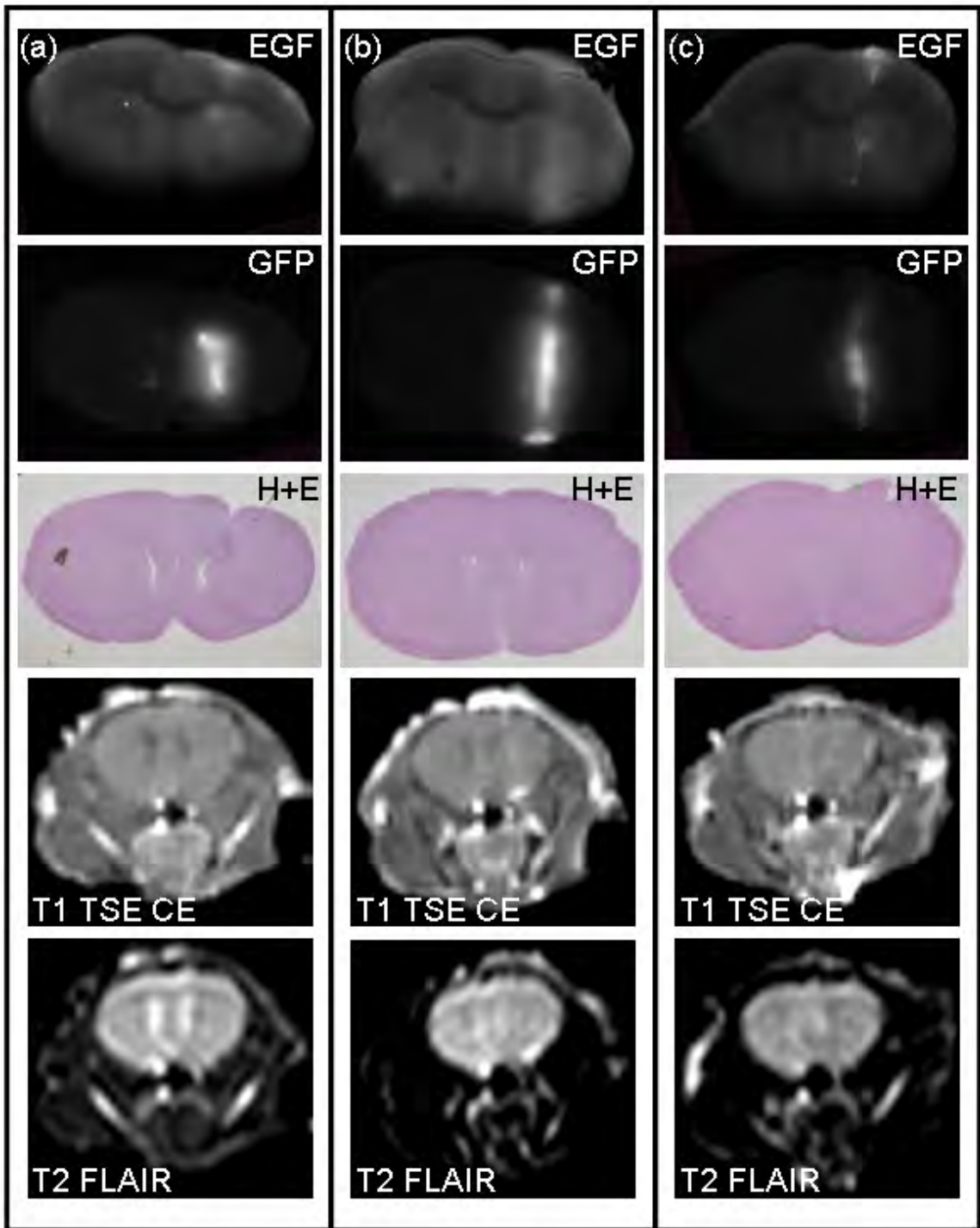


Figure 7.12 – The *ex vivo* images illustrating the EGF-IRDye fluorescence (1st row), which can be compared to the GFP fluorescence (2nd row) as well as the corresponding H+E section (3rd row) for three example mice in the U251-GFP treated group. The *in vivo* MR image that qualitatively matched the *ex vivo* brain slice is shown for comparison. T1 TSE gadolinium contrast enhanced images and T2 FLAIR images are

illustrated in the bottom two rows of the figure. A different mouse is shown in each column with (a) – (c) illustrate three representative mice in the U251-GFP treated group.

Interestingly, the U251-GFP tumors were quite difficult to visualize by MRI which was seen when the *ex vivo* slices were compared to the MRI images in Figure 7.12 and Figure 7.13. The U251-GFP tumors were significantly less visible than the 9L-GFP tumors, although the U251-GFP tumors were more readily detectable via EGF-IRDye spectroscopy measurements than that 9L-GFP tumors. Many MRI sequences were used to try to visualize the tumor tissue; however none were able to detect the tumor in all mice. This MRI visibility issue was viewed as an important area for further analysis, and thus was discussed at length in chapters 5 and will be revisited in chapter 8.

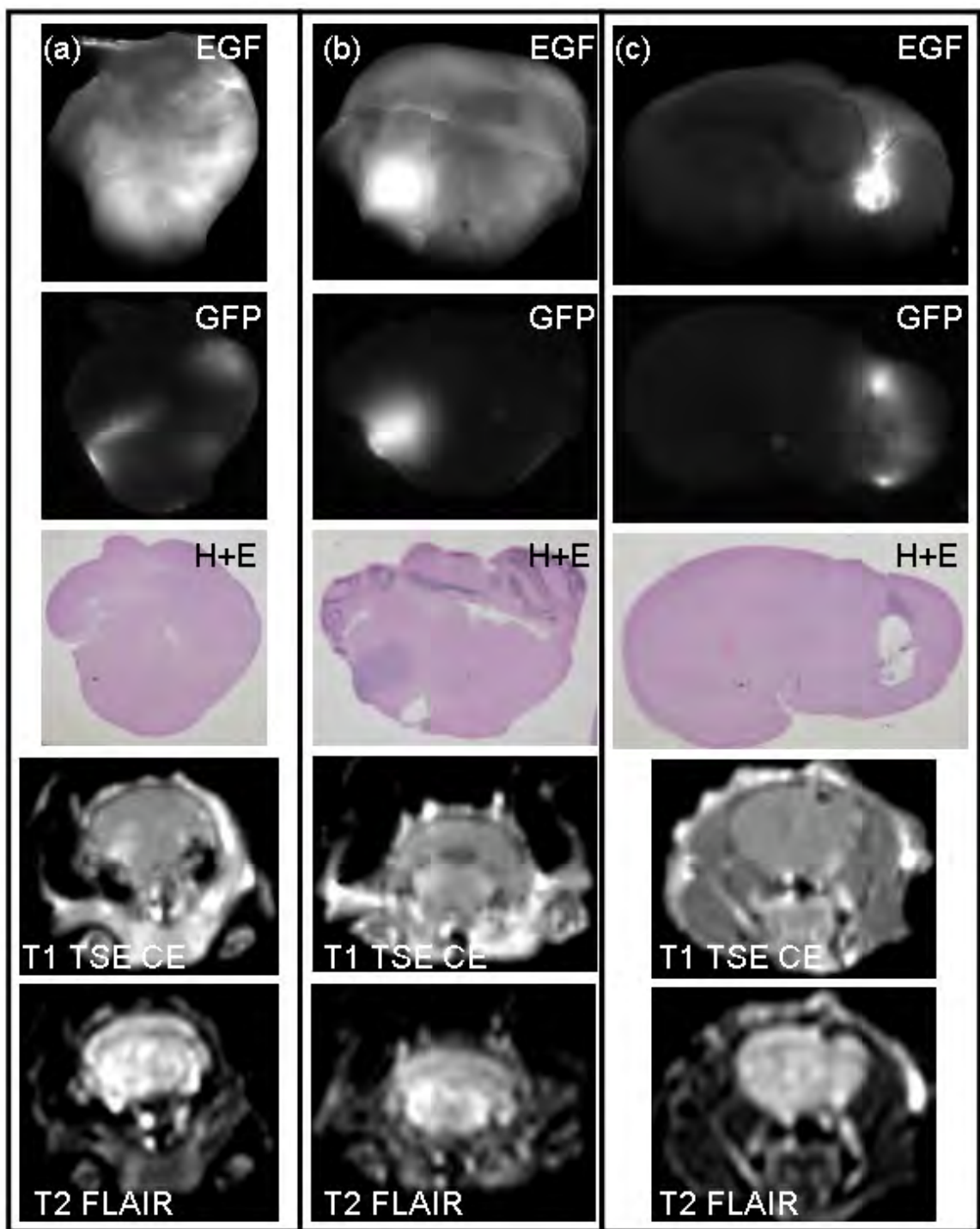


Figure 7.13 – The *ex vivo* images illustrating the EGF-IRDye fluorescence (1st row), which can be compared to the GFP fluorescence (2nd row) as well as the corresponding H+E section (3rd row) for three example mice in the U251-GFP untreated group. The *in vivo* MR image that qualitatively matched the *ex vivo* brain slice is shown for comparison. T1 TSE gadolinium contrast enhanced images and T2 FLAIR images are

illustrated in the bottom two rows of the figure. A different mouse is shown in each column with (a) – (c) illustrate three representative mice in the U251-GFP untreated group.

7.5. Discussion

Two intracranial brain tumors with different EGFR expression levels were used to study function fluorescence monitoring of EGF uptake. The U251-GFP cell line was used as the positive expression model since it had 20-fold higher EGF uptake as measured *in vitro* than the 9L-GFP cell line, used as the negative control (Figure 7.1). The fluorescence signature of EGF uptake was monitored *in vivo* for both the positive expression model and negative control during tumor growth. Function imaging was compared to structural MR images collected over the course of tumor growth. Erbitux therapy was administered to groups of animals with both the positive expression model and the negative control tumors to understand fluorescence signature changes associated with effective and ineffective therapy. Preclinical studies have shown that Erbitux inhibits cell-cycle progression, angiogenesis and metastasis in cells that overexpress EGFR, decreasing cancer growth [125]. Fluorescently labeled EGF was used to noninvasively quantify the difference in EGF uptake between Erbitux treated and untreated tumor-bearing animals.

In vitro treatment monitoring experiments showed significant fluorescence decrease following Erbitux therapy of the U251-GFP cell line, while no fluorescence difference was seen between treated and untreated 9L-GFP cells. The time between Erbitux administration and EGF-IRDye injection which created the largest fluorescence difference was determined through *in vitro* experiments and used as the interval between

Erbix therapy and EGF-IRDye administration for all *in vivo* treatment monitoring experiments.

Two sets of fluorescence spectroscopy measurements were collected 24, 48 and 72 hours after EGF-IRDye administration (Figure 7.3). Fluorescence monitoring at six time points during the tumor growth and therapy enabled visualization of tumor growth, pharmacokinetics of the EGF-IRDye and Erbix treatment efficacy. Three sets of MR images of all animals were collected at strategic points during the experiment providing structural data to augment functional fluorescence data. Interestingly, the positive expression model, U251-GFP, was very difficult to visualize as compared to the negative control tumors by MRI. However, during the first week of spectroscopy measurements the mean fluorescence of both the U251-GFP untreated (p-value = 0.003) and treated (p-value = 0.037) groups were significantly different from than of the control group 24 hours after EGF-IRDye administration (Figure 7.4(a)). At the same measurement time point, the mean fluorescence of the control group, 9L-GFP treated and untreated groups were the same. Therefore, for the positive expression model EGF uptake status could be used to determine if tumor tissue was present even though the tumor status could not be confirmed via structural imaging. The increased fluorescence signature of the positive expression model 24 hours after EGF-IRDye administration also illustrates that EGF-IRDye fluorescence could be used to noninvasively stratify tumors based on EGFR expression status, as a statistically significant difference was visible between the untreated positive expression and negative control mole (p-value = 0.002).

The fluorescence signature obtained 24 hours after EGF-IRDye administration during the second set of spectroscopy measurements showed noninvasive functional

fluorescence spectroscopy could be used to monitor Erbitux therapy. The mean fluorescence of the U251-GFP treated group was significantly lower than the U251-GFP untreated group (p-value = 0.035) due to decreased EGF uptake of the Erbitux treated tumors (Figure 7.6(a)). EGF-IRDye fluorescence was examined at each of the 56 measurement points as compared to the average of all points and the fluorescence of the untreated group was higher than the treated group at each point (Figure 7.7(a)). As expected, the negative control model had the same mean fluorescence intensity when the treated and untreated groups were compared. Since the negative control model did not overexpress EGFR, Erbitux therapy was not effective. This could be determined noninvasively through similar fluorescence intensities between the treated and untreated 9L-GFP tumor-bearing groups.

The tumor response of the positive expression model was confirmed via physical symptoms of the mice and *ex vivo* fluorescence verification. As mentioned, MRI visualization was largely impossible for these tumors, but tumor presence was confirmed in all mice upon *ex vivo* examination. Mice in the U251-GFP treated group appeared healthier than those in the untreated group as they exhibited fewer physical symptoms of large brain tumors including significant weight loss, spine hunching and involuntary shaking. *Ex vivo* fluorescence images of the U251-GFP treated group showed lower fluorescence intensity than *ex vivo* images of the untreated group, confirming *in vivo* spectroscopy measurements (Figure 7.12 & Figure 7.13). In contrast, little difference was seen between the 9L-GFP treated and untreated groups. All 9L-GFP mice had large MRI visible tumors and physical symptoms associated with large brain tumors. *Ex vivo* data showed EGF-IRDye accumulation in the tumor tissue which appeared similar

between the treated and untreated groups (Figure 7.10 & Figure 7.11), thus confirming the *in vivo* spectroscopy measurements.

In conclusion, fluorescence monitoring of EGF-IRDye fluorescence could be used to detect EGF uptake. This functional information could be used to stratify tumors into groups for treatment where Erbitux therapy would be effective based on their EGF expression pattern. The functional information could also be used to track response to Erbitux therapy in a positive EGF expression model and lack of response to Erbitux therapy in a negative control model.

Chapter 8 - Imaging Case Studies

8.1. Introduction

Molecular imaging is a rapidly emerging field with the goal of noninvasive visualization of the cellular and subcellular processes that have been illuminated through understanding of molecular signatures of disease at the level of genomics, proteomics and metabolism [56, 126-129]. Advances in molecular imaging technology will enable earlier detection, diagnosis and characterization of disease, increased understanding of integrative biology, and better assessment of treatment efficacy [56, 126]. Currently treatment efficacy and tumor response assessment is performed primarily through measurements of tumor size via noninvasive imaging. However, this approach provides a delayed indication to response as tumor size change occurs after many known quantifiable molecular changes have already taken place [130]. Using tumor size as a prognostic indicator of tumor response is also less sensitive for newer molecularly targeted therapies, such as antiangiogenic therapy, where a delayed change in gross tumor volume may occur despite more immediate changes in tumor angiogenesis [57].

Advances in molecular biology have significantly increased our understanding of cancer. It is now recognized that each tumor is an individual disease requiring characterization on a case by case basis to determine the most appropriate treatment with a shift towards individualized medicine [126]. The heterogeneity of each type of cancer and subclasses of tumors within each type stems from the fact that cancer development occurs through random genetic alterations which cause cascades of virtually unregulated molecular events within the tissue that lead to individual genetic complexity [131].

Molecular imaging can be used as a tool to assist in evaluation of tumor heterogeneity in

that it will allow visualization of the molecular signature associated with a particular cancer type and tumor.

Genetic analysis has improved understanding of primary brain neoplasms and allowed for subclassifications of groups originally thought of as a single disease such as glioblastoma multiforme (GBM) [131, 132]. The most frequently altered oncogene in GBM is amplification of the EGFR gene which results in overexpression of EGFR. EGFR is amplified in 30 – 50% of all GBM and is correlated with advantages in growth, invasiveness and resistance to chemotherapy and radiation therapy [133]. Thus, molecular imaging applications discussed in chapter 7 for assessment of EGF uptake and EGFR status of tumor tissue could be useful in assessing treatment options of GBM. Due to the unregulated genetic alterations tumors can be classified into EGFR+ or EGFR- but not all tumors have the same level of overexpression and thus will respond differently to EGFR targeted therapies. This difference in response of EGFR+ and EGFR- gliomas was illustrated through the use of a positive expression model (U251-GFP) and a negative control model (9L-GFP). However, even within the U251-GFP model there was significant fluorescence variability which appeared to be consistent with tumor growth, invasiveness and treatment response. Individual examples from the Erbitux treatment monitoring study will be discussed here to examine the relationship between EGF-IRDye fluorescence and tumor growth, invasion and response to Erbitux therapy.

PpIX fluorescence, an *in vivo* representation of cellular metabolism, was also highly variable between tumor lines as well as between tumors of the same type. PpIX fluorescence is a more general molecular imaging marker, similar to fluorodeoxyglucose (FDG) used in positron emission tomography (PET) to assess metabolic activity. FDG-

PET based imaging is used to detect tumors and monitor their response to therapy as tumor tissue generally has higher rates of aerobic glycolysis than normal tissue and thus shows increased contrast [130]. However, FDG-PET has high background signal in the brain tissue as FDG accumulation is proportional to glucose uptake and the brain, heart and any inflamed or infected tissue have high glucose uptake rates. PpIX fluorescence could be used as an alternative to FDG-PET to detect tumor tissue in the brain and assess metabolic changes post therapy. Three cases studies will be examined here to illustrate its use as a marker of cellular metabolism and examine heterogeneity in production.

8.2. Erbitux Treatment Monitoring Case Studies

The U251-GFP cell line was used as a model of positive expression for epidermal growth factor receptor (EGFR) as it showed up to 20-fold higher uptake of epidermal growth factor (EGF) *in vitro* compared to the 9L-GFP model, which was used as the negative control. U251-GFP cells treated with Erbitux had 13 – 30 times lower EGF uptake than untreated cell at the time point chosen for *in vivo* studies. The EGF uptake of 9L-GFP cells was low by comparison and largely unaffected by Erbitux therapy. Even with a substantial difference in EGF uptake visible *in vitro* between Erbitux treated and untreated U251-GFP cells, only one of the six time points tested *in vivo* show a significant difference between treated and untreated animals. All groups of mice had high EGF-IRDye fluorescence variance which could be attributed partially to the positioning of the animal during repeat measurements and partially to biological variance (Figure 8.1). Since positioning of the control animals in the fiber plane was less critical, but the fluorescence variance was still quite large, there was considerable biological

heterogeneity as measured via fluorescence (Figure 8.1(e)). None of the groups of tumor-bearing mice showed any discernable fluorescence pattern during the two weeks of spectroscopy measurements. Some animals in both the treated and untreated groups had higher and lower than average fluorescence. An example animal with each tumor type from both the treated and untreated groups with high and with low fluorescence will be shown as an individual case. The relative average difference of each example animal at each spectroscopy time point that will be discussed are shown in Table 8.1.

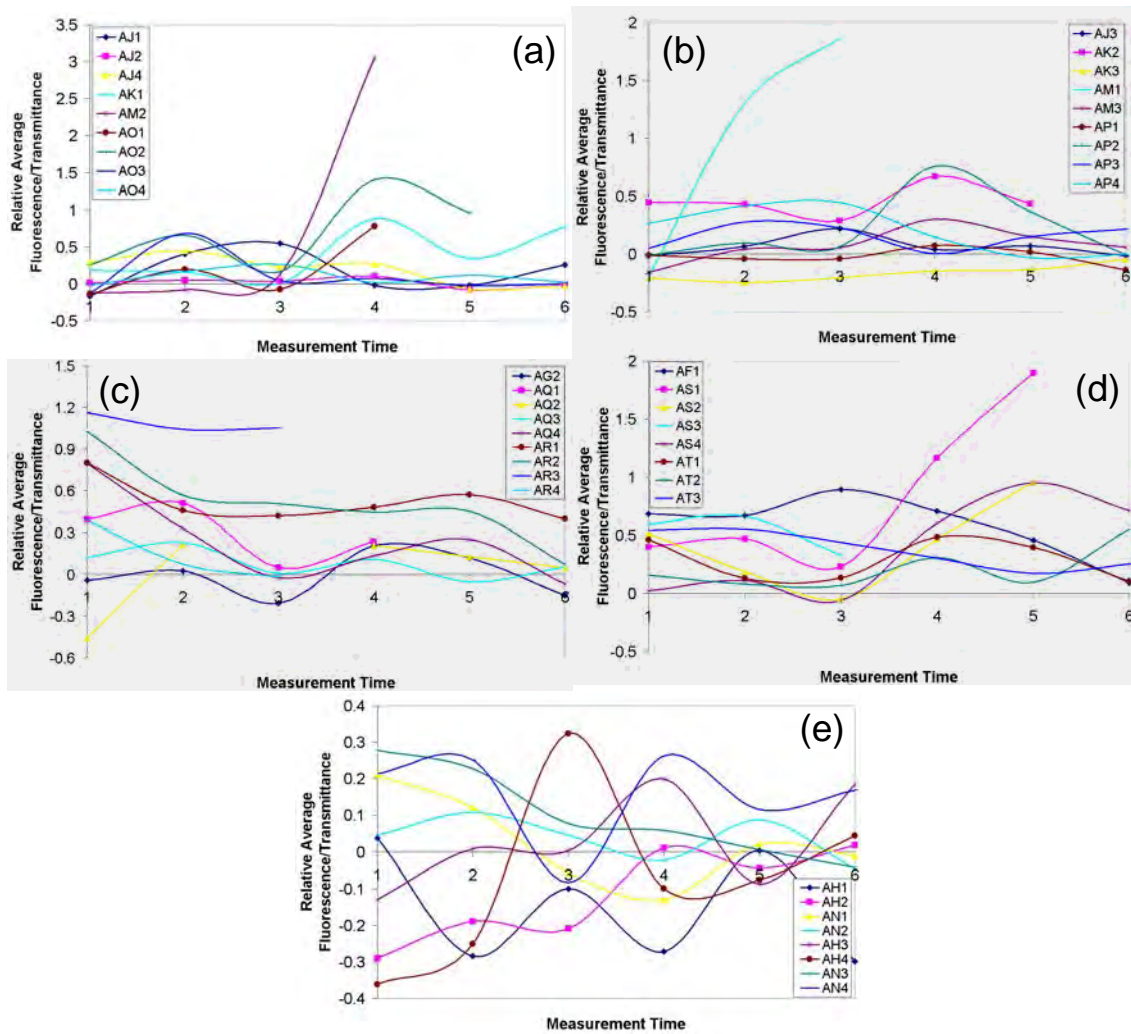


Figure 8.1 – EGF-IRDye fluorescence relative average difference from average control mouse at each measurement time point. Times points labeled 1 – 3 represent

measurements obtained during the first week of spectroscopy 24, 48 and 72 hours after EGF-IRDye administration, respectively. Time points labeled 4 – 6 represent measurements obtained during the second week of spectroscopy 24, 48 and 72 hours after EGF-IRDye administration, respectively. The individual mice in the (a) 9L-GFP treated, (b) 9L-GFP untreated, (c) U251-GFP treated, (d) U251-GFP untreated and (e) control groups are shown at each of the time points.

Mouse	Cell Line	Erbix Treated	W1 24hrs	W1 48hrs	W1 72hrs	W2 24hrs	W2 48hrs	W2 72hrs
AR1	U251-GFP	<i>Yes</i>	0.80	0.46	0.42	0.48	0.57	0.40
AQ3	U251-GFP	<i>Yes</i>	0.12	0.23	0.008	0.11	-0.05	0.06
AS4	U251-GFP	<i>No</i>	0.02	0.11	-0.06	0.61	0.95	0.71
AT3	U251-GFP	<i>No</i>	0.54	0.55	0.44	0.31	0.18	0.25
AK1	9L-GFP	<i>Yes</i>	0.19	0.16	0.01	0.88	0.35	0.77
AJ2	9L-GFP	<i>Yes</i>	0.01	0.05	0.04	0.10	-0.08	-0.01
AM3	9L-GFP	<i>No</i>	-0.16	0.04	0.05	0.30	0.15	0.06
AJ3	9L-GFP	<i>No</i>	-0.02	0.07	0.22	0.04	0.07	-0.02

Table 8.1 – The relative average difference was calculated for each mouse at each time point. The fluorescence to transmittance ratio for the average control mouse was subtracted and normalized point by point to each individual mouse. The 56 measurements in each data set were averaged to obtain the relative average difference, displayed in the table. Since this is the difference from the average control mouse, some values are negative.

8.3. Erbitux Treated Group Case Studies

8.3.1. U251-GFP Treated Mouse with Constant Fluorescence Intensity

The U251-GFP mice that received Erbitux therapy were expected to decrease in fluorescence signal over the period of the experiment as seen *in vitro*. Figure 8.1(c) shows a slight decreasing trend in fluorescence, however the fluorescence in some of the treated mice was similar at all measurement points, even after three doses of Erbitux therapy. Samples images of one such mouse, labeled AR1 in Figure 8.1(c), are shown in Figure 8.2. The tumor tissue grew in the ventricle space as illustrated by Figure 8.2(b) – (e). The EGF-IRDye fluorescence accumulated in the tumor tissue seen via *ex vivo* EGF-

IRDye and GFP fluorescence scans with fluorescence enhancement in the ventricles (Figure 8.2(a) & (b)). The fluorescence to transmittance ratio (FTR) of mouse AR1 was highest during the first week of spectroscopy measurements at the 24 hour time point (Table 8.1). Additional measurements were collected 48 and 72 hours after EGF-IRDye administration and at the same time points during the second week of spectroscopy. Following Erbitux therapy, the FTR was expected to decrease, however for mouse AR1 the measurements at the other five time points had similar fluorescence intensity (Table 8.1). The MR images which were obtained prior to the first week of spectroscopy measurements (Figure 8.2(f)), prior to the second week of spectroscopy measurements (Figure 8.2(g)) and prior to sacrifice (Figure 8.2(h)), show mouse AR1 had enlarged ventricles, consistent with tumor tissue growing in the ventricle space. As can be seen by T1 TSE CE MRI, the ventricle swelling increased over the course of the experiment, corresponding to continued tumor growth even with Erbitux therapy. The FTR as measured via spectroscopy showed similar intensity during the treatment, instead of decreased fluorescence intensity as expected. However, this appears to correspond with the response of this tumor to Erbitux therapy as seen by T1 TSE CE MRI. Since the tumor tissue continued to grow even with Erbitux therapy administration, the EGF uptake of the tissue was not substantially decreased and thus measured FTR was similar at all time points tested.

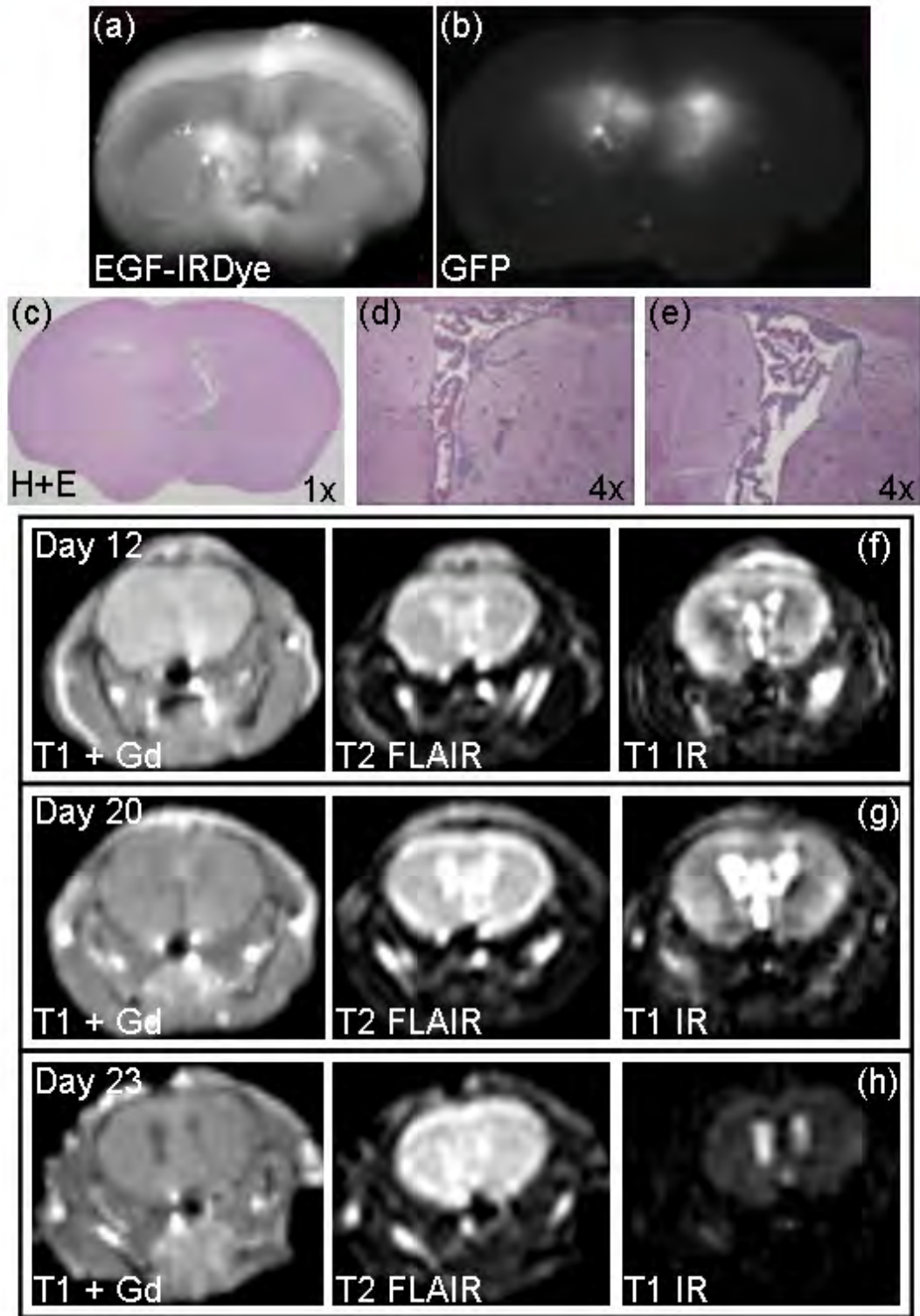


Figure 8.2 – Example mouse AR1 from the U251-GFP Erbitux treatment group. A coronal *ex vivo* section was imaged for (a) EGF-IRDye fluorescence, (b) GFP

fluorescence and was stained with (c) H+E. The tumor tissue, which grew in the left and right ventricle space, is illustrated at 4x magnification in (d) and (e). The *in vivo* MR images that were obtained during the experiment are illustrated (f) 12 days, (g) 20 days and (h) 23 days following tumor implantation. T1 TSE CE, T2 FLAIR and T1 IR MR images of the corresponding section are illustrated.

8.3.2. U251-GFP Treated Mouse with Decreased Fluorescence Intensity

In contrast to mouse AR1, many of the mice in the U251-GFP Erbitux treatment group did show decreased EGF-IRDye fluorescence during the two weeks of spectroscopy measurements. Images of an example mouse, labeled AQ3 in Figure 8.1(c), with decreased EGF-IRDye fluorescence can be seen in Figure 8.3. The FTR of mouse AQ3 was reduced at the 24 and 48 hour time points during the second week of spectroscopy measurements as compared to the first week of measurements (Table 8.1). This mouse had diffusely growing tumor tissue in one hemisphere of the brain (Figure 8.3(c) – (e)), which showed little *ex vivo* EGF-IRDye fluorescence (Figure 8.3(a)), as was expected from *in vitro* experiments. MR images obtained on the 12th, 20th and 23rd days of the experiment showed slight enhancement by T1 TSE CE MRI which match the *ex vivo* GFP fluorescence image (Figure 8.3(f) – (h)). The tumor tissue did not appear to be increasing in size over the course of the experiment as the T1 TSE CE MR images did not show increased area of enhancement. This mouse appeared relatively healthy at the end of the experiment as it did not exhibit weight loss, spine hunching or involuntary shaking. Following *ex vivo* examination, a small tumor was present illustrated in Figure 8.3. Thus, it appears from MRI, physical examination and *ex vivo* analysis that this brain tumor was responding to Erbitux therapy. The EGF-IRDye spectroscopy measurements were lower during the second week of spectroscopy as compared to the first week,

showing decreased EGF uptake of the tumor tissue and the ability to noninvasively track tumor response to therapy.

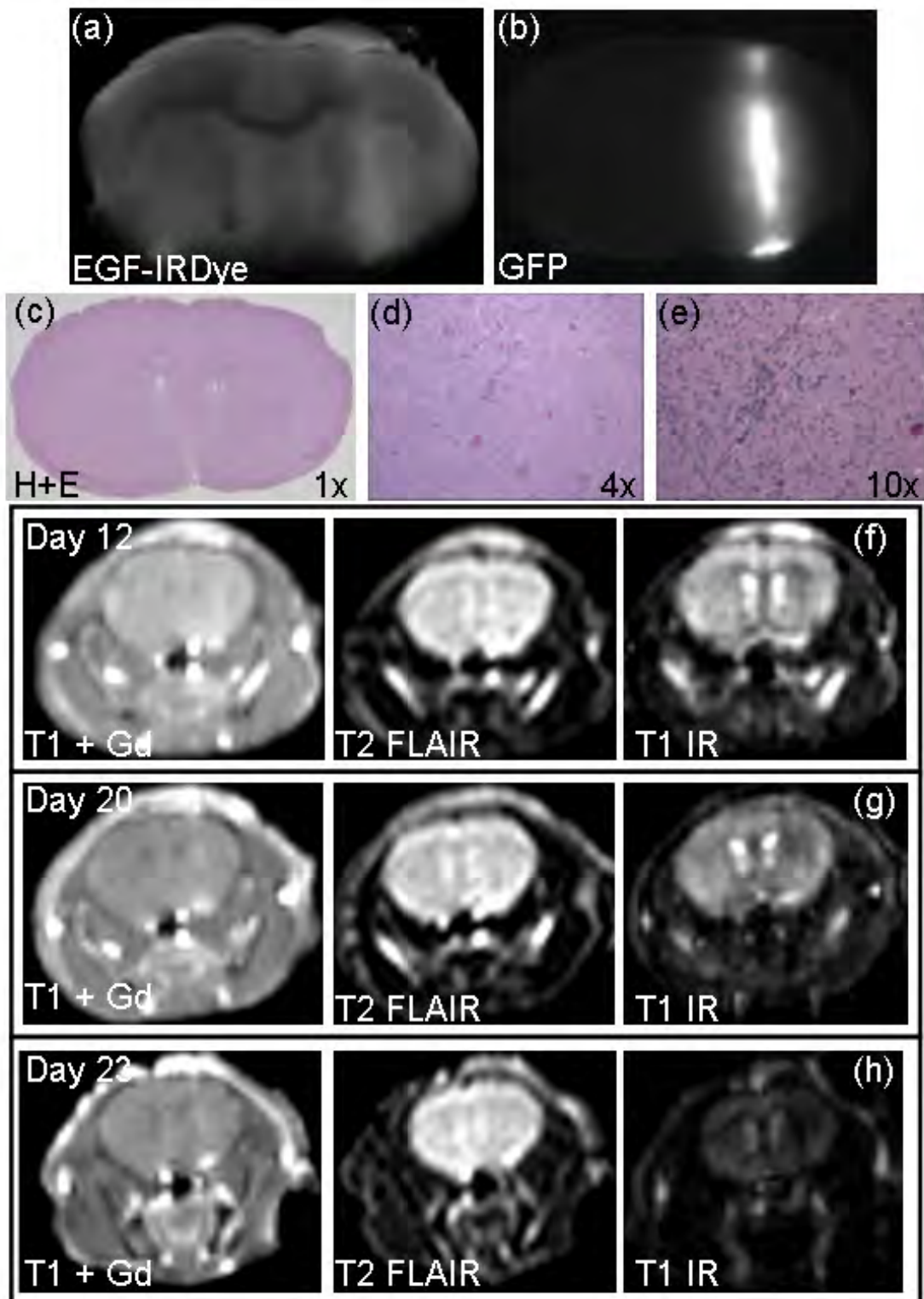


Figure 8.3 – Example mouse AQ3 from the U251-GFP Erbitux treatment group. A coronal *ex vivo* section was imaged for (a) EGF-IRDye fluorescence, (b) GFP

fluorescence and was stained with (c) H+E. The tumor tissue, which grew diffusely in one hemisphere of the brain, is illustrated at (d) 4x and (e) 10x magnification. The *in vivo* MR images that were obtained during the experiment are illustrated (f) 12 days, (g) 20 days and (h) 23 days following tumor implantation. T1 TSE CE, T2 FLAIR and T1 IR MR images of the corresponding section are illustrated.

8.3.3. 9L-GFP Tumor Mouse with Increased Fluorescence Intensity

The 9L-GFP tumor model was used as a negative control since *in vitro*, little EGF uptake was seen and EGF uptake was virtually unchanged following Erbitux therapy. When the relative average difference FTR of the animals in the 9L-GFP Erbitux treatment group was considered, a number of animals showed increased fluorescence, while some animals had similar fluorescence throughout the experiment. Sample images from a mouse with increased FTR, labeled AK1 in Figure 8.1(a), are shown in Figure 8.4. The FTR of this mouse was considerably increased at the same time points during the second week of spectroscopy measurements as compared to the first week (Table 8.1). The *ex vivo* coronal section showed EGR-IRDye accumulation in the tumor tissue as increased fluorescence was seen in the same regions of the EGF-IRDye and GFP images (Figure 8.4(a) & (b)). The *in vivo* MR images showed the development of a large tumor mass with substantially increased volume during the course of the experiment. The H+E images confirm the presence of a large tumor which had some regions that were well vascularized (Figure 8.4(d)) and other regions of considerable hemorrhage (Figure 8.4(c)). In this case, the increased FTR appears to be explained by the substantial increase in tumor size over the course of fluorescence spectroscopy measurements. As expected from *in vitro* results, this tumor did not show response to Erbitux therapy and substantially increased in size and fluorescence during the course of the experiment.

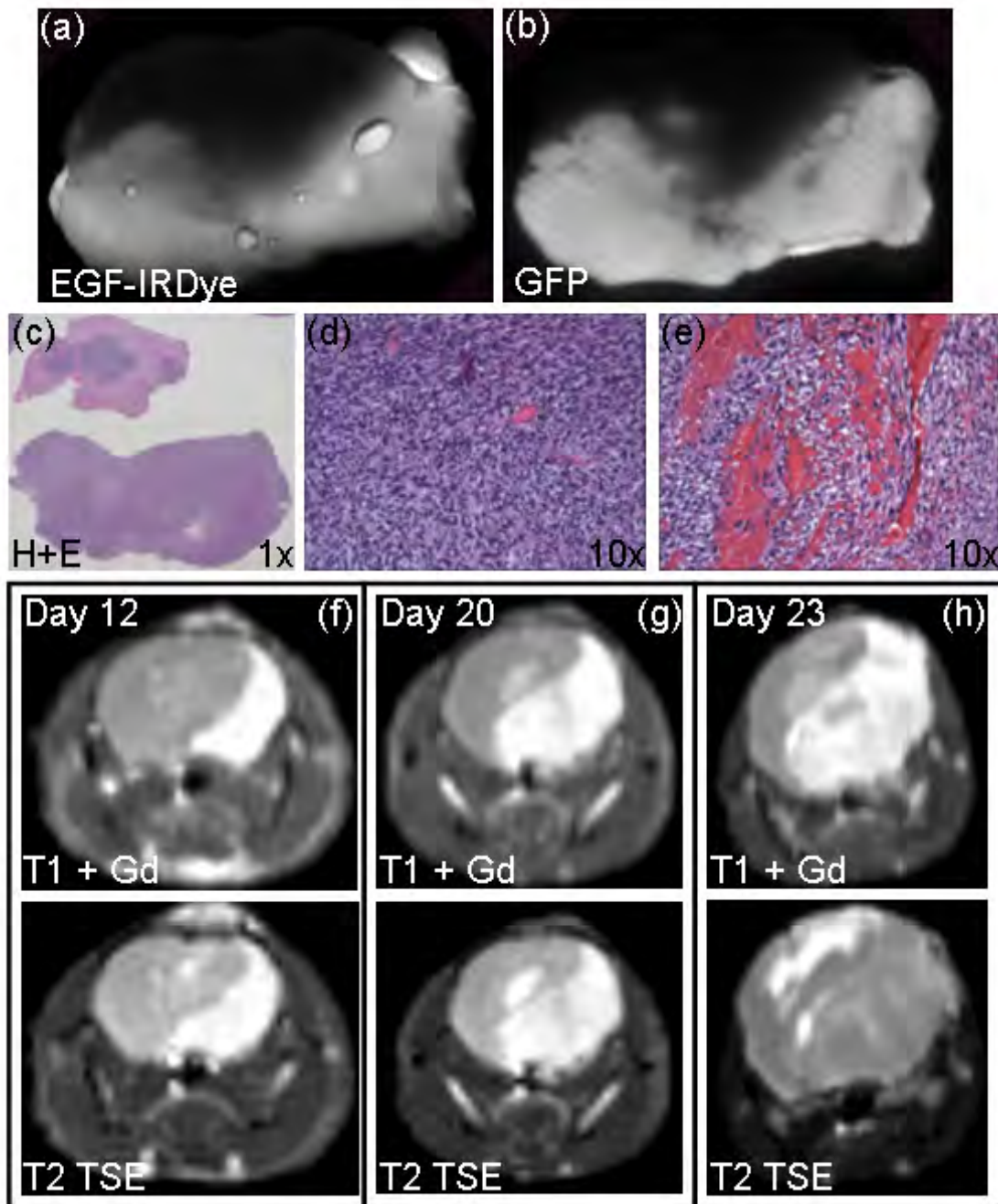


Figure 8.4 – Example mouse AK1 from the 9L-GFP Erbitux treatment group. A coronal *ex vivo* section was imaged for (a) EGF-IRDye fluorescence, (b) GFP fluorescence and was stained with (c) H+E. Healthy tumor tissue, which grew below the brain, is illustrated at (d) 10x magnification. (e) Some of the tumor tissue had significant hemorrhage as can be seen at 10x magnification. The *in vivo* MR images that were obtained during the experiment are illustrated (f) 12 days, (g) 20 days and (h) 23 days

following tumor implantation. T1 TSE CE and T2 TSE MR images of the corresponding section are shown.

8.3.4. 9L-GFP Treated Mouse with Constant Fluorescence Intensity

Some animals in the 9L-GFP Erbitux treatment group did not show increased EGF-IRDye fluorescence, but had comparable FTR throughout the spectroscopy measurements, similar to mouse AR1 of the U251-GFP Erbitux treated group. Images from an example mouse, labeled AJ2 in Figure 8.1(a), which had similar FTR throughout spectroscopy measurements can be seen in Figure 8.5. The tumor grew both as a bulk mass and in the ventricle space (Figure 8.5(c) – (e)). The FTR of the EGF-IRDye were more similar at each measurement point than mouse AK1, discussed previously. Mouse AJ2 also had lower FTR than the average of the control mice, illustrated by the negative FTR values (Table 8.1). The spectroscopy measurements were confirmed by the *ex vivo* measurements which showed heterogeneous, less intense EGF-IRDye accumulated in the tumor tissue as compared to mouse AK1 (Figure 8.4(a) & (b), Figure 8.5(a) & (b)). The *in vivo* MR images taken throughout the experiment showed the tumor increasing in size (Figure 8.5(f) – (h)), but not as substantially as mouse AK1 (Figure 8.4(f) – (h)). The spectroscopy measurements obtained for this mouse showed the expected trend with lower FTR seen than the mice in the U251-GFP group since the 9L-GFP line showed 20-fold lower EGF uptake than the U251-GFP line *in vitro*. None of the mice in the 9L-GFP Erbitux treatment group appeared to respond to the therapy as either similar or increased FTR was measured during the experiment. The mice in the U251-GFP Erbitux treatment group had either similar or decreased FTR during the course of spectroscopy measurements, and none of the mice had the same increase in EGF-IRDye fluorescence

seen in the 9L-GFP treated group (Figure 8.1(a) & (c)). Therefore, the EGF uptake of the U251-GFP tumors either remained the same or decreased during the experiment, even if the tumor size increased, showing some level of response by all mice in the U251-GFP Erbitux treated group.

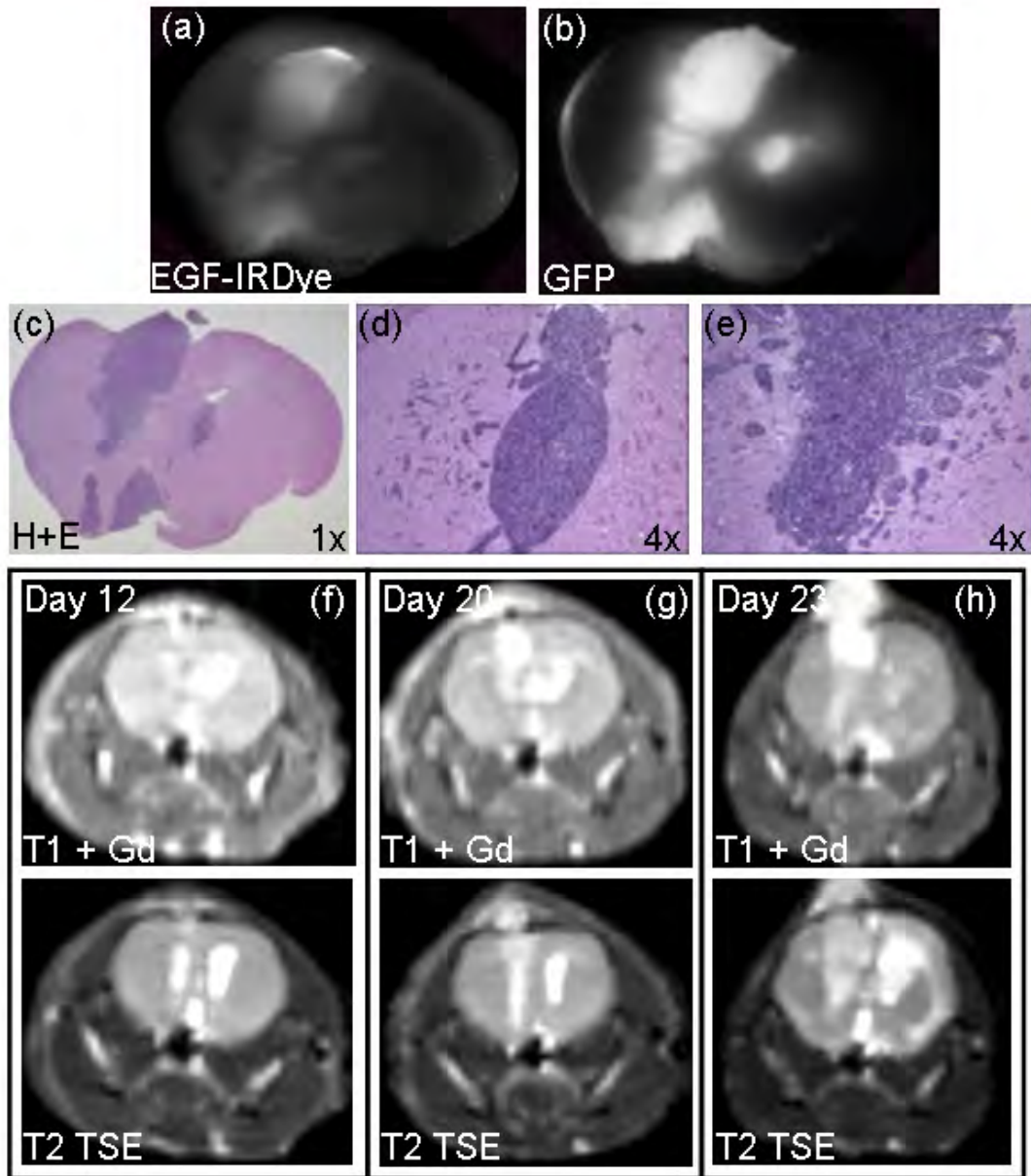


Figure 8.5 – Example mouse AJ2 from the 9L-GFP Erbitux treatment group. A coronal *ex vivo* section was imaged for (a) EGF-IRDye fluorescence, (b) GFP fluorescence and

was stained with (c) H+E. The tumor tissue, which grew both as a bulk mass and in the ventricle space, is illustrated at 4x magnification in (d) and (e). The *in vivo* MR images that were obtained during the experiment are illustrated (f) 12 days, (g) 20 days and (h) 23 days following tumor implantation. T1 TSE CE and T2 TSE MR images of the corresponding section are illustrated.

8.4. EGF Uptake Case Studies

8.4.1. U251-GFP Untreated Mouse with Increased Fluorescence Intensity

The U251-GFP mice in the untreated group were expected to show higher FTR as compared to the U251-GFP Erbitux treated mice; however a statistically significant difference was only seen during the second week of spectroscopy measurements 24 hours after EGF-IRDye administration. Figure 8.1(c) and (d) show that the FTR of many, but not all mice in the U251-GFP untreated group was higher than the FTR of the U251-GFP Erbitux treated mice. However like the treated group, considerable variance was seen in the U251-GFP untreated group where some mice had increased FTR and others had similar FTR throughout the experiment. Images from a mouse which showed increased EGF-IRDye fluorescence during the course of the experiment, labeled AS4 in Figure 8.1(d), are shown in Figure 8.6. The FTR measurements of this mouse showed considerable increase for the same measurement time points during the second week of spectroscopy measurements as compared to the first week (Table 8.1). The tumor tissue, which grew in the ventricle space, showed accumulation of EGF-IRDye *ex vivo*, as a similar pattern of fluorescence enhancement was seen in the EGF-IRDye and GFP images (Figure 8.6(a) & (b)). The *in vivo* T1 TSE CE MR images showed increased ventricle swelling during the experiment, indicating tumor growth in this space (Figure 8.6(f) – (h)). This increase in tumor size allowed for increased EGF uptake during the

second week of spectroscopy measurements as compared to the first week. Therefore, the increased FTR measured *in vivo* would seem to correlate with increased size and EGF uptake of the tumor, illustrating that EGF uptake can be detected noninvasively.

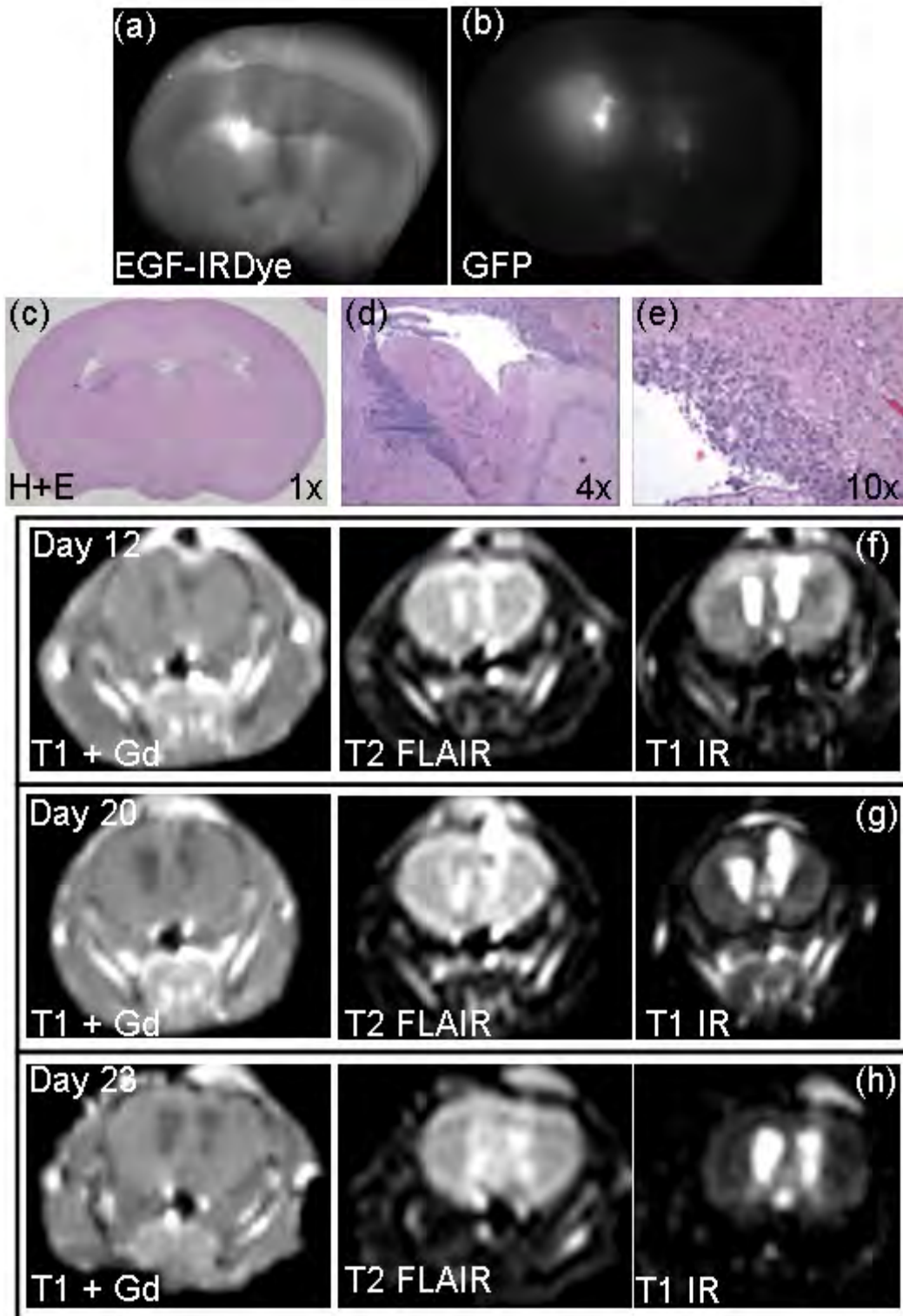


Figure 8.6 – Example mouse AS4 from the U251-GFP untreated group. A coronal *ex vivo* section was imaged for (a) EGF-IRDye fluorescence, (b) GFP fluorescence and was

stained with (c) H+E. The tumor tissue, which grew in the ventricle space, is illustrated at (d) 4x and (e) 10x magnification. The *in vivo* MR images that were obtained during the experiment are illustrated (f) 12 days, (g) 20 days and (h) 23 days following tumor implantation. T1 TSE CE, T2 FLAIR and T1 IR MR images of the corresponding section are shown.

8.4.2. U251-GFP Untreated Mouse with Constant Fluorescence Intensity

In contrast, some of the U251-GFP untreated tumors did not grow as rapidly as the example mouse AS4, shown previously. Images of one such mouse, labeled AT3 in Figure 8.1(d), are shown in Figure 8.7. This mouse had tumor which grew in one ventricle as can be seen from *ex vivo* data in Figure 8.7(b) – (e). Since the tumor only grew in one of the ventricles, it was detectable *in vivo* via asymmetry by MRI. The T1 TSE CE MR images showed a single swollen ventricle, while the T2 FLAIR and T1 IR MR images showed increased enhancement in the tumor-bearing ventricle as compared to the normal ventricle (Figure 8.7(f) – (g)). The tumor did not show significant size increase by MRI between day 12 and 23 of the experiment. Even though this mouse was not part of the Erbitux treatment group it had decreased FTR at the same time points during the second week of spectroscopy measurements as compared to the first week (Table 8.1). Upon *ex vivo* examination, EGF-IRDye accumulation did not show specificity for the tumor tissue in this example (Figure 8.7(a)). Some slight fluorescence enhancement was visible, but EGF-IRDye accumulation appear to be considerably less than that seen in mouse AS4 (Figure 8.6(a)). Even though a U251-GFP tumor was implanted in this mouse it did not show significant EGF uptake, illustrating that a portion of the fluorescence variability seen between mice must be attributed to differences in tumor biology that would account for variable EGF uptake.

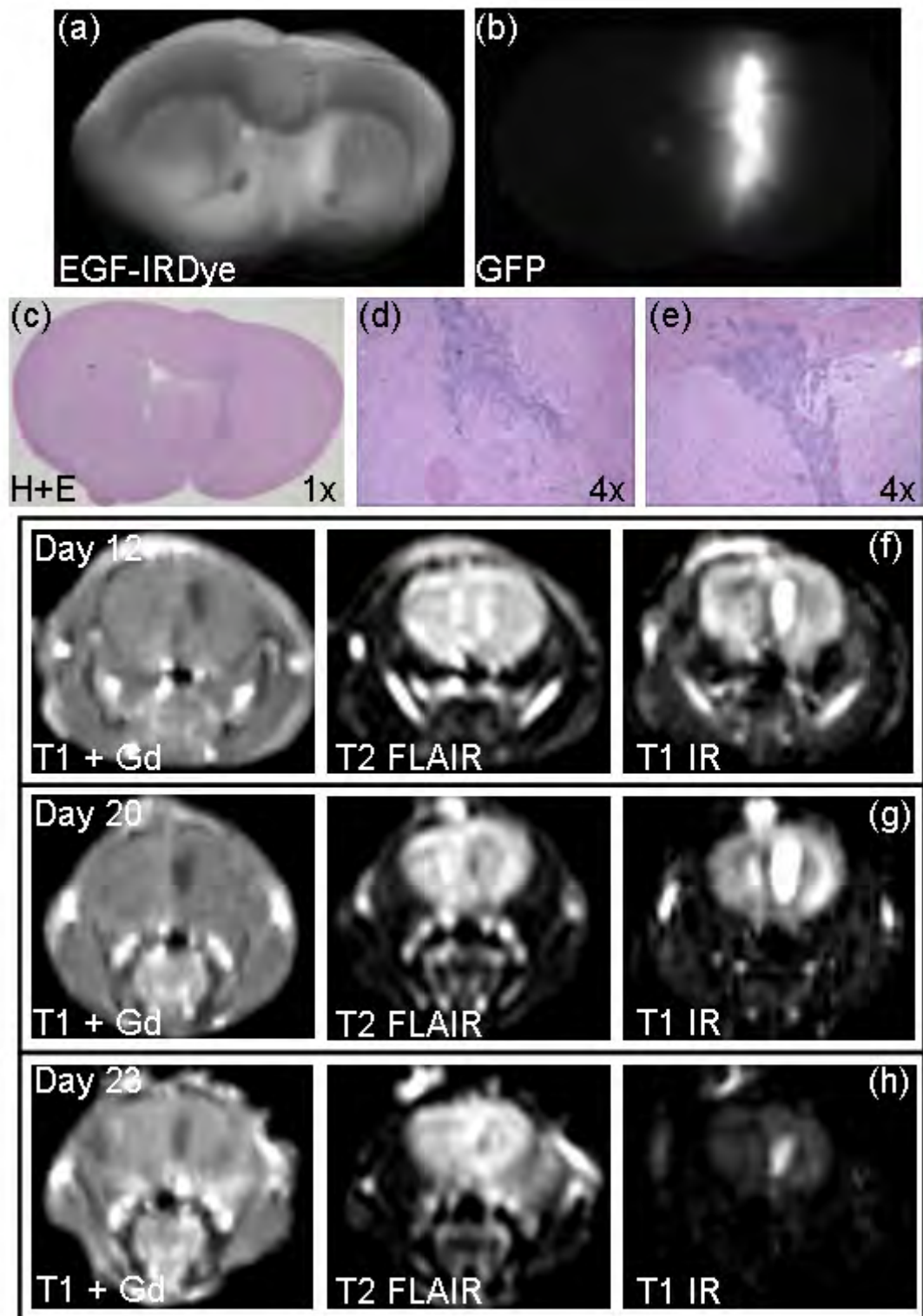


Figure 8.7 – Example mouse AT3 from the U251-GFP untreated group. A coronal *ex vivo* section was imaged for (a) EGF-IRDye fluorescence, (b) GFP fluorescence and was

stained with (c) H+E. The tumor tissue, which grew in one ventricle, is illustrated at 4x magnification in (d) and (e). The *in vivo* MR images that were obtained during the experiment are illustrated (f) 12 days, (g) 20 days and (h) 23 days following tumor implantation. T1 TSE CE, T2 FLAIR and T1 IR MR images of the corresponding section are illustrated.

8.4.3. 9L-GFP Untreated Mouse with Increased Fluorescence Intensity

Substantial variance in the FTR was seen in both the 9L-GFP Erbitux treated and untreated groups, although it appeared that on average the FTR in the treated group may have been higher than in the untreated group (Figure 8.1(a) & (b)). The fluorescence relationship between the 9L-GFP treated and untreated groups showed that the Erbitux therapy had little effect on the 9L-GFP negative control model, as expected from *in vitro* experiments. Mice in both the treated and untreated groups had mostly similar or increased FTR during the experiment (Figure 8.1(a) & (b)). Images of an example mouse, labeled AM3 in Figure 8.1(a) that had increased FTR are illustrated in Figure 8.8. The FTR was increased at each 24 and 48 hour time point in the second week of spectroscopy as compared to the same points during the first week (Table 8.1). Accumulation of the EGF-IRDye was heterogeneous in the tumor as only portions of the tissue showed EGF-IRDye fluorescence *ex vivo* (Figure 8.8 (a) & (b)). The EGF-IRDye fluorescence was increased in the portion of the tumor at the bottom of the brain which appeared to have less edema than the tumor tissue growing within the brain (Figure 8.8(d) & (e)). The tumor grew substantially during the experiment, as can be seen from *in vivo* MR images illustrated in Figure 8.8(f) – (h). Similar to mouse AK1 from the 9L-GFP Erbitux treatment group, the increase in FTR for this mouse appears to be correlated with the increase in tumor tissue size over the course of the experiment.

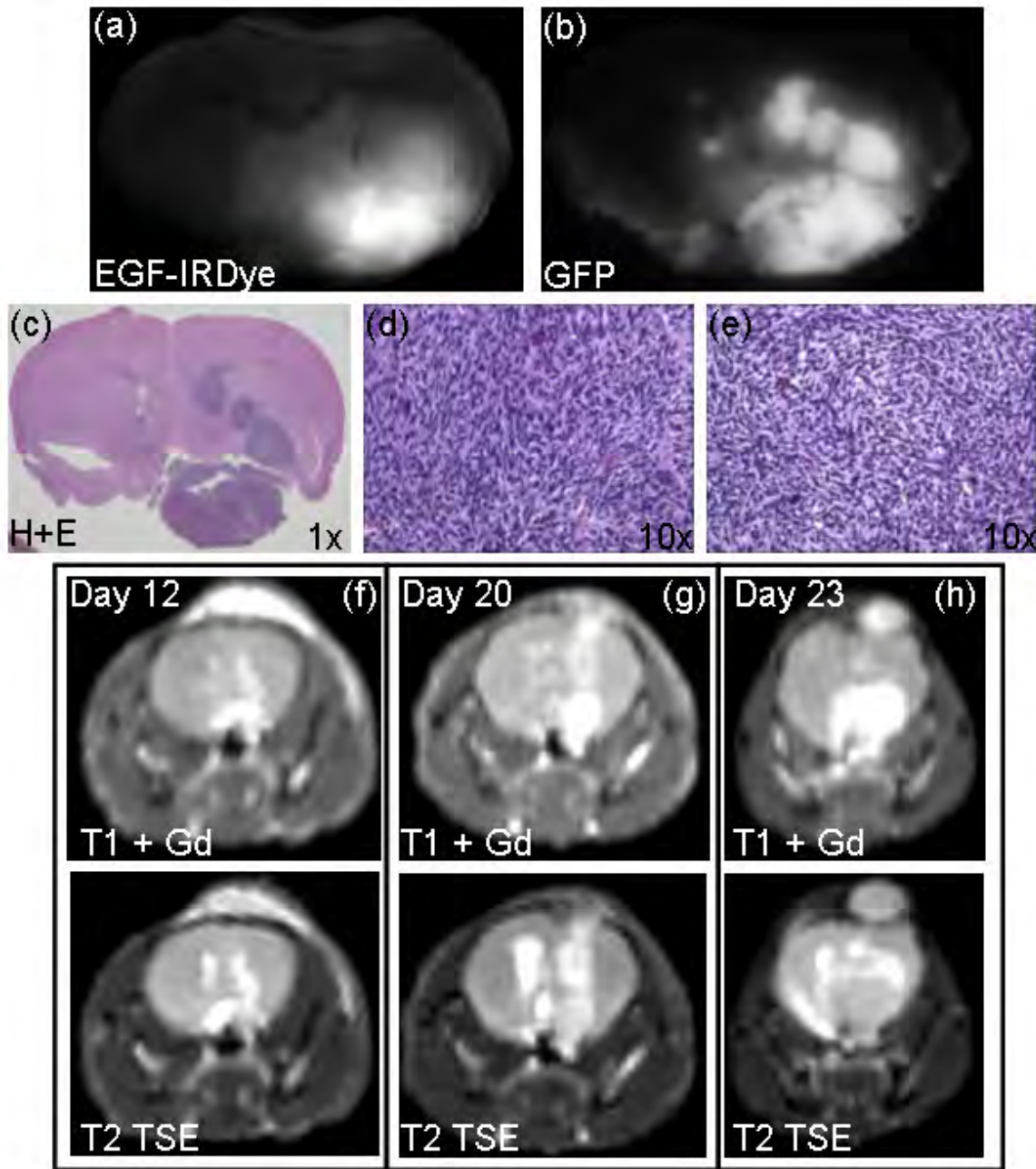


Figure 8.8 – Example mouse AM3 from the 9L-GFP untreated group. A coronal *ex vivo* section was imaged for (a) EGF-IRDye fluorescence, (b) GFP fluorescence and was stained with (c) H+E. The tumor tissue, which grew within the normal brain tissue and below the brain, is illustrated at 10x magnification in (d) and (e). The *in vivo* MR images that were obtained during the experiment are illustrated (f) 12 days, (g) 20 days and (h) 23 days following tumor implantation. T1 TSE CE and T2 TSE MR images of the corresponding section are illustrated.

8.4.4. 9L-GFP Untreated Mouse with Varied Fluorescence Intensity

As previously mention, some mice in the 9L-GFP untreated group showed little increase in FTR during the course of the experiment. Images of one such mouse, labeled AJ3 in Figure 8.1(b), are shown in Figure 8.9. The FTR of this mouse was variable at all time points, but showed lower FTR at the 72 hour time point during the second week of spectroscopy measurements as compared to the first (Table 8.1). *Ex vivo* analysis showed slight EGF-IRDye fluorescence in the portion of the tumor within the brain and higher accumulation near the top of the brain (Figure 8.9(a) & (b)). This tumor did not show significant edema in the portion with low EGF-IRDye fluorescence as seen in the previous example (Figure 8.9(d) & (e)). Mouse AJ3 had a significant tumor mass visible by T1 TSE CE and T2 TSE MRI 12 days after tumor implantation (Figure 8.9(f)). The tumor tissue did not substantially increase in size as detected by MRI from the 12th day to the 20th day of the experiment (Figure 8.9(f) & (g)). However, increased tumor size was discernable between the 20th and 23rd day of the experiment via MR imaging (Figure 8.9(g) & (h)). The FTR does not appear to be correlated to the tumor tissue size in this example as was seen in previous examples. This mouse further illustrates that the FTR of EGF-IRDye fluorescence in 9L-GFP tumor-bearing mice was not necessarily correlated to EGF uptake of the tumor tissue, as was expected from previous *in vitro* experiments.

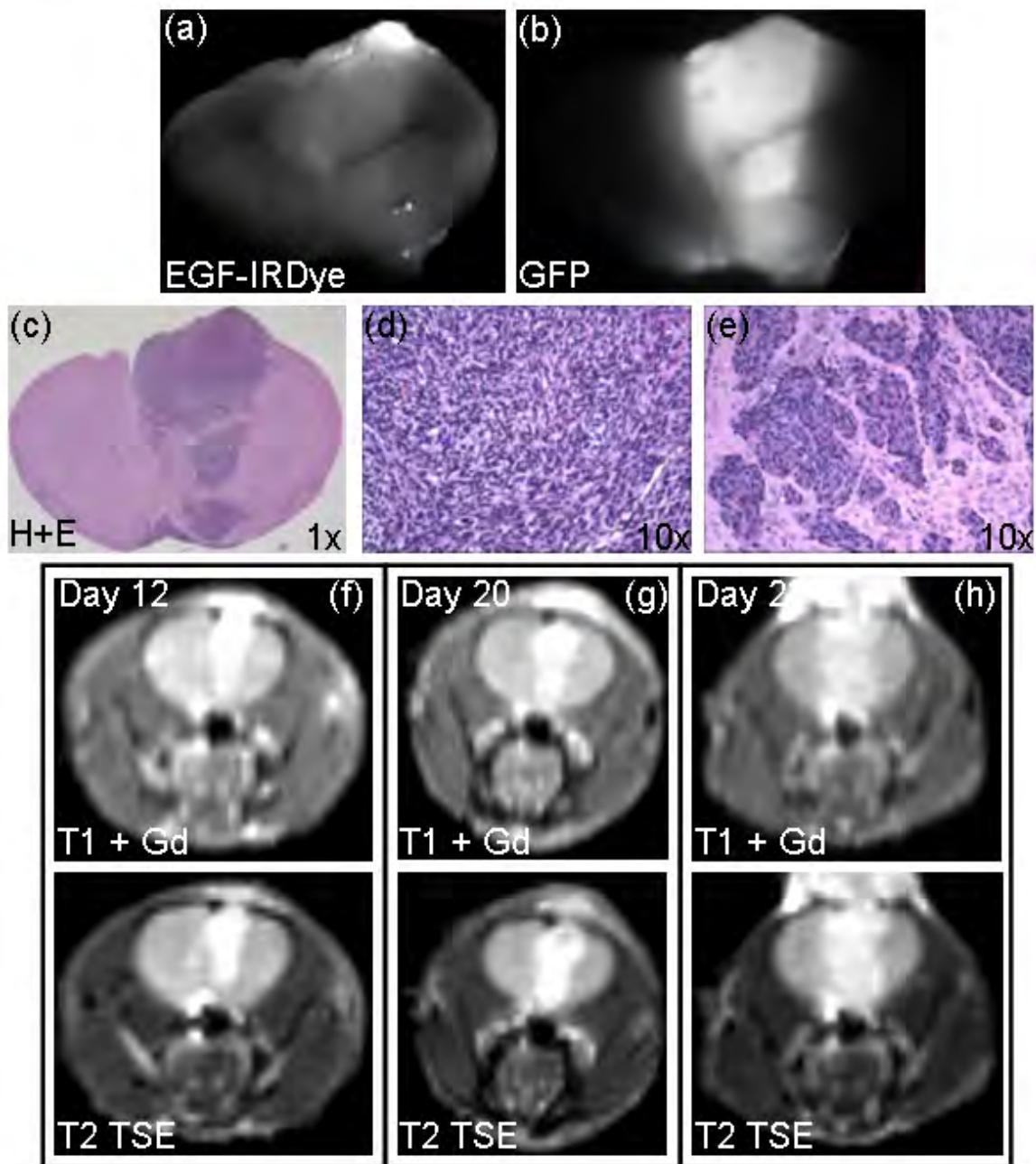


Figure 8.9 – Example mouse AJ3 from the 9L-GFP untreated group. A coronal *ex vivo* section was imaged for (a) EGF-IRDye fluorescence, (b) GFP fluorescence and was stained with (c) H+E. The tumor tissue, which grew as a mass in one hemisphere of the brain, is illustrated at 10x magnification in (d) and (e). The *in vivo* MR images that were obtained during the experiment are illustrated (f) 12 days, (g) 20 days and (h) 23 days following tumor implantation. T1 TSE CE and T2 TSE MR images of the corresponding section are illustrated.

8.5. PpIX Fluorescence Case Studies

PpIX production following ALA administration as measured via fluorescence spectroscopy had substantial variability in both *in vivo* and *ex vivo* measurements, which was discussed at length in chapter 6. 9L-GFP tumors had the largest variance in PpIX production of the tumor lines tested, while the U251-GFP tumors had the smallest variance in PpIX production. When the 9L-GFP tumor tissues were examined *ex vivo*, there were two distinct PpIX production patterns. A few 9L-GFP tumors showed PpIX production in the bulk tumor tissue, but the majority of the tumors showed PpIX production only at the periphery of the tumor. Thus, large variability in PpIX fluorescence was seen from *in vivo* and *ex vivo* measurements because tumors that had PpIX production in the bulk tumor had high PpIX fluorescence by spectroscopy and tumors that had PpIX production only in the periphery of the tumor had lower PpIX fluorescence by spectroscopy.

8.5.1. 9L-GFP Tumor with Heterogeneous PpIX Production

An example mouse with a large 9L-GFP tumor that had some areas of increased PpIX production within the tumor and some areas where tumor PpIX production was the same as normal brain tissue is illustrated in Figure 8.10. When 20x magnification H+E images were examined for the regions of the tumor with high PpIX production, rapidly proliferating tumor tissue with many mitotic figures and significant vasculature was visible (Figure 8.10(f) & (g)). In contrast, when 20x magnification H+E images of the tumor that had low PpIX production were examined, significant edema and lack of mitotic figures was seen. The areas of low PpIX fluorescence did have visible

vasculature; however the tissue did not appear as healthy and was not rapidly proliferating. Different tumors of the same line can have different metabolic rates, and as shown in Figure 8.10, even the same tumor can have regions where the metabolism varies. Thus, PpIX production is a marker of cellular metabolism and its fluorescence pattern could be used as a map of tumor metabolism. It was difficult to assess the reason for this difference in PpIX production when tumors with low PpIX production were compared to tumors with high PpIX production grown in different mice. However, when the H+E images of the same mouse with portions of the tumor that had high and low PpIX fluorescence were considered this link to cellular metabolism was clearly visible.

MR images of this mouse were collected on both the 3T and 7T MRI and were considered to determine if the *in vivo* tissue patterns were consistent with the H+E images. The tumor vasculature of the tissue at the base of the brain was leakier than the vasculature of the tissue invading the normal brain. However, this was only visible by T1 TSE CE 3T MRI and not by T1 CE 7T MRI (Figure 8.10(h) – (j)). Vasculature was visible in both portions of the tumor by H+E; however the leakiness could not be assessed through standard staining. The T2 TSE images showed increased enhancement at the bottom of the brain as compared to the portion of the tumor invading the normal brain. Enhancement in T2 TSE MR images corresponds to increased water content of the tissue, illustrating that the enhancement pattern seen by T2 MRI was consistent with the edema seen in H+E images. Assessment of tissue cellular density was made using diffusion images calculated from 7T MR images. Diffusion images show low contrast in regions where more structures exist to impede water movement and increased contrast in regions where water freely flows. Increased contrast in the diffusion images was seen

towards the base of the brain as compared to that seen in the invasive portion of the tumor (Figure 8.10(l)). This indicates that the invasive tumor was more densely cellular than the portion of the tumor beneath the brain which was confirmed via H+E images (Figure 8.10(d) – (g)).

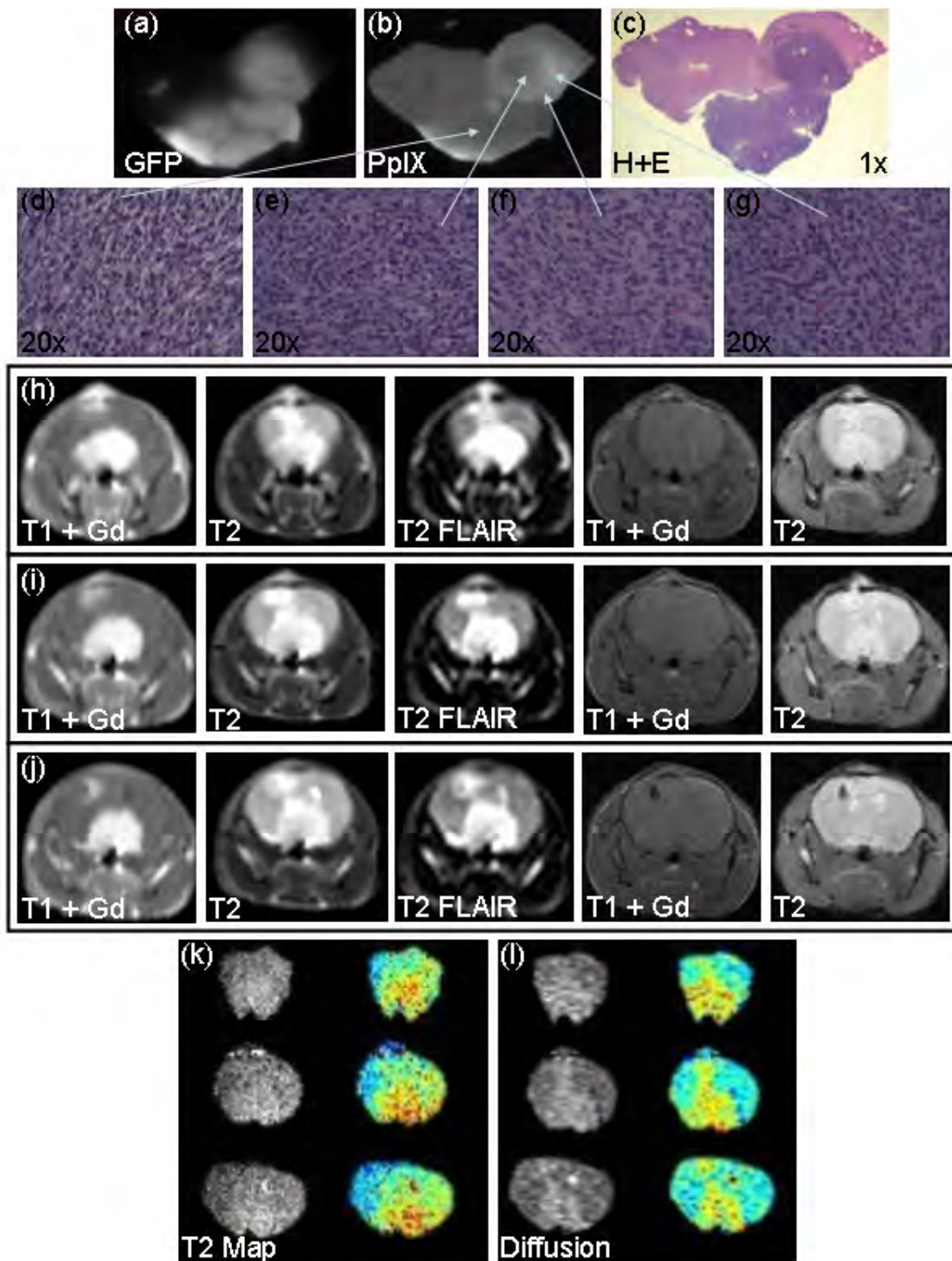


Figure 8.10 – (a) An example 9L-GFP tumor-bearing mouse with a large tumor visible by GFP fluorescence. (b) The PpIX production was high in some parts of the tumor and low in other portions. An H+E stained section at (c) 1x magnification is shown for comparison. Magnified H+E images matching portions of the brain with different PpIX

production levels are shown in (d) – (g) with arrows pointing to the appropriate region in the PpIX section. (h) – (j) MR images of the three slices which most closely represent the *ex vivo* data are shown from the 3T and 7T MRI. The 3T MRI sequences are shown at the left of the figure and included T1 TSE CE, T2 TSE and T2 FLAIR while 7T sequences shown at the right of the figure included T1 CE and T2 images. (k) T2 maps and (l) diffusion images were calculated from images obtained with the 7T MRI. The same three sections are shown by T2 maps and diffusion images as seen in (h) – (j).

8.5.2. U251-GFP Ventricle Tumor PpIX Production Pattern

The U251-GFP tumors had considerably less PpIX production variability as compared to the 9L-GFP tumors. As discussed in chapter 5, the U251-GFP tumors had different growth morphologies which included a bulk tumor, tumor tissue in the ventricle space or diffuse tumor growing in one hemisphere of the brain. All the tumors used for PpIX fluorescence spectroscopy measurements grew either in the ventricle space or diffusely in one hemisphere of the brain. Thus, due to growth morphology the tumors could not grow to the same size as the 9L-GFP tumors before fatal tumor burden was reached. These smaller diffuse tumors appear to have lower PpIX fluorescence by bulk spectroscopy measurements as compared to the 9L-GFP tumors (chapter 6). However, when *ex vivo* brain slices of both tumor types were examined relatively high PpIX fluorescence was visible in the U251-GFP tumors considering the number of tumor cells present in the brain to produce the PpIX. An example of a U251-GFP tumor growing in the ventricle space can be seen in Figure 8.11, where the PpIX fluorescence images closely match the GFP fluorescence images showing increased PpIX production in the tumor tissue (Figure 8.11(a), (b), (e) & (f)). The H+E images showed that the small nests of tumor tissue were healthy, well vascularized and had high cellular density (Figure 8.11(c), (d), (g) & (h)). Thus, each U251-GFP tumor cell produced considerably more

PpIX than each 9L-GFP tumor cell since PpIX fluorescence was detected via *in vivo* spectroscopy with very few U251-GFP cells present. Since this tumor was relatively small it did not cause ventricle swell and was virtually undetectable by either 3T or 7T MR images (Figure 8.11(i) – (m)).

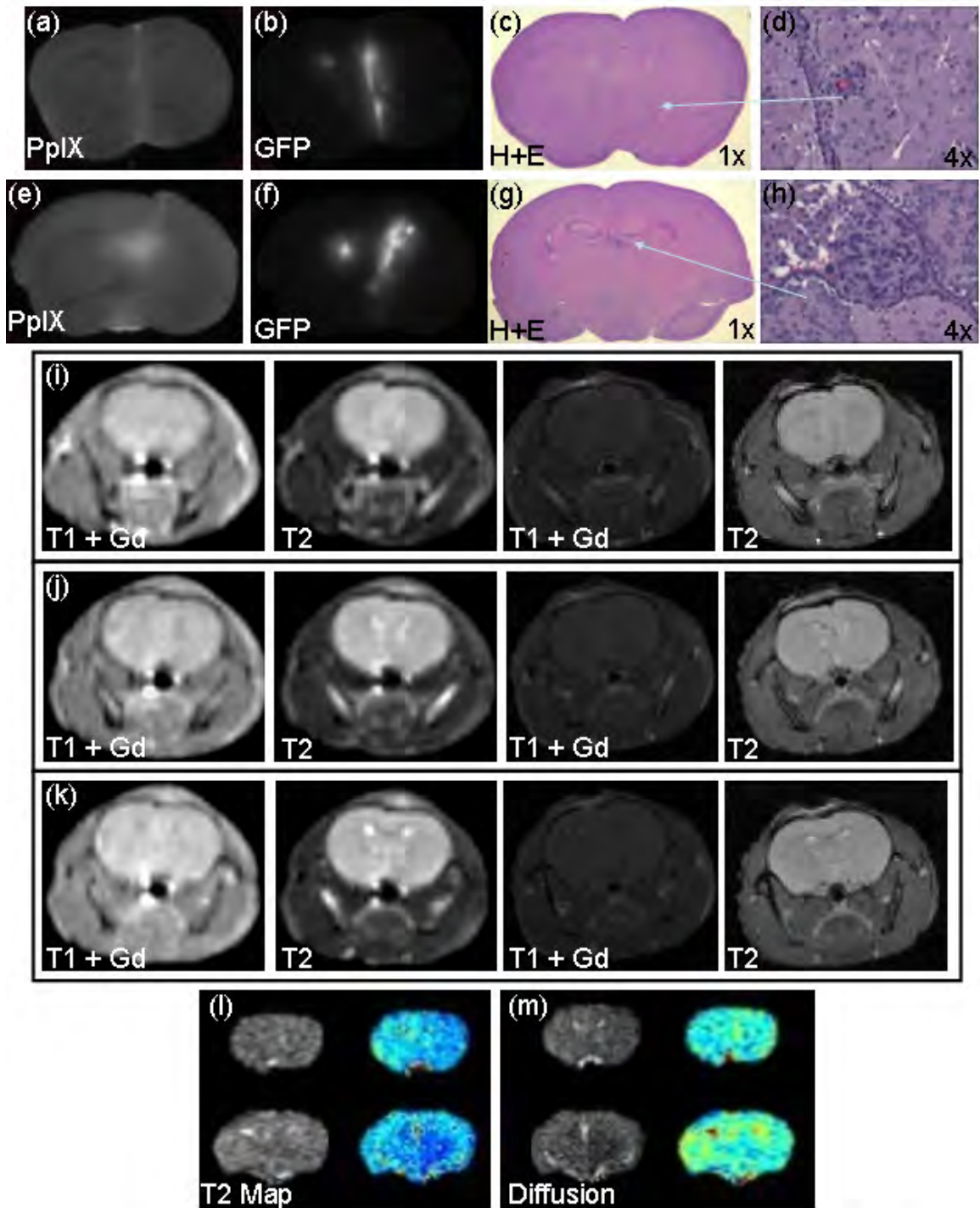


Figure 8.11 – An example U251-GFP tumor growing in the ventricle space is shown. The two *ex vivo* sections with corresponding cut faces are illustrated in (a) – (h), where PpIX and GFP fluorescence as well as H+E at 1x and 4x magnification are shown. Arrows from the 4x magnification H+E images show the approximate region of the magnified image on the 1x image. MR images were collected on the 3T (left hand side of

figure) and the 7T (right hand side of figure) MRI, with T1 CE and T2 sequences of the three slices that most closely represent the *ex vivo* data shown in (i) – (k). The two most representative slices are shown for (l) T2 maps and (m) diffusion images collected via the 7T MRI.

8.5.3. U251-GFP Diffuse Tumor PpIX Production Pattern

An example of a U251-GFP tumor which grew more diffusely in one hemisphere of the brain and did have a small mass towards the bottom of the brain is illustrated in Figure 8.12. Strong PpIX fluorescence was visible at the bottom of the brain which closely matched the *ex vivo* GFP fluorescence pattern (Figure 8.12(b) & (c)). When the H+E images were examined larger tumor nests were visible than in the tumor shown in Figure 8.11, which corresponded to stronger PpIX fluorescence signal. The 4x magnification images of two large nests of U251-GFP tumors showed well vascularized, densely cellular tumor tissue (Figure 8.12(d) & (e)). This tumor was more visible by MRI than the previous example. Some enhancement was visible towards the bottom of the brain, as can be seen in the three images on the left of Figure 8.12(h) – (j) obtained via 3T MRI, although it was difficult to determine tumor presence due to the low resolution of these images. T1 CE 7T MR images, at the right of Figure 8.12(h) – (j), showed enhancement at the bottom of the brain which seemed to overestimate the size of the tumor tissue seen through *ex vivo* images. Little enhancement was seen in the 7T MR T2 images (right most image Figure 8.12(h) – (j)). The T2 map, Figure 8.12(f), collected via 7T showed the same pattern of enhancement as the T1 CE images, which seemed to overestimate tumor size. The diffusion images did not show the presence of tumor tissue (Figure 8.12(g)). PpIX fluorescence of this tumor appeared brighter than the previous example, which could be attributed to larger tumor nests. Thus, it appears that tumor size

plays a significant role in the detection of bulk PpIX fluorescence via spectroscopy measurements.

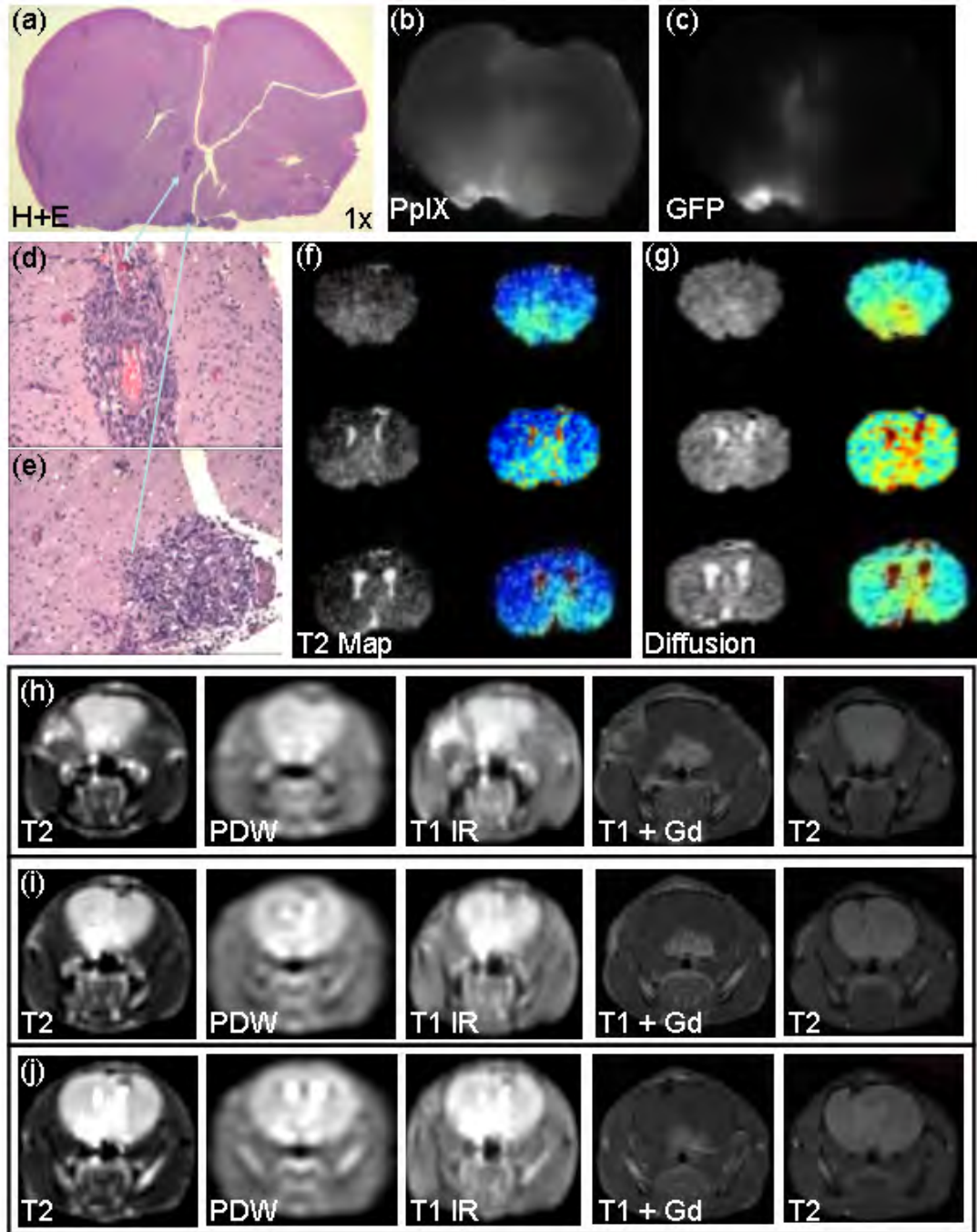


Figure 8.12 – (a) An example U251-GFP tumor with diffuse tissue and small mass towards the bottom of the brain as shown by 1x magnification H+E. The *ex vivo* (b)

PpIX and (c) GFP fluorescence of the same section are shown. 4x magnification images of the two visible tumor regions are shown in (d) & (e) with arrows pointing to the approximate location of image acquisition. *In vivo* MRI was obtained with both a 3T and 7T magnet. Three representative slices of a (f) T2 Map and (g) diffusion images collected via the 7T which match the *ex vivo* data are shown. (h) – (j) The same three slices are illustrated from the 3T and the 7T, showing T2 TSE, PDW and T1 IR from the 3T (right hand side of figure) and T1 CE as well as T2 from the 7T (left hand side of figure).

8.6. Discussion

The *in vivo* spectroscopically detected fluorescence intensity of PpIX production and EGF-IRDye uptake had high variability in the population of mice tested. A portion of this variation could be attributed to positional variability and the detection of skin fluorescence as part of the signal from the brain. However, much of the variation was due to differences in tumor biology which could not be accounted for through better positioning or light sampling. Both fluorophores used in this thesis were molecular imaging agents which detected either metabolism (ALA-induced PpIX) or EGF uptake and EGFR status (EGF-IRDye). Thus, variability in detected fluorescence intensity was inherent due to the known variability in molecular signatures of the same types of tumors [130-132].

Substantial variance was seen by *in vivo* assessment of EGF-IRDye fluorescence between mice in both the U251-GFP and 9L-GFP groups with and without treatment (Figure 8.1). Not all mice bearing the positive expression EGFR tumor model exhibited response to Erbitux therapy. Two example U251-GFP tumor-bearing mice from the treated group were shown, one which had decreased EGF-IRDye fluorescence and one which showed similar fluorescence intensity throughout the experiment. Mice in the U251-GFP group treated with Erbitux therapy were expected to show decreased EGF-

IRDye fluorescence as this was the trend seen *in vitro*, however some tumor-bearing mice did not show response to therapy even though they were implanted with the same tumor line. Interestingly, the poor response to therapy was visible through noninvasive fluorescence monitoring and was confirmed by *ex vivo* analysis and in some cases *in vivo* MR imaging (Figure 8.2). The variance in EGF-IRDye fluorescence could not be solely attributed to molecular changes that occurred post therapy, as U251-GFP tumor-bearing mice that were not treated with Erbitux therapy had variable fluorescence during the course of the experiment. While most of the untreated U251-GFP tumor-bearing mice had increased EGF-IRDye fluorescence during the experiment, some mice showed little tumor growth and had decreased EGF-IRDye fluorescence during the course of the experiment, illustrating correlation between fluorescence signal and molecular changes of the tissue (Figure 8.7).

The negative control model (9L-GFP) which had little EGF uptake *in vitro* also had large EGF-IRDye fluorescence variability *in vivo*. No discernable relationship between Erbitux treated mice or untreated mice and EGF-IRDye fluorescence was found. All 9L-GFP tumor-bearing mice regardless of treatment status had either similar or increased EGF-IRDye fluorescence throughout the experiment. The mice that showed increased fluorescence during the course of the experiment usually had substantial tumor size increase as detected by MRI during the spectroscopy measurement period. Thus, the increase in fluorescence accumulation in the tumor tissue was probably due to vascular leakage and blood pooling stemming from rapid size increase rather than specific binding of the EGFR targeted fluorophore in the 9L-GFP tumors.

As discussed in chapter 6, considerable variability in PpIX fluorescence was measured via transmission spectroscopy in the 9L-GFP tumor-bearing mice while the variance was substantially less for the U251-GFP tumor-bearing mice. PpIX production is a measure of cellular metabolism which is variable between different tumor lines, between the same tumor line implanted in different mice and between different portions of the same large tumor in a single mouse. One such example was shown in Figure 8.10, where different portions of a 9L-GFP tumor had varied PpIX production. When the H+E images of these sections were examined it could be seen that areas with high proliferation rate and high cellular density had increased PpIX fluorescence. In contrast, areas of the tumor with PpIX production similar to the normal brain tissue showed less cellular density with significant edema and thus slower growing cells.

Tumor size also contributed to the detected PpIX fluorescence heterogeneity in two ways. First, larger tumors had areas of high and low metabolism and thus they had heterogeneous PpIX fluorescence. Second, bulk PpIX fluorescence measurements as obtained by transmission spectroscopy could not account for tumor volume. So, in the case of the U251-GFP tumor where small nests of tumor cells grew in the brain as opposed to a large bulk tumor, as seen in the 9L-GFP model, less cells equated to decreased PpIX fluorescence signal as measured by transmission spectroscopy. This was true even though the individual U251-GFP cells produced more PpIX than the individual 9L-GFP cells. More 9L-GFP cells could reside in the mouse brain than U251-GFP cells before fatal tumor burden was reached. Thus, in some cases the 9L-GFP tumor-bearing mice appeared to have higher PpIX fluorescence than the U251-GFP tumor-bearing mice.

In conclusion, cancer imaging is shifting away from structural imaging toward function or molecular based imaging which provides information about changes occurring at the cellular and subcellular level. Much *in vitro* and *in vivo* work must be completed to standardize both PpIX and EGF imaging probes and systems for future use. It should be noted from the work presented here that significant heterogeneity and variability is present in the *in vitro* and *in vivo* systems which will be used as a testing platform. Detection of this variability in future imaging should be fully investigated, but should not exclude these probes from clinical use, as heterogeneity in tumor models is inherent and visualization of this heterogeneity is important.

Chapter 9 - Conclusions & Future Directions

9.1. Concluding Remarks

This thesis has explored optical methods to detect and assess murine glioma growth and response to therapy. Two fluorophores capable of providing information at the cellular and subcellular level have been characterized *in vitro*, *in vivo* and *ex vivo*. Transmission spectroscopy systems were used to assess fluorophore distribution *in vivo* and feasibility of fluorescence assessment of cellular metabolism and receptor status for *in vivo* molecular monitoring. Significant work was focused on attaining the most quantitative measurement and best detection of fluorescent anomalies. It was demonstrated that transmission measurements across the domain provide the highest signal when the fluorescent anomaly was positioned within the fiber plane. Positional phantom experiment showed significant signal decrease when the anomaly was out of the fiber plane, which was less significant when the tissue-fiber interface was large, such as in the single channel spectroscopy system (chapter 4). Fluorescence transmission measurements were normalized to transmitted excitation signals collected directly after fluorescence measurements. This normalization process and subsequent ratio data set decreased the positional dependence of the measurement as well as the optical property dependence. All fluorescence to transmittance data was spectrally fitted to appropriate phantom data to allow fluorescent signals to be deconvolved from any extraneous bleed through signal which could confound small fluorescent changes in the data. Three intracranial brain tumor models were studied in this thesis work and substantial heterogeneity in tumor growth morphology was detected and assessed *in vivo* and *ex vivo*. Tumor tissue fluorescence heterogeneity was examined on a case by case basis to better

understand the origin of fluorescence molecular signals. Anatomical magnetic resonance imaging was used to compare tumor structure to tumor function as evaluated by fluorescence transmission spectroscopy.

Cellular metabolism was monitored via protoporphyrin IX (PpIX) production following administration of the prodrug aminolevulinic acid. This fluorophore was studied as a general metabolic marker, which could be widely used as a therapy monitor of cancer cell metabolism. *In vivo* detection of PpIX fluorescence in murine glioma was more difficult than initially hypothesized due to significant PpIX skin production. In this work, detection in brain tumor tissue *in vivo* was optimized and further characterized *ex vivo*. Through *ex vivo* analysis of the fluorescence and H+E images it was determined that the PpIX fluorescence increased in proliferative tissue over senescent cells and could be used as a fluorescent map of tumor cell metabolism.

Advanced biological understanding of cancer has provided insight into cancer as an individual disease and specific molecular targets for cancer therapy and imaging on a case by case basis. In this thesis work, one of these specific molecular targets was chosen to examine transmission fluorescence spectroscopy as a tool to quantify molecular signatures of disease. As a more specific analysis of cellular morphology than PpIX fluorescence for metabolic imaging, the epidermal growth factor receptor (EGFR) was studied. Fluorescently labeled epidermal growth factor (EGF) was used to quantify *in vivo* EGFR status of the tumor tissue providing the ability to noninvasively stratify tumor-bearing animals into groups with high EGFR expression and low EGFR expression based on fluorescence intensity. Transmission fluorescence spectroscopy was also explored to monitor EGFR specific therapy. EGFR specific therapy of tumor tissues

could be monitored noninvasively with fluorescence signatures corresponding to therapy efficacy for animals bearing high EGFR expressing tumors, with a statistically significant difference seen between treated and untreated tumor-bearing mice (p-value = 0.035).

Considerable fluorescence variation was seen when both fluorophores were examined *in vitro*, *in vivo* and *ex vivo*. Fluorescence variance and heterogeneity were examined at the individual animal level to determine if the source of fluorescence variation could be attributed to engineering, tumor biology or both. The transmission spectroscopy systems were examined through phantom and model based work which pointed to animal positioning as one of the largest sources of variance in fluorescence signal detection. Mouse case studies involving concurrent evaluation of *in vivo* structural and functional data with *ex vivo* fluorescence and pathology information revealed significant variation in tumor biology between animals bearing the same tumor line as well as between the three tumor models. Although some fluorescence variance could be attributed to the transmission spectroscopy systems themselves, much of the difference in detected signal was due to differences in tumor biology. In this regard fluorescence variance is inherent in the use of molecular imaging agents as their purpose is to highlight cellular and subcellular changes that will enable more specific assessment of the individual disease, cancer.

9.2. Future Directions

The work present in this thesis is only the beginning of a plethora of fluorescence imaging applications which could be used to noninvasively detect molecular signatures of cancer to stratify treatments groups as well as monitor response to therapy. Development

of these spectrally based systems will allow for future assessment of a wide variety of fluorophores in addition to PpIX and fluorescently labeled EGF. The transmission fluorescence spectroscopy systems also enable detection of multiple fluorophores simultaneously and thus multiple molecular markers could be assessed at a single time point to understand tumor growth, progression and response to therapy at the cellular and subcellular level.

Possible improvements that could be made to both the transmission spectroscopy systems and tumor model are discussed as follows. A larger tissue-fiber interface for the multichannel transmission spectroscopy system (chapter 3) would enhance the ability of this system to detect tumors as a stand-alone system. Due to the small fiber-tissue interface this system currently has strong positional dependence and is reliant on simultaneous MRI for appropriate tumor positioning in the fiber plane. The fiber optics on the multichannel system could be adapted to enable attachment of large diameter collimators, similar to those used on the single channel spectroscopy system, to decrease the positional sensitivity of the measurements, as discussed in chapter 4. The focus of this thesis was not on development of brain tumor models, although significant growth heterogeneity was seen within the three tumor lines studied as well as between the lines. Additional work could be completed to better characterize tumor growth patterns and determine if changes in the implantation procedure could be made to decrease tumor growth pattern heterogeneity.

The ability to noninvasively detect PpIX fluorescence has been quantified and experimentation to examine tumor cell metabolism change *in situ* could be performed on conventional cancer therapies such as radiation therapy and chemotherapy as well as

molecularly targeted therapies. PpIX fluorescence could also be used as a broad assessment of tumor response and paired with more specific molecular marker for noninvasive monitoring of targeted therapies. The world of cancer therapeutics is shifting from general therapies to targeted therapies and the success of these therapies may be influenced by *in vivo* visualization and understanding which can come from improved molecular characterization technology.

REFERECES

1. Benard, F., J. Romsa, and R. Hustinx, *Imaging gliomas with positron emission tomography and single-photon emission computed tomography*. Seminars in Nuclear Medicine, 2003. **33**(2): p. 148-62.
2. Shah, K. and R. Weissleder, *Molecular Optical Imaging: Applications Leading to the Development of Present Day Therapeutics*. NeuroRx: The Journal of the American Society for Experimental NeuroTherapeutics, 2005. **2**(2): p. 215-225.
3. Ntziachristos, V., C. Bremer, and R. Weissleder, *Fluorescence imaging with near-infrared light: new technological advances that enable in vivo molecular imaging*. European Radiology, 2003. **13**(1): p. 195-208.
4. Stylli, S.S. and A.H. Kaye, *Photodynamic therapy of cerebral glioma - A review Part II - Clinical studies*. Journal of Clinical Neuroscience, 2006. **13**(7): p. 709-17.
5. Reardon, D.A. and P.Y. Wen, *Therapeutic advances in the treatment of glioblastoma: rationale and potential role of targeted agents*. Oncologist, 2006. **11**(2): p. 152-64.
6. Tam Truong, M., *Current role of radiation therapy in the management of malignant brain tumors*. Hematology Oncology Clinics of North America, 2006. **20**(2): p. 431-53.
7. Tuettenberg, J., C. Friedel, and P. Vajkoczy, *Angiogenesis in malignant glioma-A target for antitumor therapy?* Critical Reviews in Oncology Hematology, 2006. **59**(3): p. 181-93.

8. Kesari, S., N. Ramakrishna, C. Sauvageot, C.D. Stiles, and P.Y. Wen, *Targeted molecular therapy of malignant gliomas*. Current Neurology & Neuroscience Reports, 2005. **5**(3): p. 186-97.
9. Stupp, R., M.E. Hegi, M.J. van den Bent, W.P. Mason, M. Weller, R.O. Mirimanoff, J.G. Cairncross, R. European Organisation for, T. Treatment of Cancer Brain, G. Radiotherapy, and G. National Cancer Institute of Canada Clinical Trials, *Changing paradigms--an update on the multidisciplinary management of malignant glioma*. Oncologist, 2006. **11**(2): p. 165-80.
10. Stupp, R., W.P. Mason, M.J. van den Bent, M. Weller, B. Fisher, M.J. Taphoorn, K. Belanger, A.A. Brandes, C. Marosi, U. Bogdahn, J. Curschmann, R.C. Janzer, S.K. Ludwin, T. Gorlia, A. Allgeier, D. Lacombe, J.G. Cairncross, E. Eisenhauer, R.O. Mirimanoff, R. European Organisation for, T. Treatment of Cancer Brain, G. Radiotherapy, and G. National Cancer Institute of Canada Clinical Trials, *Radiotherapy plus concomitant and adjuvant temozolomide for glioblastoma.[see comment]*. New England Journal of Medicine, 2005. **352**(10): p. 987-96.
11. Soffiatti, R., F. Ruda, and E. Trevisan, *New chemotherapy options for the treatment of malignant glioma*. Anti-Cancer Drugs, 2007. **18**(6): p. 621 - 632.
12. Dehdashti, A.R., M.E. Heig, L. Regli, A. Pica, and R. Stupp, *New trends in the medical management of glioblastoma multiforme: the role of temozolomide chemotherapy*. Neurosurgical Focus, 2006. **20**(4): p. 1 - 6.
13. Sathornsumetee, S. and J.N. Rich, *New treatment strategies for malignant gliomas*. Expert Review of Anticancer Therapy, 2006. **6**(7): p. 1087-104.

14. Sathornsumetee, S., D.A. Reardon, A. Desjardins, J.A. Quinn, J.J. Vredenburgh, and J.N. Rich, *Molecularly Targeted Therapy for Malignant Glioma*. *Cancer*, 2007. **110**(1): p. 13 - 24.
15. Stylli, S.S. and A.H. Kaye, *Photodynamic therapy of cerebral glioma--a review Part I--a biological basis*. *Journal of Clinical Neuroscience*, 2006. **13**(6): p. 615-25.
16. Marshall, J., *Clinical Implications of the Mechanism of Epidermal Growth Factor Receptor Inhibitors*. *Cancer*, 2006. **107**(6): p. 1207 - 1218.
17. Halatsch, M.E., U. Schmidt, J. Behnke-Mursch, A. Unterberg, and C.R. Wirtz, *Epidermal growth factor receptor inhibition for the treatment of glioblastoma multiforme and other malignant brain tumors*. *Cancer Treatment Reviews*, 2006. **32**: p. 74 - 89.
18. Mischel, P.S. and T.F. Cloughesy, *Targeted Molecular Therapy of GBM*. *Brian Pathology*, 2003. **13**(1): p. 52 - 61.
19. Toffoli, G., E.D. Mattia, E. Cecchin, P. Bion, S. Masier, and G. Corona, *Pharmacology of epidermal growth factor inhibitors*. *The International Journal of Biological Markers*, 2007. **22**(1 (supp 4)): p. S24 - S39.
20. Kim, E.S., F.R. Khuri, and R.S. Herbst, *Epidermal growth factor receptor biology (IMC-C225)*. *Current Opinion in Oncology*, 2001. **13**: p. 506 - 513.
21. Eller, J.L., S.L. Longo, M.M. Kyle, D. Bassano, D.J. Hicklin, and G.W. Canute, *Anti-epidermal growth factor receptor monoclonal antibody cetuximab augments radiation effects in glioblastoma multiforme in vitro and in vivo*. *Neurosurgery*, 2005. **56**: p. 155 - 162.

22. Friesen, S.A., G.O. Hjortland, S.J. Madsen, H. Hirschberg, O. Engebraten, J.M. Nesland, and Q. Peng, *5-Aminolevulinic acid-based photodynamic detection and therapy of brain tumors (review)*. International Journal of Oncology, 2002. **21**(3): p. 577-82.
23. Kennedy, J.C., S.L. Marcus, and R.H. Pottier, *Photodynamic therapy (PDT) and photodiagnosis (PD) using endogenous photosensitization induced by 5-aminolevulinic acid (ALA): mechanisms and clinical results*. Journal of Clinical Laser Medicine & Surgery, 1996. **14**(5): p. 289-304.
24. Collaud, S., A. Juzeniene, J. Moan, and N. Lange, *On the selectivity of 5-aminolevulinic acid-induced protoporphyrin IX formation*. Current Medicinal Chemistry Anti Cancer Agents, 2004. **4**(3): p. 301-16.
25. Peng, Q., T. Warloe, K. Berg, J. Moan, M. Kongshaug, K.E. Giercksky, and J.M. Nesland, *5-Aminolevulinic acid-based photodynamic therapy. Clinical research and future challenges*. Cancer, 1997. **79**(12): p. 2282-308.
26. Bogaards, A., A. Varma, S.P. Collens, A. Lin, A. Giles, V.X. Yang, J.M. Bilbao, L.D. Lilge, P.J. Muller, and B.C. Wilson, *Increased brain tumor resection using fluorescence image guidance in a preclinical model*. Lasers in Surgery & Medicine, 2004. **35**(3): p. 181-90.
27. Olivo, M. and B.C. Wilson, *Mapping ALA-induced PPIX fluorescence in normal brain and brain tumour using confocal fluorescence microscopy*. International Journal of Oncology, 2004. **25**(1): p. 37-45.
28. Stummer, W., A. Novotny, H. Stepp, C. Goetz, K. Bise, and H.J. Reulen, *Fluorescence-guided resection of glioblastoma multiforme by using 5-*

- aminolevulinic acid-induced porphyrins: a prospective study in 52 consecutive patients.* Journal of Neurosurgery, 2000. **93**(6): p. 1003-13.
29. Stummer, W., U. Pichlmeier, T. Meinel, O.D. Wiestler, F. Zanella, H.J. Reulen, and A.L.-G.S. Group, *Fluorescence-guided surgery with 5-aminolevulinic acid for resection of malignant glioma: a randomised controlled multicentre phase III trial.[see comment].* Lancet Oncology, 2006. **7**(5): p. 392-401.
 30. Hebeda, K.M., A.E. Saarnak, M. Olivo, H.J. Sterenberg, and J.G. Wolbers, *5-Aminolevulinic acid induced endogenous porphyrin fluorescence in 9L and C6 brain tumours and in the normal rat brain.[erratum appears in Acta Neurochir (Wien) 1998:140(8):881].* Acta Neurochirurgica, 1998. **140**(5): p. 503-12.
 31. Bisland, S.K., L. Lilge, A. Lin, R. Rusnov, and B.C. Wilson, *Metronomic photodynamic therapy as a new paradigm for photodynamic therapy: rationale and preclinical evaluation of technical feasibility for treating malignant brain tumors.* Photochemistry & Photobiology, 2004. **80**: p. 22-30.
 32. Olzowy, B., C.S. Hundt, S. Stocker, K. Bise, H.J. Reulen, and W. Stummer, *Photoirradiation therapy of experimental malignant glioma with 5-aminolevulinic acid.* Journal of Neurosurgery, 2002. **97**(4): p. 970-6.
 33. Hirschberg, H., S. Spetalen, S. Carper, P. Hole, T. Tillung, and S. Madsen, *Minimally invasive photodynamic therapy (PDT) for ablation of experimental rat glioma.* Minimally Invasive Neurosurgery, 2006. **49**(3): p. 135-42.
 34. Madsen, S.J., E. Angell-Petersen, S. Spetalen, S.W. Carper, S.A. Ziegler, and H. Hirschberg, *Photodynamic therapy of newly implanted glioma cells in the rat brain.* Lasers in Surgery & Medicine, 2006. **38**(5): p. 540-8.

35. Bogaards, A., A. Varma, K. Zhang, D. Zach, S.K. Bisland, E.H. Moriyama, L. Lilge, P.J. Muller, and B.C. Wilson, *Fluorescence image-guided brain tumour resection with adjuvant metronomic photodynamic therapy: pre-clinical model and technology development*. Photochemical & Photobiological Sciences, 2005. **4**(5): p. 438-42.
36. Stepp, H., T. Beck, T. Pongratz, T. Meinel, F.W. Kreth, J.C. Tonn, and W. Stummer, *ALA and malignant glioma: fluorescence-guided resection and photodynamic therapy*. Journal of Environmental Pathology, Toxicology & Oncology, 2007. **26**(2): p. 157 - 164.
37. Jacobs, A.H., L.W. Kracht, A. Gossmann, M.A. Ruger, A.V. Thomas, A. Thiel, and K. Herholz, *Imaging in neurooncology*. NeuroRx, 2005. **2**(2): p. 333-47.
38. Nelson, S.J. and S. Cha, *Imaging glioblastoma multiforme*. Cancer Journal, 2003. **9**(2): p. 134-45.
39. Nelson, S.J., *Magnetic resonance spectroscopic imaging. Evaluating responses to therapy for gliomas*. IEEE Engineering in Medicine & Biology Magazine, 2004. **23**(5): p. 30-9.
40. Prigent-Le Jeune, F., F. Dubois, S. Perez, S. Blond, and M. Steinling, *Technetium-99m sestamibi brain SPECT in the follow-up of glioma for evaluation of response to chemotherapy: first results*. European Journal of Nuclear Medicine & Molecular Imaging, 2004. **31**(5): p. 714-9.
41. Vos, M.J., J. Berkhof, T.J. Postma, O.S. Hoekstra, F. Barkhof, and J.J. Heimans, *Thallium-201 SPECT: the optimal prediction of response in glioma therapy*.

- European Journal of Nuclear Medicine & Molecular Imaging, 2006. **33**(2): p. 222-7.
42. Vos, M.J., O.S. Hoekstra, F. Barkhof, J. Berkhof, J.J. Heimans, C.J. van Groenigen, W.P. Vandertop, B.J. Slotman, and T.J. Postma, *Thallium-201 single-photon emission computed tomography as an early predictor of outcome in recurrent glioma.[see comment]*. Journal of Clinical Oncology, 2003. **21**(19): p. 3559-65.
43. Henson, J.W., P. Gaviani, and R.G. Gonzalez, *MRI in treatment of adult gliomas*. Lancet Oncology, 2005. **6**(3): p. 167-75.
44. Cao, Y., P.C. Sundgren, C.I. Tsien, T.T. Chenevert, and L. Junck, *Physiologic and metabolic magnetic resonance imaging in gliomas*. Journal of Clinical Oncology, 2006. **24**(8): p. 1228-35.
45. Gagner, J.P., M. Law, I. Fischer, E.W. Newcomb, and D. Zagzag, *Angiogenesis in gliomas: imaging and experimental therapeutics*. Brain Pathology, 2005. **15**(4): p. 342-63.
46. Van de Wiele, C., C. Lahorte, W. Oyen, O. Boerman, I. Goethals, G. Slegers, and R.A. Dierckx, *Nuclear medicine imaging to predict response to radiotherapy: a review*. International Journal of Radiation Oncology, Biology, Physics, 2003. **55**(1): p. 5-15.
47. Jacobs, A.H., C. Dittmar, A. Winkeler, G. Garlip, and W.D. Heiss, *Molecular imaging of gliomas*. Molecular Imaging: Official Journal of the Society for Molecular Imaging, 2002. **1**(4): p. 309-35.

48. Galldiks, N., L.W. Kracht, L. Burghaus, A. Thomas, A.H. Jacobs, W.D. Heiss, and K. Herholz, *Use of 11C-methionine PET to monitor the effects of temozolomide chemotherapy in malignant gliomas*. *European Journal of Nuclear Medicine & Molecular Imaging*, 2006. **33**(5): p. 516-24.
49. Plotkin, M., J. Eisenacher, H. Bruhn, R. Wurm, R. Michel, F. Stockhammer, A. Feussner, O. Dudeck, P. Wust, R. Felix, and H. Amthauer, *123I-IMT SPECT and 1H MR-spectroscopy at 3.0 T in the differential diagnosis of recurrent or residual gliomas: a comparative study*. *Journal of Neuro Oncology*, 2004. **70**(1): p. 49-58.
50. Le Jeune, F.P., F. Dubois, S. Blond, and M. Steinling, *Sestamibi technetium-99m brain single-photon emission computed tomography to identify recurrent glioma in adults: 201 studies*. *Journal of Neuro Oncology*, 2006. **77**(2): p. 177-83.
51. Vallejos, V., C. Balana, M. Fraile, Y. Roussos, J. Capellades, P. Cuadras, R. Ballester, A. Ley, A. Arellano, and R. Rosell, *Use of 201Tl SPECT imaging to assess the response to therapy in patients with high grade gliomas*. *Journal of Neuro Oncology*, 2002. **59**(1): p. 81-90.
52. Carpenter, C.M., B.W. Pogue, J. S., H. Dehghani, X. Wang, and K.D. Paulsen, *Image-guided optical spectroscopy provides molecular-specific information in vivo: MRI-guided spectroscopy of breast cancer hemoglobin, water and scatter size*. *Optics Letters*, 2007. **32**(8): p. 933 - 935.
53. Srinivasan, S., B.W. Pogue, J. S., H. Dehghani, C. Kogel, S. Soho, J.J. Gibson, T.D. Tosteson, S.P. Poplack, and K.D. Paulsen, *Interpreting hemoglobin and water concentration, oxygen saturation, and scattering measurements in vivo by*

- near-infrared breast tomography*. Proceedings of the National Academy of Sciences of the United States of America, 2003. **100**(21): p. 12349 - 12354.
54. Ramanujam, N., *Fluorescence Spectroscopy In Vivo*, in *Encyclopedia of Analytical Chemistry*. 2000, John Wiley & Sons Ltd.
55. Ntziachristos, V., *Fluorescence Molecular Imaging*. Annual Review of Biomedical Engineering, 2006. **8**: p. 1-33.
56. Massoud, T.F. and S.S. Gambhir, *Molecular imaging in living subjects: seeing fundamental biological processes in a new light*. Genes & Development, 2003. **17**(5): p. 545-580.
57. Sokolov, K., D. Nida, M. Descour, A. Lacy, M. Levy, B. Hall, S. Dharmawardhane, A. Ellington, B. Korgel, and R. Richards-Kortum, *Molecular Optical Imaging of Therapeutic Targets of Cancer*. Advances in Cancer Research, 2007. **96**: p. 299 - 344.
58. Kelty, C.J., N.J. Brown, M.W. Reed, and R. Ackroyd, *The use of 5-aminolaevulinic acid as a photosensitiser in photodynamic therapy and photodiagnosis*. Photochemical & Photobiological Sciences, 2002. **1**(3): p. 158-68.
59. Brown, S.B., E.A. Brown, and I. Walker, *The present and future role of photodynamic therapy in cancer treatment*. Lancet Oncology, 2004. **5**(8): p. 497-508.
60. Bech, O., D. Phillips, J. Moan, and A.J. MacRobert, *A hydroxypyridinone (CP94) enhances protoporphyrin IX formation in 5-aminolaevulinic acid treated cells*. Journal of Photochemistry & Photobiology. B Biology, 1997. **41**(1-2): p. 136-44.

61. Hinnen, P., F.W. de Rooij, M.L. van Velthuysen, A. Edixhoven, R. van Hillegersberg, H.W. Tilanus, J.H. Wilson, and P.D. Siersema, *Biochemical basis of 5-aminolaevulinic acid-induced protoporphyrin IX accumulation: a study in patients with (pre)malignant lesions of the oesophagus*. *British Journal of Cancer*, 1998. **78**(5): p. 679-82.
62. Hilf, R., J.J. Havens, and S.L. Gibson, *Effect of delta-aminolevulinic acid on protoporphyrin IX accumulation in tumor cells transfected with plasmids containing porphobilinogen deaminase DNA*. *Photochemistry & Photobiology*, 1999. **70**(3): p. 334-40.
63. Gibson, S.L., D.J. Cupriks, J.J. Havens, M.L. Nguyen, and R. Hilf, *A regulatory role for porphobilinogen deaminase (PBGD) in delta-aminolaevulinic acid (delta-ALA)-induced photosensitization?* *British Journal of Cancer*, 1998. **77**(2): p. 235-43.
64. Krieg, R.C., S. Fickweiler, O.S. Wolfbeis, and R. Knuechel, *Cell-type specific protoporphyrin IX metabolism in human bladder cancer in vitro*. *Photochemistry & Photobiology*, 2000. **72**(2): p. 226-33.
65. Gibson, S.L., J.J. Havens, L. Metz, and R. Hilf, *Is delta-aminolevulinic acid dehydratase rate limiting in heme biosynthesis following exposure of cells to delta-aminolevulinic acid?* *Photochemistry & Photobiology*, 2001. **73**(3): p. 312-7.
66. Gibson, S.L., M.L. Nguyen, J.J. Havens, A. Barbarin, and R. Hilf, *Relationship of delta-aminolevulinic acid-induced protoporphyrin IX levels to mitochondrial*

- content in neoplastic cells in vitro*. Biochemical & Biophysical Research Communications, 1999. **265**(2): p. 315-21.
67. Chang, S.C., A.J. MacRobert, J.B. Porter, and S.G. Bown, *The efficacy of an iron chelator (CP94) in increasing cellular protoporphyrin IX following intravesical 5-aminolaevulinic acid administration: an in vivo study*. Journal of Photochemistry & Photobiology. B Biology, 1997. **38**(2-3): p. 114-22.
68. Gibson, S.L., J.J. Havens, T.H. Foster, and R. Hilf, *Time-dependent intracellular accumulation of delta-aminolevulinic acid, induction of porphyrin synthesis and subsequent phototoxicity*. Photochemistry & Photobiology, 1997. **65**(3): p. 416-21.
69. Bermudez Moretti, M., S. Correa Garcia, C. Perotti, A. Batlle, and A. Casas, *Delta-Aminolevulinic acid transport in murine mammary adenocarcinoma cells is mediated by beta transporters*. British Journal of Cancer, 2002. **87**(4): p. 471-4.
70. Correa Garcia, S., A. Casas, C. Perotti, A. Batlle, and M. Bermudez Moretti, *Mechanistic studies on delta-aminolevulinic acid uptake and efflux in a mammary adenocarcinoma cell line*. British Journal of Cancer, 2003. **89**(1): p. 173-7.
71. Wyld, L., J.L. Burn, M.W. Reed, and N.J. Brown, *Factors affecting aminolaevulinic acid-induced generation of protoporphyrin IX*. British Journal of Cancer, 1997. **76**(6): p. 705-12.
72. Liang, H., D.S. Shin, Y.E. Lee, D.C. Nguyen, T.C. Trang, A.H. Pan, S.L. Huang, D.H. Chong, and M.W. Berns, *Subcellular phototoxicity of 5-aminolaevulinic acid (ALA)*. Lasers in Surgery & Medicine, 1998. **22**(1): p. 14-24.

73. Moan, J., O. Bech, J.M. Gaullier, T. Stokke, H.B. Steen, L.W. Ma, and K. Berg, *Protoporphyrin IX accumulation in cells treated with 5-aminolevulinic acid: dependence on cell density, cell size and cell cycle*. International Journal of Cancer, 1998. **75**(1): p. 134-9.
74. Wyld, L., M. Tomlinson, M.W. Reed, and N.J. Brown, *Aminolaevulinic acid-induced photodynamic therapy: cellular responses to glucose starvation*. British Journal of Cancer, 2002. **86**(8): p. 1343-7.
75. Wyld, L., M.W. Reed, and N.J. Brown, *The influence of hypoxia and pH on aminolaevulinic acid-induced photodynamic therapy in bladder cancer cells in vitro*. British Journal of Cancer, 1998. **77**(10): p. 1621-7.
76. Georgakoudi, I., P.C. Keng, and T.H. Foster, *Hypoxia significantly reduces aminolaevulinic acid-induced protoporphyrin IX synthesis in EMT6 cells*. British Journal of Cancer, 1999. **79**(9-10): p. 1372-7.
77. Bech, O., K. Berg, and J. Moan, *The pH dependency of protoporphyrin IX formation in cells incubated with 5-aminolevulinic acid*. Cancer Letters, 1997. **113**(1-2): p. 25-9.
78. Wyld, L., O. Smith, J. Lawry, M.W. Reed, and N.J. Brown, *Cell cycle phase influences tumour cell sensitivity to aminolaevulinic acid-induced photodynamic therapy in vitro*. British Journal of Cancer, 1998. **78**(1): p. 50-5.
79. Ickowicz Schwartz, D., Y. Gozlan, L. Greenbaum, T. Babushkina, D.J. Katcoff, and Z. Malik, *Differentiation-dependent photodynamic therapy regulated by porphobilinogen deaminase in B16 melanoma*. British Journal of Cancer, 2004. **90**(9): p. 1833-41.

80. Ortel, B., D. Sharlin, D. O'Donnell, A.K. Sinha, E.V. Maytin, and T. Hasan, *Differentiation enhances aminolevulinic acid-dependent photodynamic treatment of LNCaP prostate cancer cells*. *British Journal of Cancer*, 2002. **87**(11): p. 1321-7.
81. Shu, H.K., M.M. Kim, P. Chen, F. Furman, C.M. Julin, and M.A. Israel, *The intrinsic radioresistance of glioblastoma-derived cell lines is associated with a failure of p53 to induce p21(BAX) expression*. *Proceedings of the National Academy of Sciences of the United States of America*, 1998. **95**(24): p. 14453-8.
82. Weiss, W.A., M.J. Burns, C. Hackett, K. Aldape, J.R. Hill, H. Kuriyama, N. Kuriyama, N. Milshteyn, T. Roberts, M.F. Wendland, R. DePinho, and M.A. Israel, *Genetic determinants of malignancy in a mouse model for oligodendroglioma*. *Cancer Research*, 2003. **63**(7): p. 1589-95.
83. Yount, G.L., D.A. Haas-Kogan, C.A. Vidair, M. Haas, W.C. Dewey, and M.A. Israel, *Cell cycle synchrony unmask the influence of p53 function on radiosensitivity of human glioblastoma cells*. *Cancer Research*, 1996. **56**(3): p. 500-6.
84. Tennant, T.R., H. Kim, M. Sokoloff, and C.W. Rinker-Schaeffer, *The Dunning model*. *Prostate*, 2000. **43**(4): p. 295-302.
85. Momma, T., M.R. Hamblin, H.C. Wu, and T. Hasan, *Photodynamic therapy of orthotopic prostate cancer with benzoporphyrin derivative: local control and distant metastasis*. *Cancer Research*, 1998. **58**(23): p. 5425-31.
86. Savellano, M.D., B.W. Pogue, P.J. Hoopes, E.S. Vitetta, and K.D. Paulsen, *Multiepitope HER2 targeting enhances photoimmunotherapy of HER2-*

- overexpressing cancer cells with pyropheophorbide-a immunoconjugates. Cancer Research, 2005. 65(14): p. 6371-9.*
87. Givan, A.L., *Flow Cytometry First Principles*. 2001, New York: Wiley-Liss, Inc. 25 - 30.
 88. Moore, A., E. Marecos, M. Simonova, R. Weissleder, and A. Bogdanov, *Novel Gliosarcoma Cell Line Expressing Green Fluorescent Protein: A Model for Quantitative Assessment of Angiogenesis*. *Microvascular Research*, 1998. **56**: p. 145-153.
 89. Ntziachristos, V., G. Turner, J. Dunham, S. Windsor, A. Soubret, J. Ripoll, and H.A. Shih, *Planar fluorescence imaging using normalized data*. *Journal of Biomedical Optics*, 2005. **10**(6): p. 064007-1-8.
 90. Pogue, B.W., S.C. Davis, X. Song, B.A. Brooksby, H. Dehghani, and K.D. Paulsen, *Image analysis methods for diffuse optical tomography*. *Journal of Biomedical Optics*, 2006. **11**(3): p. 033001-1 - 033001-16.
 91. Gupta, A.K. and J.E. Ryder, *Photodynamic Therapy and Topical Aminolevulinic Acid An Overview*. *American Journal of Clinical Dermatology*, 2003. **4**(10): p. 699-708.
 92. Baptista, J., C. Martinez, L. Leite, and M. Cochito, *Our PDT experience in the treatment of non-melanoma skin cancer over the last 7 years*. *Journal of the European Academy of Dermatology & Venereology*, 2006. **20**(6): p. 693-7.
 93. Braathen, L.R., R.M. Szeimies, N. Basset-Seguin, R. Bissonnette, P. Foley, D. Pariser, R. Roelandts, A.M. Wennberg, C.A. Morton, and D. International Society for Photodynamic Therapy in, *Guidelines on the use of photodynamic therapy for*

- nonmelanoma skin cancer: an international consensus*. Journal of the American Academy of Dermatology, 2007. **56**(1): p. 125-43.
94. Szeimies, R.M., C.A. Morton, A. Sidoroff, and L.R. Braathen, *Photodynamic therapy for non-melanoma skin cancer*. Acta Dermato Venereologica, 2005. **85**(6): p. 483-90.
95. Jiang, S., B. Pogue, T. McBride, and M. Doyley, *Near-infrared breast tomography calibration with optoelastic tissue simulating phantoms*. Journal of Electronic Imaging, 2003. **12**(4): p. 613-620.
96. Davis, S.C., B.W. Pogue, R. Springett, C. Leussler, P. Mazurkewitz, S.B. Tuttle, S.L. Gibbs-Strauss, S. Jiang, H. Dehghani, and K.D. Paulsen, *Magnetic resonance-coupled fluorescence tomography scanner for molecular imaging of tissue*. Review of Scientific Instruments, 2008. **Accepted**.
97. Patterson, M.S., B.C. Wilson, and D.R. Wyman, *The Propagation of Optical Radiation in Tissue. II: Optical Properties of Tissues and Resulting Fluence Distributions*. Lasers in Medical Science, 1991. **6**(379 - 390).
98. Patterson, M.S., B.C. Wilson, and D.R. Wyman, *The Propagation of Optical Radiation in Tissue I. Models of Radiation Transport and their Application*. Lasers in Medical Science, 1991. **6**: p. 155 - 168.
99. Cheong, W., S.A. Prahl, and A.J. Welch, *A Review of the Optical Properties of Biological Tissues*. IEE Journal of Quantum Electronics, 1990. **26**(12): p. 2166 - 2185.

100. Mourant, J.R., J. Boyer, A.H. Hielscher, and I.J. Bigio, *Influence of the scattering phase function on light transport measurements in turbid media performed with small source-detector separation*. Optics Letters, 1996. **21**(7): p. 546 - 548.
101. van Staveren, H.J., C.J.M. Moes, J. van Marle, S.A. Prahl, and M.J.C. van Gemert, *Light scattering in Intralipid-10% in the wavelength range of 400 - 1100 nm*. Applied Optics, 1991. **30**(31): p. 4507 - 4514.
102. Schoberl, J., *NETGEN - An advancing front 2D/3D-mesh generator based on abstract rules*.
103. van der Zee, P., *Measurement and modeling of the optical properties of human tissue in the near infrared*. 1992.
104. Alexandrakis, G., F.R. Rannou, and A.F. Chatziioannou, *Tomographic bioluminescence imaging by use of a combined optical-PET (OPET) system: a computer simulation feasibility study*. Physics in Medicine and Biology, 2005. **50**: p. 4225 - 4241.
105. Dehghani, H., M.E. Eames, P.K. Yalavarthy, S.C. Davis, S. Srinivasan, C.M. Carpenter, B.W. Pogue, and K.D. Paulsen, *Near Infrared Optical Tomography using NIRFAST: Algorithms for Numerical Model and Image Reconstruction Algorithms*. Coom. Numer.Meth.Engng: Special Issue on Recent Advances in Computational Techniques for Biomedical Imaging, 2008. **Submitted**.
106. Bode, M.K., J. Ruohonen, M.T. Nieminen, and J. Phytinen, *Potential of Diffusion Imaging in Brain Tumors: A Review*. Acta Radiologica, 2006. **47**(6): p. 585 - 594.

107. Bushberg, J.T., J.A. Seibert, E.M. Leidholdt, and J.M. Boone, *The Essential Physics of Medical Imaging*. Second Edition ed. 2002, Philadelphia: Lippincott Williams & Wilkins. 395 - 413.
108. Young, G.S., *Advanced MRI of Adult Brain Tumors*. Neurologic Clinics, 2007. **25**: p. 947 - 973.
109. Lemort, M., A.C. Canizares-Perez, A. Van der Stappen, and S. Kampouridis, *Progress in magnetic resonance imaging of brain tumors*. Current Opinion in Oncology, 2007. **19**(6): p. 616 - 622.
110. Ericson, M.B., C. Sandberg, B. Stenquist, F. Gudmundson, M. Karlsson, A.M. Ros, A. Rosen, O. Larko, A.M. Wennberg, and I. Rosdahl, *Photodynamic therapy of actinic keratosis at varying fluence rates: assessment of photobleaching, pain and primary clinical outcome*. British Journal of Dermatology, 2004. **151**: p. 1204-1212.
111. Stummer, W., S. Stocker, W. Wagner, H. Stepp, F. Clemens, C. Goetz, A. Goetz, R. Kiefmann, and H.J. Reulen, *Intraperative Detection of Malignant Gliomas by 5-Aminolevulinic Acid-induced Porphyrin Fluorescence*. Neurosurgery, 1998. **42**(3): p. 518 - 526.
112. Eleouet, S., N. Rousset, J. Carre, V. Vonarx, C. Vilatte, C. Louet, Y. Lajat, and T. Patrice, *Heterogeneity of delta-aminolevulinic acid-induced protoporphyrin IX fluorescence in human glioma cells and leukemic lymphocytes*. Neurological Research, 2000. **22**: p. 361 - 368.
113. Duffner, F., R. Ritz, D. Freudenstein, M. Weller, K. Dietz, and J. Wessels, *Specific intensity imaging for glioblastoma and neural cell cultures with 5-*

- aminolevulinic acid-derived protoporphyrin IX*. Journal of Neuro-Oncology, 2005. **71**: p. 107-111.
114. Juzenas, P., V. Iani, S. Bagdonas, R. Rotomskis, and J. Moan, *Fluorescence spectroscopy of normal mouse skin exposed to 5-aminolevulinic acid and red light*. Journal of Photochemistry & Photobiology. B Biology, 2001. **61**(1-2): p. 78-86.
115. Finlay, J.C., D.L. Conover, E.L. Hull, and T.H. Foster, *Porphyrin Bleaching and PDT-induced Spectral Changes are Irradiance Dependent in ALA-sensitized Normal Rat Skin In Vivo*. Photochemistry & Photobiology, 2001. **73**(1): p. 54-63.
116. Johansson, A., T. Johansson, M.S. Thompson, N. Bendsoe, K. Svanberg, S. Svanberg, and S. Andersson-Engels, *In vivo measurement of parameters of dosimetric importance during interstitial photodynamic therapy of thick skin tumors*. Journal of Biomedical Optics, 2006. **11**(3): p. May-Jun.
117. de Bruijn, H.S., A. van der Ploeg-van den Heuvel, H.J. Sterenberg, and D.J. Robinson, *Fractionated illumination after topical application of 5-aminolevulinic acid on normal skin of hairless mice: The influence of the dark interval*. Journal of Photochemistry & Photobiology. B Biology, 2006. **85**(3): p. 184-90.
118. Nadeau, V., M. O'Dwyer, K. Hamdan, I. Tait, and M. Padgett, *In vivo measurement of 5-aminolaevulinic acid-induced protoporphyrin IX photobleaching: a comparison of red and blue light of various intensities*. Photodermatology, Photoimmunology & Photomedicine, 2004. **20**(4): p. 170-4.

119. Krishnan, S., R.D. Rao, C.D. James, and J.N. Sarkaria, *Combination of Epidermal Growth Factor Targeted Therapy with Radiation Therapy for Malignant Glioma*. *Frontiers in Bioscience*, 2003. **8**: p. e1 - 13.
120. Eller, J.L., S.L. Longo, D.J. Hicklin, and G.W. Canute, *Activity of Anti-epidermal growth factor receptor monoclonal antibody C225 against glioblastoma multiforme*. *Neurosurgery*, 2002. **51**(4): p. 1005 - 1014.
121. Luo, F.R., Z. Yang, H. Dong, A. Camuso, K. McGlinchey, K. Fager, C. Felfleh, D. Kan, I. Inigo, S. Castaneda, W.C. Rose, R.A. Kramer, R. Wild, and F.Y. Lee, *Correlation of pharmacokinetics with the antitumor activity of Cetuximab in nude mice bearing the GEO human colon carcinoma xenograft*. *Cancer Chemotherapy and Pharmacology*, 2005. **56**: p. 455 - 464.
122. Gauthier-Balin, D., J.P. Delord, P. Rochaix, V. Mallard, F. Thomas, I. Hennebelle, R. Bugat, P. Canal, and C. Allal, *In vivo and in vitro antitumor activity of oxaliplatin in combination with cetuximab in human colorectal tumor cell lines expressing different levels of EGFR*. *Cancer Chemotherapy and Pharmacology*, 2006. **57**: p. 709 - 718.
123. Raben, D., B. Helfrich, D.C. Chan, F. Ciardiello, L. Zhao, W. Franklin, A.E. Baron, C. Zeng, T.K. Johnson, and P.A. Bunn, *The Effects of Cetuximab Alone and in Combination with Radiation and/or Chemotherapy in Lung Cancer*. *Clinical Cancer Research*, 2005. **11**: p. 795 - 805.
124. Kovar, J.L., M.A. Johnson, W.M. Volcheck, J. Chen, and M.A. Simpson, *Hyaluronidase expression induces prostate tumor metastasis in an orthotopic mouse model*. *American Journal of Pathology*, 2006. **169**(4): p. 1415-26.

125. Baselga, J., *The EGFR as a target for anticancer therapy - focus on cetuximab*. European Journal of Cancer, 2001. **37**: p. S16 - S22.
126. Glunde, K., A.P. Pathak, and Z.M. Bhujwala, *Molecular-functional imaging of cancer: to image and imagine*. TRENDS in Molecular Medicine, 2007. **13**(7): p. 287 - 297.
127. Jaffer, F.A. and R. Weissleder, *Molecular Imaging in the Clinical Arena*. Journal of the American Medical Association, 2005. **293**(7): p. 855 - 862.
128. Cherry, S.R., *In vivo molecular and genomic imaging: new challenges for imaging physics*. Physics in Medicine and Biology, 2004. **49**: p. R13 - R48.
129. Weissleder, R. and U. Mahmood, *Molecular Imaging*. Radiology, 2001. **219**: p. 316 - 333.
130. Neves, A.A. and K.M. Brindle, *Assessing responses to cancer therapy using molecular imaging*. Biochimica Et Biophysica Acta, 2006. **1766**: p. 242 - 261.
131. Mischel, P.S., T.F. Cloughesy, and S.F. Nelson, *DNA-Microarray Analysis of Brain Cancer: Molecular Classification for Therapy*. Nature Reviews Neuroscience, 2004. **5**: p. 782 - 792.
132. Boudreau, C.R., I. Yang, and L.M. Liau, *Gliomas: advances in molecular analysis and characterization*. Surgical Neurology, 2005. **64**: p. 286 - 294.
133. Shinojima, N., K. Tada, S. Shiraishi, T. Kamiryo, M. Kochi, H. Nakamura, K. Makino, H. Saya, H. Hirano, J. Kuratsu, K. Oka, Y. Ishimaru, and Y. Ushio, *Prognostic Value of Epidermal Growth Factor Receptor in Patients with Glioblastoma Multiforme*. Cancer Research, 2003. **63**: p. 6962 - 6970.